Towards assimilation of deformation measurements in volcanology

Mary Grace Bato

To cite this version:

Mary Grace Bato. Towards assimilation of deformation measurements in volcanology. Volcanology. Université Grenoble Alpes, 2018. English. NNT : 2018GREAU018 . tel-01882443v2

HAL Id: tel-01882443
https://theses.hal.science/tel-01882443v2

Submitted on 1 Oct 2018

Communauté
UNIVERSITÉ Grenoble Alpes

THÈSE

Pour obtenir le grade de

DOCTEUR DE L'UNIVERSITÉ GRENOBLE ALPES

Spécialité : **Sciences de la Terre, de l'Univers et de l'Environnement**

Arrêté ministériel : 25 mai 2016

Présentée par

Mary Grace Bato

Thèse dirigée par **Virginie Pinel**
et codirigée par **Yajing Yan**

préparée au sein de **l'Institut des Sciences de la Terre**
et de l'école doctorale **Terre Univers Environnement**

Vers une assimilation des données de déformation en volcanologie

Towards the assimilation of deformation measurements in volcanology

Thèse soutenue publiquement le **02 Juillet 2018**,
devant le jury composé de :

Dr. Marie-Pierre Doin
Directrice de Recherche, CNRS, ISTerre, Université Grenoble Alpes, France, Présidente
Dr. Andrew Hooper
Professeur & Co-Directeur, IGT, University of Leeds, UK, Rapporteur
Dr. Yosuke Aoki
Professeur Adjoint, ERI, University of Tokyo, Japan, Rapporteur
Dr. Pierre Briole
Directeur de Recherche, CNRS, Ecole Normale Supérieure-Paris, France, Examinateur
Dr. Alexandre Fournier
Professeur, Institut de Physique du Globe de Paris, France, Examinateur
Dr. Emmanuel Cosme
Maître de Conférences, IGE, Université Grenoble Alpes, France, Examinateur
Dr. Jean-Luc Froger
Maître de Conférences, LMV, Université Blaise Pascal, France, Invité
Dr. Yajing Yan
Maître de Conférences, LISTIC, Université Savoie Mont Blanc, France, Co-Encadrante de thèse
Dr. Virginie Pinel
Chargé de Recherche, IRD, ISTerre, Université Savoie Mont Blanc, France, Directrice de thèse

Et tout labeur est futile, s'il n'est pas accompli avec amour.

Kahlil Gibran

Remerciements

My PhD, while unpredictable and highly non-linear in its nature, has been truly an enriching process both in terms of my scientific and personal development.

I'd like to first acknowledge the members of my jury—Dr Marie-Pierre Doin, Dr Andy Hooper, Dr Yosuke Aoki, Dr Pierre Briole, Dr Alexandre Fournier, Dr Emmanuel Cosme and Dr Jean-Luc Froger. Having such kind of jury is so surreal. I never thought that it is possible to gather the best scientists both in volcano geodesy and data assimilation for my PhD defence. I am very happy and pleased with the intense and stimulating discussions during my defence.

I'd like to thank Dr Jean-Michel Brankart as well, who took part in my "Comité de Thèse" and has reviewed the data assimilation chapter of this manuscript.

Indeed, it has been a wonderful journey with my two supervisors, Virginie Pinel and Yajing Yan. I could never succeed in any way without them. They were the "light" in the sporadic darkness of my PhD life. Yajing, being your very first PhD student was a bit terrifying—I could've either traumatized you or encouraged you to guide more students to succeed. Fingers-crossed, I hope it is the latter. Thank you for all the time and efforts you've dedicated for my PhD. Virginie, there are no sufficient words to thank you enough. You've always opened your door for discussions on any kind of topic, from magma chambers to life in general. Despite your competence in the field of volcanology, you've always remained grounded and approachable. And, I think that's truly amazing. Thank you for providing a lot of opportunities for me, for guiding the PhD while allowing some uncertainties (and craziness) and for making the journey a smooth one. More importantly, thank you for buying my jokes! I will miss our simple conversations and definitely, I will miss working with you. You have mentored me well enough to morph from a "tetard" to a grown frog (credits to Jeanne and Victor for the life cycle of a PhD student). Now, it's time to take my big leap!

My grad school journey will not be complete without thanking Jean-Luc Froger. He built my foundations on volcano geodesy, InSAR processing in particular during my master's degree. He generously and selflessly taught me the knowledge that I need to survive the PhD. Indeed, Jean-Luc, I owe a huge part of my scientific career to you. Thank you for paving the way to my success and for always being supportive of me.

Looking back, I feel content to have completed my PhD at ISTerre-Chambéry. Although this version of our lab is small, it is complete with all the necessary craziness and sanity to survive the PhD life. Léa, Hervé, Fabien, Camille, Reverso et al, Laure, Marceau, Joaquin (and Elo), Sirel, Carlos, Anais, Delphine, Antoine, Alexandre, Yaping, Zhenlu, Youzheng, Abdel, Sandrine, Timothé. We may have chosen/soon-to-choose different directions but those happy memories will always be cherished. Special words to: Léa and Hervé, my co-bureaus—the two of you kept the perfect Yin-Yang of sanity in the office. Pousse—thank you so much for the wonderful friendship and our daily nonsense chats. You made the PhD so much fun especially when we theatrically act like TOPS vs. ScanSAR satellites. Fabien, thank you for choosing to be the cool admin person and for making the administrative process painless! Antoine, the moche version of the "knight in shining armour"(peace!)—thank you for saving me in emergency situations. Delphine, thank you for being a nice and helpful pal (and a sane version of Léa). I'd also like to acknowledge the volcano team—Jean, Jean-Luc Got, Marielle, Svet, Alain, Philippe, Olivier. Special mention to Jean whom I had the pleasure to work with and Jean-Luc Got for the scientific discussions. Also thanks to Bernard Valette for all the insightful conversations about inversion, Catherine Annen and Riccardo for the helpful comments during the "répétition" of my defence, Pascale for the coffee/my-late-lunch talks and François Jouanne for all the GPS help and funny discussions. I would also like to thank the support of the cycle team at ISTerre-Grenoble, special mention to Marie-Pierre, Cécile, Erwan, Matthieu Volat for the InSAR/NSBAS discussions and Anne, Nathalie, Andrea and Aline Deprez for the EPOS GPS processing. Anne, thank you so much for making me a part of this project. I will not learn GPS processing if not for the opportunity you provided.

Of course, I'd like to thank my friends scattered around the globe who were there to support me (and make fun of me): Pat, Silvi, Lili, Maureen, Martina, the van Wyk de Vries, Lassie, Roger, Rosealito, Niki and the Orugas, Elise and the Barrientos/Pellejeras, Teves, Gel, Ivy, Ange, Markus, the Caldito-Schicks, Katiren, Engielle, Ate Lea, Maigne and Mark, Dael, Andrew, Orly, Master, Irene, Sison, the Barrientos and the Franciscos in Geneva. Special words to Silvia Vallejo, my supportive "sister" in France and of course to Pat Ramirez, for the unlimited support, understanding and for being a wonderful companion. You made the entire adventure complete and "fun" like the "la boule" ride.

Finally, I would like to sincerely thank my family (Mama, Papa, Oying and Krsna, Kuya Jon, Ate Jeng, Kitten, Jewel, and Jija) who supported my adventures and dreams despite the fact that I had to be miles away for years. Mama and Papa, I couldn't thank you enough for never giving up on me and for always understanding the big and life changing decisions I used to make. *Mahal ko po kayo.*

Para kay Tatay David at Nanay Ingga

Résumé

Le suivi de la mise en place du magma à faible profondeur et de sa migration vers la surface est crucial pour prévoir les éruptions volcaniques. Or, la prédiction des éruptions est sans doute l'un des domaines les plus difficiles en volcanologie, non seulement à cause du comportement non linéaire complexe et de l'imprévisibilité intrinsèque des volcans, mais aussi à cause de notre manque d'observation directe de ce qui se passe sous la surface. Pourtant la nécessité de fournir des prédictions précises est fondamentale, en particulier pour les agences de protection civile afin d'évaluer correctement l'aléa et de diminuer les risques.

Avec les progrès récents de l'imagerie SAR (Synthetic Aperture Radar) et le nombre croissant de réseaux GNSS (Global Navigation Satellite System) continus sur les volcans, il est maintenant possible de fournir une évolution continue et spatialement étendue des déplacements de surface pendant les périodes inter-éruptives. Pour les volcans basaltiques, ces mesures combinées à des modèles dynamiques simples peuvent être exploitées pour caractériser et contraindre la mise en pression d'un ou de plusieurs réservoirs magmatiques, ce qui fournit une meilleure information prédictive sur l'emplacement du magma à faible profondeur. L'assimilation de données—un processus séquentiel qui combine au mieux les modèles et les observations, en utilisant parfois une information a priori basée sur les statistiques des erreurs, pour prédire l'état d'un système dynamique—a récemment gagné en popularité dans divers domaines des géosciences (par exemple, les prédictions océan-météo, le géomagnétisme et l'exploration des ressources naturelles). Dans cette thèse, je présente la toute première application de l'assimilation de données en volcanologie en allant des tests synthétiques à l'utilisation de données géodésiques réelles.

La première partie de ce travail se concentre sur le développement de stratégies afin d'évaluer le potentiel de l'assimilation de données. En particulier, le filtre de Kalman d'Ensemble (EnKF) a été utilisé avec un modèle dynamique simple à deux chambres (Reverso *et al.* [2014]) et de données géodésiques synthétiques pour aborder les points suivants : 1) suivi de l'évolution de la pression magmatique en profondeur et des déplacements de surface et estimation des paramètres statiques incertains du modèle, 2) assimilation des données GNSS et InSAR, 3) mise en évidence des avantages ou des inconvénients de l'EnKF par rapport à une technique d'inversion bayésienne (par exemple, la méthode de Monte Carlo par chaîne de Markov). Les résultats montrent que l'EnKF

fonctionne de manière satisfaisante et que l'assimilation de données semble prometteuse pour la surveillance en temps réel des volcans.

La deuxième partie de la thèse est dédiée à l'application de la stratégie mise au point précédemment à l'exploitation des données GPS inter-éruptives enregistrées de 2004 à 2011 au volcan Grímsvötn en Islande, afin de tester notre capacité à prédire la rupture d'une chambre magmatique en temps réel. Nous avons introduit ici le concept de "niveau critique" basé sur l'estimation de la probabilité d'une éruption à chaque pas de temps. Cette probabilité est définie à partir de la proportion d'ensembles de modèles qui dépassent un seuil critique, initialement assigné selon une distribution donnée. Nos résultats montrent que lorsque 25 ± 1 % des ensembles du modèle ont dépassé la surpression critique une éruption est imminente. De plus, dans ce chapitre, nous élargissons également les tests synthétiques précédents en améliorant la stratégie EnKF d'assimilation des données géodésiques pour l'adapter à l'utilisation de données réelles en nombre limité. Les outils de diagnostiques couramment utilisés en assimilation de données sont mis en oeuvre et présentés.

Enfin, je démontre qu'en plus de son intérêt pour prédire les éruptions volcaniques, l'assimilation séquentielle de données géodésiques basée sur l'utilisation de l'EnKF présente un potentiel unique pour apporter une information sur l'alimentation profonde du système volcanique. En utilisant le modèle dynamique à deux réservoirs pour le système de plomberie de Grímsvötn" et en supposant une géométrie fixe et des propriétés magmatiques invariantes, nous mettons en évidence que l'apport basal en magma sous Grímsvötn" diminue de 85 % au cours des 10 mois précédant le début de l'événement de rifting de Bárdarbunga. La perte d'au moins 0.016 km^3 dans l'approvisionnement en magma de Grímsvötn" est interprétée comme une conséquence de l'accumulation de magma sous Bárdarbunga et de l'alimentation consécutive de l'éruption Holuhraun à 41 km de distance.

Abstract

Tracking magma emplacement at shallow depth as well as its migration towards the Earth's surface is crucial to forecast volcanic eruptions. Indeed, eruption forecasting is perhaps one of the most challenging field in volcanology, not only because of the complex nonlinear behavior and intrinsic unpredicitability of volcanoes but also because of our lack of direct observation on what is exactly happening underground. Yet, the need to provide accurate forecast is certainly fundamental especially for the civil protection agencies to mitigate risks and properly assess hazards.

With the recent advances in Interferometric Synthetic Aperture Radar (InSAR) imaging and the increasing number of continuous Global Navigation Satellite System (GNSS) networks recorded on volcanoes, it is now possible to provide continuous and spatially extensive evolution of surface displacements during inter-eruptive periods. For basaltic volcanoes, these measurements combined with simple dynamical models can be exploited to characterise and to constrain magma pressure building within one or several magma reservoirs, allowing better predictive information on the emplacement of magma at shallow depths. Data assimilation—a sequential time-forward process that best combines models and observations, sometimes a priori information based on error statistics, to predict the state of a dynamical system—has recently gained popularity in various fields of geosciences (e.g. ocean-weather forecasting, geomagnetism and natural resources exploration). In this dissertation, I present the very first application of data assimilation in volcanology from synthetic tests to analyzing real geodetic data.

The first part of this work focuses on the development of strategies in order to test the applicability and to assess the potential of data assimilation, in particular, the Ensemble Kalman Filter (EnKF) using a simple two-chamber dynamical model (Reverso *et al.* [2014]) and artificial geodetic data. Synthetic tests are performed in order to address the following: 1) track the magma pressure evolution at depth and reconstruct the synthetic ground surface displacements as well as estimate non-evolving uncertain model parameters, 2) properly assimilate GNSS and InSAR data, 3) highlight the strengths and weaknesses of EnKF in comparison with a Bayesian-based inversion technique (e.g. Markov Chain Monte Carlo). Results show that EnKF works well with the synthetic cases and there is a great potential in utilising data assimilation for real-time monitoring of volcanic unrest.

The second part is focused on applying the strategy that we developed through synthetic tests in order to forecast the rupture of a magma chamber in real time. We basically explored the 2004-2011 inter-eruptive dataset at Grímsvötn volcano in Iceland. Here, we introduced the concept of "eruption zones" based on the evaluation of the probability of eruption at each time step estimated as the percentage of model ensembles that exceeded their failure overpressure values initially assigned following a given distribution. Our results show that when 25 ± 1 % of the model ensembles exceeded the failure overpressure, an actual eruption is imminent. Furthermore, in this chapter, we also extend the previous synthetic tests by further enhancing the EnKF strategy of assimilating geodetic data in order to adapt to real world problems such as, the limited amount of geodetic data available to monitor ice-covered active volcanoes. Common diagnostic tools in data assimilation are presented.

Finally, I demonstrate that in addition to the interest of predicting volcanic eruptions, sequential assimilation of geodetic data on the basis of EnKF shows a unique potential to give insights into volcanic system roots. Using the two-reservoir dynamical model for Grímsvötn 's plumbing system and assuming a fixed geometry and constant magma properties, we retrieve the temporal evolution of the basal magma inflow beneath Grímsvötn that drops up to 85 % during the 10 months preceding the initiation of the Bárdarbunga rifting event. The loss of at least 0.016 km^3 in the magma supply of Grímsvötn is interpreted as a consequence of magma accumulation beneath Bárdarbunga and subsequent feeding of the Holuhraun eruption 41 km away.

Contents

List of Figures

List of Tables

Abbreviations

3DVar	Three Dimensional VARiational analysis
4DVar	Four Dimensional VARiational analysis
AIRS	Atmospheric InfraRed Sounder
AM	Adaptive Metropolis
ASTER	Advanced Spaceborne Thermal Emission and Reflection
BEM	Boundary Element Model
BLUE	Best Linear Unbiased Estimator
COSPEC	Correlation Spectroscopy
CDF	Cumulative Distribution Function
CGPS	Continuous Global Positioning System
CMB	Core-Mantle Boundary
DA	Data Assimilation
DOAS	Differential Optical Absorption Spectroscopy
DRE	Dense Rock Equivalent
EDM	Electronic Distance Measurment
EnKF	Ensemble Kalman Filter
EKF	Extended Kalman Filter
FEM	Finite Element Method
FFM	Failure Forecast Method
FTIR	Fourier Transform-Infrared Spectroscopy
GIA	Glacial Isostatic Adjustment
GNSS	Global Navigation Satellite System
GPS	Global Positioning System
IGS	International GNSS Service
IMO	Icelandic Meteorological Office
InSAR	Interferometric Synthetic Aperture Radar
KF	Kalman Filter

LEO	Low-Earth-Orbit
LOS	Line-of-Sight
LP	Long Period
MAP	Maximum A Posterior
MCMC	Markov Chain Monte Carlo
MLE	Maximum Likelihood Estimation
MODIS	MODerate-resolution Imaging Spectroradiometer
NWP	Numerical Weather Prediction
OMI	Ozone Monitoring Instrument
PDF	Probability Density Function
PSInSAR	Persistent Scatterers InSAR
RISC-GA	Random Iterated Search and Statistical Competency Generic Algorithm
RSAM	Real-time Seismic Amplitude Measurements
RSEM	Real-time Seismic Energy Measurements
SAR	Synthetic Aperture Radar
SEVIRI	Spinning Enhanced Visible and InfraRed Imager
SBAS	Small Baseline Subset
TOMS	Total Ozone Mapper Spectrometer
TOVS	TIROS Operational Vertical Sounder
TSX	TerraSAR-X
UKF	Unscented Kalman Filter
VEI	Volcanic Explosivity Index
VLP	Very Long Period
VT	Volcano-Tectonic

General Introduction

To the best of my knowledge, this manuscript—*Towards the assimilation of deformation measurements in volcanology* —is the first dissertation dedicated on the application of data assimilation in volcanology. Here, I will attempt to demonstrate the potential of EnKF from synthetic cases to assimilation of real geodetic data. Indeed, it is too ambitious to be able to totally describe all the capabilities of volcanic data assimilation in just three years of research. However, I believe that the work that I will present in this dissertation, despite its infancy, is a leap towards a better approach in combining vast amount of dataset and physics-based models not only to forecast volcanic eruptions but also to fill-in some of the gaps in our understanding of subsurface processes occuring beneath volcanoes.

I think that we are in an era in the field of geodesy, where we benefit a lot from rapid technological developments both in terms of satellite imaging of the Earth and *in situ* measurements. Permanent GNSS stations permit daily or even hourly measurements of ground deformation such that, with GNSS we can have a good temporal resolution of the evolution of ground deformation. Because of this, having permanent GNSS network installed on an active volcano has become one of the "must-haves" of a volcano observatory. Satellite-based acquisitions, in particular, the Sentinel 1 satellite, can be considered as a game changer in the scientific community providing unprecedented spatial coverage every 6-12 days. The data availability of Sentinel-1 allowed each and everyone of us to have free access to tremendous amount of SAR data around the world. In terms of volcano deformation studies, this means we can literally observe and extract signals of every deforming volcano on Earth. However, measuring and/or monitoring volcano deformation is not enough. We have to dig deeper and understand the causative processes that brought these observations. Typically, in order to fill the gaps in our understanding, we use models to interpret our data through inversion techniques. Inversion is a proven, very effective tool for volcanologists to infer parameters of the deformation source. When bayesian-based inversion such as MCMC—which is a much sophisticated inversion technique—is coupled with physics-based forward models, important questions can be addressed that are related to the processes within the volcanic system and are expressed in the form of probabilities to allow uncertainties in the results. For example, Anderson et Segall [2013] were able to demonstrate this by estimating not only the volume of the magma chamber at Mount St. Helens but also its volatile content which is several kilometers deep into the Earth. Although the model is deterministic, the results yield probabilistic estimates since their model parameters are sampled from a prior distribution and constrained by a given dataset. As a reader, you might be wondering, if all is working well with inversion, then "What else can data assimilation bring new to the volcano community?". This basic yet very challenging question is indeed the core objective of this thesis which I will attempt to answer towards the end of this manuscript.

Thesis Roadmap

Chapter 1 describes the 1) the common volcano monitoring practices with emphasis on ground deformation monitoring, 2) the development of volcano models, from kinematic to physics-based approaches used to deduce information from deformation data, and 3) the common eruption forecasting approach in terms of long- and short-term time scales.

Chapter 2 provides an overview about data assimilation, basically, the mathematical formulation as well as the elements and the two main approaches of data assimilation based on: 1) estimation theory and 2) optimal control theory. I will give focus on sequential data assimilation in particular, EnKF which is the main assimilation method used in this thesis. In the last part of this chapter, I will provide a brief review of the studies that have applied Kalman filter-based approaches to problems in volcanology as well as the recent developments in volcanic data assimilation.

Chapter 3 is primarily concerned with the development of a strategy to assimilate GNSS and InSAR data into a two-magma chamber model based on synthetic simulations. This chapter is built on the material published in *Frontiers in Earth Science* as "Assimilation of Deformation Data for Eruption Forecasting: Potentiality Assessment Based on Synthetic Cases" (Bato *et al.* [2017]).

Chapter 4 describes an application of the strategy developed in **Chapter 3**, with slight improvements on the approach, using real GNSS data recorded at Grímsvötn volcano in Iceland between 2004 and 2011 in order to forecast the rupture of a magma chamber in real time. This chapter will be submitted as "Forecasting the rupture of a magma chamber in real-time using sequential data assimilation".

Chapter 5 showcases the potential of data assimilation other than the interest of eruption forecasting. I demonstrated the unique potential of EnKF to give insights into volcanic system roots and how neighboring volcanoes, such as Bárdarbunga and Grímsvötn volcanoes in Iceland, interact. This chapter was published as "Possible deep connection between volcanic systems evidenced by sequential assimilation of geodetic data", *Nature Scientific Reports* (2018) 8:11702, https://doi.org/10.1038/s41598-018-29811-x.

Chapter 6 concludes this thesis and gives future directions about further exploitation of data assimilation in volcanology.

Chapter 1

Volcano Monitoring and Eruption Forecasting

Contents

Forecasting volcanic eruption is perhaps one of the most challenging and at the same time, one of the most exciting field in volcanology. Not only because of the complex nonlinear behavior and intrinsic unpredicitability of volcanoes (e.g. Sparks [2003]) but also because of our lack of direct observation on what is exactly happening underground. Yet, the need to provide accurate forecast on when and where the eruption will occur, how long it will last and what other impending catastrophic or transient events that might happen, is indeed fundamental especially for the civil protection group to mitigate risks and properly assess hazards.

Current practices that lead to successful eruption forecasting are mostly based on empirical pattern recognition, which relies on combining monitoring data with information from global volcanic databases, local knowledge of a volcano's past behavior (geological and historical) and scientific insights based on experience and knowledge about the volcano (Segall [2013]). In general, volcano observatories subdivide their monitoring system based on three major categories: 1) gas emission, 2) seismicity and 3) ground deformation. Although the contributions of other datasets in volcanology (e.g. electrical resistivity, gravity, magnetics, thermal anomaly and infrasound) are also acknowledged with importance. On one hand, geochemical data are used to measure gas fluxes and fumerole compositions to constrain the dynamics of magma degassing or the separation of dissolved gases from the melt as the magma moves towards weaker pressure or shallower depth. Magmatic gas fluxes in volcanic plumes allow estimation of the volume of degassing magma, magma supply rates (Allard *et al.* [1994], Sutton *et al.* [1992]) and the depth of a residing magma reservoir (Harris et Stevenson [1997], Lu et Dzurisin [2014]). Gas fluxes can also aid in detecting recently active volcanic systems (e.g. Sutton *et al.* [1992], Lu et Dzurisin [2014]). On the other hand, seismicity as well as ground deformation are often associated with the ascent of magma, such that geophysical signals recorded on active volcanoes are used to infer magma path and magma plumbing system characteristics (e.g. Swanson *et al.* [1983], Voight *et al.* [1998], Aoki *et al.* [1999], Roult *et al.* [2012], Sigmundsson *et al.* [2015]).

Geodetic observations are proven effective and have always provided meaningful insights on what is going-on beneath the Earth's surface. Traditionally, simple kinematic models are constrained by geodetic data to infer properties of magma reservoirs such as source location and volume change (Anderson et Segall [2013]). Kinematic models provide a way to interpret these surface displacements at a given time step in terms of "source" by a distribution of the displacement field at depth (i.e. displacement field induced by magma inflow) without considering the processes, forces and mechanisms at the origin of this displacement field. When they are used in inversion, a lot of information (e.g. overpressure evolution in the magma chamber) that often gives rise to the temporal evolution of the dataset is not fully exploited. Recently, major advancement in forecasting involves the development of more realistic physics-based models where diverse datasets are coupled with dynamical models of volcanic processes to relate properties of volcanic systems (Segall [2013]). Sparks [2003] have previously noted the need to evolve from forecasting based on empirical pattern recognition to forecasting based on the understanding of the physics of causative processes, and the forecast should be expressed in probabilistic terms to account for uncertainties. Recent studies in Mount St. Helens have demonstrated such idea with success by applying a probabilistic (Bayesian-based) inversion technique to a deterministic (physics-based) model and geophysical datasets such as lava dome extrusion and GPS data (Anderson et Segall [2013], Wong *et al.* [2017]).

In this chapter, I will present the common volcano monitoring practices with emphasis on ground deformation monitoring. Afterwards, I will discuss the development of volcano models, from kinematic to physics-based approaches, that are used to deduce information (e.g. change in pressure, change in volume, radius of the reservoir, etc.) from deformation data. Finally, I will briefly discuss common eruption forecasting methods in terms of: 1) long-term (i.e. also known as long-range forecasting) and 2) short-term (i.e. also known as short-range forecasting) time scales. Long-range forecasting involves interpretations of the evidences of magma emplacement at depth in storage zones (i.e. increasing pressure) which can take up to several years or decades. Determining the moment of rupture of the chamber walls is crucial since this will give an idea when the magma will further migrate after being stored in a chamber. Indeed, long-range forecasting is largely the motivation of this work by integrating a dynamical model and dense amount of incoming deformation data during inter-eruptive periods, particularly, at basaltic volcanoes. Short-range forecasting is more of intended to track the migration of magma. It could be within weeks, days or minutes prior to the eruption. In this kind of forecasting, determining if, when, and where the magma will reach the surface (e.g. Cannavò *et al.* [2015], Guldstrand *et al.* [2018]) are essential to aid in the decision-making of the authorities or civil protection groups.

1.1 Monitoring volcanic unrest

The ascent of magma towards the Earth's surface often leads to anomalous signals (precursors) that are detectable by geochemical and geophysical instruments. As the magma moves, it actually interacts with the surrounding rock, such that subsurface process occuring beneath the volcano can be recorded. The behavior of each volcano is unique, as a consequence, interpreting the precursors should be done per specific case. Volcano monitoring serves two purposes: 1) it provides deeper understanding on the physical and chemical processes that governs the volcanic system, and 2) it is crucial to mitigate risks, assess hazards and issue warnings in times of unrest (Pallister et McNutt [2015]). The 1991 Pinatubo eruption in the Philippines and the 2010 Merapi eruption in Indonesia are two of the most successful eruption forecasting in the history of mankind. Although the events are catastrophic, costing millions of euros in properties, still, thousands of lives were saved. In this section, I will discuss the monitoring practices currently implemented in volcano observatories around the world (**Figure 1.1**).

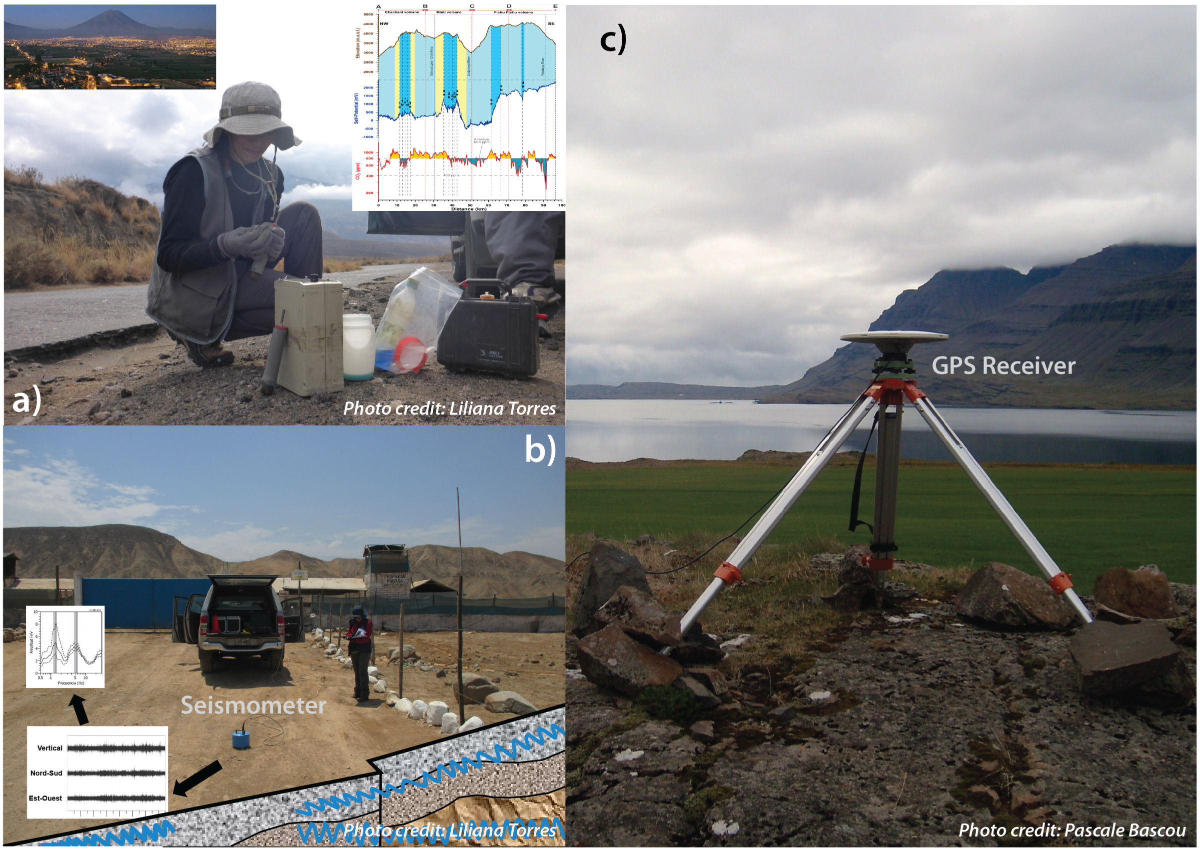

Figure 1.1: Three major monitoring practices carried out by volcano observatories around the world. Liliana Torres of the Instituto Geofísico del Perú, taking a) gas and b) seismic measurements. c) CGPS instrument for monitoring deformation installed near Hofn in Iceland.

Volcanic gases

Magmatic chambers contain gas volume fraction of volatiles (insoluble and relatively soluble gases). As the magma depressurizes during ascent, volatiles escape from the magma, leading to magma degassing which consequently supplies gas flux to the atmosphere and also lowers the density of the residing magma in the chamber. When volatiles are released as gases through active vents, fumeroles and hotsprings, they can be considered as precursors to an imminent eruption. Such that, monitoring volcanic gases have long been acknowledged as an important aspect in volcano monitoring. Magma degassing mainly controls the eruption style (i.e. explosive or effusive) by either releasing or not the magmatic pressure. It can also provide insights about the sources of magma and how magma interacts [if present] with a hydrothermal system beneath a volcano. However, the interpretation of volcanic gases alone is not always straightforward and requires expertise and years of experience.

When magma is located very deep into the Earth, it is rich in SO_2, CO_2, H_2O and HCl. However, as it moves towards lower pressure conditions, less soluble gases such as SO_2 and CO_2 are gradually lost while gases with high solubility such as H_2O and HCl are retained. Magmatic water often mixes with atmospheric and/or meteoric water hence water obviously dominates the gas emitted at the surface of the Earth. Typically, when volcanoes are reactivated, elevated volcanic gas flux is observed. If continuous degassing of magma occurs but without any injection of fresh magma into the chamber, SO_2 and CO_2 concentrations decline with time whereas H_2O concentration progressively increases due to the infiltration of surface water into the system. In 1980 at Mount St. Helens (Washington, USA), CO_2 measurements were initially high but declined slowly towards the end of 1981 as the gas was enriched in water due to the absence of new magma input (Stix et Gaonach [2000]).

Monitoring volcanic gases can also indicate if there is any transient process that occurred within the volcano (i.e. if the plumbing system was initially "open" and afterwards became partially sealed due to plug formation). Elevated magmatic gas flux and increased amounts of SO_2 and HCl are often indicative that the volcanic system is "open" whereas, the decline in magmatic gas flux and increased concentrations of CO_2 and H_2S (i.e. produced by the interaction of acidic magmatic water with meteoric water) are often associated with "closed or partially closed" system. Note that when the system is sealed, undegassed magma can result in accumulation or built-up of internal pressures within the volcano. For example, in early June of 1991, prior to the Pinatubo eruption, SO_2 flux suddenly decreased indicating that the system was sealed, pressurizing and soon to reach critical conditions for an explosive eruption (Daag *et al.* [1996], Sparks [2003]).

Measuring volcanic gases can either be done by direct sampling (i.e. from a fumerole, crater or volcanic flanks) or through ground-based (e.g. FTIR spectrometer, COSPEC, DOAS) and satellite-based remote sensing (e.g. ASTER, MODIS, OMI, SEVIRI, TOMS, TOVS). Although magma degassing plays a crucial role in understanding the behavior of a volcano, measuring volcanic gases remains challenging up to now. Direct measurements are often dangerous as it requires sampling close to the vent or crater. If the volcano is very active or in the course of unrest, sampling may only be limited (i.e. weeks, months or even years in terms of sampling interval), thus inhibits our ability to use gas emission data alone to forecast eruption. Remote sensing can often circumvent the issue, but detectability of volcanic gases other than SO_2 remains a limitation for satellite-based measurements. Basically, SO_2 emissions from satellite-based measurements are only useful when gas plumes reach high in the atmosphere, that is to say, when the eruption already occured. For a more comprehensive review of satellite measurements of global volcanic degassing, the reader should refer to Carn *et al.* [2016]. The 2018 Mayon volcano eruption provides as an example of the difficulty of using satellite data to detect and quantify SO_2 emissions. The Mayon phreatic eruption started on the 13 January 2018 followed by lava dome formation and lava flow eruption the next day. However, SO_2 gases were only detected by satellite measurements after the volcano spewed $\sim 3-5$ km of ash into the atmosphere. Ground-based gas sensors are often more useful for forecasting eruption and can complement the satellite measurements. As for the 2018 Mayon eruption, elevated SO_2 emission was measured using ground-based instruments at an average of 856 tonnes/day weeks before the unrest (PHIVOLCS [2018]).

Seismicity

Prior to volcanic eruption, as the magma finds its way to the surface, rocks are pushed apart resulting in fracturing and small earthquakes. Earthquakes are often clustered around magma chambers or on fractures associated with magma conduit or dyking events. Migrating magma can also be tracked with migrating earthquakes. As a consequence, seismicity has been used effectively for decades as a forecasting tool. Seismic monitoring is relatively cheap and more importantly, provides real-time data. To properly evaluate precursors, it requires years of gathering data to first establish a baseline for each volcano. When seismicity rates are above ambient, they usually signal magma migration that could potentially lead to eruption. Seismicity before eruption typically occurs in swarms characterized by: 1) earthquake magnitude $M < 5$, 2) many similar events of the same waveform, 3) high b-values (i.e. b is the slope in the Gutenberg-Richter relation; it is used to determine large vs. small earthquake events), and 4) occur near the eruption locations (McNutt *et al.* [2000]). In many cases, seismic precursors are often presented in terms of the number of events, energy released or RSAM/RSEM (Endo *et al.* [1996], Boué [2015]). Note that not all detected seismic events lead to eruptions (Newhall [2000], McNutt *et al.* [2000], Sparks [2003]). This is because seismic sources at volcanoes are difficult to distinguish as they involve complex interaction of melts, gases and the host rock (McNutt *et al.* [2000]).

Seismologists are adept at classifying different types of volcanic events. Four of the important types of events are: 1) High-frequency earthquakes (i.e. also known as VT events), 2) Low-frequency earthquakes (i.e. also known as LP events), 3) Explosion and 4) Tremors. VT events correspond to the formation of fractures as the magma forcibly creates its path. The number of recorded VT events is usually high at the beginning of volcanic unrest because of the accumulation of damage in the edifice of the volcano. LP events are more complex. They are possibly due to: a) resonance in magmatic conduit, b) magmatic-hydrothermal interactions, c) degassing of magma, d) brittle failure of melt, e) stick-slip of a plug (e.g. Boué [2015]). Explosion events, sometimes accompanied by shock-waves are, by its name, related to explosive eruptions. Although smaller explosions can also be detected, they are usually indicative of intense surface degassing. Volcanic tremors are periods of long-lasting vibrations that can last from minutes to years suggesting: a) the movement of magma, gas and/or hydrothermal fluids, b) excitation and resonance of fluid-filled cracks, c) magma wagging (i.e. alternate compression and restoration of gas spring force in a bubble-filled part of the magma conduit) and d) hydrothermal processes in the volcano (Newhall [2007]). The last mechanism can result in phreatic eruptions. Other recorded seismic signals on volcanoes include: 5) Hybrid earthquakes (i.e. earthquakes that share the characteristics of high- and low-frequency events), 6) Very Long Period earthquakes (i.e. also known as VLP events) and 7) Superficial events (e.g. landslides, rockfalls, glacier activities, shore ice events, pyroclastic flows, and outburst floods and lahars).

The Pinatubo 1991 plinian eruption is by far, one of the most succesful forecasting that was based mainly on seismic data. Although visual observations, reconnaissance mapping, gas emission (e.g. SO_2), and deformation (e.g. tiltmeter) were also considered. Between March and April 1991, seismicity increased at Pinatubo due to the magma rising towards the surface, roughly $\sim$ 32 km beneath the volcano. In early April, phreatic eruption occured, blasting three craters located on the North flank of the volcano. Seismic events intensified and epicenters shifted towards shallower depth beneath the NW flank near the summit of the volcano on 03 June. At the same time, tremors were also detected. By 07 June, a lava dome was emplaced. The first plinian eruption occurred on 12 June accompanied by the build up of LP events before Pinatubo's cataclysmic eruption on 15 June.

The 2014 Bárdarbunga dyking event in Iceland is another remarkable example of monitoring volcanic unrest using seismicity. Seismic data allowed scientists to actually "see-through" beneath the ground to follow the propagation of the dyke until its eruption on 29 August 2014 at Holuhraun. The volcanic unrest started as intense seismic swarm beneath Bárdarbunga volcano, followed by its $\sim$ 41 km lateral migration, overcoming topographic barriers, before breaching the surface and becoming a fissure eruption (Sigmundsson *et al.* [2015], Gudmundsson *et al.* [2016]).

Deformation

Magma from the deep part of the Earth (e.g. lower crust, CMB) migrates towards shallower depths in the form of melt "pockets" or series of dyke injections. Discontinuities within the crust allows favourable condition for these pockets of melt and/or intrusions to accumulate, forming a so-called "magma chamber" or "magma reservoir". As the chamber is continuously filled with magma, pressure increases within the system, also driven by the exsolution of gases from the melt. An excess pressure (i.e. also known as overpressure) is generated if the chamber pressure exceeds the lithostatic pressure (i.e. pressure of the surrounding rock). This continuous pressurization causes the ground to deform (i.e. inflate in this case) and can be measured as displacement, tilt or strain on the surface of the Earth. Once the overpressure reaches a critical value, the magma chamber may rupture allowing the stored magma to "leak" and further migrate towards the surface. When the overpressure is released, a "deflating" signal can be observed.

For many volcanoes, ground deformation is a powerful indicator of their long-term and short-term behaviors. Although in terms of timescales, inflation and/or deflation varies from volcano to volcano. It is worth noting that ground deformation measured on volcanoes is not only limited to the behavior of magmatic storages at depth that can be linked to volcanic unrest. Indeed, some of the deformations related to volcanic activities have been discussed by Pinel *et al.* [2014], including: a) the emplacement and displacement of erupted volcanic materials (e.g. Voight [1981], Briole *et al.* [1997], Grandin *et al.* [2010], Bato *et al.* [2016]), b) hydrothermal system activity (e.g. Vadon et Sigmundsson [1997]), c) intrusion propagation and emplacement (e.g. Froger *et al.* [2004], Sigmundsson *et al.* [2015]), d) flank sliding (e.g. Clarke *et al.* [2013], Tridon *et al.* [2016], Chen *et al.* [2017]), e) caldera collapse (e.g. De Natale *et al.* [1997], Gudmundsson *et al.* [2016], Coppola *et al.* [2017]) and glacier surface loading (e.g. Pinel *et al.* [2014], Spaans *et al.* [2015]).

Measuring ground deformation can be performed in several ways using: 1) GNSS, 2) InSAR, 3) tiltmeter, 4) strainmeter and 5) precision leveling. Although in this thesis, we have mainly developed strategies using GNSS and InSAR as they are nowadays the common tools used to study deformation on volcanoes.

GPS or more generally called as GNSS (i.e. generic term for satellite navigation systems including but not limited to GPS (US), GLONASS (Russia), Galileo (Europe) and Beidou (China)) is a constellation of satellites, where each satellite transmits radio navigation signals about its location and time at current intervals. The information is then intercepted by a receiver, which computes the distance between each satellite based on the timing of the arrival of information. The position of the receiver can be derived when these distances are combined with ephemerides for the satellite orbits and satellite clock corrections (i.e. available from commercial vendors or IGS). Multi-GNSS receivers are becoming common, allowing simultaneous measurements from multiple navigation satellite systems, therefore providing high-precision measurements. Typically, the positions are averaged in either static (i.e. daily or hourly) or kinematic mode (i.e. series of independent position at each epoch). Static mode is preferred for permanent GNSS measurements whereas kinematic mode is favoured for the campaign type of measurement (i.e. field surveying). An accuracy of ~ 1 mm for the horizontal component and ~ 3 mm for the vertical component is typical from static daily postprocessed data and about one order of magnitude higher for kinematic measurements (Freymueller *et al.* [2015]). Note that

Table 1.1: Past and present (highlighted in gray) SAR systems. The wavelengths of the satellite missions are: L-band=23.5 cm, C-band=5.6 to 5.8 cm, X-band=3 to 3.1 cm. Modified after Pinel *et al.* [2014].

Mission	**Band**	**Period of operation**	**Repeat orbit time**
SEASAT	L	Jun-Oct 1978	17 days
JERS-1		Feb 1992 to Oct 1998	44 days
ALOS		Jan 2006 to Apr 2011	46 days
ALOS-2		2014 to present	14 days
ERS-1	C	Jul 1991 to Mar 2000	3 or 35 days
ERS-2		Apr 1995 to Sep 2011	3 or 35 days
RADARSAT-1		Nov 1995 to Mar 2013	24 days
ENVISAT		Mar 2002 to Apr 2012	35 days
RADARSAT-2		Dec 2007 to present	24 days
SENTINEL-1A		Apr 2014 to present	6 or 12 days
SENTINEL-1B		Apr 2016 to present	6 or 12 days
COSMO-SKYMED	X	Jun 2007 to present	16 days
(constellation		Dec 2007 to present	16 days
of 4 satellites)		Oct 2008 to present	16 days
		Nov 2010 to present	16 days
TerraSAR-X		Jun 2007 to present	11 days
TanDEM-X		Jun 2010 to present	11 days
SIR-C/X-SAR	L,C,X	09-20 Apr 1994; 30 Sept to 11 Oct 1994	NA
SRTM	C,X	11-22 Feb 2000	NA

the vertical component is always less accurate than the horizontal component because it is more sensitive to atmospheric delays. Most active volcanoes around the world have at least one CGPS installed to monitor its activity in real-time. Indeed, a network of permanent GNSS scatterred around the volcano is an ideal monitoring system. Campaign GNSS measurements can be performed at least once a year to provide better spatial coverage, however, this painstaking fieldwork is sometimes very costly especially when the volcano of interest is in a remote area.

Radar interferometry or more commonly known as InSAR, circumvents the spatial coverage issue of GNSS. SAR technology uses the microwave region of the electromagnetic

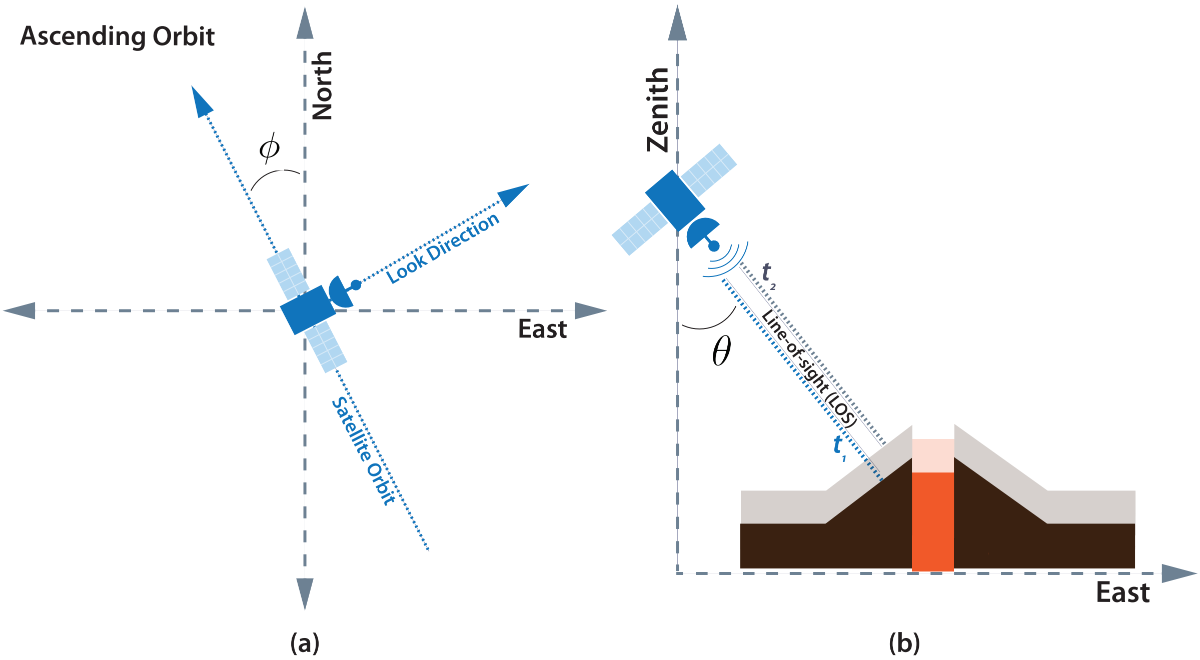

Figure 1.2: How SAR system acquires image on Earth. (a) The radar satellite follows a LEO polar orbit in a side-looking view (i.e. normally right-looking). (b) The satellite emits signal towards the LOS direction with a look angle (i.e. θ incidence angle) that varies from $20 - 50$ degrees. Radar interferometry measures the phase difference between two acquisitions (i.e. t_1 and t_2). This will give the actual ground displacement (e.g. displacement due to the inflation of the volcano) along the LOS direction.

spectrum to image the Earth, thus it can work even with the presence of clouds. SAR is usually mounted in a satellite or aircraft while orbitting the Earth. The satellite-based SAR systems, for example, move in a sun-synchronous LEO polar orbit (**Figure 1.2**). SAR satellites operate as an active system (i.e. no need for the radiation emitted by the sun), thus they have the capabilities to image the Earth during day and night. Most of the operational SAR systems today are in L, C and X-bands (**Table 1.1**). SAR images are formed when microwave signals emitted by the satellite are backscattered by the ground after it has been "illuminated" by a radar pulse. Each pixel in a radar image contains amplitude and phase information. The amplitude is the record of the reflected energy transmitted by the radar to the ground and then back to the radar. A calm water body for example, appears dark in a radar image because it acts as a perfect reflector, similar to a mirror. The incident radar wave in this case is reflected away from the satellite. Indeed, cornered structures such as built-ups (e.g. buildings, roads, bridges, roofs) appear bright in a radar image because they transmit part of the energy back to the radar sensor (i.e. multiple scattering process).

A SAR image alone cannot give information about any surface change. Obviously, at least two properly co-registered SAR images taken at two distinct dates are needed. The first image acquired by the satellite is called the “master” image which is typically the reference image. The second acqisition is called the “slave” image. This pair of SAR image can be useful to detect any surface change (e.g. emplacement of volcanic materials) by calculating the amplitude and/or phase variation. Amplitude change can be quantified by differencing the amplitude of the master and slave images or by computing for their ampitude ratio. Although in some cases, amplitude information is also used in the family of offset tracking methods to calculate for ground surface displacements. The phase variation on the other hand, can be measured by calculating the decorrelation of the pixels or “coherence”, $\hat{\gamma}$, between the two images:

$$\hat{\gamma} = \frac{\mathcal{E}[z_1 z_2]}{\sqrt{\mathcal{E}[|z_1|^2]\mathcal{E}[|z_2|^2]}} \tag{1.1}$$

where $\mathcal{E}[]$ is the expectation, z_1 and z_2 are the complex values of the images. **Figure 1.3** provides a good example on mapping and estimating the area of recently emplaced lava flow by computing for the coherence.

The principle of InSAR exploits the phase differences of the two SAR images (**Figure 1.2**). If there is a local surface displacement of the ground occurring between two acquisition, concentric pattern of “fringes” can be observed. The resulting phase map (e.g. **Figure 1.4**) is basically the sum of the phases contributed by the topography, ϕ_{topo}, orbit of the satellites, ϕ_{orb} (i.e. ϕ_{topo} and ϕ_{orb} are due to the small difference of satellite position between the two acquisitions), ground displacement, ϕ_{disp}, atmospheric delay, ϕ_{atm}, and other noise signals, ϕ_{ϵ}, (Massonnet et Feigl [1998]). Such that,

$$\Delta\phi = \phi_{topo} + \phi_{disp} + \phi_{orb} + \phi_{atm} + \phi_{\epsilon} \tag{1.2}$$

Obviously in monitoring volcanic unrest, only the phase due to the displacement of the ground is important whereas the others are corrected and/or reduced (e.g. ϕ_{orb} for example can be removed by using the satellite's orbit data). In other cases where mapping and possibly quantifying the volume of erupted volcanic deposits (e.g. lava flow emplacement and lava dome formation) are of priorities, the phase due to topography is rather retained (Bato *et al.* [2016]); provided that the temporal baseline (i.e. difference

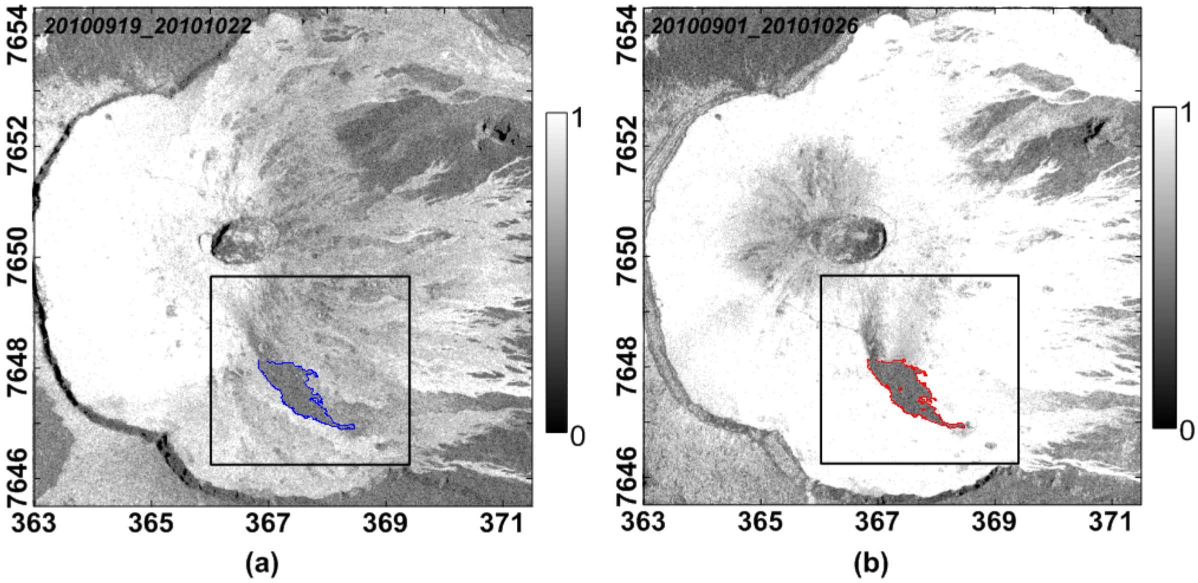

Figure 1.3: The coherence map computed from (a) ascending (20100919 and 20101022) and (b) descending (20100901 and 20101026) TSX radar data used to map the October 2010 lava flow emplacement at Piton de la Fournaise, La Reunion, France. A value close to zero signifies strong decorrelation, whereas closer to 1 means strong correlation between the master and slave images. Note that the area covered by the lava flow in (a) is 0.71 km^2 (blue outline), whereas in (b) the area is 0.75 km^2 (red outline). The maps are in UTM km coordinate systems. From Bato *et al.* [2016].

between the acquisition dates) remains small such that the magnitude of displacement can be ignored.

The ground displacement retrieved from one pair of interferogram is in fact the displacement along the LOS direction. In order to derive the three-component displacement vector, a more discriminating dataset characterized by several interfergrams having different acquisition geometries (i.e. different look angles and orbit directions) is needed (e.g. Wright *et al.* [2004],Yan [2011]).

When interferograms are stacked together, persistent deformation can be highlighted while minimizing the contribution of unwanted signals. Indeed, this can only be appropriate when the source of deformation is episodic or in steady-state (Pinel *et al.* [2014]). InSAR time-series analysis addresses decorrelation issues as well as permits the estimation of non-deformation signals. Most of the multi-temporal InSAR processing algorithms nowadays are based on: 1) PSInSAR (e.g. Perissin et Ferretti [2007], Hooper *et al.* [2004]),

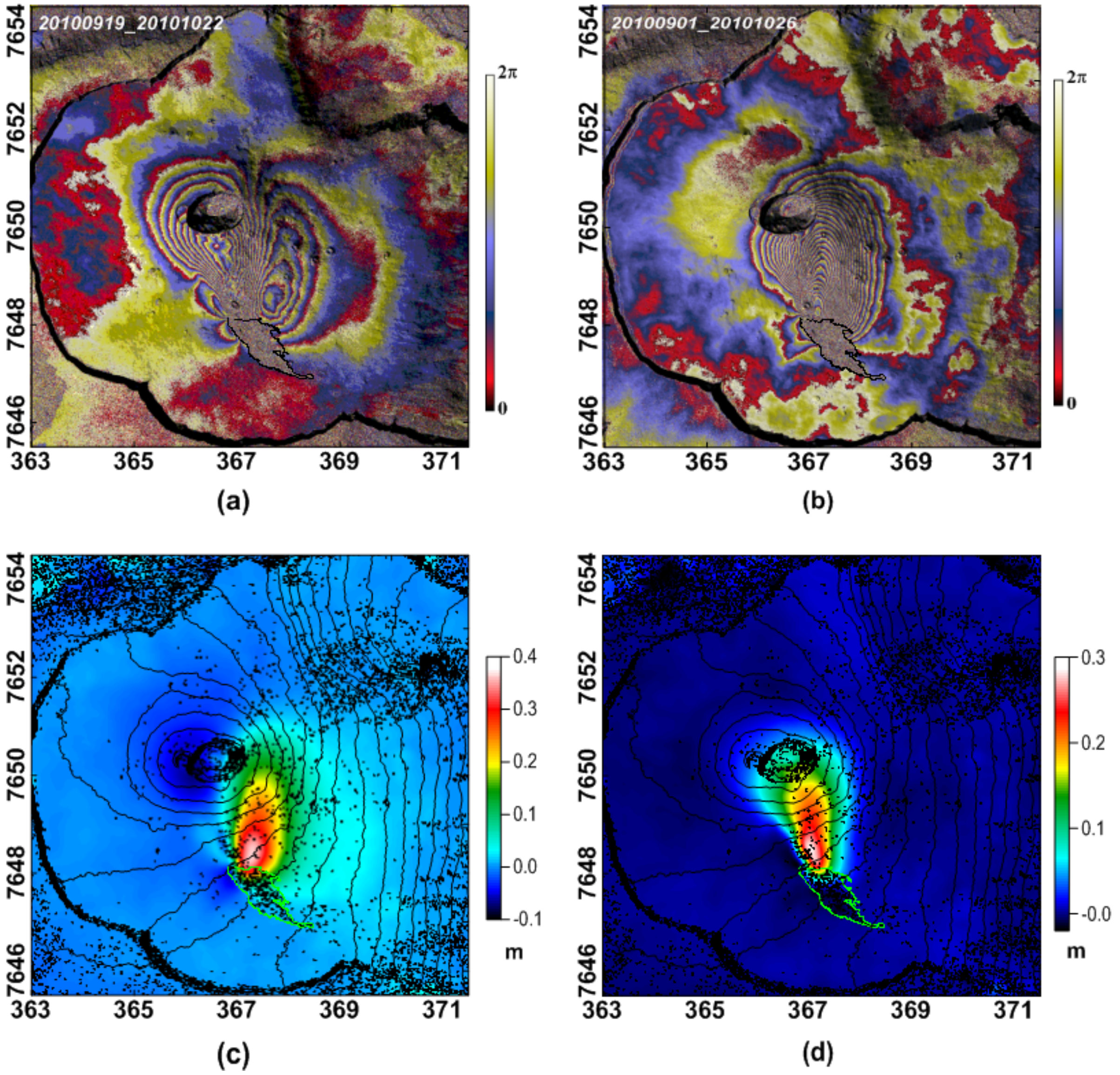

Figure 1.4: Example of InSAR ground deformation data covering the October 2010 eruption at Piton de la Fournaise, La Reunion Island, France. (a) Interferogram calculated from ascending TSX radar images. (b) Interferogram calculated from descending TSX radar images. (c) Corresponding horizontal and (d) vertical displacements, obtained from (a) and (b). The maps are in UTM km coordinate system. From Bato *et al.* [2016].

2) SBAS (e.g. Berardino *et al.* [2002], Doin *et al.* [2011]) and 3) phase linking or phase triangulation (e.g. Ferretti *et al.* [2011], Samiei-Esfahany et Hanssen [2013], Fornaro *et al.* [2015]). For a comprehensive review of PS-based and SBAS multi-temporal processing, the reader is encouraged to see Hooper *et al.* [2012]. Note however, that another huge family of multi-temporal InSAR processing methods have been developed after 2012 (e.g. Ferretti *et al.* [2011], Samiei-Esfahany et Hanssen [2013], Fornaro *et al.* [2015]). To learn more about the recent progress and application of SAR data in volcanology, see Pinel *et al.* [2014].

All in all, InSAR is a valuable tool in deformation monitoring. Although it cannot beat the [near] real-time data capability of GNSS, still, the progress in terms of temporal and spatial resolution of InSAR has escalated over the years. The launch of Sentinel-1A satellite in 2014 and Sentinel-1B in 2016 are indeed a game changer for everyone working on deformation monitoring, given that one can have access to free SAR data once every 6 or 12 days. This is crucial especially during volcanic crisis. Surely, the next challenge is how to integrate and use the large amount of datasets to fill the gaps in our understanding of Earth processes.

Tiltmeters and strainmeters are also important tools to measure ground deformation continuously. Tiltmeters measure the relative inclination due to the movement of the ground. They are known as a good indicator of deformation source geometry (Dzurisin [2003]). Wheareas borehole strainmeters measure small changes (i.e. strains on the order of 10^{-11}) in the dimension of a borehole (e.g. diameter or volume). However, both the tiltmeters and strainmeters are also known to suffer from instrument drift (Freymueller *et al.* [2015]). Moreover, strainmeters are very expensive to install and maintain and require expertise in order to properly position them in a volcano.

The 2000 Hekla eruption in Iceland is one of the most remarkable forecasting story using strainmeters. Five borehole strainmeters, located $\sim 15 - 45$ km away from the volcano detected the injection of a dyke, 30 mins before the magma reached the surface (Sturkell *et al.* [2006]). Thanks to this, along with seismic data, Icelandic scientists were able to issue aviation warning of an impending eruption $\sim$ 17 mins prior to the actual eruption (Sparks [2003]).

Precision leveling and other conventional ground surveying methods such as using EDM, theodolite and total stations, are already classified as obsolete defomation monitoring practices. Before, leveling was used to study the 1910 Usu and 1914 Sakurajima eruptions in Japan (Freymueller *et al.* [2015]). Indeed, surveying techniques still remain as the most accurate means to measure relative displacements up until today (i.e. 0.88 mm for 1 km area, Freymueller *et al.* [2015]). With the advances in GNSS technology, in particular, the installation of permanent GPS stations, these surveying techniques are only conducted when submillimeter accuracy is needed. The reason behind involves intensive amount of fieldwork and that it requires a lot of time as well as expensive logistics.

Other monitoring tools: gravity, magnetics, electrical-resistivity, thermal anomaly, water level and infrasound

Other precursory to volcanic unrest involves changes in microgravity, magnetic and electrical resistivity. However, these are typically performed irregularly since they require fieldwork and expensive logistics, and sometimes the results are ambiguous. The resolution of the resulting maps is also dependent on the density of points taken in the field. Furthermore, solid expertise and experience is crucial for modeling and more importantly for the interpretation. Microgravity measures small gravitational changes (i.e. usually in Gal units; $1 \text{ Gal} = 0.01 \text{ m s}^2$) due to variation in elevation or heteregeneities in subsurface density. Spatial variation mapping of gravity changes allows to identify buried dykes, feeder conduits and magma chamber (Freymueller *et al.* [2015]). It follows that repeated surveys can detect the addition or removal of magma. One important application of microgravity monitoring refers to its ability to distinguish changes in pressurization due to variations in mass from those that reflect exsolution of volatiles or other chemical processes (Freymueller *et al.* [2015]). Similarly, muon tomography, electrical-resistivity and magnetic monitoring can be used to model internal structures of a volcano and to characterize its plumbing system. For example, fumerolic system at Solfatara volcano in Italy was imaged using 3D resistivity tomography (Gresse *et al.* [2017]) and muon radiography was used to determine average density of geologic bodies at La Soufriére volcano in Guadeloupe (Lesparre *et al.* [2012]).

Thermal anomaly and infrasound monitoring are used in complementary with volcanic gas and seismic monitoring, respectively, especially for well-monitored active volcanoes.

The advances in satellite remote sensing permit automatic global “hotspots” (i.e. areas with anomalously high temperatures) detection (e.g. Wright *et al.* [2002, 2004]) that would indicate that an eruption already occured. But of course, these thermal anomalies can often be confused with forest fires resulting in false warnings. One advantage of detecting hotspots and taking their surface radiances during an on-going eruption allows daily estimations of lava discharge rates and volume of the lava flow (e.g. Harris *et al.* [2007]). Infrasound monitoring is rather a new field in volcano monitoring. Infrasound sensors measure sound waves below 20 GHz as a result of explosive release of fluid into the atmosphere (e.g. explosions, degassing bursts, jetting and eruption tremor, Pallister et McNutt [2015]) and can therefore act as an indicator that an eruption already happened.

Lastly, changes in water level measurements are often use as another precursory to an impending eruption. The rationale was based on the water’s response to mechanical compression or dilatation of confined aquifers (Newhall [2007]). In Mayon volcano for example, local residents typically correlate the lowering of the water table to an eruption that is soon to happen. However, in most cases of volcanic unrest worldwide, changes in water level are not often observed, therefore can be inconclusive.

Further discussion

It has long been recognized that deformation alone is not sufficient to provide comprehensive insights about the mechanism of a volcano. For example, at Campi Flegrei, three episodes of rapid uplift have been documented for the last seven decades but no eruption occurred (Kilburn *et al.* [2017]). Indeed, integrated datasets are highly recommended to ensure successful forecasting and timely delivery of warning especially to population at risk. However, geodesy as a whole, has also been proven effective to detect volcanic unrest that might have been neglected otherwise. For instance, out of the 198 volcanoes systematically monitored by InSAR, Biggs *et al.* [2014] reported that 54 deformed and 25 from these deforming volcanoes actually erupted. Moreover, several basaltic volcanoes have demonstrated pre-eruptive inflation behaviour such as: Kilauea and Mauna Loa volcanoes in Hawaii (e.g. Dvorak et Dzurisin [1993], Lengliné *et al.* [2008]), Axial Seamount in Pacific ridge (e.g. Nooner et Chadwick [2009]), Grímsvötn, Krafla and Askja volcanoes in Iceland (e.g. Sigmundsson [2006], Sturkell *et al.* [2006], Lengliné *et al.* [2008], Reverso *et al.* [2014]) and Okmok volcano in Alaska (e.g. Lu et Dzurisin [2014]). It is worth emphasizing that although magma can accumulate or be intruded at shallow depths,

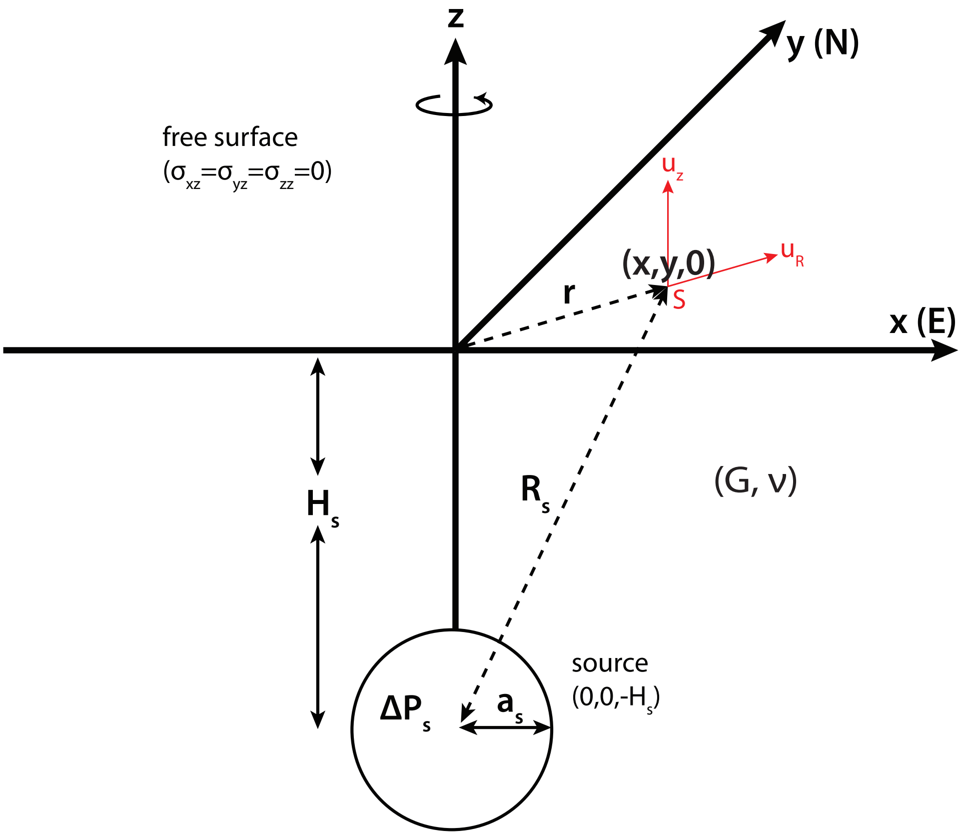

Figure 1.5: The mogi model in Cartesian coordinate system, N and E denote Northings and Eastings. H_s is the depth and a_s is the radius of the magma chamber (spherical cavity). Elastic constants, ν and G are the Poisson's ratio and shear modulus (i.e. modulus of rigidity of the medium surrounding the sphere), respectively. In practice, modelers use $\nu = 0.25$ and $G = 10 - 30$ GPa. u_R and u_z are the radial and vertical displacements measured by GNSS and/or InSAR at point S. The radial distance of S from the magma chamber is $R_s = \sqrt{x^2 + y^2 + {H_s}^2}$ whereas, from the center of the volcano axis it is given by, $r = \sqrt{x^2 + y^2}$. Modified after Mogi [1958] and Lisowski [2007].

resulting in deformation at the surface, they can be arrested by cooling and solidification or by intersection with a stress barrier (Rivalta *et al.* [2015], Biggs *et al.* [2016]). Thus, volcanic eruption may be postponed or impeded. Nonetheless, deformation can be used to detect precursors earlier than what volcanic gas and seismic monitoring can. For example, according to Sparks [2003], seismicity does not start until $\sim 10^{-4}$ of strain is exceeded. Dzurisin [2003] believes, including the author of this thesis, that the next step is to formulate a deformation monitoring strategy especially at volcanoes where magma accumulates aseismically, due to subsurface processes that are not detectable at the surface by other monitoring techniques.

1.2 Modeling deformation

Modeling deformation data is necessary not only to understand the forces that acted beneath the Earth but more importantly because it gives information regarding a potential eruption. For example, what volume of magma must be injected into the shallow reservoir to facilitate the rupture of this magma chamber and allow the magma to propagate as hydrofracture? Or perhaps, what is the critical overpressure value (or displacement value) required to initiate the tensile failure of the surrounding rock? (e.g. Pinel et Jaupart [2003], Albino *et al.* [2018]).

Scientists approach the problem by comparing or fitting the data to the model predictions provided by mathematical/numerical models. Often times, kinematic models are used because of their simplicity and convenience. As mentioned earlier, kinematic models interpret the observations without considering the processes, forces and mechanisms that lead to these observable fields. In the context of volcano source modeling, kinematic models are characterized by the location, shape and strength of the source of deformation. In many cases, these models are based on elastic half-space assumption—a first approximation of the Earth. Basically, the Earth's crust is assumed to be an ideal semi-elastic body that is materially homogeneous and mechanically isotropic, such that it behaves as an isotropic linear elastic solid (Lisowski [2007]). Laboratory tests show that rocks behave elastically at low temperatures such that this becomes a valid approximation at least for the upper crust. It follows that a viscoelastic medium is more appropriate for the lower crust.

The most famous and widely used model is the Mogi model (i.e. also known as point pressure source, Mogi [1958]) or more generally known as the spherical pressure source model after the corrections made by McTigue [1987]. The spherical source model can actually be either kinematic or dynamical, depending on how the modeler approaches the problem. If the change in volume is inferred at depth, then it is purely kinematic, however if the change in pressure is rather estimated then it becomes dynamical. Note however, that change in pressure can only be inferred if the radius of the magma chamber is quite known (e.g. obtained from tomography), otherwise, it is impossible to separate the radius and the pressure change for Mogi model. In Iceland, most of the deformation data are interpreted using this spherical pressure source (Sigmundsson [2006]). Although, there are other existing volcano source models which are tied to specific geometries such as sills, dykes, and ellipsoidal shapes (i.e. a comprehensive discussion on analytical volcano deformation source models is written by Lisowski [2007]).

In this section, I will not review all the models used in deformation modeling, rather, I will attempt to build a discussion on the development of volcano deformation source models, starting from a simple Mogi source model to more complex physics-based dynamical models (e.g. Lengliné *et al.* [2008], Anderson et Segall [2011, 2013], Reverso *et al.* [2014], Wong *et al.* [2017]). The latter offers great potential for eruption forecasting.

The point pressure source model (**Figure 1.5**) was proposed by Kiyoo Mogi after observing that the vertical and horizontal displacements at Sakurajima volcano, Japan and Kilauea volcano, Hawaii (Mogi [1958]) can be explained by the inflation and deflation of a magma body within the volcanoes. The accumulation of magma is represented as a dilating point source in an elastic half-space. Given the elastic assumptions, the 3D surface displacement generated by the hydrostatic pressure change, ΔP_s, within the spherical shell is expressed as:

$$\begin{bmatrix} u_E \\ u_N \\ u_z \end{bmatrix} = {a_s}^3 \Delta P_s \frac{(1-\nu)}{G} \begin{bmatrix} \frac{x}{{R_s}^3} \\ \frac{y}{{R_s}^3} \\ \frac{H_s}{{R_s}^3} \end{bmatrix} \tag{1.3}$$

It follows that the radial displacement can be written as, $u_R = \sqrt{{u_E}^2 + {u_N}^2}$.

One assumption of the point source model is that a_s and ΔP_s cannot be separated since they are characteristics of the source strength, C:

$$C = {a_s}^3 \Delta P_s \tag{1.4}$$

To show this, consider the two cases in **Figure 1.6**. Indeed, the same deformation field can be observed given two different sets of a_s and ΔP_s.

Mogi [1958] assumes that the radius of the magma chamber is very small compared to its depth so that it acts like a dilating point. But this is not often the case because magma bodies can be shallow and have finite shapes. McTigue [1987] introduced a correction to account for the finite shape of the source by applying higher order corrections for stresses reflected back on the source by its image (Lisowski [2007]). **Equation (1.3)** therefore becomes:

$$\begin{bmatrix} u_E \\ u_N \\ u_z \end{bmatrix} = \left(C \frac{(1-\nu)}{G} \right) \left(1 + \left(\frac{a_s}{H_s} \right)^3 \times \left(\frac{(1+\nu)}{2(-7+5\nu)} + \frac{15{H_s}^2(-2+\nu)}{4{R_s}^2(-7+5\nu)} \right) \right) \begin{bmatrix} \frac{x}{{R_s}^3} \\ \frac{y}{{R_s}^3} \\ \frac{H_s}{{R_s}^3} \end{bmatrix} \tag{1.5}$$

The first term describes the point pressure source and the second term is the correction for a finite-sized cavity. If Mogi's assumption is satisfied (i.e. $a_s << H_s$), the ratio of the radius and the depth of the cavity will approach to zero (i.e. $(a_s/H_s) \rightarrow 0$), and everything will be simplified to **equation (1.3)**.

In practice, modelers typically follow Mogi's assumption as this offers diverse applications. For example, the point pressure source is valid to represent either a magma intruding into a non pre-existing magma chamber or into a pre-existing one.

Volume estimation is one interesting advantage of using deformation data when compared with any other monitoring techniques. Deformation can directly give information about the volume of magma that flows in or out of the reservoir (ΔV_{magma}) based on the volume of the uplifted/subsided surface, $\Delta V_{edifice}$. The latter is defined as the integrated ground surface change expressed as (Sigmundsson [2006]):

$$\Delta V_{edifice} = \int_{r=0}^{\infty} u_z 2\pi r dr = 2\pi C \frac{(1-\nu)}{G} \tag{1.6}$$

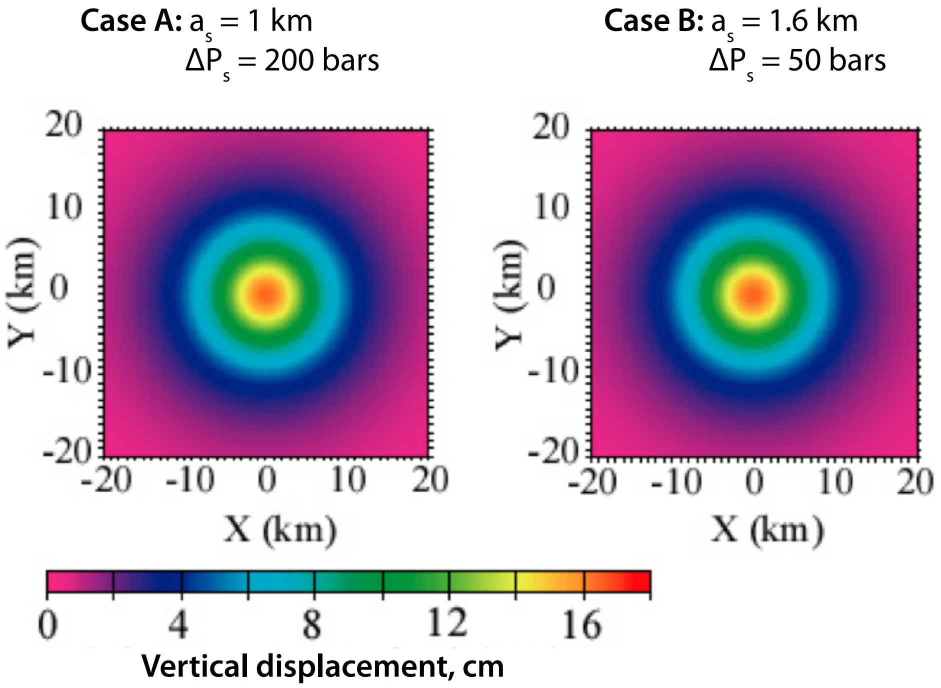

Figure 1.6: Vertical displacement maps given two different conditions of the magma reservoir: Case A) smaller radius but higher overpressure, Case B) larger radius but lower overpressure. Obviously, there is almost no difference between the two deformation maps. This example is based on Westdhal volcano, Alaska (Lu *et al.* [2000]) where an inflation of 16 cm was measured by InSAR between September 1993 and October 1998 due to an inferred 9 km deep reservoir. After Pinel [2015].

According to Delaney et McTigue [1994], for a spherical chamber, the ratio between the surface volume change, $\Delta V_{edifice}$, and the change in the chamber's volume, $\Delta V_{chamber}$, only depends on the Poisson's ratio:

$$\frac{\Delta V_{edifice}}{\Delta V_{chamber}} = 2(1-\nu) \tag{1.7}$$

This implies that for incompressible materials (i.e. $\nu = 0.5$), $\Delta V_{edifice} = \Delta V_{chamber}$. In practice, modelers use $\nu = 0.25$ (i.e. Poisson's ratio for perfectly isotropic elastic material). In this case,

$$\Delta V_{chamber} = \frac{2}{3}\Delta V_{edifice} \tag{1.8}$$

Note that the volume of expansion/contraction of the magma chamber is not necessarily equal to the volume of magma that flows in/out of the chamber (i.e. $\Delta V_{chamber} =$

ΔV_{magma}). This can be true, only if, the magma can be considered as incompressible, otherwise if the magma is considered compressible, according to Johnson *et al.* [2000]:

$$\Delta V_{magma} = \frac{\left(1 + \frac{4G}{3K}\right)}{2(1-\nu)} \Delta V_{edifice} \tag{1.9}$$

where G is the modulus of rigidity of the host rock and K is the bulk modulus of magma in the chamber.

For an oblate reservoir with a small thickness compared to its lateral dimension (i.e. sill-type), a scaling factor, $\gamma_s = \frac{8(1-\nu)}{3\pi}$, can be introduced (Amoruso et Crescentini [2009], Reverso *et al.* [2014]), **equation (1.9)** then becomes:

$$\Delta V_{magma} = \gamma_s \frac{\left(1 + \frac{4G}{3K}\right)}{2(1-\nu)} \Delta V_{edifice} \tag{1.10}$$

$$= \frac{4}{3\pi}\left(1 + \frac{4G}{3K}\right) \Delta V_{edifice} \tag{1.11}$$

and **equation (1.7)** is expressed as (i.e. if $\Delta V_{magma} = \Delta V_{chamber}$):

$$\Delta V_{magma} = \frac{4}{3\pi} \Delta V_{edifice} \tag{1.12}$$

Although the mathematics is simple and beautifully formulated to model volcanic deformation, the spherical/point pressure source is mostly used as kinematic (i.e. because it is not at all times that the radius of the reservoir is known to infer the change in pressure). Therefore, it is not well-suited for constraints given by diverse time-dependent data (Anderson et Segall [2013]). For example, the ambiguity in **Figure 1.6** can easily be determined by exploiting the temporal evolution of the displacement field considering similar magma and crustal rheologies—the pressurization of a small chamber is much quicker than the larger one. Furthermore, although we can estimate the location of the source and the surface volume change using the spherical pressure source model, the magmatic processes (e.g. evolution of the stresses) or magma properties (e.g. viscosity, magma compressibility) that give rise to the observations are difficult to obtain. Physics-based dynamical models can rather relate magmatic processes to diverse sets of time-dependent observations and allow predictions of the full evolution of the system (Anderson et Segall

[2013]).

Consider a simple case where there is a continuous flow of magma towards the magma chamber as shown in the physical model in **Figure 1.7**. Under these circumstances, magma travels towards shallow depth like a fluid flowing through a cylindrical conduit (or pipe). Assuming that the ascent of magma follows a Poiseuille flow, then we can derive the volumetric flow rate within the pipe (i.e. also equivalent to mass flux when considering a given density) using (Pinel et Jaupart [2003]):

$$Q = \frac{\pi {a_c}^4}{8\mu}\left[-\frac{dP}{dz} - \rho_m g\right] \tag{1.13}$$

where a_c is the radius of the conduit, μ is the viscosity of magma, ρ_m is the density of magma, g is the gravitational force and dP/dz is the vertical pressure gradient.

In this model, there are two different pressures acting on the magma in the conduit: 1) the [deep] source pressure, P_d, which can be considered as a constant and 2) the evolving pressure at the top of the hydraulic pipe within the magma chamber, $P_s(t)$. The latter is caused by the constant replenishment from the deep source (Lengliné *et al.* [2008]). After accounting for these pressure sources, the evolution of the flow rate, $Q(t)$, can be expressed as (Pinel et Jaupart [2003]):

$$Q(t) = \frac{\pi {a_c}^4}{8\mu H_c}\big[(\rho_r - \rho_m)gH_c + \Delta P_s(t) - \Delta P_d\big] \tag{1.14}$$

where ρ_r is the density of the surrounding rock, $\Delta P_s(t)$ is the overpressure on top of the conduit (within the magma chamber) and ΔP_d is the overpressure that corresponds to the deep source pressure. If no magma flows out of the chamber during the accumulation period, then using **equations (1.4), (1.6), (1.7) and (1.14)**, the overpressure evolution within the chamber is given by the differential equation (modified from Lengliné *et al.* [2008]):

$$\frac{d\Delta P(t)}{dt} = \frac{G a_c^4}{8\mu\gamma_s H_c a_s^3}(P - \Delta P(t)) \tag{1.15}$$

where $P = \Delta P_d - \Delta P_{s,t_0} + (\rho_r - \rho_m)gH_c$ with $\Delta P_{s,t_0}$ being an initial overpressure value.

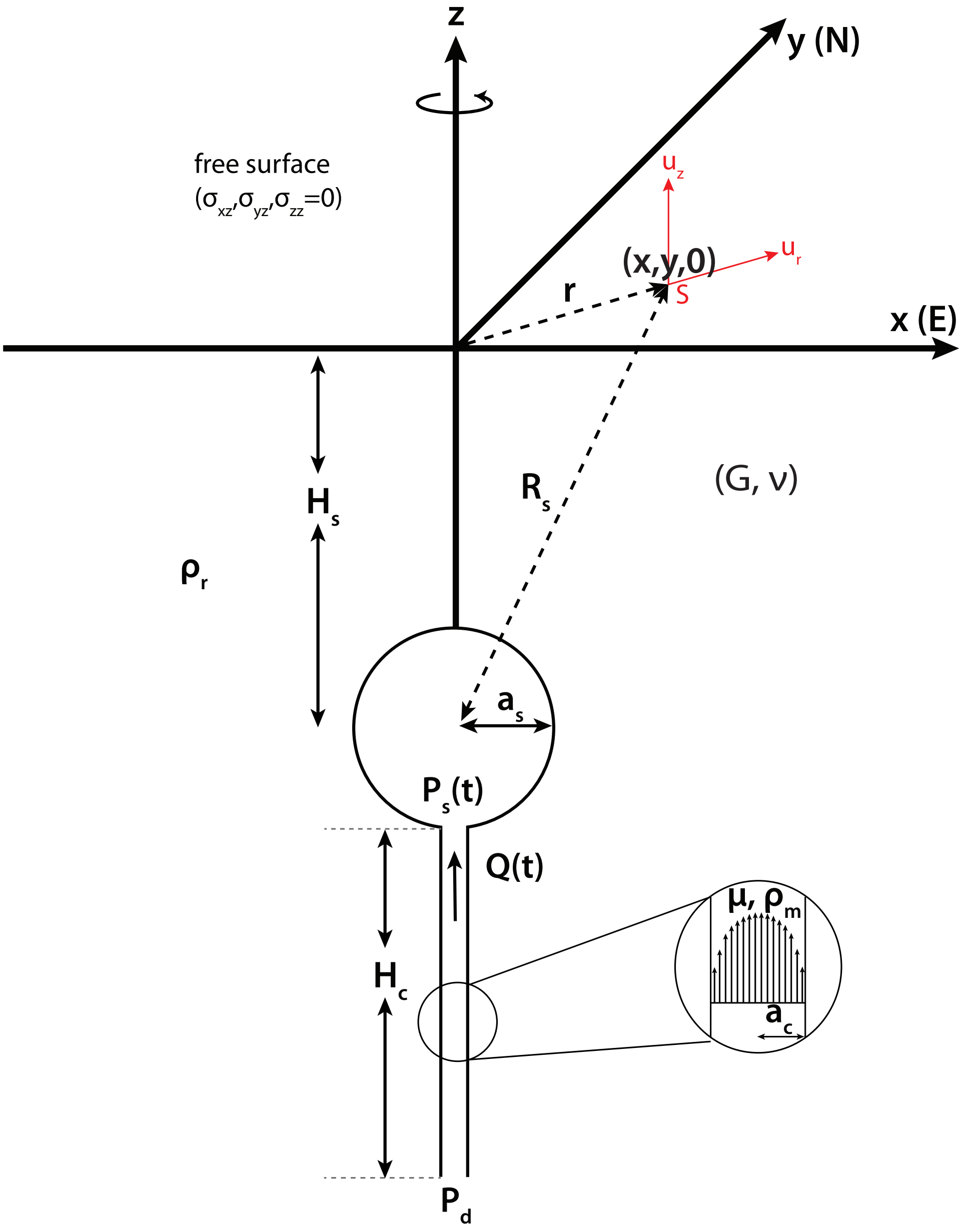

Figure 1.7: A spherical reservoir fed by constant inflow of magma through a cylindrical conduit. The model is presented in cartesian coordinate system (N and E denote Northings and Eastings). H_s is the depth and a_s is the radius of the magma chamber (spherical cavity). H_c and a_c are the length and radius of the conduit, respectively. The magma is defined by its viscosity, ν, and density, ρ_m. The host rock is characterized by its density, ρ_r, and elastic constants, ν (i.e. Poisson's ratio, $\nu = 0.25$) and G (i.e. shear modulus, $G = 10 - 30$ GPa). u_R and u_z are the radial and vertical displacements measured by GNSS and/or InSAR at point S. The radial distance of S from the magma chamber is $R_s = \sqrt{r^2 + {H_s}^2}$ where $r = \sqrt{x^2 + y^2}$ is the radial distance from the center of the volcano to point S. Modified after Lengliné *et al.* [2008].

The analytical solution to this differential equation is simply:

$$\Delta P(t) = P\left(1 - exp(\frac{-t}{\tau})\right) \tag{1.16}$$

where $\tau = \frac{8\mu\gamma_s H_c a_s^3}{G a_c^4}$. For a sill-like reservoir, $\gamma_s = \frac{8}{3\pi}(1-\nu)$ whereas for a Mogi source, $\gamma_s = 1$. It follows that **equation (1.3)** remains valid in relating the pressure evolution to the time-dependent surface displacements.

Reverso *et al.* [2014] extended the physical forward model of Lengliné *et al.* [2008] to having a deep magma reservoir fed by a basal magma inflow rate, Q_{in}, instead of having only a deep pressure source that supplies the upper magma reservoir (**Figure 1.8**). Basically, in this case, there are two magma chambers embedded in an elastic medium that are connected by a hydraulic pipe and fed by a constant basal magma inflow. The model fits well with the post-eruptive displacements observed at Grímsvötn for its last three eruptions (e.g. 1998, 2004, 2011). Instead of **equation (1.15)**, the evolution of the overpressures for the shallow and deep reservoirs are given by:

$$\Delta P_{s_{t_i}} = A(1 - e^{-\frac{t_i}{\tau}}) + \frac{GQ_{in}}{\pi({a_s}^3\gamma_s + {a_d}^3\gamma_d)}t_i + \Delta P_{s_{t_0}} \tag{1.17}$$

$$\Delta P_{d_{t_i}} = \frac{\gamma_s A}{\gamma_d}(1 - e^{-\frac{t_i}{\tau}}) + \frac{GQ_{in}}{\pi({a_s}^3\gamma_s + {a_d}^3\gamma_d)}t_i + \Delta P_{d_{t_0}} \tag{1.18}$$

with $A = \frac{{a_d}^3\gamma_d}{{a_s}^3\gamma_s + {a_d}^3\gamma_d}[\Delta P_{d_{t_0}} - \Delta P_{s_{t_0}} + (\rho_r - \rho_m)gH_c - \frac{8\gamma_s Q_{in}\mu H_c {a_s}^3}{\pi {a_c}^4({a_s}^3\gamma_s + {a_d}^3\gamma_d)}]$, a_d is the radius of the deep reservoir and γ_d is a scaling factor defined for the shape of the deep reservoir. The overpressures are related to the displacements via:

$$u_R(r, t_i) = \frac{(1-v)}{G} r\left(\alpha_s \frac{{a_s}^3}{R_s^3}\Delta P s_{t_i} + \alpha_d \frac{{a_d}^3}{R_d^3}\Delta P_{d_{t_i}}\right) \tag{1.19}$$

$$u_z(r, t_i) = \frac{(1-v)}{G}\left(H_s\alpha_s \frac{{a_s}^3}{R_s^3}\Delta P s_{t_i} + H_d\alpha_d \frac{{a_d}^3}{R_d^3}\Delta P_{d_{t_i}}\right) \tag{1.20}$$

where α_s and α_d are scaling factors for the shape of the reservoirs (i.e. 1 for Mogi source and $\frac{4H^2}{\pi R^2}$ for a sill), H_d and R_d are the depth and radial distance of the reservoir, respectively.

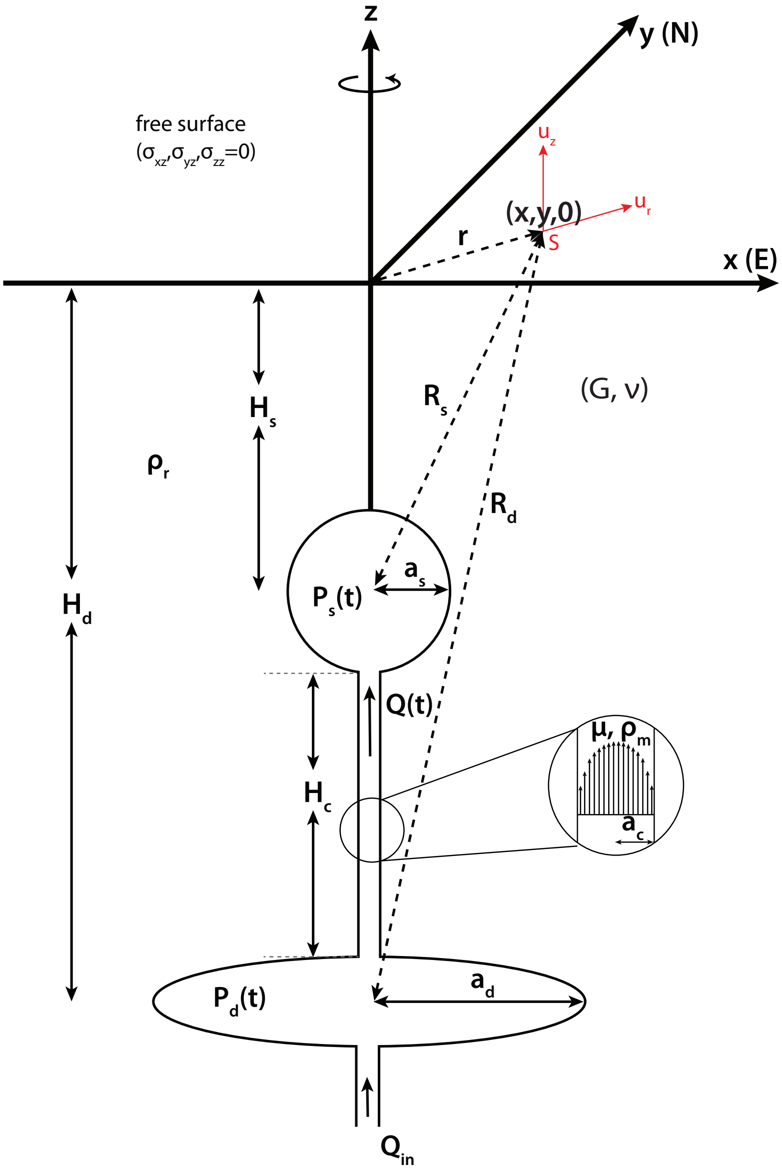

Figure 1.8: The sketch of Reverso *et al.* [2014]'s two-chamber model presented in cartesian coordinate system (N and E denote Northings and Eastings). The shallow reservoir with dimensions, H_s (depth) and a_s (radius), is connected to a deeper reservoir with dimensions, H_d (depth) and a_d (radius), by a hydraulic pipe of radius, a_c, and length, H_c. The shape of the reservoirs can either be a sill or a sphere. This would only depend on some scaling factor, $\gamma_{s,d}$ (i.e. for volume-pressure relationship) or $\alpha_{s,d}$ (i.e. for displacement-pressure relationship). The magma flowing through the hydraulic pipe is defined by its viscosity, ν, and density, ρ_m. Note that the deep reservoir is continuously fed by basal magma inflow rate, Q_{in}. The host rock is characterized by its density, ρ_r, and elastic constants, ν (i.e. Poisson's ratio, $\nu = 0.25$) and G (i.e. shear modulus, $G = 10 - 30$ GPa). u_R and u_z are the radial and vertical displacements measured by GNSS and/or InSAR at point S. The distance between S and the shallow chamber is $R_s = \sqrt{r^2 + {H_s}^2}$ whereas, $R_d = \sqrt{r^2 + {H_d}^2}$ for the deep chamber. Note that $r = \sqrt{x^2 + y^2}$ is the radial distance from the center of the volcano axis to point S. Modified after Reverso *et al.* [2014].

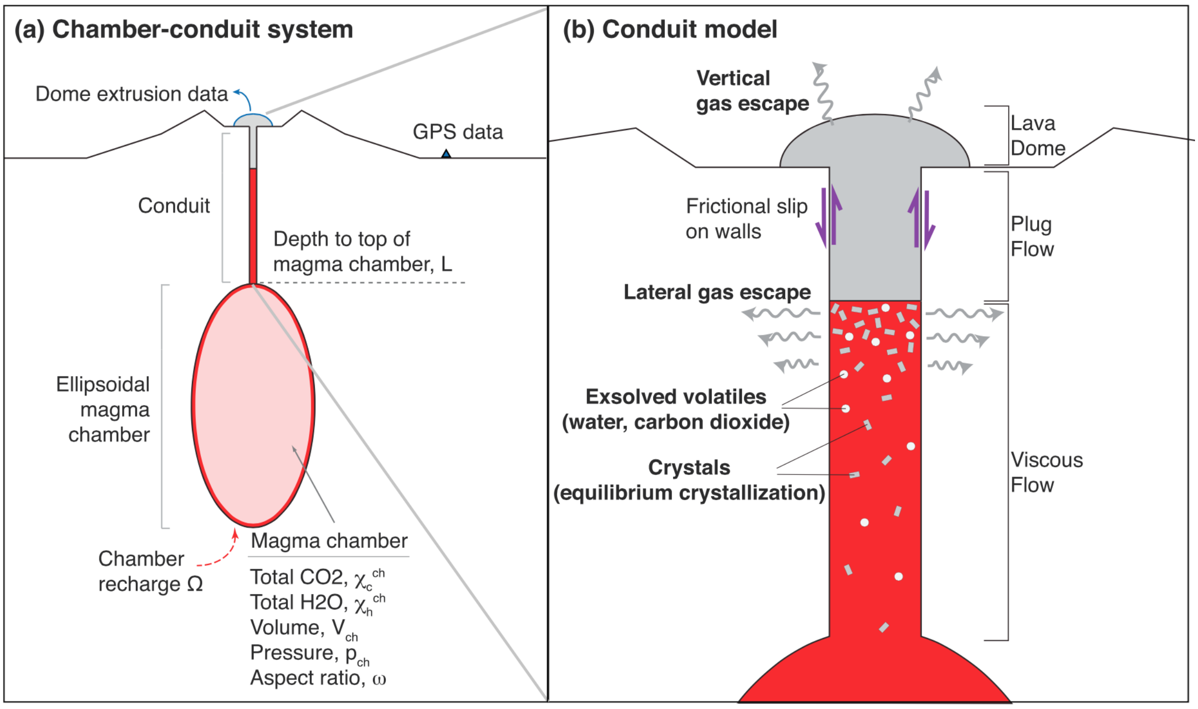

Figure 1.9: a) The physics-based forward model of Anderson et Segall [2011] for effusive silicic eruptions, which was further developed by Wong *et al.* [2017] to include gas transport and crystallization (b). After Wong *et al.* [2017].

Physics-based models that rather relate magma ascent from a magma chamber flowing to a conduit and then exiting to a vent (e.g. **Figure 1.9**) have been developed to understand intermediate and silicic eruptions (e.g. Melnik et Sparks [1999, 2002], Mastin *et al.* [2008]). Anderson et Segall [2011] developed a physics-based forward model of an effusive silicic eruption that links magmatic processes to observed time-dependent data. The authors successfully estimated the volume, pressure, depth, volatile content and properties of the conduit, by combining the model with Bayesian-based inversion (i.e. MCMC) of GPS and lava dome extrusion data of Mount St. Helens volcano, USA (Anderson et Segall [2013]). Wong *et al.* [2017] elaborated Anderson et Segall [2011]'s model to include crystallization and gas transport in the conduit to more realistically emulate phase changes during magma ascent.

Other existing models like BEM, which is also a dynamical model, can account for realistic topographies and any shape of a pressurized source (Cayol et Cornet [1997]). BEM, however, requires intensive calculations as stresses are calculated within patches or mesh.

Further discussion

Kinematic models can be considered as valuable proxies to explain the displacements measured at the surface despite the inherent simplifications in their formulation. However, because they are kinematic, the magmatic processes and/or magma properties that give rise to the time-dependent dataset are not fully and directly determined. Therefore kinematic models are not really suitable for analyzing time series of data and thus, become less interesting in terms of forecasting and undestanding the temporal behavior of a volcano.

Concerning the Reverso *et al.* [2014]'s two-chamber model, indeed, the model is based on idealized assumptions representing the complex plumbing system. For example, magma compressibility and different crustal rhelogies have so far been disregarded in the model. However, it is also worth mentioning that the two-chamber model is generic as it can represent either a single or a multiple reservoir system. The former would require that $a_d/a_s \approx \infty$ with $Q_{in} = 0$. As for the latter case, the model only represents the upper part of the multi-reservoir system. Furthermore, the two-chamber forward model can be implemented with ease and speed. Therefore it becomes an attractive tool, at least for first-order approximations, to relate the evolution of subsurface processes to time-dependent displacements observed at the surface. When coupled with an optimal estimation technique, which can also accommodate large amount of incoming data, the strategy can offer great potential to perform [near] real-time forecasting of the rupture of a magma chamber that may subsequently lead to an eruption. These arguments justify the choice of using the Reverso *et al.* [2014]'s two-chamber model as the [only] forward dynamical model used in this thesis. This choice is to first build a fast and effective data assimilation strategy which is a crucial requirement during the monitoring of volcanic unrest. Further discussion regarding the pros and cons of using this dynamical model will be presented in the succeeding parts of this work.

1.3 Eruption forecasting

The emplacement and migration of magma at shallow depth leads to precursors that can be recorded by geophysical and/or geochemical instruments signaling that the volcano is restless. Eruption forecasting can be divided in at least two phases (**Figure 1.10**): 1) long-range (i.e. forecasting up to the rupture of the magma chamber) and 2) short-range (i.e. forecasting the timing and location of a possible eruption) forecast. Geodesy allows tracking of the pressure while it builds up inside the magma chamber during inter-eruptive periods (typically in years or decades) such that scientists are able to issue long-range forecast on whether the inflating shallow magma chamber will likely to rupture or not. Indeed, this thesis is focused mainly on this time window of forecasting by using the two-chamber dynamical model and fixing a failure overpressure value that would indicate that the reservoir is already in a critical stage of rupturing. Others link seismicity to the progressive failure of rocks to model the strain weakening of rocks and the subsequent acceleration of the deformation prior to the failure of the magma chamber using the "damage" concept (Carrier *et al.* [2014], Got *et al.* [2017]). However, one limitation of the damage model is related to the downtrending pressure evolution leading to an eruption, which is actually inconsistent with what is empirically observed and the volume of extruded magma.

One of the most traditional approaches in eruption forecasting is the material failure forecast (i.e. popularly known as FFM) introduced by Voight [1988]. The basic idea of FFM is to predict the timing at which failure can be reached and eventually initiate an eruption by fitting a power law curve into the seismicity. However, its successful application in real-time eruption forecasting as in the case of the explosive eruption

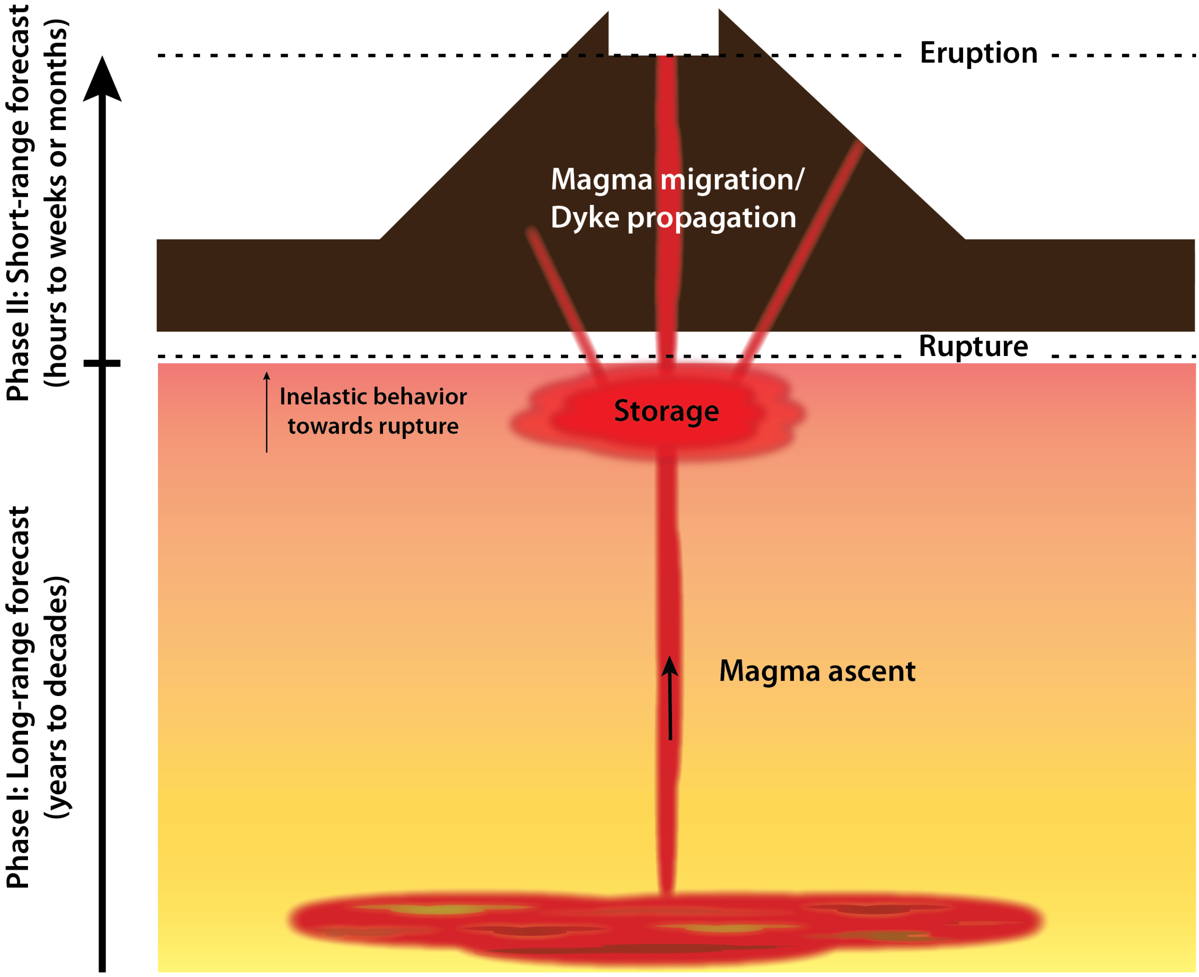

Figure 1.10: Sketch showing the two phases in eruption forecasting—long-range and short-range forecasting.

at Tungurahua volcano in Ecuador (Tárraga *et al.* [2008]), is not always the scenario especially when seismicitiy is characterized by multiple acceleration patterns (Boué *et al.* [2015]).

The fate of a rising magma or propagating dyke once tensile failure has started remains unknown. More often, the propagating magma does not get through at the surface of the Earth as they get arrested at depth. Nevertheless, once magma migration is evidenced, the exact timing and the location of the eruption needs to be estimated in real-time to ensure the timely delivery of warnings. Recent studies in tracking the migration of magma have been proposed by Cannavò *et al.* [2015] and Guldstrand *et al.* [2018], highlighting the importance of high-rate deformation data to ensure accuracy in predicting the location of its emplacement at the surface. In particular, Guldstrand *et al.* [2018] demonstrated through scaled laboratory experiments that following the evolution of the "vector" between the center of the uplifted area and the point of maximum uplift can eventually provide the timing and location of the eruption. Cannavò *et al.* [2015] takes advantage of real-time GPS data and a free geometry magmatic source model to track the inflation and deflation sources in time also allowing to estimate the location of eruption. Both studies are great examples of helpful tools to activate eruption warning in time which are indeed beneficial for the civil protection groups. Segall [2013] on the other hand, emphasized the need to combine diverse datasets, such as seismic and geodetic data to improve the "imaging" of a propagating dyke. This has been proven effective during the 2014 Bárdarbunga-Holuhraun eruption (Sigmundsson *et al.* [2015]).

Following the onset of eruption, the next step is to predict the future state of the volcano. In Segall [2013]'s work, the author was able to successfully combine the physics-based dynamical model of Anderson et Segall [2011] and MCMC inversion. The model parameters from the inversion were used as input to the physics-based forward model in order to estimate the total erupted volume at Mount St. Helens after 3.5 yrs, given only 2 yrs of data. The resulting volume agrees well with the observed eruptive volume. However, since the model does not include cooling and crystallization, it was impossible to actually determine when the eruption will cease.

Newhall [2007] is rather focused on disaster risk and mitigation as well as the timely delivery of warnings, believing that information from short-term and long-term forecast must be integrated through the use of event trees (e.g. Newhall et Hoblitt [2002], Neri *et al.* [2008], Marzocchi *et al.* [2008]) and Bayesian belief (e.g. Aspinall et Woo [2014], Hincks *et al.* [2014]) by estimating the probabilities at each node of an event tree and then performing a Bayesian update once new pieces of information come.

1.4 Summary and Perspectives

Volcano monitoring techniques allow us to record subsurface processes occuring beneath the volcano and to detect anomalous signals that can be correlated with imminent volcanic eruption. However, when used individually, they provide ambiguous analyses and sometimes unrealiable forecasting results. It has long been recognized the need to use various datasets and combine them with realistic physics-based dynamical models (Sparks [2003], Segall [2013]) in order to fill the gaps in our understanding of the causative processes that lead to volcanic unrest. In the next chapter, I will address the issue of filling the gaps in information and how one can objectively combine models and data to obtain an optimum result in forecasting.

Without a doubt, in terms of eruption forecasting, we have to move from pattern-based recognition to a more intuitive physics-based approach. The first step is to build realistic and deterministic models that we can use as a framework to include various observation datasets in a single forecast. Subsequently, these physics-based models should be coupled with a probabilistic technique in order to consider and estimate uncertainties. In this case, Bayesian-based inversion like the MCMC as adopted by Anderson et Segall [2013], demonstrated great potential to infer unknown model parameters. The estimated model parameters which are in a form of posterior distributions, can then be used as input to the physics-based forward model to allow forecasting of the next state of the system, in this case, the next behavior of the volcano. Indeed, although the model is deterministic, the results yield probabilistic forecast since the model parameters are sampled from a prior distribution and constrained by given dataset. However, inversion still has some limitations which includes: a) inefficiency to incorporate data in real time, b) model errors are often neglected during the process and c) difficulty in estimating time-dependent parameters. In the following chapters, I will address these issues by proposing a complementary tool to inversion in order to follow the evolution of the pressures within the magma chambers as well as to estimate constant and/or evolving uncertain parameters of the model.

Chapter 2

Overview of Data Assimilation

Contents

The motivation of this chapter is to present the mathematical formulation of data assimilation. I will begin by discussing the role of data assimilation in filling the gaps in information, followed by the fundamentals of data assimilation, its elements and the two main approaches of data assimilation based on: 1) ***estimation theory*** and 2) ***optimal control theory***. I will give focus on sequential data assimilation which is a subcategory of estimation theory, discussing the family of Kalman Filter methods, in particular, EnKF which is the main assimilation method used in this thesis. Then, I will present the strengths and weaknesses of the two standard techniques currently used in NWP centers—EnKF and 4DVar. Finally, I will provide a review of several studies that have applied KF-based approaches to problems in volcanology as well as the recent developments in volcanic data assimilation.

2.1 Data assimilation and the need to fill information gaps

Whether we are talking about climate change, thinning of the ozone layer, impact of natural disasters to humans or simply asking “will it rain tomorrow?”, there is the obvious need for information in order to make intelligent decisions about our future actions. Information are obtained not only from observations but also from the results of model simulations, as such, the reader should refer to this definition of information. Indeed, the more accurate the information that we have, the better that we can design our plan of actions. According to Lahoz *et al.* [2010], there is a generic chain of information processing which involves the following:

1. Gathering of information.
2. Testing of hypotheses given the information.
3. Building strategies using the information in order to change, mitigate and/or adjust to the course of events.
4. Making predictions based on these strategies.

There are two important steps in this processing chain: the first one corresponds to acquiring information and the second one is developing methodologies using these information. On one hand, observations are the measurements of a particular system-of-interest. However, because observations are discrete in space and time whereas the true state of the system is continuous, these often result in [information] gaps. Linear interpolation is one of the common ways to fill the gaps in the observations especially if a dense amount of observation is available. Although this approach is consistent [1], it is not objective and we gain little to nothing of the actual system properties that would explain these observations. Furthermore, observations are not free of noise, particularly during acquisition and pre- or post-processing. Models on the other hand, provide quantitative and/or qualitative understanding on how the system evolves (i.e. spatially and temporally) and give rise to the observations. In practice, we seek for models that are realistic and tractable. Take note that it is impossible to represent the true state of the system hence models always incorporate errors. Combining models with observations while taking into account their

---

[1] An estimator is consistent when it converges towards the true value of the parameter if the number of samples or measurements approach towards infinity

respective errors are the best way to fill information gaps. However, to determine the optimal combination that will give the best result remains a challenge.

Thanks to ***data assimilation***, one can have the "best" estimate of the state of the system objectively by either minimizing a so-called penalty function (i.e. cost function) or taking the maximum of the *a posteriori* distribution (i.e. MAP) given an *a priori* information about the state. In terms of formal definition, data assimilation refers to a set of statistical method that uses all the information available in order to improve our knowledge about the past, present and most importantly, the future state of a system. It is the opposite of a forward problem where model parameters are known and are used to estimate or predict the model state that is fully or partially observed. Data assimilation is rather an inverse problem that utilizes observations to gain information about the sources of the phenomenon under consideration. The basic concept of data assimilation consists of correcting the trajectory of a dynamical model of a phenomenon such that it will provide an optimal fit with the observations over a time window of interest (Fournier *et al.* [2010]) by controlling: 1) the state variables[2] and/or 2) other model parameters (Jarlan et Boulet [2014]). State variables are updated at each time step once observations are available (e.g. case of KF-based approaches and the Particle Filter) or corrections are made to the initial state of the state variables while using all the observations within a given time window (e.g. case of the variational techniques, Kalman Smoother-based approach). Other model parameters are adjusted or calibrated in order to reduce the discrepancy between forecasts and observations.

A rough timeline of the development of data assimilation (i.e. based on Fournier *et al.* [2010] and Cosme [2017]) is presented in **Figure 2.1**. It was initially intended for NWPs and started even before the invention of computers. Nowadays, it also gained popularity in many other fields of geosciences (e.g. natural land surfaces, hydrology, natural resource exploration and geomagnetism), including the very recent interest to solve problems in volcanology.

---

[2] Model parameters or variables that fully define the physical state of a dynamical system. They have direct link to the observations through an operator and can evolve from one step to another via model operator; also known as the prognostic variables.

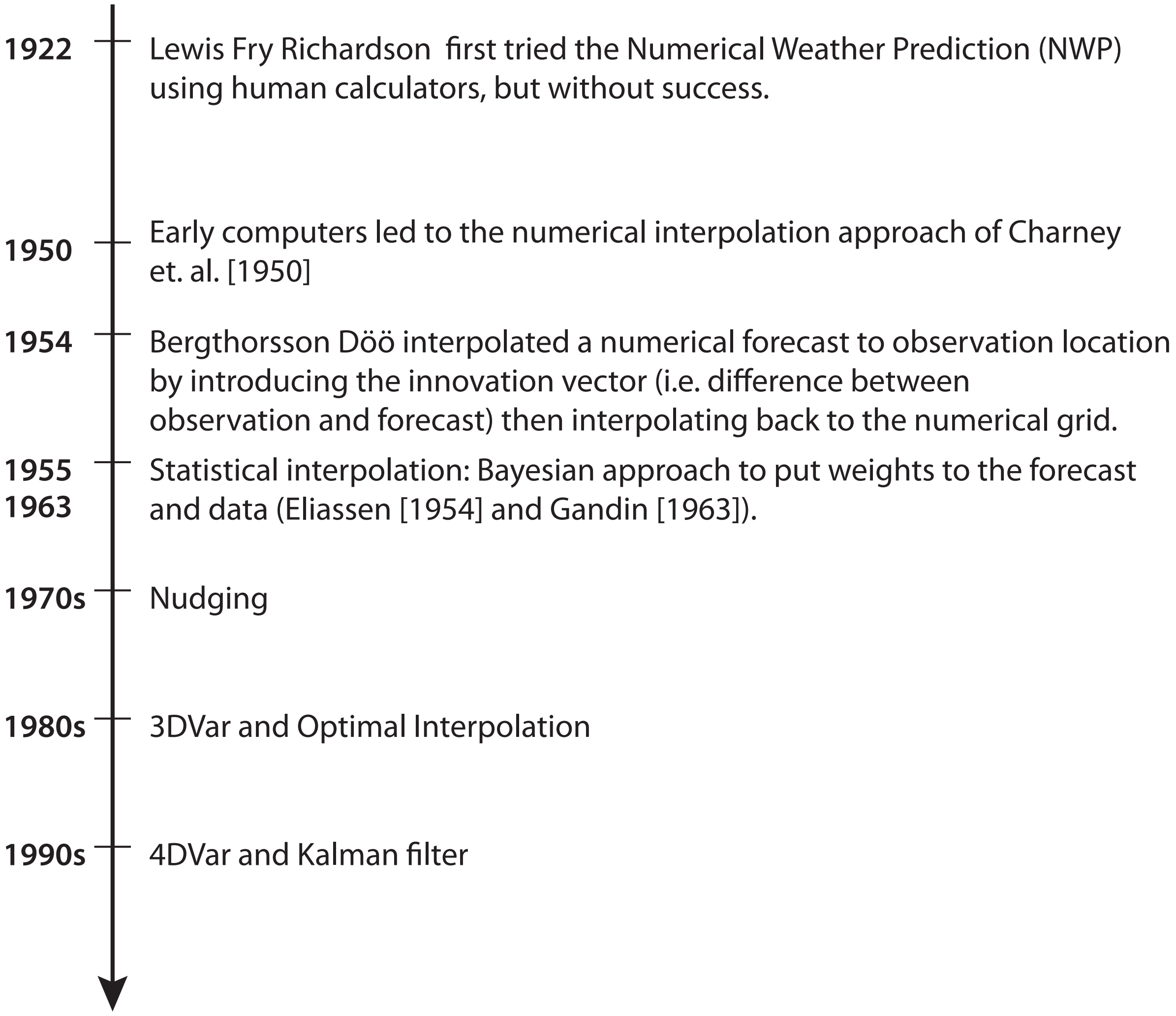

1922	Lewis Fry Richardson first tried the Numerical Weather Prediction (NWP) using human calculators, but without success.
1950	Early computers led to the numerical interpolation approach of Charney et. al. [1950]
1954	Bergthorsson Döö interpolated a numerical forecast to observation location by introducing the innovation vector (i.e. difference between observation and forecast) then interpolating back to the numerical grid.
1955 **1963**	Statistical interpolation: Bayesian approach to put weights to the forecast and data (Eliassen [1954] and Gandin [1963]).
1970s	Nudging
1980s	3DVar and Optimal Interpolation
1990s	4DVar and Kalman filter

Figure 2.1: The historical perspective of atmospheric data assimilation.

2.2 The physical system: State, observations and errors

The main elements of data assimilation include the dynamical model, the observations of all or part of the model variables, the variables related to the model variables and the error statistics. In this section I will further elaborate their definitions as presented in data assimilation.

Consider a vector, X, of size N_x. Each element of X is a variable defining the full physical state of a dynamical system (i.e. magma overpressure or volume change). However, in practice, we may also want to correct and/or estimate several variables which include control variables such as the initial conditions, the forcing function and/or uncertain model parameters (e.g. height of the conduit, radius of the reservoir, magma inflow rate and etc.). If other control variables are included in X, we call it as the ***augmented state vector***. X represents a continuous state in time and space rather than a vector of finite dimensional discrete variables. One way to represent a continuous variable consists of discretizing it:

$$X^{\dagger} = \Pi(X) \tag{2.1}$$

Π is the operator that projects the infinite dimensional space to a finite-dimensional vector and $X^{\dagger}$ is the projection or sample of X, such that, $X^{\dagger}$ can be considered as the numerical true state vector or simply the "truth". The explicit estimate of the true state $X^{\dagger}$ is written as:

$$X^{b} = X^{\dagger} + \epsilon^{b} \tag{2.2}$$

X^b stands for the ***background*** estimate of the unknown state vector X or the prior obtained from a recent forecast or model simulation, and ϵ^b is the background error.

The data measurements or vector of observations, D, with size N_m is linked to the continuous space via:

$$D = h(X) + \epsilon^{m} \tag{2.3}$$

h is the vector that maps the infinite-dimensional state into the observation space and ϵ^m is the instrumental error often related to acquisition process. Discretizing **equation**

(2.3), it then takes the form:

$$D = \mathcal{H}\Pi(X) + \epsilon^m \tag{2.4a}$$

$$D = \mathcal{H}(X^\dagger) + \epsilon^r + \epsilon^m \tag{2.4b}$$

$$D = \mathcal{H}(X^\dagger) + \epsilon \tag{2.4c}$$

$\mathcal{H}$ is the discretised observation operator that creates a link between the numerical true state and the observations, ϵ is the combined representation, ϵ^r, and instrumental errors, ϵ^m. The representation error, ϵ^r, provides an additional source of error to account for the imperfect representation of the map $\mathcal{H}$, as our knowledge of D only gives a partial and flawed information about $X^\dagger$ (Bocquet [2017]). Moroever, in some cases, there is no absolute relationship between the true state of the system and the observations. For example, in volcano deformation studies, we measure the ground deformation at the Earth's surface through ground-based or satellite-based instruments and then relate it to a reservoir beneath a volcano to infer the pressure. However, simple relationship between ground deformation and pressure such as the Mogi model (Mogi [1958]), is characterised by geometrical parameters like the radius or the depth of the reservoir, which are often an oversimplified representation of the actual shape and form of a magma reservoir. Also, traditionally, volcanologists only consider a single reservoir contributing to the surface deformation when in reality there may be multiple reservoir governing the system. All of these arguments further complicate the transformation between D and $X^\dagger$.

Note that ϵ^b and ϵ are usually uncorrelated (i.e. $\mathcal{E}\epsilon^b\epsilon^T = 0$) in data assimilation. The covariance of ϵ^b is called the background error covariance with dimension, $N_x \times N_x$. It is defined by:

$$P^b = \mathcal{E}[\epsilon^b {\epsilon^b}^T] \tag{2.5}$$

whereas the error covariance of ϵ is called the observation error covariance having a dimension, $N_m \times N_m$ and is of the form:

$$R = \mathcal{E}[\epsilon\epsilon^T] \tag{2.6}$$

A good knowledge about P^b and R are important in data assimilation, since they condition the quality of the analysis. In most cases, a diagonal matrix is used for R for the sake of simplicity, implying that observation errors are assumed independent from each other. However, temporally and/or spatially correlated noise may be present in the displacement measurement dataset. For instance, in radar interferometric data, atmospheric noise is embedded within the displacement signal over large area. Bekaert *et al.* [2016] pointed out that ignoring the covariance of InSAR measurement errors would result in treating the spatially correlated atmospheric noise as part of the signal. It is worth noting that a precise characterization of the covariance between observation errors is not always possible. An ill-estimated observation error covariance may result in erroneous estimations. In order to take into account the observation error correlation, the observation error is usually increased.

Given a discrete series of observations (i.e. $t_i = [0, 1, 2, ...K]$), **equation (2.4c)** takes the following form:

$$D_{t_{i+1}} = \mathcal{H}_{t_{i+1}}(X^{\dagger}_{t_{i+1}}) + \epsilon_{t_{i+1}} \tag{2.7}$$

In practice, we use a dynamical model, $\mathcal{M}$, to propagate the true state from one time step to another (i.e. t_i to t_{i+1}):

$$X^{\dagger}_{t_{i+1}} = \mathcal{M}_{t_{i+1}}(X^{\dagger}_{t_i}) + q_{t_{i+1}} \tag{2.8}$$

where q is the model error. The model error can be related to errors due to the: 1) misrepresentation of the system (i.e. simplification and idealization in the modeling), 2) computational grid and discretization of the model, and 3) errors related to model parameters. In the case of ***"perfect model"*** assumption, the dynamical model uniquely translates the state of the system at all times. Note that data assimilation methods may or may not consider model errors. For instance, in 4DVAR, model errors are typically neglected on the basis of "strong constraint" assumption (Talagrand [2010]) whereas in Kalman-based assimilation, the model errors are taken into account. The covariance matrix of the model error, Q, is written as:

$$Q = \mathcal{E}[qq^T] \tag{2.9}$$

Similar to R, a good knowledge about Q is necessary to satisfy the quality of the resulting state estimation.

Theoretically, it is impossible to exactly know even the numerical true state vector, thus we estimate it and the result of the optimal estimation is called the ***analysis***, X^a:

$$X^a = X^\dagger + \epsilon^a \tag{2.10}$$

The error covariance of the analysis, ϵ^a, (i.e. dimension is $N_x \times N_x$) is defined as:

$$P^a = \mathcal{E}[\epsilon^a \epsilon^{aT}] \tag{2.11}$$

2.3 Data assimilation methods

If the model and observation errors are considered as random variables, as in the case of **equations (2.7)** and **(2.8)**, the model state and observations can also be interpreted as stochastic variables allowing a Bayesian probabilistic approach of combining them to obtain an optimal estimation. In this section, I will discuss the Bayesian foundation of data assimilation followed by the mathematics behind data assimilation methods based on either the 1) estimation theory or 2) optimal control theory.

The discussion about data assimilation methods that are based on estimation theory begins with the statistical interpolation technique, in which under special conditions would lead to the BLUE equations. After that, the KF is introduced. KF is basically an extended but a more sophisticated approach of the BLUE analysis as it considers an important factor—the temporal evolution of the system. Afterwards, I will present some spin-offs of KF that were previously applied in volcanology with focus on the EnKF approach. EnKF is the assimilation method used in this thesis.

A general discussion about data assimilation methods based on optimal control theory will be presented. In particular, I will briefly introduce 3DVar and 4DVar. 3DVar is the variational equivalence of the BLUE analysis (i.e. if the errors are Gaussian) and under some conditions, the 4DVar becomes a rigorous equivalence of the KF at the end of a certain time window of interest (i.e. 1) the observation operator $\mathcal{H}$, and model operator, $\mathcal{M}$, are linear and 2) the evolution of the model is deterministic, meaning, the error of the model is negligible).

The last part of this section focuses on the advantages and limitations of EnKF and 4DVAR—the two operational methods currently used in NWP.

2.3.1 Bayesian formulation of data assimilation

Here, I will revisit the bayesian formulation discussed by Evensen [2009] as the basis of the assimilation methods. Consider the Bayes' theorem:

$$p(x|D) = \frac{p(x)p(D|x)}{p(D)} \tag{2.12}$$

where p(x|D) is the posterior density of x given observation D, $p(x)$ is the prior density for the first guess X^b, $p(D|x)$ is the likelihood of the observations given x, $p(D)$ is a normalization factor necessary to ensure that the integral of the posterior distribution is equal to one. **Equation (2.12)** can be expressed as:

$$p(x|D) \propto p(x)p(D|x) \tag{2.13}$$

Assuming that the prior and likelihood functions are Gaussian, then from **equations (2.2)** and **(2.10)** we can define:

$$x \sim \mathcal{N}(X^b, P^b), \quad p(x) \propto exp\Big(-\frac{1}{2}(x - X^b)^T P^{b^{-1}}(x - X^b)\Big) \tag{2.14}$$

and

$$D|x \sim \mathcal{N}(\mathcal{H}x, R), \quad p(D|x) \propto exp\Big(-\frac{1}{2}(D - \mathcal{H}x)^T R^{-1}(D - \mathcal{H}x)\Big) \tag{2.15}$$

This will allow us to write the posterior density as:

$$p(x|D) \propto exp\Big(-\frac{1}{2}\mathcal{J}(x)\Big) \tag{2.16}$$

where

$$\mathcal{J}(x) = \Big[(X^b - x)^T P^{b^{-1}}(X^b - x) + (D - \mathcal{H}x)^T R^{-1}(D - \mathcal{H}x)\Big] \tag{2.17}$$

The optimal solution for x (i.e. $x = X^a$) can be done in many ways, such as 1) finding the mode of $p(x|D)$ (i.e. MLE) by least squares solution or 2) computing for the minimum variance estimation (i.e. $\nabla J(x) = 0$). Note that in the case of Gaussian distribution, the least square solution is also the minimum variance estimation.

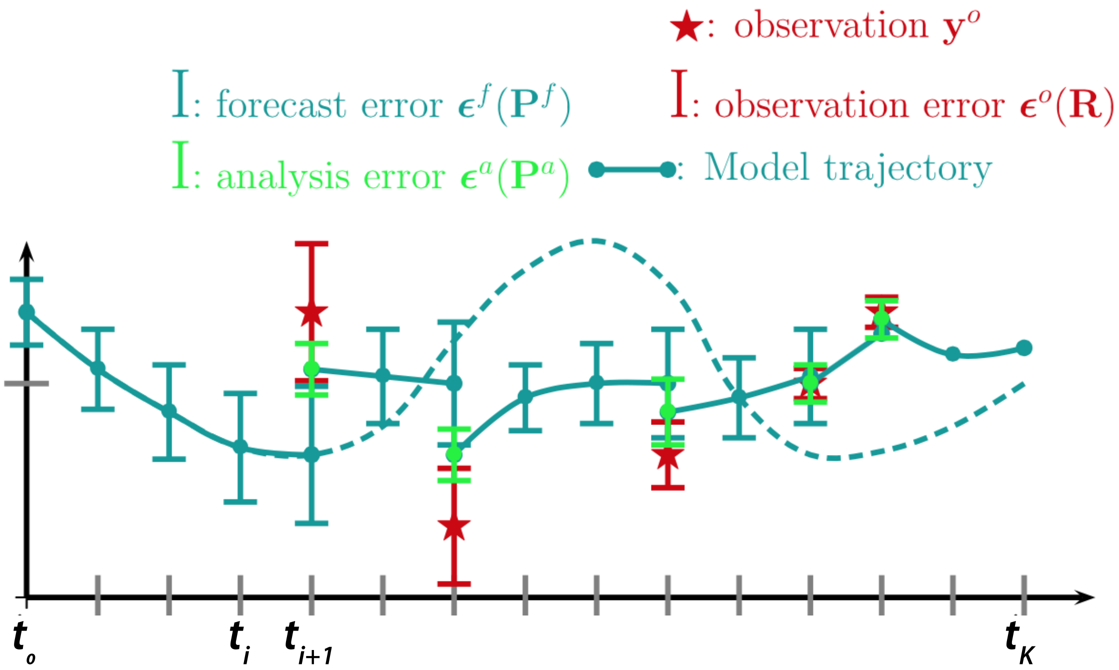

Figure 2.2: The sequential assimilation approach (from Fournier *et al.* [2010]). Given initial conditions at t_0, the model can be propagated forward without any constraints up to a time window of interest, t_K. The result is the green dashed line. Notice the growth of the forecast error while no observation (red star) is available (i.e. error bars of the green points from t_0 to t_{i+1}). When observation is entered into the sequential data assimilation method (i.e. at t_{i+1}), an analysis (bright green point characterized by a small error) is performed, correcting the trajectory of the state initially given by the forecast. The process is repeated until the next observation is available.

2.3.2 Data assimilation based on estimation theory

Statistical interpolation: Best linear unbiased estimate (BLUE)

Statistical interpolation is a basic approach that consists of extrapolating the data based on statistics and its historical behavior. Under certain conditions that the mean and covariance of the variables being estimated satistfy the BLUE analysis (i.e. optimal, linear and unbiased), the statistical interpolation becomes the “optimal” estimator.

Consider X^a as the final estimate described by the linear combination of the background state and the observations, such that:

$$X^a = AX^b + KD \tag{2.18}$$

A is a matrix of size $N_x \times N_x$ and K is a matrix of dimension $N_x \times N_m$. To achieve optimality, we seek for A and K such that:

$$\mathcal{E}[\epsilon^a] = 0 \tag{2.19}$$

$$tr(Pa) \to minimum \tag{2.20}$$

$tr(P^a)$ is the trace of the analysis error covariance. These conditions can be satisfied if:

$$A = I - K\mathcal{H} \tag{2.21}$$

$$K = P^b\mathcal{H}^T(\mathcal{H}P^b\mathcal{H}^T + R)^{-1} \tag{2.22}$$

The following analysis equation (i.e. updated **equation (2.18)**) and corresponding error covariance define the best linear unbiased estimate (BLUE) equations based on minimum variance constraint:

$$X^a = X^b + K \underbrace{(D - \mathcal{H}X^b)}_{\text{innovation vector}} \tag{2.23}$$

$$P^a = (I - K\mathcal{H})P^b \tag{2.24}$$

Sequential data assimilation: Kalman Filter

The sequential assimilation method on the basis of Kalman Filtering, extends the BLUE analysis to a temporal dimension. It introduces the dynamical model in order to simulate the real evolution of the system through time. Resulting model predictions are corrected whenever data are made available (**Figure 2.2**).

KF or often called as linear KF is the optimal sequential assimilation for linear dynamical problems initially proposed by Kalman [1960] to track the evolution of the error covariance. However, KF has been extended to further applications depending on a given time of observation, t_i. There are three possible scenarios (**Figure 2.3**) to constrain the state of the system (Kalman [1960], Fletcher [2017]):

1. If $t_i < t_K$, this is called ***data interpolation*** or ***smoothing*** problem. All observations are used to estimate the past state of the system.

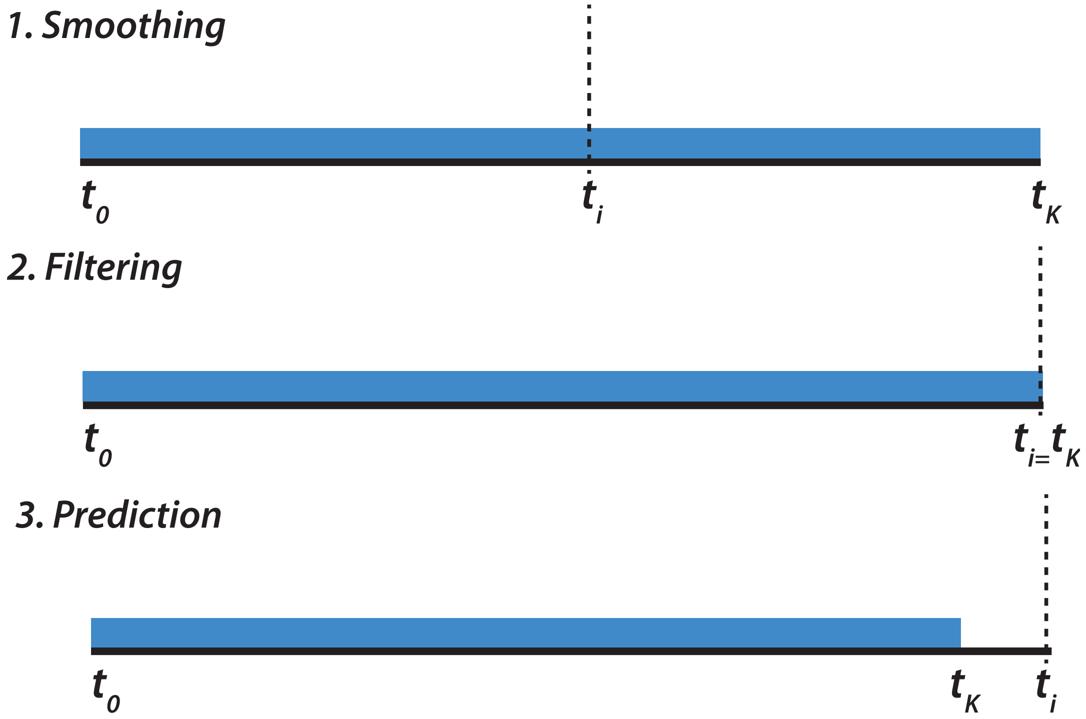

Figure 2.3: Schematic diagram describing the three possible scenarios of the estimation problem: estimating the 1) past (smoothing), 2) present (filtering) and 3) future (prediction) state of the system. The blue bar corresponds to the dataset used to estimate the state of the system at t_i (vertical broken line).

2. If $t_i = t_K$, this is called ***filtering*** problem. All observations are used to estimate the state of the system at all times (i.e. estimating the present state of the system).

3. If $t_i > t_K$, this is then called ***prediction*** problem. Observations up to t_K are used to estimate the future state of the system.

Note that all of these cases are considered by Kalman [1960] as an ***estimation*** problem.

The KF method follows a two-step procedure: 1) the forecast step and 2) the analysis step. In the previous sections, we denote the prior knowledge about the state and its error covariance as X^b and P^b, respectively, where b stands for the ***background***. In the context of sequential assimilation, we shall use X^f and P^f (i.e. f denotes the term ***forecast***) instead as this comes from a previous forecast. If $t_i = 0$, then f is simply the ***background*** state that often comes from initial conditions.

Forecast step. The forecast step is basically time stepping the system from t_i to t_{i+1}. As presented in **equation 2.8**, the true state will evolve according to the dynamical model, $\mathcal{M}$. The numerical state will evolve by:

$$X^f_{t_{i+1}} = \mathcal{M}_{t_{i+1}}(X^a_{t_i}) \tag{2.25}$$

$X^a_{t_i}$ is the result of the analysis from the previous time step. From **equation (2.2)** we can write the forecast error as:

$$\begin{aligned} \epsilon^f_{t_{i+1}} &= X^f_{t_{i+1}} - X^\dagger_{t_{i+1}} && (2.26)\\ &= \mathcal{M}_{t_{i+1}}(X^a_{t_i}) - X^\dagger_{t_{i+1}} && (2.27) \end{aligned}$$

If $\mathcal{M}$ is linear, then using **equation (2.10)** will give us:

$$\epsilon^f_{t_{i+1}} = \mathcal{M}_{t_{i+1}}\epsilon^a_{t_i} + \underbrace{\mathcal{M}_{t_{i+1}}(X^\dagger_{t_i}) - X^\dagger_{t_{i+1}}}_{q_{t_{i+1}}} \tag{2.28}$$

and the forecast error covariance matrix:

$$\begin{aligned} \mathcal{E}\left[\epsilon^f_{t_{i+1}}(\epsilon^f_{t_{i+1}})^T\right] = P^f_{t_{i+1}} &= \left[(\mathcal{M}_{t_{i+1}}\epsilon^a_{t_i} + q_{t_{i+1}})(\mathcal{M}_{t_{i+1}}\epsilon^a_{t_i} + q_{t_{i+1}})^T\right] && (2.29)\\ &= \mathcal{M}_{t_{i+1}}\mathcal{E}\left[\epsilon^a_{t_i}(\epsilon^a_{t_i})^T\right]\mathcal{M}^T_{t_{i+1}} + \mathcal{E}\left[q_{t_{i+1}}(q_{t_{i+1}})^T\right] && (2.30)\\ P^f_{t_{i+1}} &= \mathcal{M}_{t_{i+1}}P^a_{t_i}\mathcal{M}^T_{t_{i+1}} + Q_{t_{i+1}} && (2.31) \end{aligned}$$

Analysis step. This step is where corrections to the forecast state vector are made using available observations at time step, t_{i+1}. Unless necessary, I will drop the time descriptor when presenting the analysis step equations for the sake of simplicity. This will also be the case for the succeeding subsections describing other members of the KF-family. The KF analysis step follows exactly the BLUE equations in **section 2.3.2**, such that:

$$K = P^f\mathcal{H}^T(\mathcal{H}P^f\mathcal{H}^T + R)^{-1} \tag{2.32}$$

$$X^a = X^f + K(D - \mathcal{H}X^f) \tag{2.33}$$

$$P^a = (I - K\mathcal{H})P^f \tag{2.34}$$

Practical implementation: Kalman Filter (KF)

1. **Initialisation**

$$X_{t_0}^f \text{ and } P_{t_0}^f$$

2. **Forecast step**

   a. Propagate the model (i.e. t_i to t_{i+1}):

$$X_{t_{i+1}}^f = \mathcal{M}_{t_{i+1}}(X_{t_i}^a)$$

   b. Calculate the forecast covariance error:

$$P_{t_{i+1}}^f = \mathcal{M}_{t_{i+1}} P_{t_i}^a \mathcal{M}_{t_{i+1}}^T + Q_{t_{i+1}}$$

3. **Analysis step (i.e. for t_{i+1})**

   a. Calculate the Kalman Gain:

$$K = P^f \mathcal{H}^T (\mathcal{H} P^f \mathcal{H}^T + R)^{-1}$$

   b. Update the state estimate:

$$X^a = X^f + K(D - \mathcal{H} X^f)$$

   c. Compute for the analysis covariance error:

$$P^a = (I - K\mathcal{H})P^f$$

K is called the Kalman gain, which gives weight to the innovation vector (i.e. additional information brought in by the observations in comparison with the model prediction). Because this step follows the conditions of the BLUE analysis, X^a becomes the optimal estimate of $X^\dagger$ given a vector of observations D. Note that, X^a is often called the ***updated*** state vector or ***analysis*** state vector.

The innovation vector, $\mathcal{Y} = D - \mathcal{H}X^f$, and the residual, $\mathcal{R} = D - \mathcal{H}X^a$, are common diagnostic tools to assess the posterior consistency of the data assimilation method (Fournier *et al.* [2010]).

Discussions: No observation. What happens when there is lack of data that can be sequentially assimilated due to unexpected events such as perhaps, problems with the instrument itself or poor quality of the data? For example, ground-based instruments such as GPS (or GNSS in general) may require on-site maintenance, replacement of antennas or in a more unfortunate scenario, total destruction of the instrument. Another example concerns the quality of received data, in operational weather forecasting, low quality data are often disregarded. InSAR data are often perturbed by the atmosphere and the ionosphere (i.e. for L-Band radar data) and most volcanoes are highly covered by vegetation which then affects the coherence of the pairs of radar data therefore affecting their quality. These examples can obviously result in losing several days up to months of data.

In sequential data assimilation, the dynamical model has the ability to predict the next state of the system hence the answer simply boils down to the forecast step equations (e.g. **equations (2.25)** and **(2.31)**) while no observation is available. However, it is important to note that if the dynamics is unstable and the interval without observation is sufficiently long, the error will grow uncontrolled and only the re-introduction of data will reduce the error (Bocquet [2017]) as shown in **Figure 2.2**.

Perfect observations. Assuming a strong confidence on the observations (i.e. $\epsilon = 0$) the Kalman gain from **equation (2.32)** is equal to $\mathcal{H}^{-1}$ and provided that there are as many observations as the state variables and that they are independent (Bocquet [2017]) (i.e. $\mathcal{H}$ is invertible). The rest of the KF equations follow the forms:

1. The analysis covariance, $P^a = 0$.
2. The analysis state, $X^a = \mathcal{H}^{-1}D$.
3. The forecast error covariance, $P^f = Q$.
4. The forecast state, $X^f = \mathcal{M}\mathcal{H}^{-1}D$.

In the case that $\mathcal{H}$ is an identity matrix, the system is fully estimated by the observations (i.e. $X^f_{t_{i+1}} = \mathcal{M}_{t_{i+1}}(X^a_{t_i}) = \mathcal{M}_{t_{i+1}}(D_{t_i})$) and the errors are only dependent on the model error (i.e. $P^f_{t_{i+1}} = \underbrace{\mathcal{M}_{t_{i+1}} P^a_{t_i} \mathcal{M}^T_{t_{i+1}}}_{=0} + Q_{t_{i+1}} = Q_{t_{i+1}}$).

Limitations. Two main issues arise from the KF algorithm (Evensen [2009]): 1) storage and computational cost considering high dimensional problems, and 2) when the dynamical model model, $\mathcal{M}$, is non-linear. For the first issue, the forecast/analysis error covariance is of the size ${N_x}^2$ given a state vector of dimension N_x. Rank reduction could address the issue in dimensionality (Cosme [2017]). Furthermore, the computational cost of propagating the error covariance becomes $2N_x$ of the model integration time. This makes it impractical for volcano applications especially if one is using a finite element model with high resolution mesh. A way to get around this is to use the square root formulation of the covariance matrix. Others settle to adopt a frozen covariance matrix instead (i.e. known as the optimal interpolation) however, this approach suffers from the lack of the dynamical information on the error statistics (Sanchez [2016]).

The second problem concerns the non-linearity of the dynamical model which can destroy the Gaussianity of statistics. Although replacing $\mathcal{M}$ by its tangent linear operator $\mathcal{M}'$ (i.e. EKF) can solve the issue at least for those systems that are weakly non-linear.

In addition to the aforementioned limitations, take note that KF equations require to have an estimate of Q in order to calculate P^f. This is something that is very difficult if not impossible to accurately define. In volcanology, available dynamical models are oversimplified representation of the reality. Besides, there is no direct observation on how the volcanic system works which adds to the complication when defining the model error.

Kalman Filter spin-offs

Since the development of the linear KF, a lot of studies have been dedicated to improve and address its main issues. Three of these are discussed below and have been applied to problems in crustal deformation: 1) EKF, 2) UKF and 3) EnKF.

Extended Kalman Filter As briefly mentioned above, in the case of weakly non-linear dynamics, the model and observation operators can be linearised by their tangent linear approximations extending the application of KF to non-linear case hence the name ***Extended Kalman Filter***:

$$\mathcal{M}' = \left.\frac{\partial \mathcal{M}}{\partial X}\right|_{X_{t_0}} \tag{2.35}$$

$$\mathcal{H}' = \left.\frac{\partial \mathcal{H}}{\partial X}\right|_{X_{t_0}} \tag{2.36}$$

Forecast step. The forecast step for the state vector uses the non-linear model propagator whereas for the error covariance the tangent linear approximation is adopted:

$$X^f_{t_{i+1}} = \mathcal{M}_{t_{i+1}}(X^a_{t_i}) \tag{2.37}$$

$$P^f_{t_{i+1}} = \mathcal{M}'_{t_{i+1}} P^a_{t_i} \mathcal{M}'^T_{t_{i+1}} + Q_{t_{i+1}} \tag{2.38}$$

Analysis step. The analysis step at t_{i+1} of the EKF is desribed below, except for X^a, the rest of the equations use the tangent linear operator.

$$K = P^f \mathcal{H}'^T (\mathcal{H}' P^f \mathcal{H}'^T + R)^{-1} \tag{2.39}$$

$$X^a = X^f + K(D - \mathcal{H}X^f) \tag{2.40}$$

$$P^a = (I - K\mathcal{H}')P^f \tag{2.41}$$

Discussion. The EKF equations are similar in form to the linear KF equations replacing $\mathcal{M}$ and $\mathcal{H}$ with their tangent linear approximations for the calculation of the error covariances and the Kalman Gain. Although it addresses the issues related to the non-linearities of the model operator or observation operator, EKF often leads to poor error covariance evolution and unstable error covariance growth (Evensen [2009]). Furthermore, like in the linear KF method, EKF can only be used with low-dimensional dynamical models. UKF and the ensembled-based KF are improvements of the EKF, targeting high-dimensional non-linear data assimilation problems.

Unscented Kalman Filter UKF is an improvement of the EKF algorithm based on a deterministic sampling approach (Wan et Van Der Merwe [2000]). Like in the EKF, the state of the system is also a Gaussian Random Variable for UKF. We know from **section 2.3.2** that in the case of EKF, the state is propagated by computing the tangent linear approximations of $\mathcal{M}$ and $\mathcal{H}$ to perform first-order linearisation of a non-linear system. However, this often leads to suboptimal performance and also divergence of the filter (Wan et Van Der Merwe [2000]). A rigorous discussion and derivation of the UKF equations can be found from the works of Julier et Uhlmann [1997] and Wan et Van Der Merwe [2000]. Below, we will only provide the necessary equations to implement the technique.

Practical implementation: Extended Kalman Filter (EKF)

1. Initialisation

$$X^f_{t_0} \text{ and } P^f_{t_0}$$

2. Forecast step:

a. Propagate the model (i.e. t_i to t_{i+1}):

$$X^f_{t_{i+1}} = \mathcal{M}_{t_{i+1}}(X^a_{t_i})$$

b. Compute for the tangent linear of $\mathcal{M}$:

$$\mathcal{M}' = \left.\frac{\partial \mathcal{M}}{\partial X}\right|_{X_{t_0}}$$

c. Calculate the forecast covariance error:

$$P^f_{t_{i+1}} = \mathcal{M}'_{t_{i+1}} P^a_{t_i} \mathcal{M}'^T_{t_{i+1}} + Q_{t_{i+1}}$$

3. Analysis step (i.e. for t_{i+1}):

a. Compute for the tangent linear of $\mathcal{H}$:

$$\mathcal{H}' = \left.\frac{\partial \mathcal{H}}{\partial X}\right|_{X_{t_0}}$$

b. Calculate the Kalman Gain

$$K = P^f \mathcal{H}'^T (\mathcal{H}' P^f \mathcal{H}'^T + R)^{-1}$$

c. Update the state estimate:

$$X^a = X^f + K(D - \mathcal{H} X^f)$$

d. Compute for the analysis covariance error:

$$P^a = (I - K\mathcal{H}')P^f$$

Selection of sigma points. In UKF, the state distribution is represented by a set of sample points called ***sigma points***, therefore the algorithm starts by carefully selecting these points. The vector of sigma points, $\mathcal{X}$, is a collection of $2L + 1$ sigma points defined as:

$$\mathcal{X}^a_{t_i} = \left[\hat{X}^a_{t_i} \pm \sqrt{(L + \lambda) P^a_{t_i}} \right] \tag{2.42}$$

where λ is a composite scaling parameter (hyperparameter), L is the dimension of the augmented state, $\hat{X}^a_{t_i} = [X^{a\,T}_{t_i} {q_{t_i}}^T {\epsilon_{t_i}}^T]$. Note that hyperparameters are used to optimize the performance of the filter to get an efficient choice of sample points (Fournier *et al.* [2009]).

Forecast step. The forecast state step follows the equation of the linear KF (i.e. **equation (2.25)**) when propagating the state to the next time step. The equation is applied for each of the sigma points, $l = 0, ..., 2L$:

$$X^f_{l,t_{i+1}} = \mathcal{M}_{t_{i+1}}(\mathcal{X}^a_{l,t_i}) \tag{2.43}$$

The mean and covariance of the forecast state is given by:

$$\overline{X^f} = \sum_{l=0}^{2L} \mathcal{W}^m_l(\mathcal{X}^a_l) \tag{2.44}$$

$$P^f = \sum_{l=0}^{2L} \mathcal{W}^c_l(X^f_l - \overline{X^f})(X^f_l - \overline{X^f})^T \tag{2.45}$$

$\mathcal{W}^m_l$ and $\mathcal{W}^c_l$ are the mean and covariance weights, respectively. Where, $\mathcal{W}^m_l = \mathcal{W}^c_l = \frac{1}{2(L+\lambda)}$. Note that at $l = 0$, $\mathcal{W}^m_0 = \frac{\lambda}{(L+\lambda)}$ and $\mathcal{W}^c_0 = \frac{\lambda}{(L+\lambda)} + 1 - \alpha^2 + \beta$. α is used to determine the spread of the sigma points and β is used to incorporate prior knowledge of the distribution (e.g. $\beta = 2$ for Gaussian distribution, Wan et Van Der Merwe [2000]).

The sigma points are projected to the observation space via:

$$\mathcal{D}^f_l = \mathcal{H}(X^f_l) \tag{2.46}$$

with its mean defined as:

$$\overline{\mathcal{D}}^f = \sum_{l=0}^{2L} \mathcal{W}^m_l(\mathcal{D}^f_l) \tag{2.47}$$

Analysis step. To calculate the Kalman Gain, K, it is necessary to first calculate the covariance of the forecast observation vector $\mathcal{D}$ and the cross-covariance of the forecast state X^f and $\mathcal{D}$:

$$P^f_{\mathcal{D},\mathcal{D}} = \sum_{l=0}^{2L} \mathcal{W}^c_l(D^f_l - \overline{D}^f)(D^f_l - \overline{D}^f)^T \tag{2.48}$$

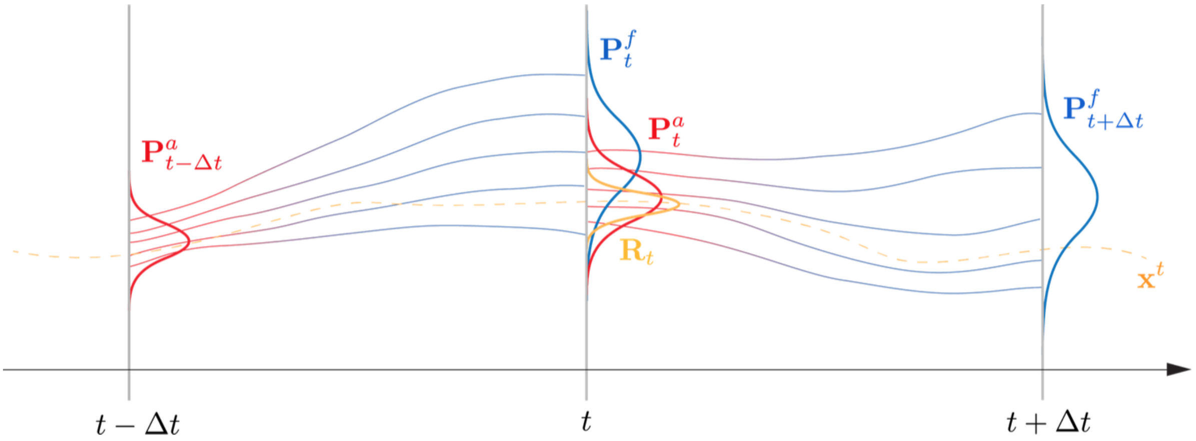

Figure 2.4: The construction of the error covariances in EnKF (from Sanchez [2016]).

$$P^f_{X,\mathcal{D}} = \sum_{l=0}^{2L} \mathcal{W}^c_l (X^f_l - \overline{X}^f)(D^f_l - \overline{D}^f)^T \tag{2.49}$$

$$\mathcal{K} = P^f_{X,\mathcal{D}} {P^f_{\mathcal{D},\mathcal{D}}}^{-1} \tag{2.50}$$

The analysis state vector and the error covariance at t_{i+1} are given by:

$$X^a = \overline{X^f} + \mathcal{K}(D^f_l - \overline{\mathcal{D}^f}) \tag{2.51}$$

$$P^a = P^f - \mathcal{K} P^f_{\mathcal{D},\mathcal{D}} \mathcal{K}^T \tag{2.52}$$

Discussion Although UKF can better address non-linear dynamics than EKF by capturing accurately the posterior mean and covariance up to the 3rd order (Wan et Van Der Merwe [2000]), the technique is highly dependent on initialization task and the selection of hyperparameters that are typically problem-dependent (Julier et Uhlmann [1997], Shirzaei et Walter [2010]). Moreover, it is more computationally intensive than EKF as it requires Cholesky factorizations on every step.

Stochastic Ensemble Kalman Filter EnKF was first developed by Evensen [1994] to address issues related to EKF in the case of stronger non-linear dynamics of the state. There are two basic approaches to EnKF: 1) stochastic and 2) (deterministic) square root filter (e.g. Evensen [2004], Yan *et al.* [2015]). In this thesis, we will mostly present

Practical implementation: Unscented Kalman Filter (UKF)

1. Initialisation

$$X^f_{t_0};\ P^f_{t_0};\ \text{and}\ \hat{X}^a_{t_0} = [(X^f_{t_0})^T \quad 0 \quad 0]$$

a. Selection of sigma points:

$$\mathcal{X}^a_{t_i} = \left[\hat{X}^a_{t_i} \pm \sqrt{(L+\lambda)P^a_{t_i}}\right]$$

2. Forecast step:

a. Propagate the model for each sigma points (i.e. from t_i to t_{i+1}):

$$X^f_{l,t_{i+1}} = \mathcal{M}_{t_{i+1}}(\mathcal{X}^a_{l,t_i})$$

b. Compute the mean and covariance of the forecast points:

$$\overline{X^f} = \sum_{l=0}^{2L} \mathcal{W}^m_l(\mathcal{X}^a_l)$$

$$P^f = \sum_{l=0}^{2L} \mathcal{W}^c_l(X^f_l - \overline{X^f})(X^f_l - \overline{X^f})^T$$

where, $\mathcal{W}^m_l = \mathcal{W}^c_l = \frac{1}{2(L+\lambda)}$. At $l = 0$, $\mathcal{W}^m_0 = \frac{\lambda}{(L+\lambda)}$ and $\mathcal{W}^c_0 = \frac{\lambda}{(L+\lambda)} + 1 - \alpha^2 + \beta$.

3. Analysis step (i.e. for t_{i+1}):

a. Calculate the observation error covariance, $P^f_{\mathcal{D},\mathcal{D}}$:

$$P^f_{\mathcal{D},\mathcal{D}} = \sum_{l=0}^{2L} \mathcal{W}^c_l(D^f_l - \overline{D}^f)(D^f_l - \overline{D}^f)^T$$

where, $\mathcal{D}^f_l = \mathcal{H}(X^f_l)$ and $\overline{\mathcal{D}}^f = \sum_{l=0}^{2L} \mathcal{W}^m_l(\mathcal{D}^f_l)$.

b. Calculate the cross-covariance, $P^f_{X,\mathcal{D}}$:

$$P^f_{X,\mathcal{D}} = \sum_{l=0}^{2L} \mathcal{W}^c_l(X^f_l - \overline{X}^f)(D^f_l - \overline{D}^f)^T$$

c. Compute for the Kalman Gain:

$$\mathcal{K} = P^f_{X,\mathcal{D}} {P^f_{\mathcal{D},\mathcal{D}}}^{-1}$$

d. Update the state estimate:

$$X^a = \overline{X^f} + \mathcal{K}(D^f_l - \overline{\mathcal{D}^f})$$

e. Compute for the analysis covariance error:

$$P^a = P^f - \mathcal{K}P^f_{\mathcal{D},\mathcal{D}}\mathcal{K}^T$$

results based on the stochastic EnKF which is the classic prototype of EnKF. This was proposed by Burgers *et al.* [1998] to avoid the underestimation of the analysis covariance error by perturbing the observations prior to the computation of the analysis. Unlike the EKF and UKF which are deterministic, the stochastic EnKF is a Monte Carlo alternative route to address non-linearities (Evensen [2009]). Basically, EnKF is rooted on the N_n-ensemble of realizations to approximate the mean and covariance of the state vector. Each ensemble member is propagated by the model without the need for linearizion (i.e. computation of the tangent linear approximations). Because of its simplicity, relative ease on implementation and low computational cost when compared with KF, the EnKF algorithm has gained a lot of development recently and has been proven effective to solve operational data assimilation problems, thus, adopted by many operational NWP centers.

One important feature of EnKF is the way to construct the model error covariance, given by **equations (2.55) and (2.58)**). **Figure 2.4** illustrates the construction of the forecast and analysis covariance error in EnKF. The initial model ensemble of size N_e from the previous time step (i.e. $t - \Delta t$) are forecasted toward t. These result in the evolution of the model covariance error, P^f. Once the observations characterized by observation error covariance, R, are available, the model ensemble is updated with a new model error covariance, P^a. The process reiterates to the next time step.

Forecast step. The forecast is carried out by the model integration under the control of the model operator that represents the physical process governing the system. For each ensemble member, $n = 1, ..., N_n$ (i.e. where N_n is the size of the ensemble):

$$X^f_{t_{i+1},n} = \mathcal{M}_{t_{i+1}}(X^a_{t_i,n}) \tag{2.53}$$

The forecast estimate is the mean of the forecast ensemble:

$$\overline{X}^f = \frac{1}{N_n}\sum_{e=1}^{N_n} X^f_n \tag{2.54}$$

The forecast error covariance is of the form:

$$P^f = \overline{(X^f_n - \overline{X^f})(X^f_n - \overline{X^f})^T} \tag{2.55}$$

Practical implementation: [Stochastic] Ensemble Kalman Filter (EnKF)

1. Initialisation

$$X^f_{t_0} \text{ and } P^f_{t_0}$$

2. Forecast step:

a. Propagate the model for each ensemble member (i.e. from t_i to t_{i+1}):

$$X^f_{t_{i+1},n} = \mathcal{M}_{t_{i+1}}(X^a_{t_i,n})$$

b. Compute the mean of the forecast ensemble:

$$\overline{X}^f_{t_{i+1}} = \frac{1}{N_n}\sum_{n=1}^{N_n} X^f_{t_{i+1},n}$$

c. Calculate the forecast covariance error for t_{i+1}:

$$P^f = \overline{(X^f_n - \overline{X^f})(X^f_n - \overline{X^f})^T}$$

3. Analysis step (i.e. for t_{i+1}):

a. Calculate the Kalman Gain

$$K = P^f\mathcal{H}^T(\mathcal{H}P^f\mathcal{H}^T + R)^{-1}$$

b. Perturb each observation point (i.e. $m = 1, ..., N_m$):

$$\hat{D}_m = D_m + \eta$$

c. Update the state estimate:

$$X^a_n = X^f_n + K\left(\hat{D} - \mathcal{H}X^f_n\right)$$

d. Compute the mean of the forecast ensemble:

$$\overline{X}^a = \frac{1}{N_n}\sum_{n=1}^{N_n} X^a_n$$

e. Compute for the analysis covariance error:

$$P^a = \overline{(X^a_n - \overline{X^a})(X^a_n - \overline{X^a})^T}$$

Analysis step. To update the estimation, **equation (2.33)** is applied to each of the ensemble members once observations are available. However, there is a slight issue with the analysis error covariance when the observation vector is used directly. In order to mimic the BLUE equations, P^a should be equal to $(I_{N_x} - K\mathcal{H})P^f(I_{N_x} - K\mathcal{H})^T + KRK$. However, **equation (2.33)** leads only to $(I_{N_x} - K\mathcal{H})P^f(I_{N_x} - K\mathcal{H})^T$, hence underestimating the error. This can give rise to filter divergence (Bocquet [2017]). One solution is to perturb the observations prior to the computation of the analysis; hence the term ***stochastic***. Consider a dataset, D_m, having a total of N_m observation points. Each of the points $m = 1, ..., N_m$ will take the form:

$$\hat{D}_m = D_m + \eta$$

where η is a random variable with distribution $\mathcal{N}(0, R)$. Now, replacing D with $\hat{D}$, the stochastic EnKF analysis becomes :

$$X^a = X^f + K(\hat{D} - \mathcal{H}X^f) \tag{2.57}$$

The Kalman Gain is similar to the formalism given by **equation (2.32)** and the analysis covariance is of the form:

$$P^a = \overline{(X_n^a - \overline{X^a})(X_n^a - \overline{X^a})^T} \tag{2.58}$$

where the mean analysis state is :

$$\overline{X}^a = \frac{1}{N_n} \sum_{n=1}^{N_n} X_n^a \tag{2.59}$$

Discussion When the error covariance is sampled from a small number of ensemble that is insufficiently representative of the model error, divergence of the filter is often the consequence. Fortunately, ***localisation*** and ***inflation*** can overcome this issue. Localisation is more to reduce spurious long range correlation in the model error covariance. By performing localisation, the computational cost can also be reduced since only a portion of the model state is updated (Caya *et al.* [2005]). Assuming a short time scale, distant observations are almost independent such that they can be restricted spatially. One localisation approach is to multiply each term of the forecast error covariance P^f by, for example, an approximation of the Gaussian function $exp(-r_{ij}^2/2S^2)$ (i.e. r_{ij} is the distance between grid points i and j. S is the localisation length.) (Houtekamer et Mitchell [2001], Hamill *et al.* [2001], Lahoz *et al.* [2010]). This is called as the ***P-localisation***. Another is to multiply the inverse of the observation error covariance R^{-1} by a Gaussian function (Hunt [2005], Miyoshi [2005], Lahoz *et al.* [2010], Barth *et al.* [2016]). This is called the ***R-localisation***.

Proper localisation can reduce long range correlation errors (i.e. just part of the sampling error, however localisation cannot work for covariance error that does not correspond to the real error due to small ensemble size) in the model error covariance, but these errors can accumulate and propagate through time. ***Multiplicative inflation*** is a trick performed before or after the analysis, by multiplying a factor of $(1+\rho_{infl})^2$, i.e. ρ_{infl} is between 0 and 1, to the forecast/analysis error covariance:

$$P^f \rightarrow (1+\rho_{infl})^2 P^f \tag{2.60}$$

or $(1+\rho_{infl})$ to each ensemble of the state vector:

$$X_n^f \rightarrow (1+\rho_{infl}) X_n^f \tag{2.61}$$

Sampling errors and the approximate assumption of Gaussianity are compensated by the multiplicative inflation in the case of a "perfect" model therefore "curing" the intrinsic source of the EnKF method (Bocquet [2017]). There is also an ***additive*** way of inflation in order to compensate underestimated errors due to the presence of unaccounted model errors. This is implemented by perturbing the ensemble members or adding Q to the forecast error covariance:

$$P^f \rightarrow P^f + Q \tag{2.62}$$

$$X_n^f \rightarrow X_n^f + q_n, \quad \mathcal{E}[q_n {q_n}^T] = Q \tag{2.63}$$

Note that Q is the model error and as discussed previously in the KF approach, it requires a good knowledge of the dynamics of the sytem to define it. Either way, inflation allows the expansion of the distribution (before or after the analysis) such that it helps the filter to converge to the true state of the system (rather reduce the ensemble collapse problem).

2.3.3 Data assimilation based on optimal control theory: The variational methods

3DVar vs. 4DVar

All the variational methods aim to minimize the cost function J rather than finding the maximum of a certain probability distribution function given an analyzed state, as in the case of the sequential assimilation methods. The 3DVar analysis is the simplest case where the observations and the background are both available at the same time or over a period of time, short enough to assume that the state is fixed (Talagrand [2010]). Its cost function is given by **Equation (2.17)** which can be minimized at the analysis time, t_i. Clearly, The first term in the right hand side of **equation (2.17)** evaluates the deviation of x from the background state, X^b and the second term measures the distance between the observations and the model predictions.

In the case where the evolution of the state cannot be neglected (i.e. time-dependent problem) the following objective function is defined (Fournier *et al.* [2010], Talagrand [2010]):

$$\mathcal{J}(x = X_{t_0}) = \frac{1}{2}\left[\sum_{i=0}^{K}(x - X^b_{t_0})^T {P^b}^{-1}(x - X^b_{t_0}) + (\mathcal{H}_{t_i}x_{t_i} - D_{t_i})^T {R_{t_i}}^{-1}(\mathcal{H}_{t_i}x_{t_i} - D_{t_i})\right] \quad (2.64)$$

The minimization of J over a time window of interest, K, is now termed as the four-dimensional variational analysis or 4DVar. The state evolves the same way as described in **equation 2.8**. Note that **equation (2.64)** remains valid only if the model error is neglected. Here, it stresses the fact that the dynamical model is perfect and determines exactly the sequence of the estimated state vector, hence the term ***strong constraint***. **Equation (2.64)** follows the form of **equation (2.17)** where the first term evaluates the distance between the initial state and the background state weighted by the background error covariance matrix, P^b. While the second term measures the discrepancy between the model predictions and the observations performed over a time window of interest and is weighted by the confidence given by the observation error covariance, $R_{t_{i \to K}}$.

If the model error is considered, the cost function takes the following form:

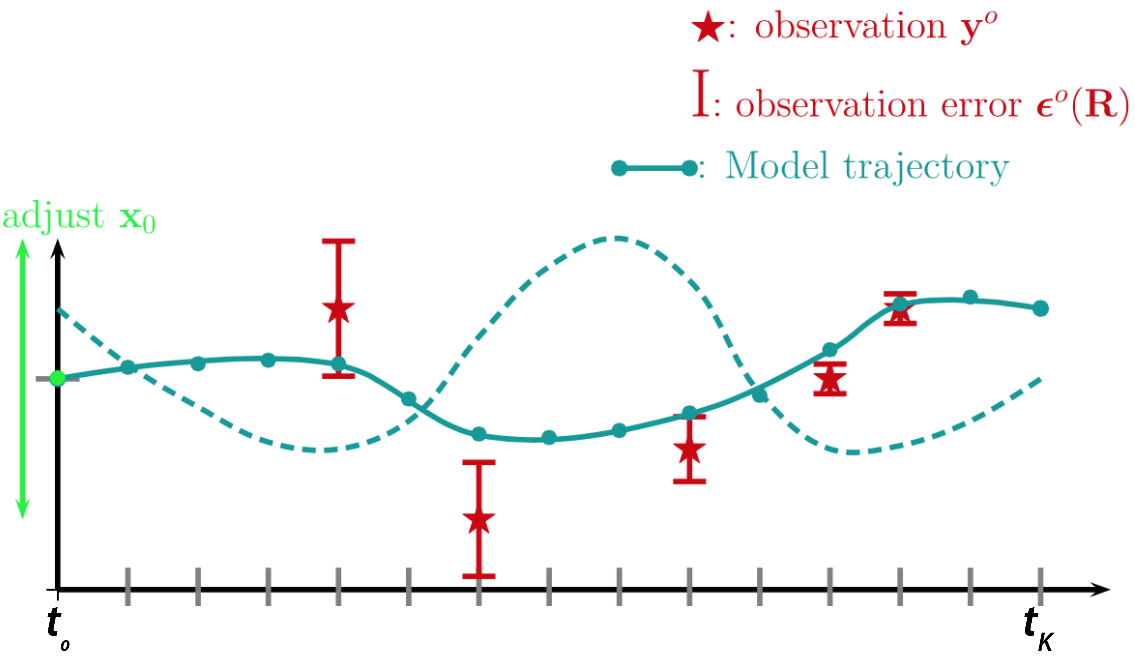

Figure 2.5: The variational approach to data assimilation. Given a time window of interest, the initial condition, X_0 is adjusted using iterative minimization algorithms. The result is an optimal fit to the data. The dashed line corresponds to the model trajectory prior to adjustment of the initial condition. (from Fournier *et al.* [2010])

$$\begin{aligned}\mathcal{J}([X_{t_0}, X_{t_1}, ...X_{t_K}]) = \frac{1}{2}\Bigg[&\sum_{i=0}^{K}(X_{t_0}-X_{t_0}^b)^T {P^b}^{-1}(X_{t_0}-X_{t_0}^b)+(\mathcal{H}_{t_i}x_{t_i}-D_{t_i})^T {R_{t_i}}^{-1}(\mathcal{H}_{t_i}x_{t_i}-D_{t_i}) \\ &+\sum_{i=0}^{K-1}(X_{t_{i+1}} - \mathcal{M}_{t_{i+1}}X_{t_i})^T {Q_{t_i}}^{-1}(X_{t_{i+1}} - \mathcal{M}_{t_{i+1}}X_{t_i})\Bigg] \end{aligned} \tag{2.65}$$

defined for the whole sequence $[X_{t_i}, i = 0, ...K]$. Note that Q is the model error covariance, uncorrelated with either the background or the observations. This model error is presented as an additional set of “noisy” data (Talagrand [2010]) to be fitted by the analyzed state and is termed as the ***weak constraint*** 4DVar analysis. However, this is obviously computationally expensive as it requires to evaluate the cost function over the whole sequence $[X_{t_i}, i = 0, ...K]$ and a proper modeling of the not so-well known Q can also be an issue. Having said the issues, the strong constraint 4DVar analysis is typically implemented especially in operational weather forecasting centers.

Note that in 4DVar analysis, the initial condition or ***control vector***, X_{t_0}, is adjusted while everything else is fixed through an iterative minimization algorithm within the chosen time window. This minimization can become numerically costly and almost impossible to calculate with increasing size of the state vector, N_x, as it requires the computation of the gradient of J (i.e. $\nabla_{X_{t_0}} J^T$) therefore implying N_x realizations of the forward model over the time window of interest. The so-called adjoint method (Le Dimet et Talagrand [1986], Talagrand et Courtier [1987]) is typically implemented wherein the computation of one gradient requires one forward integration of the full model equations over the time interval on which the observations are available, followed by one backward integration of the adjoint equation (Talagrand et Courtier [1987]). The term adjoint approach introduces the transpose of the tangent linear equations as initially described in the EKF where both the model operator and the observation operator are nonlinear. The computational cost of the adjoint equations makes it possible to then use iterative minimization algorithms such as the descent methods and quasi-Newton algorithm to accommodate large-scale problems.

Advantages and limitations of EnKF and 4DVar

Many studies have already discussed the pros and cons of EnKF and 4DVar (e.g. Lorenc [2003], Caya *et al.* [2005], Fournier *et al.* [2010], Talagrand [2010]). Here, I have itemized in **Table 2.1** and summarized below their strengths and limitations.

The variational approach is versatile and flexible. It allows easy introduction of the new observations although its ability to fit detailed observations is limited by the resolution of simplified model. Static model parameters can also be adjusted and be consequently part of the control vector. In 4DVar, information are automatically propagated forward and backward in time, making it easy to account for temporally correlated errors (either observation or model error). Furthermore, variational approach has the natural ability to handle time-dependent observation operators and non-Gaussian observation errors as long as $\mathcal{H}$ is differentiable. There are three drawbacks that limit the variational approach: 1) it is costly in a way that it requires expertise to develop, validate and even maintain the adjoint model; 2) there is no direct access to the error statistics of the analysis and 3) most of the time, the model is assumed perfect; although the weak constraint approach has already gained attention after its successful introduction and implementation.

Table 2.1: The advantages (+) and limitations (-) of EnKF and 4DVar.

EnKF	**4DVar**
(+) Ease of implementation.	(+) Versatile and flexible.
(+) Direct access to the forecast and analysis error statistics.	(+) Propagates error forward and backward in time within the time window of interest.
(+) Allows the use of nonlinear observation operator, H.	(+) Natural ability to handle time-dependent observation operators and non-Gaussian observation errors.
(+) Although it can be tunned through localisation and inflation,	(-) Costly in terms of the development, validation and maintenance of the adjoint of the model and observational operators.
(-) EnKF can suffer from undersampling issues that would lead to ensemble collapse and long range spurious correlation in the error covariance matrix.	(-) No direct access to the analysis error statistics.
(-) Forbids the use of non-Gaussian observational errors.	(-) Generally assumes the model is perfect (strong constraint).

The sequential assimilation approach via EnKF is practically much simpler to implement than the 4DVar. Mainly, because 1) it does not require the development and maintenance of an adjoint model and 2) the forecast and analysis error covariances are always provided. EnKF permits nonlinear observation operator, $\mathcal{H}$, but it treats the resulting posterior density function as Gaussian. It is worth mentioning that non-Gaussian observational errors are prohibited. As discussed in **section 2.3.2**, EnKF is known to suffer from undersampling issues due to insufficient ensemble size and could result in ensemble collapse and long range spurious correlation in the error covariance matrix.

In summary, EnKF and 4DVar are the two most advanced and powerful data assimilation techniques currently used as standard forecasting methods in NWP. Despite the aforementioned weaknesses, their estimates are convergent at the end of the assimilation period in the case of having linear operators, perfect model and Gaussian statistics (Talagrand [1997], Sanchez [2016]). Kalnay [2010] proposed hybrid analysis using 4DVar and EnKF to better assimilate data and obtain more reliable results.

2.4 Application to problems in volcanology

Although data assimilation is already an operational technique in the field of numerical weather prediction, its application to solve problems in volcanology is still very much in infancy. Early efforts to follow the behavior of volcanoes are focused on applying various KF spin-offs using kinematic models (e.g. Mogi [1958], McTigue [1987], Yang *et al.* [1988]) and geodetic data. It is only until recently that dynamical models have been proposed to assess the potential of volcanic eruptions by assimilating synthetic deformation data. Kinematic models have no predictive capability and cannot be used to determine the evolution of deformation with time given a set of initial parameters (Anderson et Segall [2013]). For example, the physical and chemical processes that gave rise to the observed deformation are not taken into account when using kinematic models. In this section, I will attempt to provide a chronological listing of the publications involving the recent developments of volcanic data assimilation and also discuss their limitations.

The first application of KF to understand changes that occurs beneath a volcano was performed by Fournier *et al.* [2009]. The authors applied UKF to track the magma recovery at Okmok volcano using GPS data and a Mogi source model. This allowed them to quantify $\sim 60 - 80$ % of total volume recovery from 1997 to 2007 at Okmok and simultaneously follow the evolution of the source strength which is a nonlinear parameter. However, there are some initialization issues in the strategy that can result in trade-offs between parameters, then leading to incorrect parameter estimates. Furthermore, selection of hyperparameters (i.e. λ in **section 2.3.2**) are problem-dependent (Shirzaei et Walter [2010], Julier et Uhlmann [1997]).

A hybrid approach of combining Random Iterated Search and Statistical Competency Generic Algorithm (RISC-GA) and KF was next introduced by Shirzaei et Walter [2010]. The rationale of the hybrid approach is based on the "good a priori" requirement of KF. The strategy was developed to monitor the volcano source underneath Campi Flegrei volcano in Italy and provide new insights about the physical process that occurs at this volcano. However, the three-step method (i.e. RISC-GA→LKF→RISC-GA) that they developed requires repeating the steps until a stopping criteria is reached making the whole process computationally expensive.

Gregg et Pettijohn [2016] have successsfully first applied the EnKF technique using a viscoelastic finite element model (FEM) of an inflating magma reservoir and synthetic geodetic data to assess volcanic unrest. However, the shear modulus and the host rock viscosity which controls the evolution of the medium are considered constant in the synthetic tests. These limit the interests of considering the temporal evolution of the system and the ability to gain more information about the magmatic properties controlling the system. Moreover, the comparison made between inversion and EnKF is not consistent. The authors used a viscoelastic FEM for EnKF wheareas an analytical elastic model (McTigue [1987]) for the inversion.

Zhan et Gregg [2017] extended the synthetic tests of Gregg et Pettijohn [2016] by: 1) setting up a 3D viscoelastic FEM in order to allow future efforts in volcanic data assimilation to account for asymmetric magma reservoirs, topography, faults, and host rock heterogeneities; 2) adding distance-correlated noise in the InSAR data and a combination of white and flicker noise for the GPS data; and 3) adopting an iterative EnKF approach and performing sensitivity analyses. Although the numerical model was designed for a 3D environment, the authors performed synthetic tests using a highly idealized terrestrial volcano (e.g. no topographic change was considered and the material properties of the crust were fixed). Also, the distance-correlated and combination of noise added in the synthetic data were removed prior to EnKF implementation by applying a low-pass filter. This limit the ability to assess the performance of EnKF when non-Gaussian observation errors are embedded in the signal. It is suggested that in proper assimilation practice, one should incorporate direct (raw) observations (Talagrand [1997], Sanchez [2016]). The iterative EnKF approach allowed better convergence of their uncertain parameters to the nominal values except for a few (e.g. radius of the magma chamber) that diverged tremendously. Furthermore, note that the joint usage of FEM and the iterative assimilation strategy requires expensive calculations making it unsuitable for real-time forecasting of volcanic unrest.

Zhan *et al.* [2017] first applied the EnKF using real InSAR data to perform hindcasting of the 2009 Kerinci volcanic eruption in Indonesia. Using the estimated overpressure and chamber radius, Mohr-Coulomb failure models were used to assess tensile failure in the host rock that could potentially signal an impending eruption. However, similar to the studies of Fournier *et al.* [2009] and Shirzaei et Walter [2010] which are based on kinematic pressurized source model, Zhan *et al.* [2017] used two-step kinematic modelling (e.g. spherical pressurized source (McTigue [1987]) and then deflating near-vertical oblate source (Yang *et al.* [1988])) to reproduce the deformation observed at Kerinci volcano. Due to the lack of predictive capability in using kinematic models, the authors were not able to forecast the evolution of the system when there is a gap in the acquisition of InSAR data. This diverged from the concept and huge potential of the sequential assimilation methods discussed in the aforementioned sections and EnKF synthetic tests (e.g. Zhan et Gregg [2017]). The use of a dynamical model and not only a time-dependent kinematic model is crucial in implementing the sequential assimilation methods, of particular interest is the EnKF approach. It is worth noting that in physical volcanology, dynamical models allow better understanding of the evolution of magmatic processes that lead to observations measured on the surface of the Earth.

2.5 Summary and Perspectives

Clearly, there is a need to combine observations and models objectively in order to fill the gaps in information and be able to gain knowledge about the past, present and future state of our system-of-interest. Data assimilation has been proven effective in NWP and shows great potential in other fields of geosciences. In volcanology, however, data assimilation is still an emerging topic and there are a lot of things that are yet to be explored. This thesis aims to further build and improve data assimilation strategies that are useful not only in terms of forecasting but also to improve our knowledge on how volcanoes behave. In particular, the next chapters will focus on EnKF assimilation method, discussing the approach that we developed using synthetic and real geodetic observations in order to: 1) forecast the rupture of a magma chamber potentially leading to an eruption, 2) better understand subsurface processes occuring underneath a volcano and 3) improve our knowledge on how neighboring volcanoes interact with each other.

Chapter 3

Assimilation of Deformation Data for Eruption Forecasting: Potentiality Assessment Based on Synthetic Cases

Contents

This chapter was published as: "Assimilation of Deformation Data for Eruption Forecasting: Potentiality Assessment Based on Synthetic Cases", *Frontiers in Earth Science, 5, 48*. doi.org/10.3389/feart.2017.00048 and afterwards gained several local and international media attention in 2017. Furthermore, parts of this work were also presented in AGU Fall Meeting in 2016 where I [we] received the *Outstanding Student Paper Award* in Geodesy.

Abstract

In monitoring active volcanoes, the magma overpressure is one of the key parameters used in forecasting volcanic eruptions. This parameter can be inferred from the ground displacements measured on the Earth's surface by applying inversion techniques. However, in most studies, the huge amount of information about the behaviour of the volcano contained in the temporal evolution of the signal is not fully exploited by inversion. Our work focuses on developing a strategy in order to better forecast the magma overpressure using data assimilation. We take advantage of the increasing amount of geodetic data (i.e. Interferometric Synthetic Aperture Radar (InSAR) and Global Navigation Satellite System (GNSS)) recorded on volcanoes nowadays together with the wide-range availability of dynamical models that can provide better understanding about the volcano plumbing system. Here, we particularly built our strategy on the basis of the Ensemble Kalman Filter (EnKF). We predict the temporal behaviours of the magma overpressures and surface deformations by adopting a simple and generic two-magma chamber model and by using synthetic GNSS and/or InSAR data. We prove the ability of EnKF to both estimate the magma pressure evolution and constrain the characteristics of the deep volcanic system (i.e. reservoir size as well as basal magma inflow). High temporal frequency of observation is required to ensure the success of EnKF and the quality of assimilation is also improved by increasing the spatial density of observations in the near-field. We thus show that better results are obtained by combining a few GNSS temporal series of high temporal resolution with InSAR images characterized by a good spatial coverage. We also show that EnKF provides similar results to sophisticated Bayesian-based inversion while using the same dynamical model with the advantage of EnkF to potentially account for the temporal evolution of the uncertain model parameters. Our results show that EnKF works well with the synthetic cases and there is a great potential in using the method for real-time monitoring of volcanic unrest.

3.1 Introduction

Tracking the migration of magma as it propagates to the Earth's surface is crucial in eruption forecasting as well as in volcanic hazard assessment. When magma accumulates at shallow depth or propagates towards the surface, it induces seismicity as well as surface displacements, such that geophysical signals recorded at volcanoes have long been used to infer magma path and magma plumbing system characteristics (e.g. Swanson *et al.* [1983], Voight *et al.* [1998], Aoki *et al.* [1999], Roult *et al.* [2012], Sigmundsson *et al.* [2015]). Recently the ability of geodesy to provide continuous and spatially extensive evolution of surface displacements during inter-eruptive periods has been drastically improved as a consequence of the increasing number of continuous Global Navigation Satellite System (GNSS) networks installed on volcanoes (e.g. Geirsson *et al.* [2012], Peltier *et al.* [2016]) together with the improvement of the availability of Synthetic Aperture Radar (SAR) data (i.e. better spatial coverage, improved spatial and temporal resolution of SAR data from new satellite missions) (e.g. Pinel *et al.* [2014]). This progress allows to characterise the geometry of magmatic plumbing systems underlying volcanoes in terms of reservoir shapes, depths and numbers. In particular, at some specific volcanoes, deep magmatic reservoirs, which had been ignored so far, are evidenced (e.g. Elsworth *et al.* [2008], Hautmann *et al.* [2014], Chadwick *et al.* [2011], Bagnardi et Amelung [2012]). However, most of the models used to interpret geodetic data are kinematic and cannot provide information on the pressure within the magmatic system, which is the key parameter to control the timing of magma reservoir rupture as well as the ability of magma to reach the surface and thus to feed an eruption. Besides, the difficulty to determine independently the size of a magma chamber and its pressure change has been recognized for many years (McTigue [1987], Segall [2013]). Basically, the same displacement field is expected from a small pressure change affecting a large magma reservoir and from a large pressure change experienced in a small magma chamber. However, consequences are not the same as the latter case is more prone to end in a short-term eruption. The good point is that the temporal evolution of the displacement field should help deciphering between those two cases, considering similar magma and crustal rheologies, the pressurization of a small chamber being much quicker than for a large one. One limitation of this approach, as recently demonstrated by Segall [2016], is that the temporal evolution actually results from of a convolution between the history of a pressure source and the magma and crustal rheology (Reverso *et al.* [2014]). It follows that additonal observations such as gravity data might be useful to discriminate both effects.

In addition to the recent progress in geodetic observations, several dynamical models of magmatic system evolution have been recently derived. They provide an interpretation of the temporal evolution of geodetic data as well as seismic observations considering either the rheology of the encasing medium (Nooner et Chadwick [2009], Carrier *et al.* [2014], Got *et al.* [2017]) or the evolution of the magma inflow at the bottom (Lengliné *et al.* [2008], Pinel *et al.* [2010], Reverso *et al.* [2014]). The latter type of models has proven to be useful in recovering information of the deepest part of the magma plumbing system, such as the size of the deep storage zone as well as the bottom magma inflow (Reverso *et al.* [2014]), which is always quite difficult to constrain. Segall [2013] has nicely demonstrated the interest to combine deformation data and a physics-based model of the plumbing system with a bayesian-based approach in order to forecast eruptions. In particular, the Markov Chain Monte Carlo method was applied with success to Mount St Helens (Anderson et Segall [2011, 2013]). As noticed by Segall [2013], a limitation of this approach is that it cannot account for epistemic uncertainties. Another limitation is potentially that it is not efficient to estimate model parameters evolving through time. Also, the challenge remains in accommodating incoming data and using them efficiently. Inversion methods are data intensive (i.e. uses all observations from the beginning) and typically requires expensive calculations at each observation period, hence may not be suitable for real-time eruption forecasting. To address these issues, data assimilation–a common method used in ocean-weather forecasting and monitoring–is here applied as a way to combine volcano deformation data and physics-based models.

Data assimilation is a time-stepping process that combines models, observations and a priori information based on error statistics to predict the state of a dynamical system. It was initially developed in ocean-atmosphere science (e.g. Talagrand et Courtier [1987], Talagrand [1997], Houtekamer et Mitchell [2005], Yan *et al.* [2014]), and has gained popularity in many other fields of geosciences such as vegetation and soil moisture (e.g. Reichle *et al.* [2007], Barbu *et al.* [2011]), natural resource exploration (e.g. Lorentzen *et al.* [2001], Geir *et al.* [2003], Gu *et al.* [2005], Chen *et al.* [2010], Zoccarato *et al.* [2016]) and geomagnetism (e.g. Fournier *et al.* [2007, 2010], Kuang *et al.* [2010], Gillet *et al.* [2015]). Many assimilation algorithms are already available nowadays. Among them, is the Kalman Filter (KF). It was first introduced by R.E. Kalman in 1960 (Kalman [1960]) and was regarded as the greatest achievement in estimation theory and control systems applications of the twentieth century, enabling the precise and efficient navigation of spacecrafts in the solar system (Grewal et Andrews [2008]). In earthquake research, KF has been used to determine fault slip evolutions (Segall et Matthews [1997], McGuire et Segall [2003], Bartlow *et al.* [2014], Bekaert *et al.* [2016]). At active volcanoes where nonlinear processes are typical, variants of KF have been used in order to solve nonlinear equations. For example, Fournier *et al.* [2009] used unscented KF to track the magma recovery at Okmok, but the strategy is strongly dependent on assumptions such as initialisation task and selection of hyperparameters that are typically problem-dependent

(Shirzaei et Walter [2010], Julier et Uhlmann [2004]). Shirzaei et Walter [2010] coupled genetic algorithm with KF to monitor volcano source at Campi Flegrei, which requires rerunning of KF for several times. In all these studies in the Earth Science field, the KF is used as a temporal filter without considering any forward dynamical model. So far, the application to volcanology of the KF based on a dynamical model has been restricted to one study (i.e. Gregg et Pettijohn [2016]) using a forward model accounting for a viscous rheology of the encasing medium. However, the model parameter controlling the temporal evolution of the medium and the crustal viscosity, was in this study considered as a fixed parameter, thus limiting the interest of considering the temporal evolution of the system. Also, their approach was based on a finite element model which limits the application to real-time forecasting and their joint assimilation of GNSS and InSAR data was still problematic.

In this work, our main goal is to test the ability of Ensemble Kalman Filter (EnKF) to quantify the magma pressure evolution at depth from surface displacement data and thus to forecast pressure-based volcanic eruptions. As a first attempt, we focus on a specific dynamical model that well-describes the behavior of several often erupting basaltic volcanoes. We developed an efficient approach to assimilate GNSS and InSAR data into a two-magma reservoir model, which is a simple and generic dynamical model for the magma plumbing system, in order to predict the overpressures and to constrain two model parameters related to the deepest part of the reservoir system. We begin by briefly discussing the two-magma reservoir model of Reverso *et al.* [2014] in section 3.2.1, then reviewing the fundamentals of the EnKF approach in section 3.2.2, followed by the experiment setup and the step-by-step implementation of our EnKF strategy in section 3.2.3. We then present two synthetic cases (i.e. case A and case B) when considering the magma inflow at the bottom of the system as well as the size of the deepest reservoir as uncertain and given two kinds of initial conditions about the uncertain parameters (i.e. biased or unbiased distribution). In particular, case A is about state estimation wherein we only track the behavior of the overpressures, while case B demonstrates state-parameter estimation where the uncertain model parameters are estimated in parallel with the overpressures. In the discussion part, we tackle the effects of the spatial and temporal characteristic of the datasets (i.e. GNSS-like and InSAR-like data) used during the assimilation and how far-field data affect the performance of assimilation. We also compare the performance of EnKF with a bayesian-based inversion. Then we present the advantages and limitations of the dynamical model we considered as well as the possibility

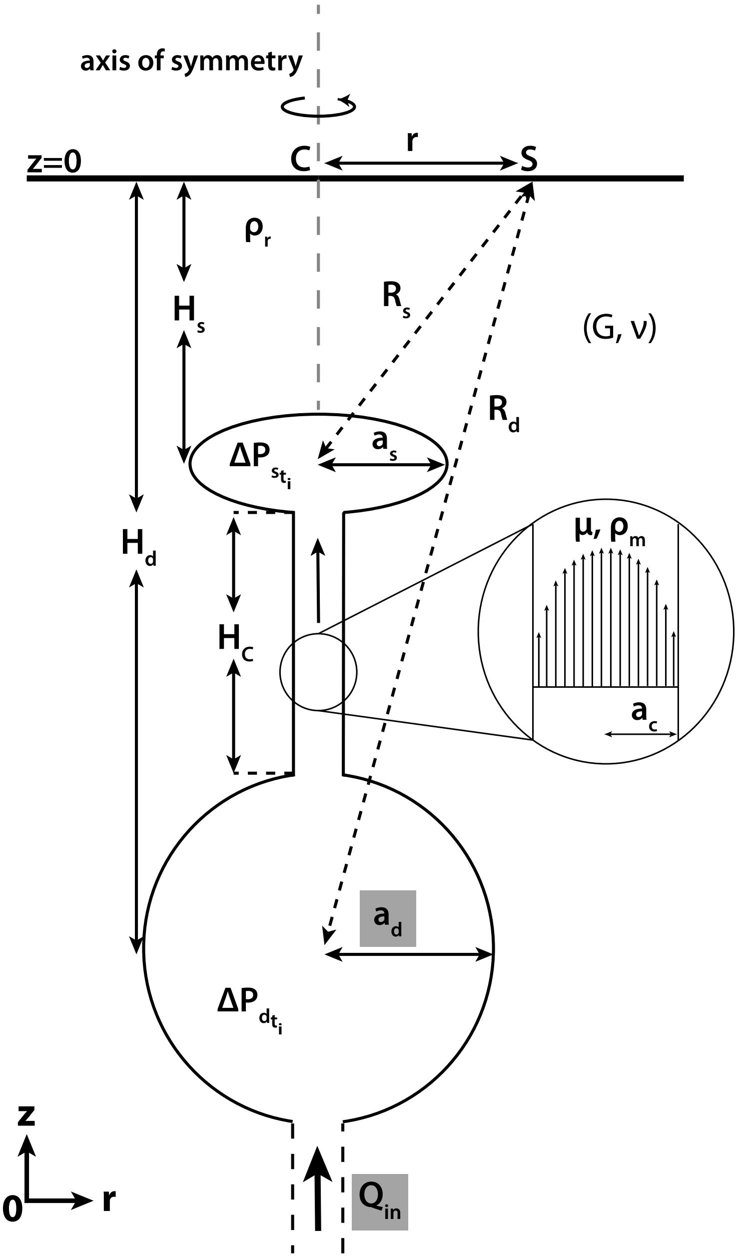

Figure 3.1: Schematic sketch of the two chamber model, modified after Reverso *et al.* [2014]. The magma inflow rate at the bottom chamber Q_{in} and the radius of the deep reservoir a_d are the two parameters considered to be uncertain in this study. Observations (vertical and horizontal displacements) are recorded at the surface at a given location S characterized by its distance r from the center of the volcanic system C. $R_s = \sqrt{r^2 + {H_s}^2}$ and $R_d = \sqrt{r^2 + {H_d}^2}$ are distances between S and the shallow and deep reservoirs, respectively.

of applying data assimilation to other types of models. Lastly, we discuss the ease of implementing our strategy and the future of EnKF for real-time volcano monitoring.

3.2 Methods

3.2.1 Forward Dynamical Model

We use the two-magma reservoir model proposed by Reverso *et al.* [2014]. This model consists of two reservoirs embedded in an elastic medium and connected by a hydraulic pipe. The deeper reservoir is assumed to be fed by a constant magma inflow, which corresponds to the bottom boundary condition of the system. The magma is assumed to be incompressible. This model, presented on **Figure 3.1**, is characterized by a set of geometrical and rheological parameters listed in **Table 3.1** and solves for the temporal evolution of the magma overpressures, ΔP_s and ΔP_d, for the shallow and the deep reservoirs, respectively. As shown by Reverso *et al.* [2014], this simple model provides a consistent explanation for the temporal evolution of the post-eruptive displacement measured at Grímsvötn volcano, Iceland after the three last eruptions (1998, 2004 and 2011). The initial and transient exponential behavior is due to the refilling of the shallow reservoir by the deeper one after the eruption. Then, once the system has been readjusted, a constant displacement rate is observed due to the constant magma inflow at the bottom of the system.

In this model, the values of the overpressure within the shallow and deep reservoirs, respectively, ΔP_s and ΔP_d, at a given time, t_{i+1}, are derived from their values at the previous time step, t_i, using the following discrete time-step equations (see equations derived in Appendix A of Reverso *et al.* [2014]):

$$\frac{\Delta P_{s_{t_{i+1}}} - \Delta P_{s_{t_i}}}{t_{i+1} - t_i} = \frac{G{a_c}^4}{8\mu\gamma_s H_c {a_s}^3}((\rho_r - \rho_m)gH_c + \Delta P_{d_{t_i}} - \Delta P_{s_{t_i}}) \tag{3.1}$$

$$\frac{\Delta P_{d_{t_{i+1}}} - \Delta P_{d_{t_i}}}{t_{i+1} - t_i} = \frac{G}{\gamma_d \pi {a_d}^3} Q_{in} - \frac{\gamma_s {a_s}^3}{\gamma_d {a_d}^3} \frac{\Delta P_{s_{t_{i+1}}} - \Delta P_{s_{t_i}}}{t_{i+1} - t_i} \tag{3.2}$$

The shapes (i.e. spherical or sill-like) of the shallow and deep reservoirs are characterised by two geometrical constants, respectively, γ_s and γ_d (Reverso *et al.* [2014]). The discrete formula stays valid as long as the time interval $\Delta t = t_{i+1} - t_i$ remains small

Table 3.1: Model parameters and true values assigned for the synthetic case. The highlighted parameters are the ones which are considered as uncertain in this study.

Parameters	**Description**	**Value**	**Unit**
Geometry			
a_c	Radius of the conduit.	1.6	m
a_d	Radius of the deep reservoir.	2.2	km
a_s	Radius of the shallow reservoir.	2.0	km
H_d	Depth of the deep reservoir.	35.0	km
H_s	Depth of the shallow reservoir.	3.0	km
γ_d	1.0 for Mogi point source, $8(1-\nu)/3\pi$ for sill.	1.0	
γ_s	1.0 for Mogi point source, $8(1-\nu)/3\pi$ for sill.	$8(1-\nu)/3\pi$	
α_d	1.0 for Mogi point source, $(4{H_d}^2)/(\pi{R_d}^2)$ for sill.	1.0	
α_s	1.0 for Mogi point source, $(4{H_s}^2)/(\pi{R_s}^2)$ for sill.	$(4{H_s}^2)/(\pi{R_s}^2)$	
Physics			
G	Shear modulus.	81.9	GPa
ν	Poisson's ratio.	0.25	
μ	Viscosity.	2000.0	Pa s
ρ	Density contrast, $(\rho_r - \rho_m)$.	300.0	kg m^{-3}
g	Gravity.	9.81	m s^{-2}
Basal condition			
Q_{in}	Magma flow rate in the deep reservoir.	0.02	km^3 y^{-1}
Initial conditions			
ΔP_{s_0}	Value of the shallow chamber overpressure at t_0.	0.0	Pa
ΔP_{d_0}	Value of the deep chamber overpressure at t_0.	0.0	Pa

compared to the time constant τ of the system given by $\tau = \frac{8\mu H_c {a_s}^3 {a_d}^3 \gamma_s \gamma_d}{G {a_c}^4 ({a_s}^3 \gamma_s + {a_d}^3 \gamma_d)}$ (Reverso *et al.* [2014]). Note that when Q_{in} is set to zero and the deep reservoir is sufficiently large when compared to the shallower one ($a_d/a_s \approx \infty$), this model corresponds to the case of a unique magma reservoir fed by a deep magma source which remains at constant pressure as previously proposed for several basaltic volcanoes (Lengliné *et al.* [2008]). This model can also represent the upper part of more complex plumbing system made of a large number of magma reservoirs lying at increasing depth. It thus benefits from the advantage of being both generic and simplistic.

Based on the Mogi model (Mogi [1958]), the radial u_R and vertical u_z displacements observed at the surface can be expressed using:

$$u_R(r,t_i) = \frac{(1-v)}{G} r \Big(\alpha_s \frac{{a_s}^3}{R_s^3} \Delta P s_{t_i} + \alpha_d \frac{{a_d}^3}{R_d^3} \Delta P_{d_{t_i}} \Big) \tag{3.3}$$

$$u_z(r,t_i) = \frac{(1-v)}{G} \Big(H_s \alpha_s \frac{{a_s}^3}{R_s^3} \Delta P s_{t_i} + H_d \alpha_d \frac{{a_d}^3}{R_d^3} \Delta P_{d_{t_i}} \Big) \tag{3.4}$$

The shapes (i.e. spherical or sill-like) of the shallow and deep reservoirs are characterised by two geometrical constants, respectively α_s and α_d (Reverso *et al.* [2014]). Provided that one has access to the deformation fields related to the activity of the volcano (i.e. inferred from GNSS observations and/or InSAR), **equations (3.3)** and **(3.4)** create a link between the dynamical model and the observations, necessary for data assimilation.

3.2.2 Data Assimilation: Ensemble Kalman Filter

On one hand, predictions given by a dynamical model incorporate errors due to the choices or limitations related to the model physics and parameters: including errors associated with assumptions, theory and/or conceptualisations within the underlying equations, errors due to the computational grid and its discretisation, numerical errors related to the time-step or numerical methods used to solve the mathematical equations, and errors associated with the model parameters. On the other hand, uncertainties are also present in the observations due to the instrument itself, different perturbations during data acquisition, and noise generated during pre- and post-processing of data. Moreover, in most cases, observation is not spatially nor temporally complete because of the limitation in data acquisition. Data assimilation takes advantage of the complementary information provided by the dynamical model and the observations. It corrects model predictions whenever observations are available in order to provide model state trajectory as accurate as possible. In ocean-atmosphere science, it has become the common approach for monitoring and forecasting.

Ensemble Kalman Filter is an ensemble-based stochastic data assimilation technique developed by Evensen (Evensen [1994, 2003]) as an alternative route to solve the limitations of the classic Kalman Filter. The main characteristic lies on the use of N-ensemble of realisations to construct a Monte Carlo approximation of the mean and covariance of the state vector (i.e. vector containing all the model parameters to be improved by data assimilation).

We adopted the EnKF method in this work. In general, the assimilation is divided into two steps: 1) the forecast step and 2) the update step (also known as the analysis step). The EnKF begins with the ensemble generation. N realisations (ensembles) of uncertain model parameters are performed according to an a priori distribution. Then, Monte Carlo simulation is performed while running forward the dynamical model for each ensemble member, resulting to the ensemble of model state forecast X, i.e. $X = \begin{bmatrix} x_{1,1} & x_{1,2} & x_{1,N_n} \\ x_{2,1} & \ddots & \vdots \\ \cdots & & \\ x_{N_x,1} & \cdots & x_{N_x,N_n} \end{bmatrix}$ where N_x is the number of state variables and N_n is the ensemble size, and the associated covariance error P^f.

In the following section we further describe the EnKF scheme and equations based on Evensen [1994, 2003].

Forecast step

The forecast is carried out by the model integration under the control of the model operator that represents the physical process governing the system. The model predicts the state at the current instance from the model state at previous instance according to the model operator as expressed in **equation (3.5)**.

$$X^f_{t_{i+1}} = \mathcal{M} X^a_{t_i} + q_{t_i} \tag{3.5}$$

f and a: denote the forecast and analysis, respectively, $\mathcal{M}$: the model operator derived from equations (3.1) and (3.2) that relates the state of the system at time, t_i to t_{i+1} (see **Appendix A.1** and **A.2**), and q: the model error. Initial conditions of the model state variables are necessary to start the model.

At each time step, the error covariance, P^f, of the model forecast which is an $N_x \times N_x$ matrix can be obtained using:

$$P^f = \overline{(X^f - \overline{X^f})(X^f - \overline{X^f})^T} \tag{3.6}$$

Update step

The update stage consists of correction of the model prediction by the observations in order to obtain a more precise estimation of the model state. The observations, D, i.e. $D = \begin{bmatrix} d_1 \\ d_2 \\ \cdots \\ d_{N_m} \end{bmatrix}$ where N_m is the total number of observations, can be anything that are related to the true model state $x^\dagger$ by the observation operator $\mathcal{H}$.

$$D = \mathcal{H}x^\dagger + \epsilon \tag{3.7}$$

Note that the observation error ϵ allows the derivation of the error covariance of the observations R, i.e. $R = \mathcal{E}(\epsilon\epsilon^T)$.

Updating X^f is straightforward and can be performed by first computing the Kalman gain, K, using **equation (3.8)**. The Kalman gain simply represents the magnitude of which the incoming observation corrects the model estimates in **equation (3.5)**.

$$K = P^f\mathcal{H}^T(\mathcal{H}P^f\mathcal{H}^T + R)^{-1} \tag{3.8}$$

To formalise the update, we use **equation (3.9)**.

$$X^a = X^f + K(D - \mathcal{H}X^f) \tag{3.9}$$

The result of the update is called the analysis, X^a. It is the linear sum of the model forecast and the correction introduced by the observation given the difference between the observations and model predictions. In general, the analysis must be at least statistically as accurate as any of the individual observation or the model prediction.

Lastly, the error covariance of the analysis, P^a, is calculated using **equation (3.10)**.

$$P^a = \overline{(X^a - \overline{X^a})(X^a - \overline{X^a})^T} \tag{3.10}$$

3.2.3 Experiment Set-up

We will now describe in detail how the assimilation experiments are implemented. The state variables are the magma overpressures ΔP_s and ΔP_d within the shallow and deep magma reservoirs, respectively. The observations are the vertical and the radial surface displacements observed at a given time, t_i, and at a given distance, r, from the axis of symmetry of the system. From a model simulation with a given set of parameters listed in **Table 3.1** (see **section 3.2.3**), we generate a set of synthetic observations and then using these observations and considering two of the parameters as uncertain, we perform the assimilation as described in **section 3.2.3** and compare the derived overpressures and model parameters obtained in two synthetic cases (i.e. state-only, state-parameter).

Generating synthetic observation

We perform a model simulation to produce synthetic data by setting each model parameter to a given value as defined in **Table 3.1**, in data assimilation, this step is referred to as the true run. These values are chosen such that they are consistent with the case of Grímsvötn volcano in Iceland. In particular, at Grímsvötn Volcano, the shallow storage zone has been well characterized by seismic and geodetic studies (Alfaro *et al.* [2007], Hreinsdóttir *et al.* [2014]). Other geometrical parameters are chosen in consistent with the study of Reverso *et al.* [2014]. The value taken for the shear modulus, G, however, represents an upper bound for the lower part of the crust (Auriac *et al.* [2014]). This large value results in large magma overpressure values but it does not influence the interpretation of the assimilation technique.

To produce the synthetic overpressures, the analytical solution of Reverso *et al.* [2014] to the differential equations (3.1) and (3.2) are used, i.e. $x^\dagger = \begin{bmatrix} \Delta P_s^\dagger \\ \Delta P_d^\dagger \end{bmatrix}$:

$$\Delta P_{s_{t_i}}^\dagger = A(1 - e^{-\frac{t_i}{\tau}}) + \frac{G Q_{in}}{\pi({a_s}^3 \gamma_s + {a_d}^3 \gamma_d)} t_i + \Delta P_{s_{t_0}}^\dagger \tag{3.11}$$

$$\Delta P_{d_{t_i}}^\dagger = \frac{\gamma_s A}{\gamma_d}(1 - e^{-\frac{t_i}{\tau}}) + \frac{G Q_{in}}{\pi({a_s}^3 \gamma_s + {a_d}^3 \gamma_d)} t_i + \Delta P_{d_{t_0}}^\dagger \tag{3.12}$$

with $A = \frac{{a_d}^3 \gamma_d}{{a_s}^3 \gamma_s + {a_d}^3 \gamma_d}[\Delta P_{d_{t_0}}^\dagger - \Delta P_{s_{t_0}}^\dagger + (\rho_r - \rho_m) g H_c - \frac{8 \gamma_s Q_{in} \mu H_c {a_s}^3}{\pi {a_c}^4 ({a_s}^3 \gamma_s + {a_d}^3 \gamma_d)}]$. The resulting overpressures are considered as the true values and are then used as input in equations

(3.3) and (3.4) in order to generate synthetic displacements $d_m^\dagger$, i.e. $d_m^\dagger = \begin{bmatrix} u_{R_m}^\dagger \\ u_{z_m}^\dagger \end{bmatrix}$.

The observation is then generated by adding a white Gaussian noise, i.e. $\mathcal{N}(\mu_u = 0, \sigma_u^2)$, to the synthetic displacements, where σ_u represents the instrument precision along the radial and vertical directions. We use the typical GNSS instrument errors that are 1 mm and 10 mm for u_R and u_z, respectively.

Figure 3.4 shows the observations (vertical and radial displacements) generated at various distances from the volcanic center (i.e. $r = 1$ to 4.9 km). Notice that for all the radial displacements and for those vertical displacements that are nearest to the volcano axis (i.e. $r = 1$ to 2.5 km), it is very difficult to discern the synthetic observation because the amplitude of the noise is very small relative to the signal. Note that in the results part (section 3.3) we use a total of 80 observations (i.e. $N_m = 80$) to define the observation vector D, which comprises the vertical and radial displacements, uniformly (every 100 m) located at distance $r = 1$ to 4.9 km away from the volcano axis. The effect of the number of observations used as well as the frequency of incoming observations are discussed in **Section 3.4**.

Assimilation Strategy: Using EnKF

The state variables are the overpressures ΔP_s and ΔP_d and we consider two parameters a_d and Q_{in} as uncertain. We focused on these particular parameters characterizing the deeper part of the magma pumbing system because they are the most difficult to recover using surface displacement data.

The time interval, Δt, is fixed to 2 days, which is much smaller than the true time constant τ (i.e. $\tau = 0.11$ y). The start of the assimilation begins just after an eruption when the reservoirs are refilling and terminates after 500 time-steps (i.e. $t_f \sim 2.74$ y). The initial values of magma overpressures are set to zero (See **Table 3.1**), assuming that both reservoirs had been fully depressurized by the previous eruption. The frequency of available observation, f_{obs}, is usually fixed to one; meaning that at each assimilation step (i.e. every 2 days) there is always an available observation. In the case where no observation ($f_{obs} = 0$) is available, the model prediction cannot be corrected by the observation. This particular case is hereafter called the free run and is presented for comparison.

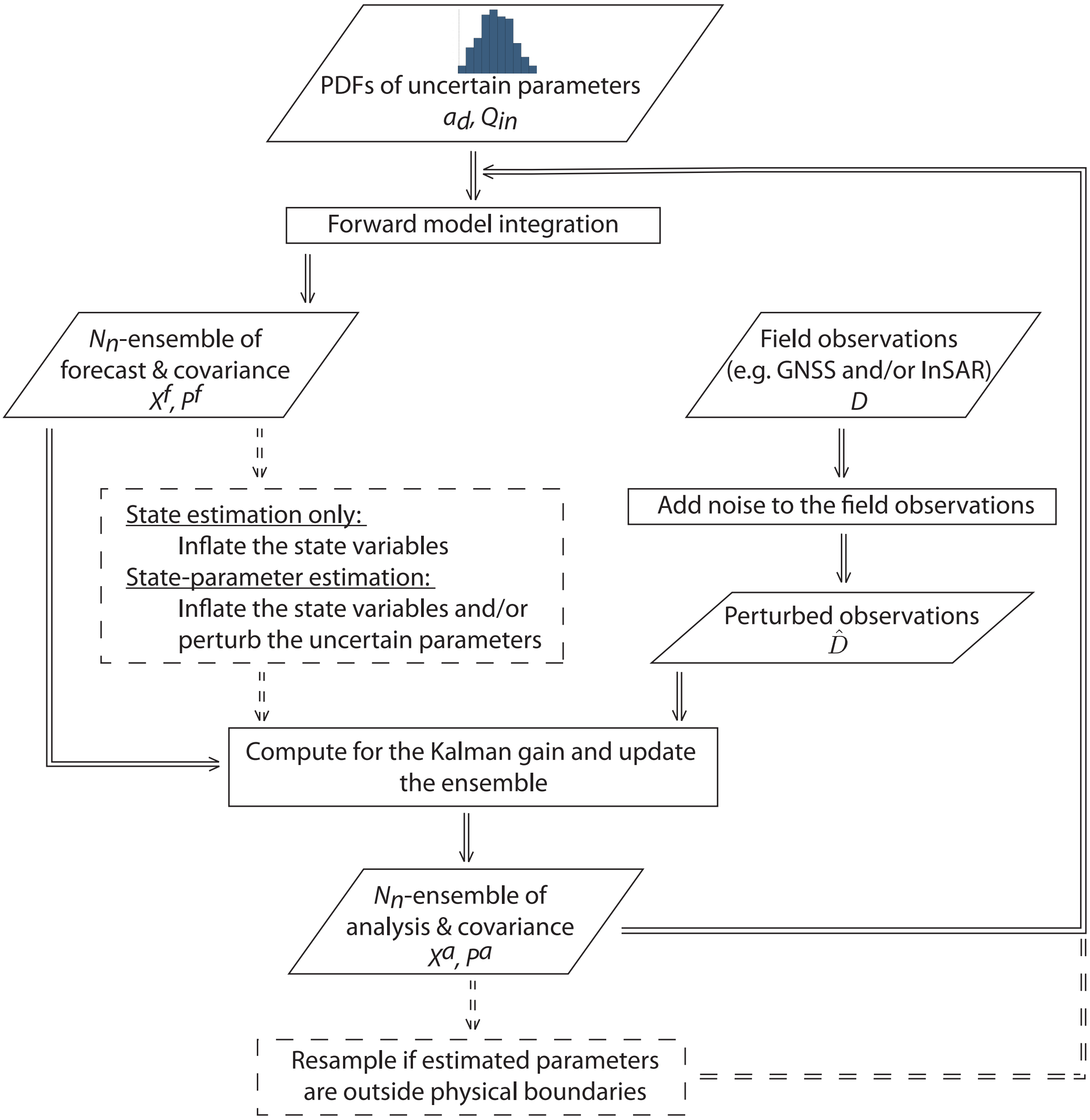

Figure 3.2: The step-by-step EnKF strategy that we implemented in this study. The broken borders and lines imply that the step is optional.

Two cases are considered here: case A) where only the state variables are predicted and case B) where the state variables and the two uncertain parameters are both estimated. We used the classic EnKF where the observations are perturbed prior to assimilation (Burgers *et al.* [1998]). Below we describe in detail the practical implementation of EnKF as summarized in **Figure 3.2**:

1. We start by defining an initial ensemble of 1000 members. For ensemble generation, two distributions are considered for the uncertain parameters: 1) using a truncated-Gaussian distribution wherein the mean of each distribution is centered on the true value of the uncertain parameters (hereafter called *unbiased*) and 2) using a Gaussian-prior distribution that does not include the true value of the uncertain parameters, the mean of each distribution being very far from their true values (hereafter called *biased*).

2. For each of the ensemble members:

    (a) We run the forward model step-by-step from the initial condition until the data assimilation step t_{i+1}. The state vector is built depending on which case is being tested. See **Appendix A.1** and **A.2** for the state-only estimation and state-parameter estimation, respectively.

    Tip 1: When performing either state-only estimation or state-parameter estimation, an inflation factor $\rho_{infl} \in [0, 1)$ can be multiplied to the ensemble of state variables, i.e. $X^f = (1 + \rho_{infl})X^f$, to prevent the ensemble from collapsing to a single value. For all the synthetic cases performed (**section 3.3**), we used an inflation factor equal to 0.1 at each assimilation step. Note that prior to the application of an inflation factor, the forecast state vector must be mean-centered.

    Tip 2: In state-parameter estimation using EnKF, the parameters are only updated by the covariance between them and the state variables. When doing so, we randomly perturb the uncertain parameters by adding noise, $\mathcal{N}(0, \alpha_p^2)$, where α_p is the additive inflation. This would help the filter to explore more possible values since their values do not change during the forecast step, i.e., $p^f_{t_{i+1},n} = p^a_{t_i,n}$. In our synthetic cases, we used an additive inflation of $\alpha_{a_d} = 5$ and $\alpha_{Q_{in}} = 0.005$ to tune the uncertain parameters during the assimilation. These are derived from empirical observations after several adjustments.

(b) The error covariance of the forecast, P^f, is computed using **equation (3.6)**.

(c) We perturb the field observation vector using:

$$\hat{d}_m = d_m + \eta \tag{3.13a}$$

$$\hat{D} = [\hat{d}_1, \hat{d}_2, ..., \hat{d}_{N_m}] \tag{3.13b}$$

where η is a random variable with distribution $\mathcal{N}(0, R)$.

(d) The state vector is then updated using **equation (3.9)**, replacing D with $\hat{D}$:

$$X^a = X^f + K(\hat{D} - HX^f) \tag{3.14}$$

Tip 3: Resample the analysis state vector, X^a, using the strategy proposed by (Evensen [2009]) before moving to the next data assimilation time step if the updated values of the uncertain parameters fall beyond or exceed the boundary conditions.

(e) The error covariance of the analysis, P^a, is obtained using **equation (3.10)**.

3.3 Results

Synthetic Case A: State Estimation

The first test case tracks only the evolution of the overpressures in the shallow and deep reservoirs, i.e. **equation (A.1)**, given an initial condition where the distributions of the uncertain parameters are unbiased (**Figure 3.3C**) or biased (**Figure 3.5C**).

In both cases, the EnKF performed well in predicting the shallow and deep overpressures towards the end of the assimilation as evidenced by the red line (i.e. EnKF) that closely follows the black broken line (i.e. true value) in **Figures 3.3** and **3.5**. In fact for the shallow overpressure, even with a poor knowledge about the uncertain parameters, the EnKF was able to catch almost perfectly the true overpressure. Unsurprisingly, the predicted overpressure for the deep reservoir is more likely affected by poor parameter initialisation because the displacement induced by the deeper chamber is smaller, such that its overpressure is indirectly constrained by the dynamical model and consequently more influenced by the two uncertain parameters.

Table 3.2: Results of EnKF via state estimation after 500 time steps.

	True Value	Free Run						EnKF					
		Unbiased			Biased			Unbiased			Biased		
		Mean	Stdev	% error	Mean	Stdev	% error	Mean	Stdev	% error	Mean	Stdev	% error
$\Delta P_s (MPa)$	150.81	153.02	50.23	1.47	180.12	18.38	19.44	150.71	0.05	0.07	149.78	0.04	0.69
$\Delta P_d (MPa)$	62.02	64.02	53.44	3.22	91.79	19.55	48.00	62.00	0.73	0.04	59.38	0.40	4.25

In **Figure 3.5B**, the result of EnKF is found closer to the free model prediction (i.e. results in green, labeled as free run) at the start of the experiment when the prior information about the uncertain parameters is far from their true values (see inset 2 for a magnified version). The model error seems smaller at the beginning as compared to the observation error, hence, the contribution of the model prediction is found to dominate the process. As the experiment goes on, the model error increases tremendously (i.e. the mean overpressure from the free run deviates away from the true overpressure) but thanks to the small measurement error, the analysis was able to converge closer to the true state of the system. Although overpressure estimation may have been unsuccessful towards the end of the assimilation, still, the resulting error differences between the true values and the EnKF-estimates are very small (i.e. 0.69 % and 4.25 % for the shallow and deep reservoirs, respectively). Note that this error difference may increase if the assimilation window is extended. The failure of estimation is due to the observation operator that relates the model and the observation, since it incorporates an uncertain parameter a_d which is fixed to a bad value in this case.

In **Table 3.2**, we present the summary of the synthetic results after performing the experiments for the state estimation case. As expected, there is a significantly higher percentage of error when the model is freely propagated forward in time without the correction of the observations (free run).

We estimated the displacements using the overpressures derived from the assimilation run, i.e. applying **equations (3.3)** and **(3.4)**. **Figures 3.4** and **3.6** show 10 out of the 80 combined radial and vertical displacements used during the assimilation. Notice that in the case where the uncertain parameters are well-constrained (i.e. **Figure 3.3C**), the displacements are well forecasted even at distances where the signal-to-noise ratio starts to weaken (i.e. vertical displacements at $r \geq 3$ km, see **Figure 3.4**) . However, in the case of poorly initialised parameters (i.e. **Figure 3.5C**), displacement prediction is not favorable especially along the vertical component (**Figure 3.6**) where the forecast worsens as one goes farther away from the volcano axis.

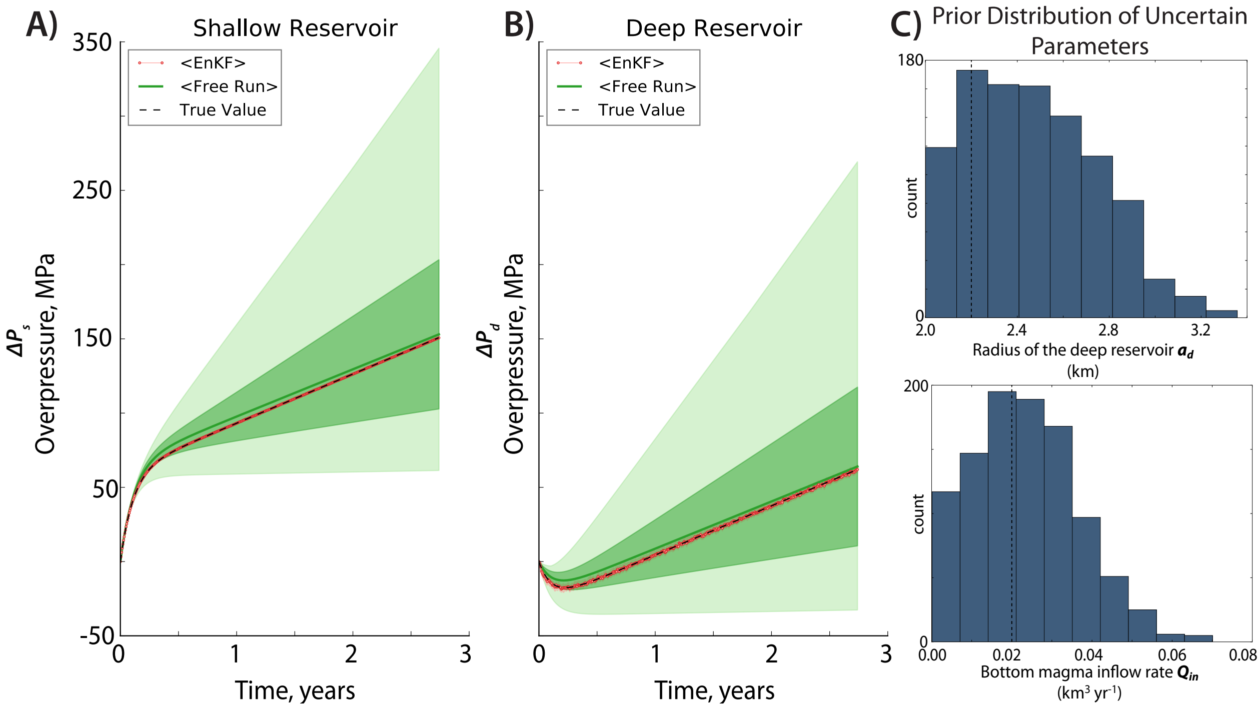

Figure 3.3: The evolution of the overpressures after performing the state estimation (Figure 3.3A and 3.3B), given that the initial ensemble of the uncertain parameters (Figure 3.3C) are **non-Gaussian**, **centered** on their true values (black broken lines). In Figures 3.3A and 3.3B, the black broken line represents the true value of the overpressures. The green ones represent the model forecasts where the green solid line is the mean, the dark green fill is the spread (1σ) and the light green fill covers the full extent of the ensemble (i.e. [min, max]). The red ones represent the result of EnKF where the red solid line is the mean, the dark red fill is the spread (1σ) and the light red is the full extent of the ensemble. Notice that the spread of the ensemble is very narrow for the assimilation case ($\sim 10^4 - 10^6$).

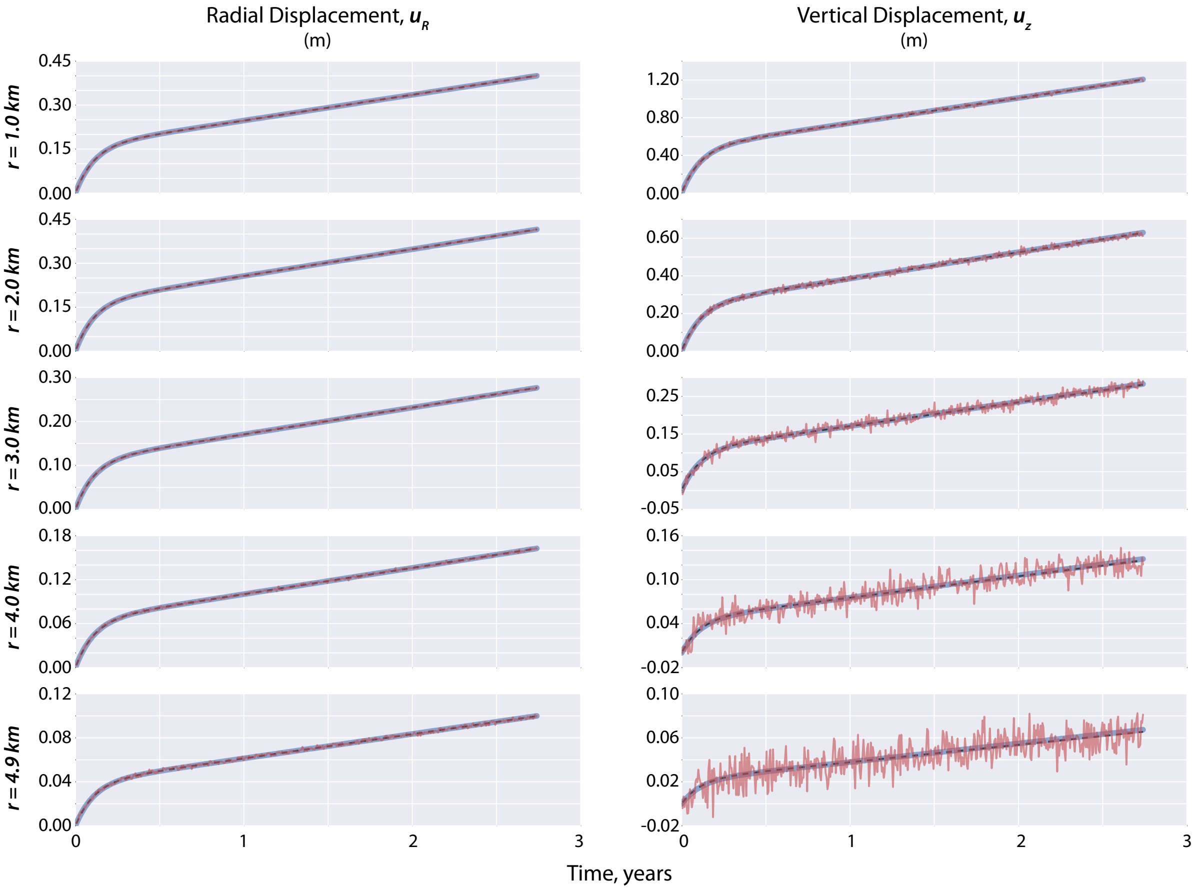

Figure 3.4: The EnKF-estimated displacements after performing assimilation via state estimation (i.e. blue solid line) given that the prior distribution of the uncertain parameters are close to their true values (Figure 3.3C). The synthetic displacements used as D during assimilation are the noisy red lines that are more evident in the vertical component at far-field distances. The black broken lines correspond to the true values.

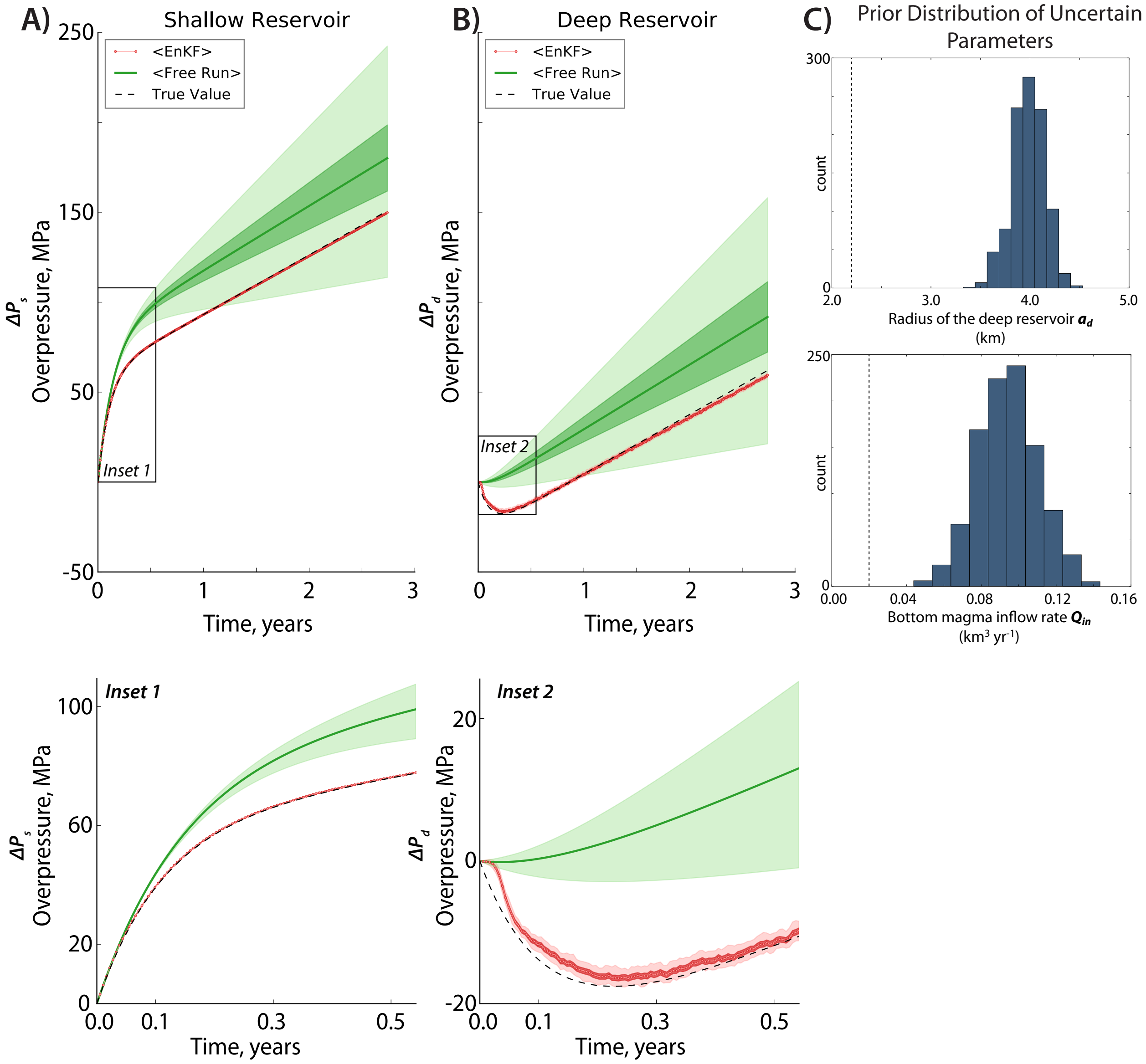

Figure 3.5: The evolution of the overpressures after performing the state estimation (Figures 3.5A and 3.5B); given that the initial ensemble of the uncertain parameters (Figure 3.5C) are **Gaussian**, **not centered** on their true values (black broken lines). The insets provide a magnified image of the overpressures at the beginning of the assimilation. In Figures 3.5A and 3.5B as well as in the insets, the black broken line represents the true value of the overpressures; the green ones represent the result of the free run where the green solid line is the mean, the dark green fill is the spread (1σ) and the light green fill covers the full extent of the ensemble (i.e. [min, max]); the red ones represent the result of EnKF where the red solid line is the mean, the dark red fill is the spread (1σ) and the light red is the full extent of the ensemble. Notice that the spread of the ensemble is very narrow for the assimilation case ($\sim 10^4 - 10^6$).

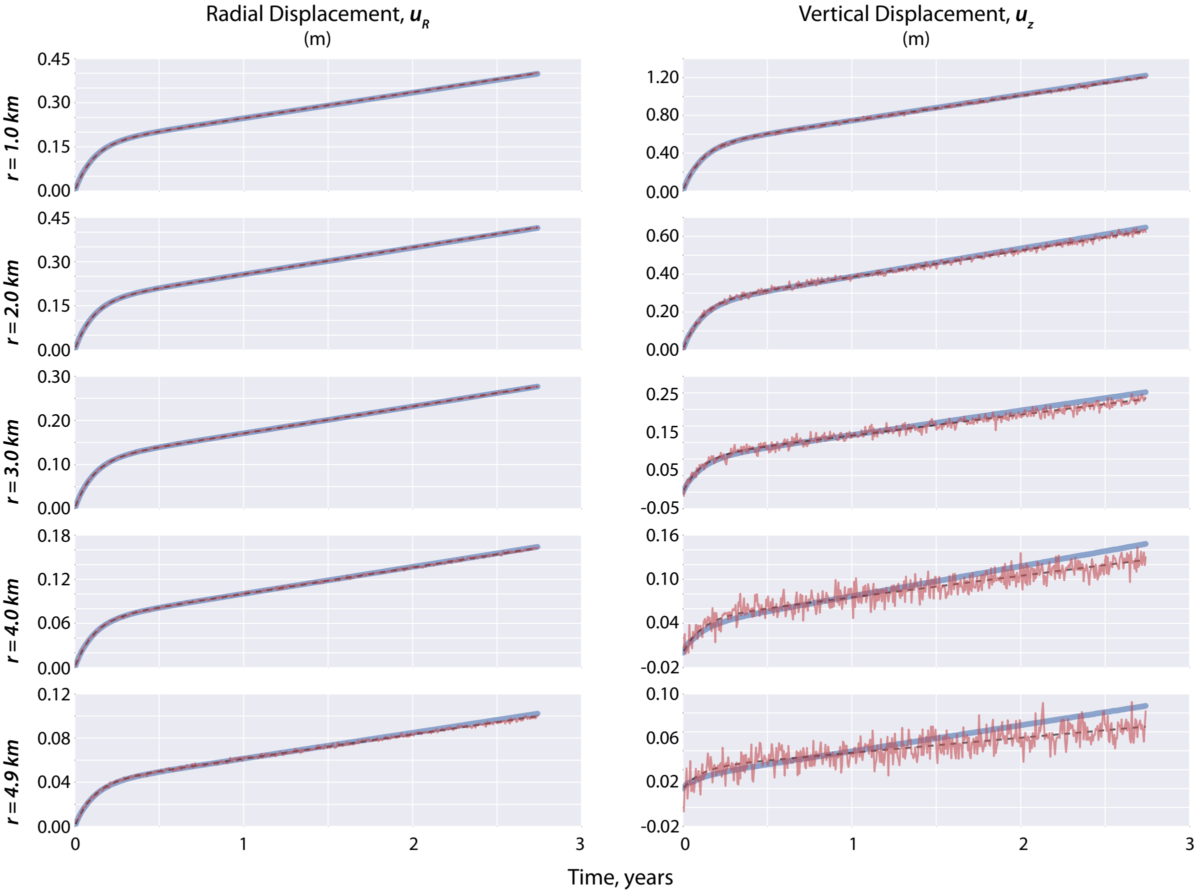

Figure 3.6: The EnKF-estimated displacements after performing assimilation via state estimation (i.e. blue solid line) given that the prior distribution of the uncertain parameters are far from their true values (Figure 3.5C). The synthetic displacements used as D during the assimilation are the noisy red lines that are more evident in the vertical component at far-field distances. The black broken lines correspond to the true values.

Synthetic Case B: State-Parameter Estimation

There are two possible ways to solve the issue in displacement prediction: 1) extend the state vector X incorporating the model-predicted displacements, i.e., $X = \begin{bmatrix} x^f \\ d^f \end{bmatrix}$, where $d^f = Hx^f$ and 2) extend the state vector incorporating the uncertain parameters (i.e. **equation (A.4)**). We opted for the second strategy because it will not only improve the field observation estimates but will also allow us to properly estimate the overpressures and to be able to constrain and gain more knowledge about the uncertain parameters. Furthermore, in performing the first option, the computational cost can increase significantly when we increase the number of observations used during the assimilation, i.e. using InSAR data.

Parameter estimation is very challenging especially when the parameters have no direct link to field observations and if there are no means to compare them to the actual values. The characteristics of the deep magmatic reservoir for example is poorly known in volcanology since it is buried very deep (i.e. > 10 km) into the Earth.

We followed the same initial conditions performed in the first case given that: 1) the uncertain parameters are “unbiased” or have truncated-normal distributions, centered on their true values (**Figure 3.3C**) and 2) the uncertain parameters are “biased” or have normal distributions but are not centered on their true values (**Figure 3.7C**). We used the augmented state vector in **equation (A.4)** to include the uncertain parameters in the forecasting.

Results show that the filter tracks almost perfectly the true behavoir of the overpressures given the two different types of parameter initialisation as shown for example in **Figure 3.7**, where the prior distributions of a_d and Q_{in} are biased. In fact, the final values of the overpressures have as little as $0.0 - 0.01\%$ and $0.04 - 0.06\%$ error difference with respect to their true values for the shallow and deep overpressures, respectively.

In **Figure 3.8**, we plotted a_d and Q_{in} at each assimilation step given two diferent a priori assumptions for the uncertain parameters. Notice how the EnKF-estimated

Table 3.3: Results of EnKF via state-parameter estimation after 500 time steps.

	True Value	Free Run						EnKF					
		Unbiased			Biased			Unbiased			Biased		
		Mean	Stdev	% error	Mean	Stdev	% error	Mean	Stdev	% error	Mean	Stdev	% error
$\Delta P_s(MPa)$	150.81	153.51	51.29	1.79	180.53	18.15	19.71	150.82	0.04	0.01	150.81	0.04	0.00
$\Delta P_d(MPa)$	62.02	64.54	54.57	4.06	92.22	19.31	48.70	62.05	0.22	0.04	62.06	0.23	0.06
$a_d(m)$	2200.00							2141.67	91.08	2.65	2249.62	89.13	2.26
$Q_{in}(km^3y^{-1})$	0.02							0.019	0.002	4.91	0.021	0.002	5.47

parameters converged well near their true values regardless of how they were initialised. In fact, at the beginning of the assimilation, the filter immediately recognises its supposed trajectory hence decreases a_d and Q_{in} allowing convergence to their true values. Interestingly, we find Q_{in} more sensitive to the estimation than a_d as evidenced by the steep drop at the start especially when the prior parameter distribution is biased. To a greater extent, it fell beyond the true value but eventually recuperates and adjusts to its correct behavior. In **Table 3.3** we summarized the results of synthetic case B, showing that there is a very good fit between the EnKF-estimated state variables and model parameters and their true values.

Figure 3.9 confirms our initial recommendation that augmenting the state vector to include the uncertain parameters in the estimation will result to well-predicted radial and vertical displacements.

3.4 Discussions

Influence of Spatial and Temporal Resolutions

High spatial resolution vs. high temporal resolution dataset

Our results show the huge potential of EnKF in predicting the overpressures and displacements as well as in estimating the uncertain model parameters. However, having 40 near-field GNSS stations that will provide 80 observations every two days is often not the case for most volcanoes. In **Figure 3.10** we show how EnKF performs when the number of observations is varied using two types of dataset: 1) a GNSS-like dataset and 2) an InSAR-like dataset. The GNSS-like dataset is composed of 10 observations (i.e. five radial and five vertical displacements) located at distance $r = 1 - 5$ km away from the volcano axis and is uniformly spaced every 1 km. The InSAR-like data is an 11 x 11 grid centered on zero-axis (i.e. $r = 0$ as the volcano axis) with two components (i.e.

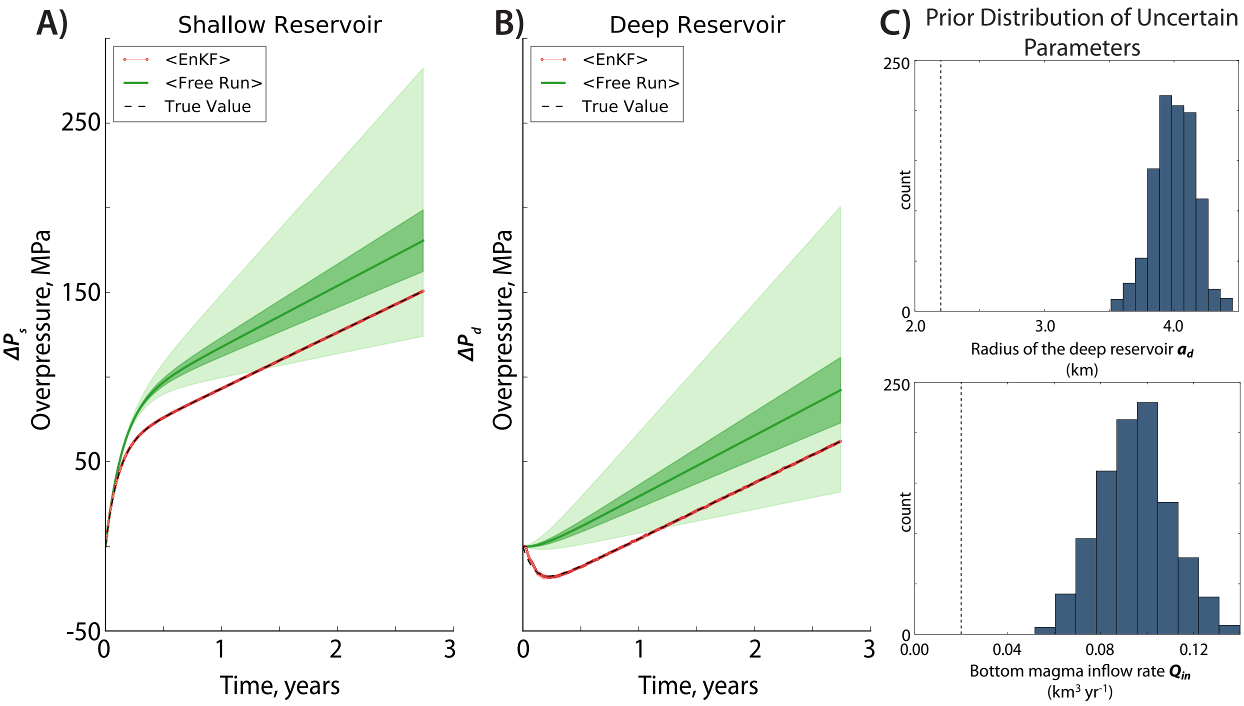

Figure 3.7: The evolution of the overpressures after performing the state-parameter estimation (Figures 3.7A and 3.7B); given that the prior distributions of the uncertain parameters (Figure 3.7C) are **Gaussian**, **not centered** on their true values (black broken lines). In Figures 3.7A and 3.7B, the black broken line represents the true value of the overpressures; the green ones represent the result of the free run where the green solid line is the mean overpressure, the dark green fill is the spread (1σ) and the light green fill covers the full extent of the ensemble (i.e. [min, max]); the red ones represent the result of EnKF where the red solid line is the mean, the dark red fill is the spread (1σ) and the light red is the full extent of the ensemble. Notice that the spread of the ensemble is very narrow for the assimilation case.

A) Using unbiased prior distribution

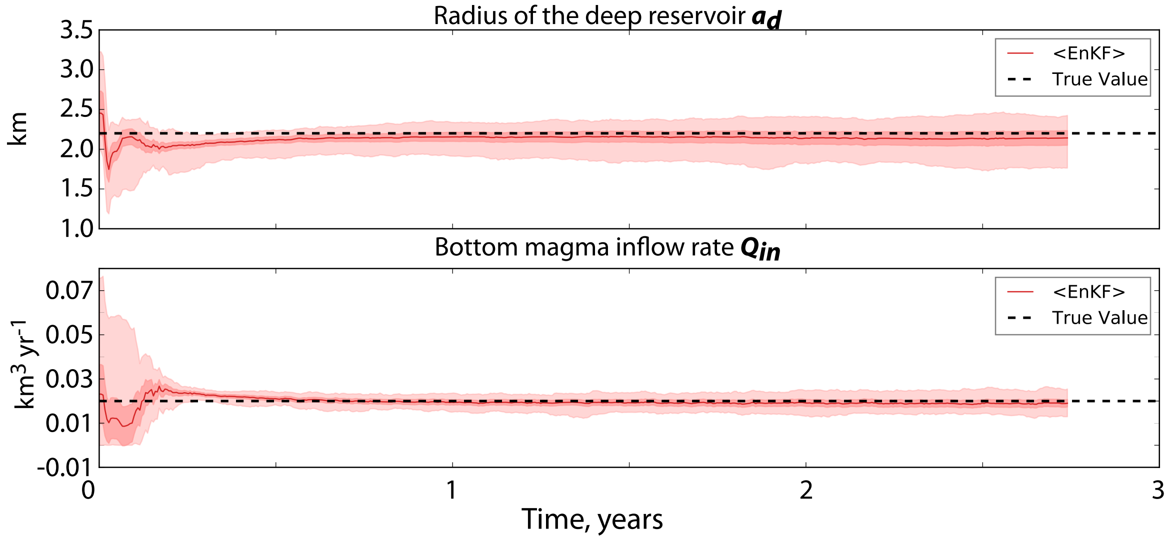

B) Using biased prior distribution

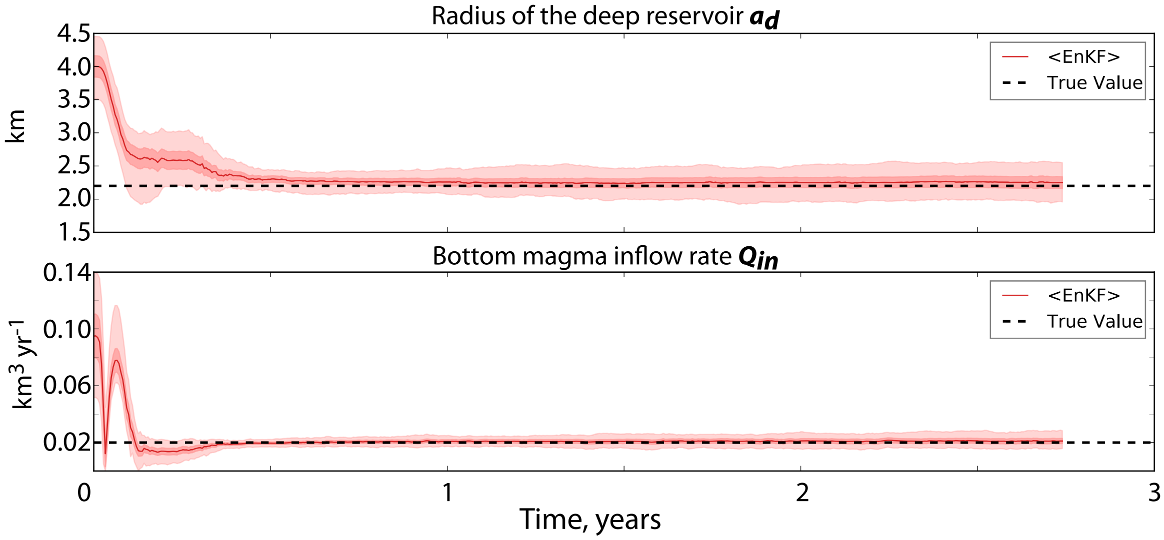

Figure 3.8: The EnKF-predicted uncertain parameters after performing state-parameter estimation given that the prior distributions of the uncertain parameters are A) unbiased or B) biased. The solid orange line is the mean value of the uncertain parameters. The dark-shaded and light-shaded orange colors represent the spread (1σ) and the [min,max] of the ensemble, respectively. The true values are the black broken lines.

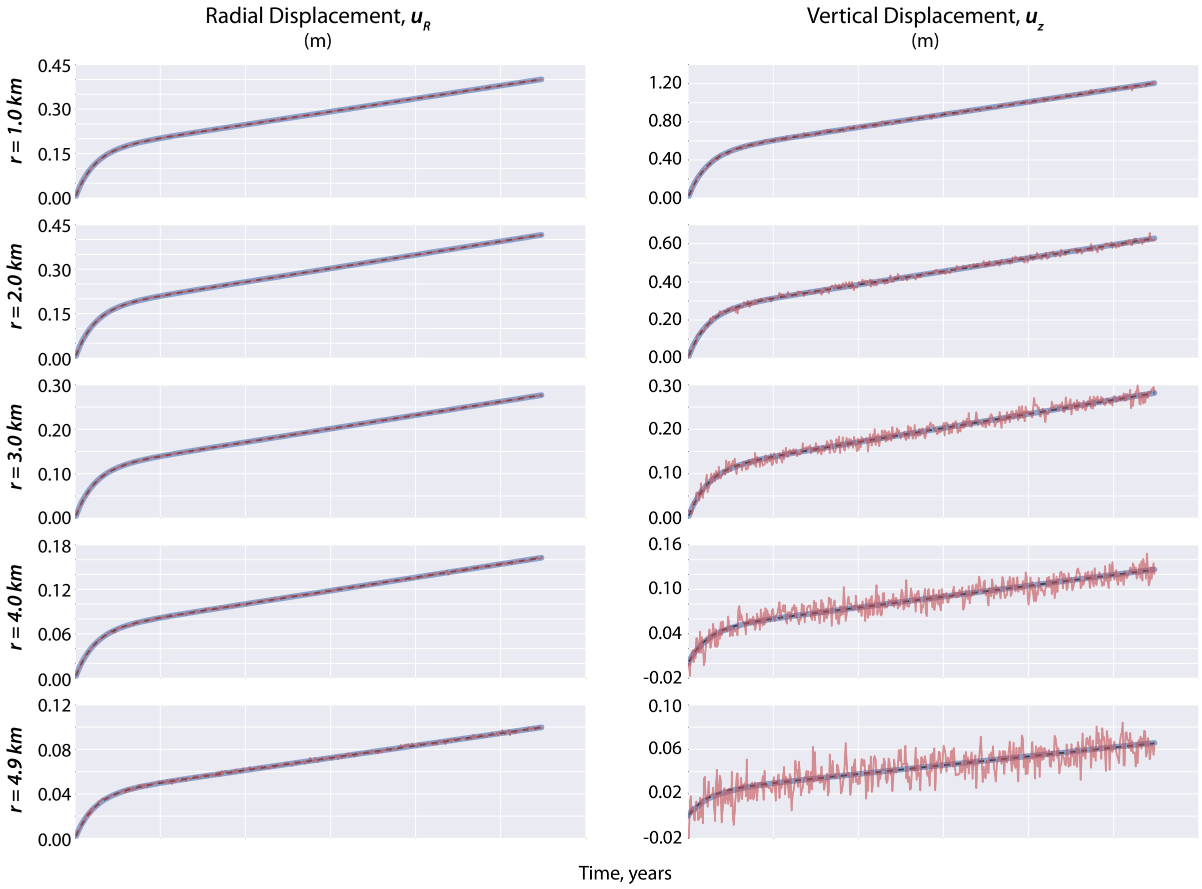

Figure 3.9: Ten of the 80 EnKF-estimated displacements after performing assimilation via state-paremeter estimation (i.e. blue solid line) given that the prior distributions of the parameters are biased (Figure 3.7C). The synthetic observations used as D during assimilation are the noisy red lines that are more evident in the vertical component at far-field distances. The black broken lines correspond to the true values of the displacements.

vertical and radial directions) that have spatial resolutions of 1 km. This provides a total of 242 observations located at distance $r = 1$ to $5\sqrt{2}$ km away from the volcano axis. Each of the datasets is assimilated every two days ($f_{obs} = 1$), consistent with the time interval of the model. We use a prior distribution which is Gaussian and not centered on the true values for the uncertain parameters (**Figure 3.7C**) because it is the most realistic and most critical case. Our findings show that both datasets are able to track the true behaviour of the shallow and deep overpressures. However, when it comes to estimating the uncertain model parameters, only the InSAR-type data were able to allow convergence of Q_{in} and a_d to their true values.

The challenge remains with the availability of InSAR data every two days. At the time of writing, only the Sentinel-1 satellite has the capability to provide radar data as frequent as every 6-12 days. TerraSAR-X can provide data every 11 days whereas COSMO SkyMed's routine return period can acquire data every 8 days by using different satellites in its constellation. To be more realistic, we then assimilated the InSAR-like dataset every 12 days ($f_{obs} = 1/6$) and kept the frequency of available GNSS data to two days ($f_{obs} = 1$). This means that for the InSAR-like data, the model predictions are only corrected every 12 days. **Figure 3.11** illustrates that the InSAR-like data failed to recover the true behavior of the overpressures towards the end of the assimiliatin experiment. More precisely, it failed to recover the exponential part of the system or during the time when the shallow reservoir is refilled by the deep one after an eruption. As a consequence of the poor overpressure prediction at the beginning, parameter estimation cannot be performed because their resulting posterior distributions are physically meaningless (i.e. negative radius of the deep reservoir). Performing the resampling option cannot even solve the issue. Take note that in EnKF, uncertain model parameters are only updated by the sample covariance between them and the state variables (i.e. in this case, the overpressures), and that the model evolution for them is simply an identity.

Given the aforementioned results, we know that the advantage of using GNSS data to capture the behavior of the overpressures is its high temporal resolution, in which it is possible to obtain daily observations that can be used for assimilation. InSAR data on the other hand, are less frequent to acquire but provide better spatial information about the surface deformations and constraints on the uncertain parameters. In order to exploit the advantages of both dataset, we jointly assimilated the GNSS-like and InSAR-like data. **Figure 3.12** shows how the evolution of the overpressures is well captured and

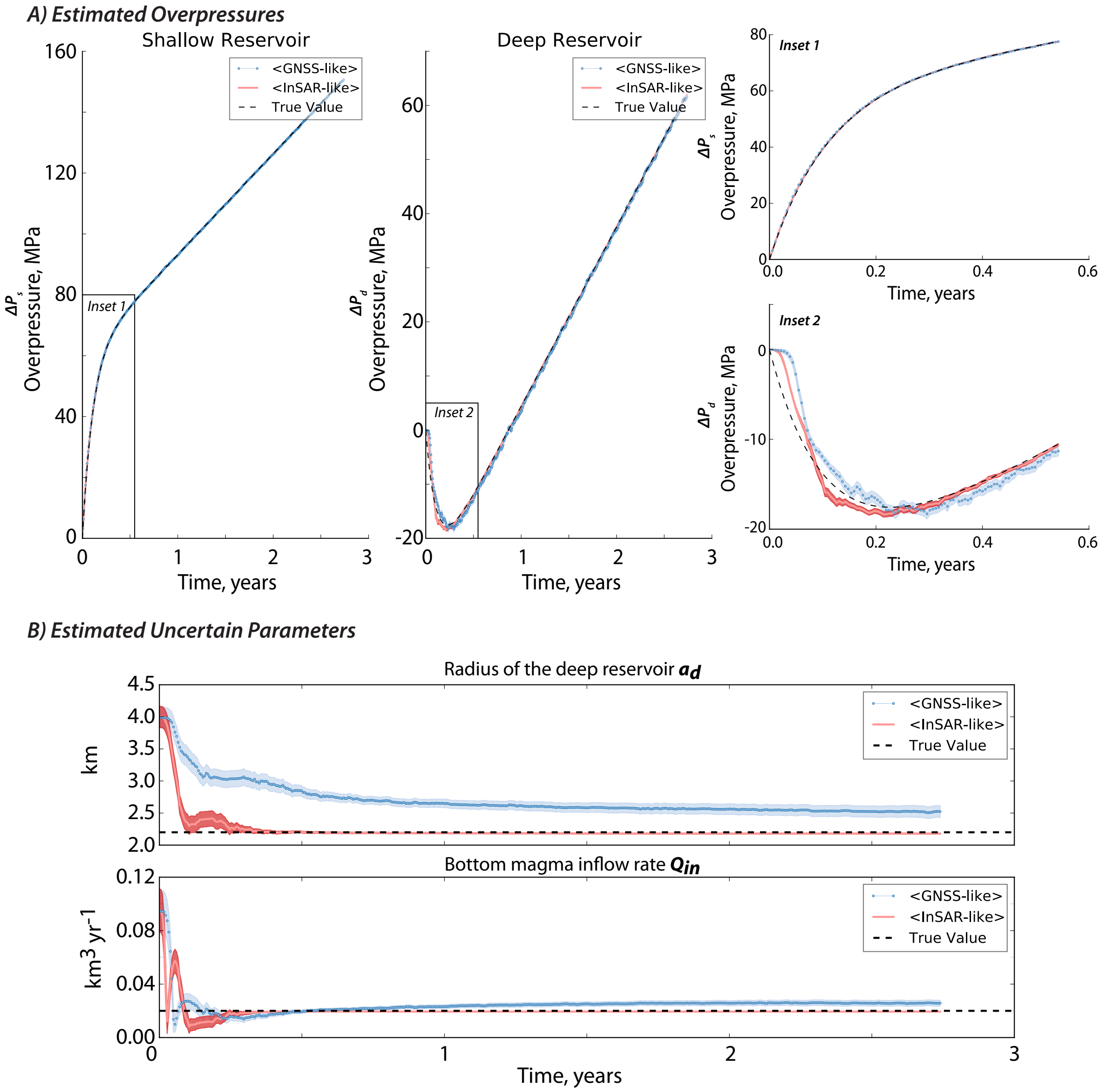

Figure 3.10: **Influence of the spatial density of observations on the assimilation: GNSS** (10 observations that are assimilated every time-step, $f_{obs} = 1$, with distance to the volcanic center ranging from 1 to 5 km) **vs. InSAR-like dataset** (242 observations that are assimilated every time-step, $f_{obs} = 1$, with distance to the volcanic center ranging from 1 to $5\sqrt{2}$ km). Figure 3.10A and 3.10B illustrates the estimated overpressures and uncertain parameters, respectively, given that the initial conditions of the uncertain parameters are similar to those of in Figure 3.5C. The insets in Figure 3.10A provide a closer look on the overpressures at the beginning of the assimilation. The light blue and red shades correspond to the spreads (1σ). Note that for the overpressures, the spreads are difficult to discern since they are very small when compared to the scale of the plot. The black broken lines represent the true values.

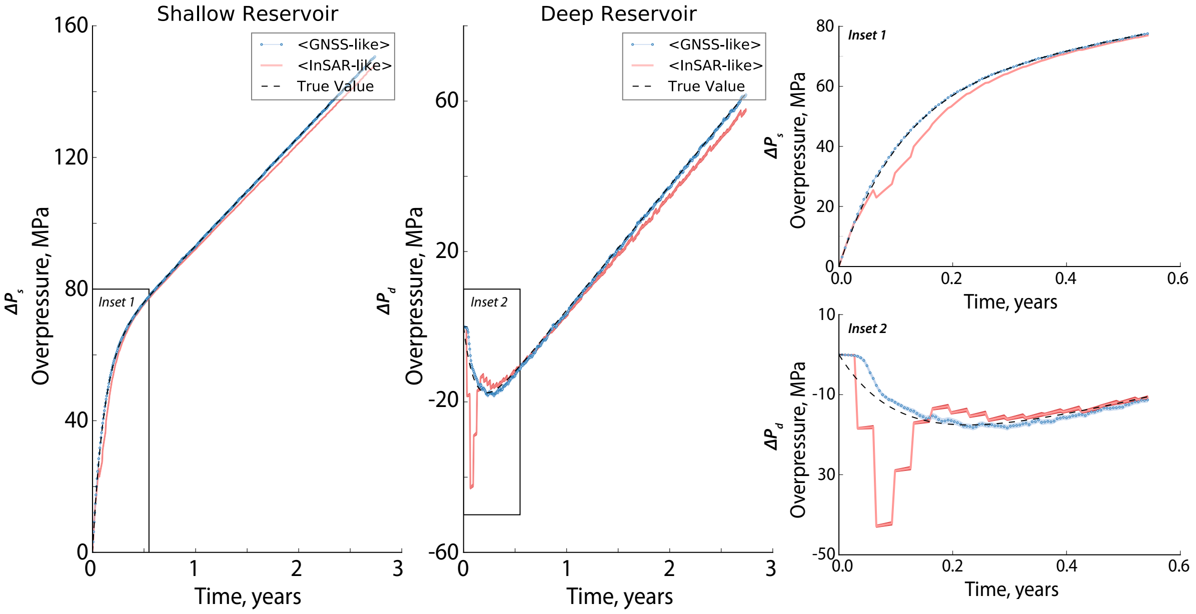

Figure 3.11: **Influence of the frequency of observations on the assimilation: GNSS** (10 observations that are assimilated every time step, $f_{obs} = 1$, with distance to the volcanic center ranging from 1 to 5 km) **vs. InSAR-like dataset** (242 observations that are assimilated every 12 days, $f_{obs} = 1/6$, with distance to the volcanic center ranging from 1 to $5\sqrt{2}$ km). Since parameter estimation is not possible to perform when InSAR dataset is used (see text), only the estimated overpressures are presented. Note that the initial conditions of the uncertain parameters are similar to those of in Figure 3.5C. The insets provide a closer image of the overpressures at the beginning of the assimilation. The light blue and red shades correspond to their spread (1σ). Note that these values are difficult to discern since they are very small when compared to the scale of the plot. The black broken lines represent the true values.

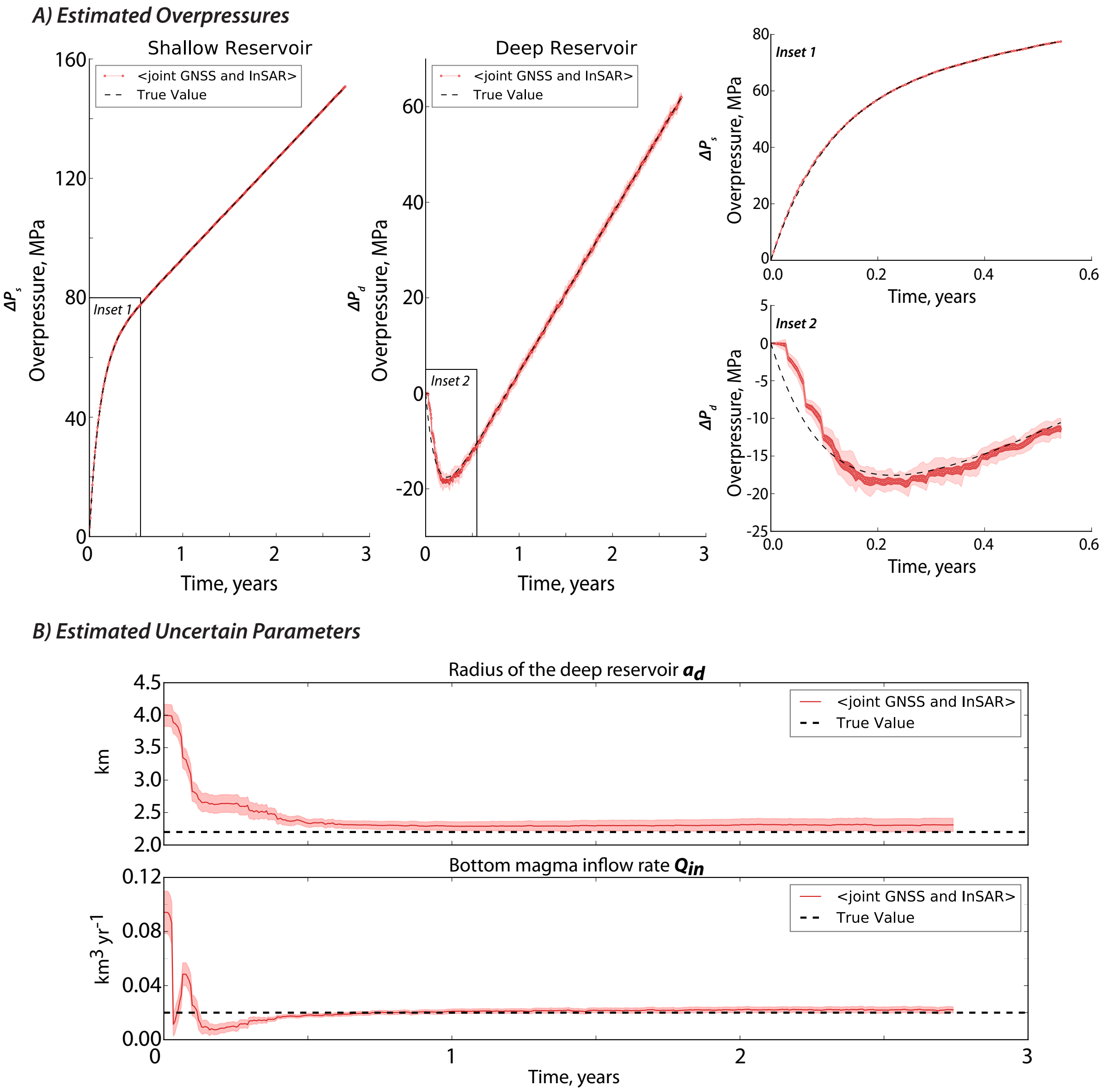

Figure 3.12: The estimated overpressures (A) and uncertain parameters (B) after jointly assimilating GNSS (10 observations that are assimilated every time-step, $f_{obs} = 1$, with distance to the volcanic center ranging from 1 to 5 km) and InSAR-like observations (242 observations that are only assimilated every 12 days, $f_{obs} = 1/6$, with distance to the volcanic center ranging from 1 to $5\sqrt{2}$ km). The initial conditions of the uncertain parameters are similar to those of in Figure 3.5C. The inset in A) provides a magnified view of the overpressures at the start of the assimilation. The pink shade corresponds to the spread (1σ). The black broken lines represent the true values.

how the uncertain model parameters converged to their true values. In fact for this case, in as early as ~ 6 months of jointly assimilating GNSS and InSAR, it may already be possible to forecast the long term overpressure values that can later tell whether a critical ovepressure–unique for each volcano–will most likely be achieved.

Retrieving the three-dimensional (3D) displacement vector using InSAR is not always possible and most of the time, only the line-of-sight (LOS) displacement is available. In the supplementary section, we show that the joint assimilation of GNSS and InSAR in either ascending or descending LOS view can still capture the temporal behavior of the overpressures as well as estimate the two uncertain model parameters, thereby allowing the possibility of near-real time forecasting.

Including far-field data

While InSAR data can cover up to hundreds of kilometers with one swath, most volcanoes are small in size and thus volcano deformation signals may cover only a small portion in the image. In **Figure 3.13** we plot the radial and vertical displacements as a function of the distance from the volcano axis given the values of the parameters in **Table 3.1**. As one goes farther away from the volcano axis (i.e. r is increased), the deformation signal weakens and almost decay to zero. Decomposing the source of deformation, we find that the near-field signals are mostly related to the shallow reservoir whereas at farther distances (i.e. > 16 km and > 10 km for the radial and vertical displacements, respectively), the signals became dominated by the deep one. Given this, one can infer that far-field data can bring more information about the deep reservoir but note also that as one goes farther away from the volcano axis, the signal-to-noise ratio also weakens. Thus, when assimilating InSAR data, it is important to know the effect of including far-field data in order to avoid spikes in the root mean square error (RMSE) between the predicted and the synthetic surface deformation associated with the use of InSAR especially when coupled with GNSS data as previously performed by Gregg et Pettijohn [2016].

To do so, we generated an 11 x 11 grid InSAR-like dataset with two components (i.e. vertical and radial directions), giving a total of 242 data points. However, unlike in the previous section where we assimilate near-field observations that are equally spaced every 1 km, here, we use non-uniform spacing and intentionally limit the number of far-field points to avoid overwhelming the dataset with noise. In **Figure 3.14A**, we

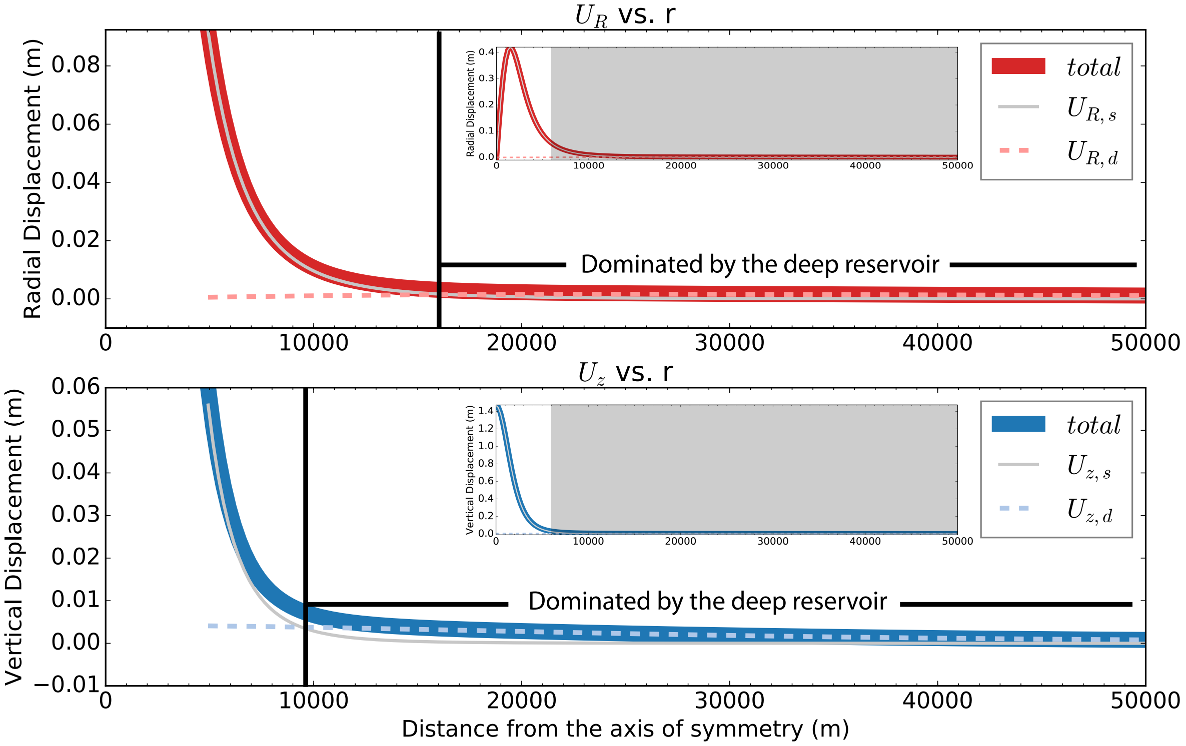

Figure 3.13: The radial and vertical displacements as a function of the radial distance from the volcano axis given the values of the parameters listed in Table 3.1. The scale of the vertical axis is chosen to emphasize the far-field displacements (i.e. $r = 6 - 50$ km), whereas, the smaller figures show the full extent of displacements (i.e. $r = 0 - 50$ km). The grey solid lines are displacements related to the shallow reservoir and the broken lines (red and blue) are from the deep reservoir.

plotted the location of these observations. **Figures 3.14B** and **3.14C** show the estimated overpressures and the uncertain parameters after assimilating near-field and far-field observations every two days. Results show that while the true overpressures are well predicted, the uncertain parameters failed to converge to their true values. In fact, the estimated uncertain parameters worsen when we compare them to the InSAR results in **Figure 3.10** where we only assimilated near-field data. Perturbing the uncertain parameters was not even helpful. Cropping the InSAR data, then downsampling using quadtree (e.g. Simons *et al.* [2002], Sudhaus et Sigurjón [2009]) and/or placing weights on each pixel may be useful in the future in order to allow strategical assimilation of both near-field and far-field data.

We emphasize that all these discussions are based on specific set of parameters we

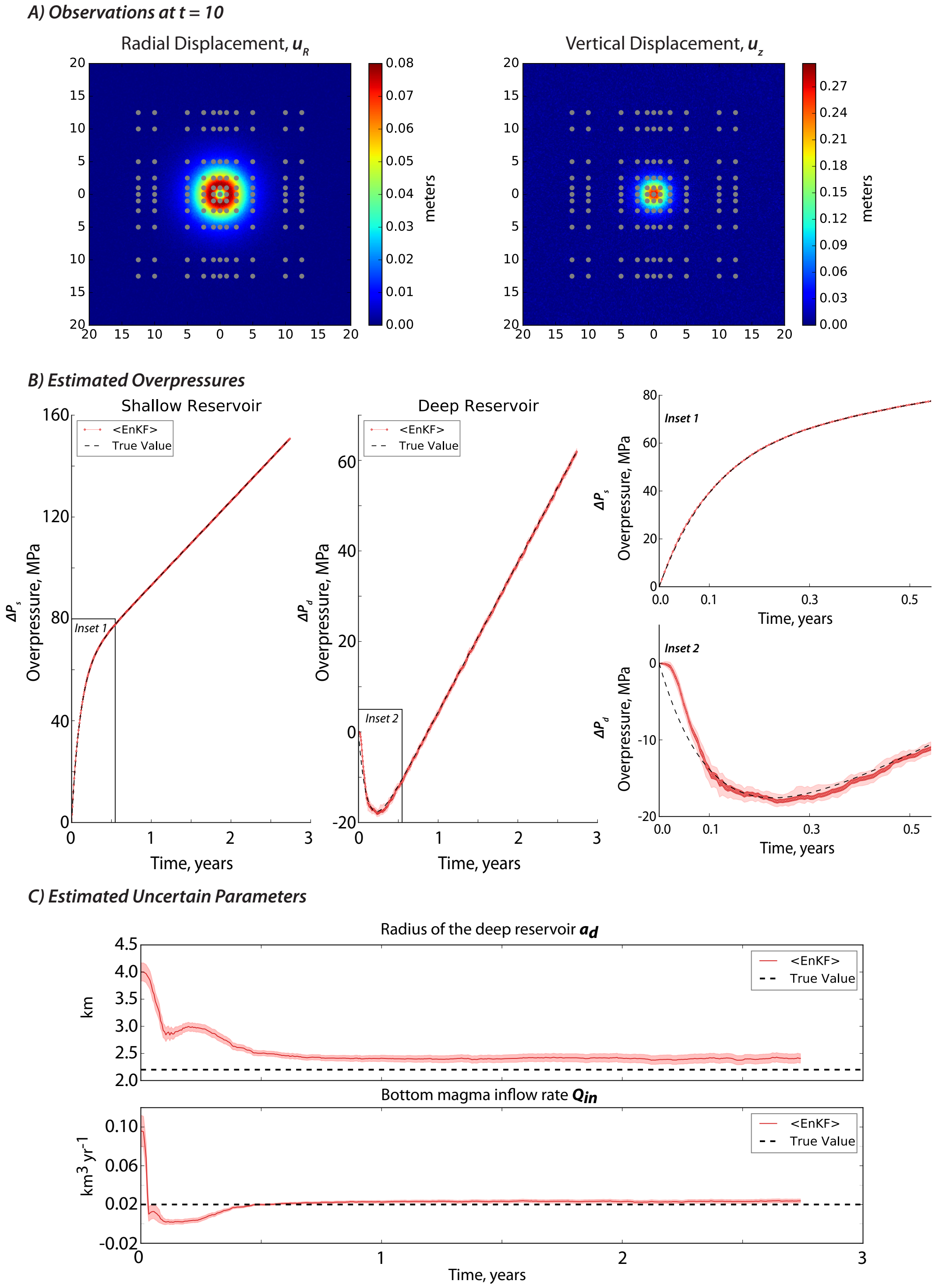

Figure 3.14: A) The locations of the 242 observations (i.e. 121 radial and 121 vertical points) in gray dots and their corresponding displacement values at $t = 10$. The observations are assimilated every time-step such that $f_{obs} = 1$. Note that the x and y axis are in kilometers. The EnKF-estimated B) overpressures and C) uncertain parameters after performing state-parameter estimation using the observations in A). We used a biased prior distribution for the uncertain parameters like in Figure 3.5C or Figure 3.7C. Note that the pink shades represent the spread (1σ) of the estimation. The true values are the black broken lines.

chose for the synthetic case. In particular, the influence of the spatial and temporal resolution strongly depends on the time constant, $\tau = 0.11$ years and reservoir depths set to 3 and 35 km for the shallow and deep reservoirs, respectively.

Defining the Observation Error Covariance, R

In this study, we added a white Gaussian noise to generate all the observations. This is one of the fundamental assumptions and a common approach in data assimilation that implies the use of diagonal observation error covariance, R, during the computation. Even in many operational weather forecast centers, this simplification is adopted in order to facilitate the implementation on one hand and to ensure the quality of the results on the other hand. In the case of complex data noise, it is usually difficult to precisely characterise the error. Using non-reliable information of observation errors in the computation may worsen the results. Here, we adopted a simple observation error covariance, but in practice, the error variance can be increased in order to take into account the part of error not represented by the error covariance used.

Spatially correlated noise can be present, especially in the case of InSAR data where atmospheric noise are usually embedded in the data. The spatial correlation can change the results depending on the quality, quantity and the distribution of the data points. Bekaert *et al.* [2016] suggest that neglecting InSAR covariance should be avoided as it may result to treating spatially correlated atmospheric noise as part of the signal. In the future, InSAR variance-covariance shall be applied when dealing with real case data. Furthermore, the approach presented by Brankart *et al.* [2009] and Ruggiero *et al.* [2016] can be considered.

Comparing with Inversion

When performing the comparison between EnKF and inversion, we want to make sure first that the model and the a priori information that we used are the same and are suitable for the two techniques. For example, if we start from a parameter distribution which does not cover the true values of the uncertain parameters (e.g. **Figure 3.5C**), the inversion will not work. On the other hand, if we start from a uniform distribution as we used to do in inversion, the EnKF estimation will not be the optimal solution since it requires a prior assumption that is Gaussian in nature. We then built the prior distributions for a_d and Q_{in} (**Figure 3.15B**) that agrees with the prerequisites of both the assimilation and inversion.

Gregg et Pettijohn [2016] have previously compared data assimilation with inversion using two different models–a viscoelastic assumption for EnKF and an elastic one for the inversion. In our case, to be fair and consistent, the same forward dynamical model (the two-magma-chamber model) is applied to the two techniques.

For the EnKF, we performed the state-parameter estimation strategy similar to that in synthetic case B. Whereas, we implemented a bayesian-based estimation, i.e. Markov Chain Monte Carlo (MCMC), for the inversion. MCMC is most useful in cases where models are non-linear and expressing an analytical solution is not possible (Segall [2013]). Note that we used 80 synthetic observations (i.e. 40 radial and 40 vertical displacements) that are uniformly (every 100 m) located at a distance $r = 1 - 4.9$ km with frequency of available observation consistent with the time interval (i.e. $\Delta t = 2$ days; $f_{obs} = 1$) for the two techniques.

In performing MCMC, the posterior distribution of the uncertain parameters is sampled given their a priori distribution using the forward model and a proposed likelihood distribution. Models are selected based on the Metropolis-Hastings rules, which always accept models that fit better to observations than the previous iteration and randomly accept those that do not fit to avoid being trapped to a local minima (Segall [2013]). For example, at t_i, a set of a_d and Q_{in} values are drawn from their initial distributions, generating model-predictions using the two-chamber model. These model predictions are then compared to the GNSS and/or InSAR data and are always accepted if the fit is better than the last sampling iteration, creating the so-called Markov-Chain. The sampling iteration can be performed thousand to million times in order to build a full posterior distribution. In our case, we performed 11000 MCMC sampling iterations at each time-step and burned-in the first 10000 so that in the end we have a similar ensemble size (e.g. 1000) to that of the EnKF. Take note that unlike in EnKF which is sequential and only uses incoming observations to capture the temporal evolution of the overpressures, MCMC utilizes all the observations from t_0 up to the preferred time of observation t_i. We performed up to 400 time-steps with interval similar to that in EnKF (i.e. $\Delta t = 2$ days).

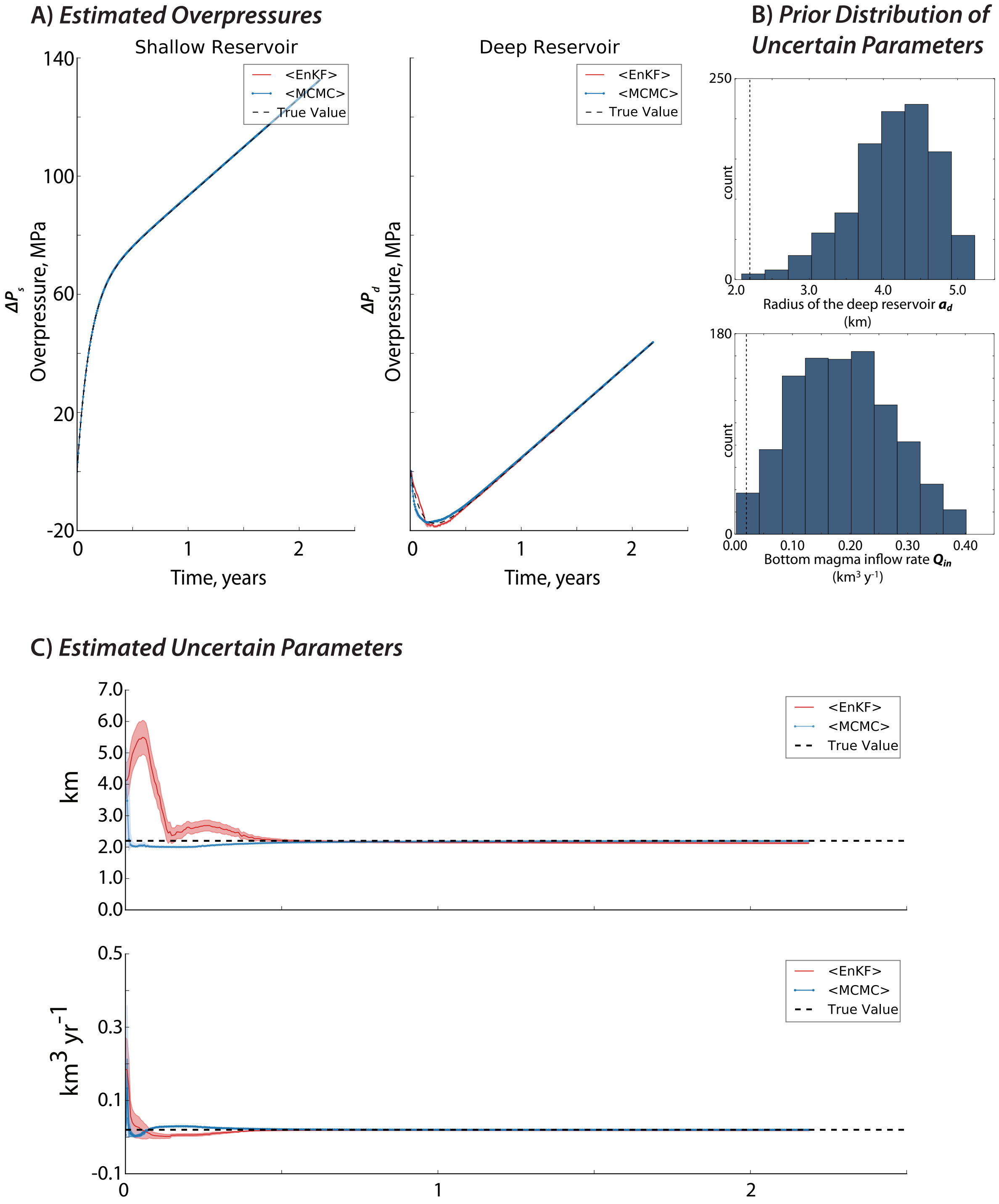

Figure 3.15: Comparison between the EnKF-predicted and MCMC-predicted A) overpressures and C) uncertain model parameters given the prior distributions of a_d and Qin in B). For the two techniques, we used 80 synthetic observations (i.e. combined radial and vertical displacements) located uniformly, every 100 m, at $r = 1 - 4.9$ km and are available every time-step. The light blue and pink shades represent the spread (1σ) of the estimation. The true values are the black broken lines.

Figure 3.15A presents the resulting overpressures after performing EnKF and MCMC. The shallow overpressure is well-estimated by the two approaches, whereas the overpressures in the deep reservoir both started from a deviated value but eventually converged to their true values. The MCMC-estimates are also found smoother than the EnKF-predictions especially in the deep reservoir. Since EnKF always assumes that the dynamical model is uncertain and needs to be corrected by incoming observations, it then tends to closely follow the behavior of the observations, hence we observe a noisier estimation with EnKF. It follows that MCMC cannot account for epistemic model errors or those uncertainties related to processes not included in the physical forward model (Segall [2013]).

If we observe how the uncertain parameters are estimated by the two techniques in **Figure 3.15C**, we will find that both are able to estimate accurately the true values, but MCMC is faster to converge. Take note however, that the uncertain parameters we used in this study are static parameters. In the case of an evolving model parameter, which could be the case for the basal magma inflow (i.e. Poland *et al.* [2012]), the inversion may not be the optimal method to use for estimation.

Towards More Realistic Physics-Based Models

The model that we used here is a highly simplified view on how a volcano plumbing system works based on idealised assumptions (e.g. elastic medium in a homogeneous half-space, incompressible magma). It can be implemented easily for real-time prediction of effusive eruptions as contrary to the finite element model of Gregg et Pettijohn [2016]. Although we only considered two uncertain model parameters in this study, since they are the most difficult to constrain using geodetic data through conventional approach, future work can be extended to explore other parameters such as the depth and the shape of the reservoirs and the strength of the hydraulic connection between them.

In addition to the simplicity and specificity of the model that we tested, we base the potentiality assessment of data assimilation on a synthetic case that is consistent with observations recorded at a specific volcano –Grímsvötn in Iceland. In fact, similar behavior has been observed at other basaltic volcanoes: Kilauea and Mauna Loa in Hawaii (Lengliné *et al.* [2008]), Westdahl Volcano (Lu *et al.* [2003]) and Axial Seamount Volcano (Nooner et Chadwick [2009]) such that it can be accepted as generic for this type of frequently erupting volcanoes. However, except for Axial Seamount, the time constant derived at other places are larger than the one observed at Grímsvötn (Reverso *et al.* [2014]). This parameter is expected to only influence the impact of the temporal frequency of available observations. In the case of Grímsvötn, it is indeed expected to be more restrictive regarding the importance of a high temporal resolution dataset. It was beyond the scope of this first paper to modify the parameters chosen for the synthetic case, but a systematic exploration of the dimensionless parameters will be required in further studies.

We emphasize that the focus of this work is to give a preliminary assessment of how EnKF can be utilised in eruption forecasting rather than validating the dynamical model that we considered. Unlike in the field of ocean-atmosphere science where models are more advanced and established, realistic and generic physics-based models of volcanoes are still in progress. However, one of the main interests in using data assimilation is that it takes into account the fact that models are not perfect and are mostly based on the simplification of the complex reality. This is represented by the model error, q, as depicted in **equation (3.5)**. Evensen [2003] have shown that the model error can be accounted in the EnKF scheme using the following expression:

$$P^{f}_{t_{i+1}} = \mathcal{M} P^{a}_{t_i} \mathcal{M}^{T} + Q_{t_i} \tag{3.15}$$

where $Q_{t_i} = \overline{q^2_{t_i}}$ is the model covariance. $P^{f}_{t_{i+1}}$ represents the accumulated model errors from the beginning of the assimilation until the instant t_{i+1}. In order to overcome the difficulty in quantifying directly the model error at each time-step, the EnKF represents the model error by an ensemble of model state generated from a large number of perturbations of uncertain model parameters. The model error covariance P in the EnKF paractice is an approximation of the real model error. In case of infinite ensemble members, P is considered to equal the real model error. For this reason, a large ensemble size is always required. Any dynamical model can actually be used in data assimilation as long as there is a link between the model and the observations and the model can be restarted at any instant. However, take note that models that are too far from the reality would result in large model errors that would be difficult or impossible to correct by the observations, especially when the condition of the observations is not good enough (i.e. in terms of quantity, distribution and accuracy). The use of more realistic physics-based models that could better interpret field observations such as those that could account for magma rheology and compressibility (e.g. Got *et al.* [2017], Segall [2016], Anderson et Segall [2011, 2013]) are then highly encouraged. Data assimilation can also be extended to models representing other plumbing mechanism such as magma reservoirs recharged by dikes at depth (e.g. Karlstrom *et al.* [2009]) or even those eruptions that are related to dike intrusions.

Implications to Real-time Volcano Monitoring

While parameter-estimation allows us to gain more knowledge about the plumbing system and the behavior of the volcano, in real-time crisis, one of the key variables to infer an impending effusive eruption is the overpressure. The EnKF strategy presented here uses a simple dynamical model that can be easily integrated with large amount of real-time geodetic data, allowing to quickly and accurately track the value of the overpressures both in short-term and long-term periods. Assuming a statistic distribution for the threshold magma overpressure leading to reservoir wall rupture, based on previous eruption for instance, the updated overpresssure forecast provided by EnKF can be used to estimate the timing of an impeding eruption. Although the critical overpressure value is not always known, especially for volcanoes that don't erupt frequently, it depends on the rock strength that can be estimated and on the local stress field strongly influenced by the edifice geometry (Pinel et Jaupart [2003]).

Another important challenge of the assimilation approach is the availability of frequent data. Although for GNSS we can obtain daily observations, InSAR data are less frequent and are still dependent on the quality of interferograms produced. Also, in reality, the 3D-displacement field vector from InSAR are not always retrievable due to the satellite's acquisition geometry. Furthermore, while we only used deformation data alone, the observation vector can include gas emission and seismic data for a more deterministic approach in forecasting (i.e. seismic data in particular can be used to estimate the timing of an eruption), as long as they can be related to the dynamical model used.

Interestingly, when it comes to near-real time monitoring, it may be possible to use inversion and data assimilation jointly in order to accomodate vast amount of incoming data. MCMC allows faster prediction of non-evolving model parameters whereas EnKF via state-estimation is easy to implement and only requires incoming observations. Meaning, the uncertain model parameters can be first constrained by MCMC and the overpressures will then be predicted using EnKF via state-estimation strategy (e.g. synthetic case A).

3.5 Conclusions and Perspectives

Our work presents a simple yet efficient model-data fusion strategy using data assimilation (i.e. EnKF) that can be applied to real-time volcano monitoring. Synthetic GNSS and/or InSAR data are assimilated to a simple yet generic dynamical model (i.e. two-chamber model) to mainly forecast the overpressures–one of the key parameters when assessing volcanic eruptions. The EnKF method is tested on two synthetic cases: A) state-estimation and B) state-parameter estimation using different a priori information about the uncertain model parameters. This technique allowed us to provide posterior distributions of the overpressures and the uncertain model parameters at each time step. Our results show that the filter can successfully track the evolution of the overpressures both in the shallow and deep reservoirs using near-field observations if the prior assumptions about the uncertain parameters are well defined or if the uncertain parameters are also estimated along with the state variables (overpressures).

Based on the specific case considered in this study, frequent but spatially sparse observations like GNSS are more likely to recover the true evolution of the overpressures than with an infrequent but spatially dense dataset (e.g. InSAR). Although, using an InSAR-like data will better constrain the uncertain model parameters. While Gregg et Pettijohn [2016] pointed that the assimilation of InSAR creates spikes in the RMSE between the predicted and the synthetic displacements when coupled with GNSS, our strategy presents a successful joint assimilation of these datasets for the first time, allowing to exploit both the high temporal characteristic of GNSS and the high spatial characteristic of InSAR. An important point to consider is the use of far-field data. While far-field displacements can provide more information about the deep reservoir, it can generate noisier and less accurate predictions because of their weaker signal-to-noise ratio. Future work must be dedicated to strategically balance them with near-field observations when used for assimilation (i.e. resampling by quadtree and/or imposing weights on the data points). Although, we did not investigate the effect of spatially correlated noise especially in InSAR data, we acknowledge the need to apply InSAR variance-covariance matrix especially in real data as suggested by Bekaert *et al.* [2016].

The ability of the EnKF and sophisticated Bayesian inversion (MCMC) to constrain parameters of a dynamical model are similar. Both techniques can thus be used to forecast the temporal evolution of magma overpressure through time. Although the use of MCMC allows faster convergence of the uncertain model parameters to their true values, the advantage of data assimilation is clearly to improve the forecasts in near real-time by updating the parameter estimations (thus accounting for the temporal variations of the parameters) based on incoming observations. Interestingly, it may also be possible to combine both techniques in which MCMC will be used to first constrain the non-evolving model parameters followed by applying EnKF in order to predict only the state variables (e.g. overpressures).

The strategy that we have developed here aims to give a preliminary assessment of EnKF as a tool to assess volcanic unrest. While our framework is simple, it offers a great potential in using the method towards a more deterministic approach in eruption forecasting and better understanding of the magma plumbing system. The use of more sophisticated physics-based models as well as other types of datasets such as gas emission and seismic data are highly encouraged for future studies. In terms of the real case application of the strategy to Grímsvötn volcano, additional uncertain model parameters such as the depth of the deep reservoir and the hydraulic strength between the two reservoirs should be accounted.

Author Contributions

All the authors contributed to the conceptualisation and design of the study as well as to the writing of the manuscript. MGB: performed the simulations and detailed analyses. VP: contributed to the dynamical model and volcanological point-of-view. YY: contributed mainly to data assimilation.

Acknowledgements

The authors would like to thank Dr. Bernard Valette and Dr. Jean-Michel Brankart for their helpful discussions about the inversion method and data assimilation, respectively. We are also grateful for the scientific comments of Dr. Marie-Pierre Doin and Dr. Jean-Luc Froger. Furthermore, we also acknowledge our two reviewers and Dr. Valerio Acocella for their constructive comments that helped to improve our work.

Chapter 4

Forecasting the rupture of a magma chamber in real-time using sequential data assimilation

Contents

This chapter will be submitted as: “[Near] real time forecasting of the rupture of a magma chamber using sequential data assimilation”, in preparation for *Journal of Geophysical Research: Solid Earth*

Abstract

The fundamental goal of eruption forecasting is to be able to deliver an effective and timely forecast especially to the population at risk. We focused on forecasting the tensile failure of a magma chamber at basaltic volcanoes that exhibit inflation-deflation behaviors. In this study, we propose a new method to mainly track the evolution of the overpressures by sequentially assimilating geodetic data using Ensemble Kalman Filter (EnKF). We explored the 2004-2011 inter-eruptive dataset at Grímsvötn volcano in Iceland. Given that the overpressure is a key parameter that would indicate the failure of a magma chamber, we introduced the concept of "eruption zones" based on a pre-defined distribution of the failure overpressure. We also presented the probability of the magma chamber to rupture at each time instant, estimated as the percentage of model ensembles that exceeded their failure overpressure values initially assigned following a given distribution. Our results show that when 25 ± 1 % of the model ensembles exceeded the failure overpressure, an actual eruption is imminent. We further tested our approach using the 2011 post-eruptive dataset. Our findings show that just before the 2014 rifting event, Grímsvötn's shallow magma chamber was already at the critical stage of rupturing and could have erupted in 2015. However, no eruption has occurred up to now, suggesting that a transient event may have happened and postponed Grímsvötn's supposed eruption. This is consistent with our results discussed in **Chapter 5**.

4.1 Introduction

Eruption forecasting is one of the most challenging field in volcanology, covering a wide range of approaches and perspectives. We have to provide accurate forecasts on when and where the eruption will occur, how long it will last and what other impending catastrophic or transient events might happen in order to help in mitigating risks and properly assessing hazards. In general, we can divide eruption forecasting into two phases: 1) forecasting the failure of a magma chamber and 2) forecasting the onset and location of a possible eruption after the magma chamber ruptured. The first one is attributed to long time scales as gases exsolve and pressure builds up within the magma chamber until it ruptures (i.e. years to decades). The second phase occurs in a shorter time scale (i.e. probably hours to weeks or months). Basically, after the failure of a magma chamber, the next step is to predict whether the propagating magma will end up as an intrusion or an eruption. If an eruption is bound to happen, then we have to forecast its timing and location. In some cases, there is a thin line between the failure of a magma chamber and a subsequent eruption depending on how quickly the magma can reach the surface after the chamber wall ruptured. However, it is important to point out that the rupture of a magma chamber does not always guarantee an eruption. There are also cases that dykes get arrested at depth by cooling and solidification or by intersection with a stress barrier (Rivalta *et al.* [2015], Biggs *et al.* [2016]). Most success stories in eruption forecasting are based on empirical analysis and extrapolations of seismic and/or deformation data to determine the timing of eruption (Voight [1988], Nooner et Chadwick [2016], Blake et Cortés [2018]). Material failure forecast method introduced by Voight [1988] is perhaps one of the most traditional approaches. It is used to predict the timing at which the failure can be reached and eventually initiates an eruption by fitting a power law curve into the seismicity. More recently, Nooner et Chadwick [2016] were able to forecast the 2015 eruption at Axial Seamount based on an observed inflation threshold of deformation pattern. Blake et Cortés [2018] introduced a statistical approach to determine the probability of the onset of deflation depending on a time window and a given trend for the temporal evolution of deformation data. However, none of these methods have attempted to infer the magma overpressure value. The drawback of these methods is that if the rupture of a magma chamber occurs, there is actually no way to predict whether or not the magma will reach the surface since we have no clue whether the propagating dyke will result to an intrusion or an eruption.

In this study, we focus on the initial phase of eruption forecasting—forecasting the failure of a magma chamber—at a basaltic volcano. We propose a new approach that would allow us to have an updating information on the magma chamber overpressure at each preferred time interval such that:

1. We can predict the eruption time given some assumptions on the threshold failure overpressure.
2. We can have information on the volcanic system (e.g. state of stress, geometry of the reservoir).
3. We can have an idea on the initial magma overpressure, such that we can infer whether or not the magma will reach the surface.

We tested our approach at Grímsvötn volcano in Iceland using the 2004-2011 inter-eruptive deformation dataset. In the methods part (**Section 4.3**), we discuss the forward dynamical model that we used. Followed by the strategy on how to first constrain uncertain model parameters that are assumed constant in time, such that we can only follow the evolution of the overpressures and the basal magma inflow rate using a spatially-limited dataset via EnKF. Note that the basal inflow rate is considered as a parameter that may or may not vary in time, hence, it is necessary to estimate it at each time step. Afterwards, we introduced the concept of "eruption zones" based on the evaluation of the probability of rupture at each time step. The latter is estimated as the percentage of model ensembles that exceeded a given failure overpressure condition. Then we provided some discussions about the comparison between using bayesian-based inversion and data assimilation, as well as the failure criterion that we defined in this work. Futhermore, we also give insights after the 2011 eruption at Grímsvötn until and even after the 2014 rifting event.

4.2 Grímsvötn volcano: 2004-2011

Grímsvötn volcano—a subglacial basaltic volcano located beneath the Vatnajökull icecap (**Figure 4.1**) and sitting on top of a mantle plume (Wolfe *et al.* [1997])—is one of Iceland's most active volcanoes erupting at least once per decade (Larsen *et al.* [1998]). In fact, its last historic eruptions are in 1934, 1983, 1998, 2004 and 2011 (**Figure 4.1**). Geochemical studies show that the erupted basalts at Grímsvötn are homogeneous and have evolved thoelitic composition (Haddadi *et al.* [2017]). The volcano has a composite caldera of 10-12 km in diameter and 200-300 m in depth. A permanent subglacial lake is present at Grímsvötn volcanic system, formed by the intense heat flux from geothermal and volcanic activities (Björnsson et Einarsson [1990], Albino *et al.* [2010]). Evidences from geophysical studies show a sill-shaped shallow magma chamber (i.e. $2.0 - 2.5$ km horizontal major and 0.5 km vertical minor axis,) at around 3 km and a deeper intrusive complex beneath the volcano (Alfaro *et al.* [2007], Albino *et al.* [2010], Hreinsdóttir *et al.* [2014]). Although modeling of recent geodetic data indicates a rather shallower magma chamber at ~ 1.7 km (Hreinsdóttir *et al.* [2014]) and another deeper chamber is suggested at $10 - 35$ km depth (Reverso *et al.* [2014]).

Before the 2004 Grímsvötn eruption, increased seismic activity has been detected by the IMO since the mid of 2003 with ground inflation observed around September 2004 through GPS measurements. On 28 October 2004, three days prior to the eruption, signs of advancing jökulhlaup beneath the icecap have been detected, forcing the IMO to issue a warning on a possible jökulhlaup event and eventually an impending eruption following the drainage of Grímsvötn's lake (Vogfjörd *et al.* [2005]). At $\sim$ 21h50 UTC of 01 November 2004, the eruption started. Although there was a lack of visual confirmation at the beginning of the eruption, seismic data and later, meteorological observations (i.e. 8-12 km plume was detected by radar at 22h50 of 01 November 2004) became complementary monitoring tools to verify the eruption onset and location (Vogfjörd *et al.* [2005]). The last sign of crater explosion was reported on 06 November 2004.

After the 2004 eruption, progressive seismic events and inflation were observed. In particular, the deformation patterns at Grímsvötn volcano show a short exponential behavior followed by a linear trend (**Figure 4.2**). According to Reverso *et al.* [2014], the former suggests pressure readjustments due to the replenishment of the shallow magma chamber from the deep chamber during the early post-eruptive period. The authors attribute the subsequent linear inflation to the continuous pressurization within the system caused by the constant basal inflow of magma. On 21 May 2011, an explosive eruption at Grímsvötn occurred (i.e. VEI 4) with a plume that reached up to 25 km in height and spewed around 0.27 km^3 DRE of basaltic magma (Hreinsdóttir *et al.* [2014]). Precursory earthquakes and tremors were detected a few hours before the actual eruption, in particular, earthquakes from $2-4$ km depth migrated towards <1 km just minutes before the eruption (Hreinsdóttir *et al.* [2014]). **Figure 4.1B** shows the evolution of the co-eruptive horizontal displacement between 21 and 23 May 2011. The 2011 Grímsvötn eruption ceased after seven days of volcanic crisis.

In this work, we investigate the 2004-2011 inter-eruptive period measured at GFUM GPS station located at Mount Grímsfjall—a nunatak at Grímsvötn volcano. The GPS time series was processed using Bernesse 5.2 software (Dach *et al.* [2015]) providing daily solutions from 21 November 2004 to 21 May 2011 (**Figure 4.2**). We corrected for the tectonic trend following the measurements of Reverso *et al.* [2014], with slopes of -2.7 mm yr^{-1} and 7.5 mm yr^{-1} for the NS and EW components, respectively. However, due to the uncertain GIA contribution and low accuracy of the vertical component at GFUM GPS station we only use the cumulative vertical displacement to verify if the estimated model parameters during the inversion are consistent with the observations.

4.3 Methods

4.3.1 Forward dynamical model

Similar to the previous chapter, we utilize the two-chamber model of Reverso *et al.* [2014] (**Figure C.1**) to infer the behavior of the overpressures beneath Grímsvötn using

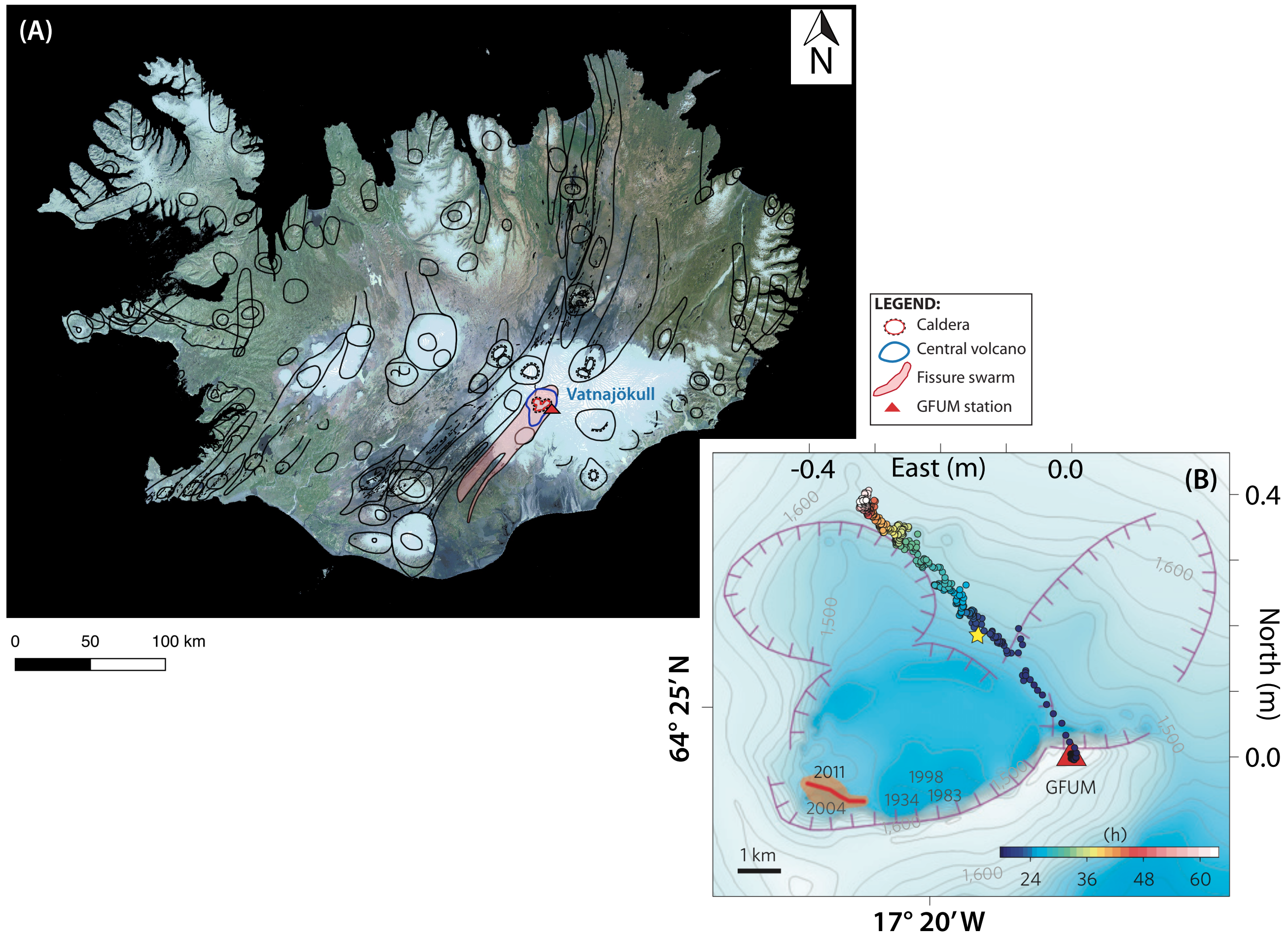

Figure 4.1: (A) Landsat TM map of Iceland in RGB colors showing the outlines of the volcanic zones with emphasis on the Grímsvötn volcanic system. The image is based on the mosaicked data from the National Land Survey of Iceland (Landmaelingar Islands [1995]).(B) The caldera of Grímsvötn volcano with the location of its past eruptions (e.g. 1934, 1983, 1998, 2004 and 2011). The red line and brown outline mark the 2011 fissure eruption and the melted part of the glacier as a result of the eruption, respectively. The colored data points are the North and East components of the horizontal displacement measured from GFUM station indicating the evolution of the displacements from the day of the eruption (e.g. 0h00 UTC of 21 May 2011); from Hreinsdóttir *et al.* [2014].

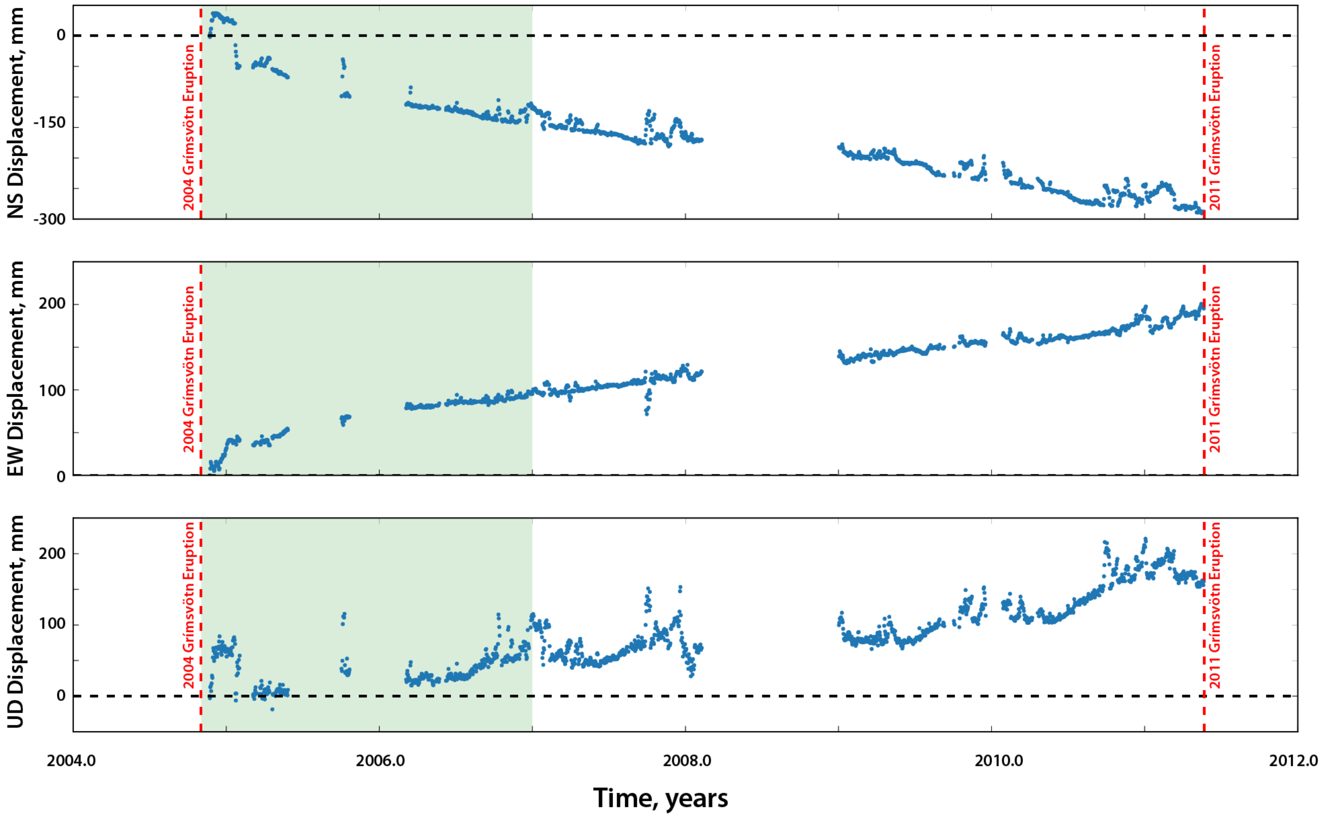

Figure 4.2: The GPS time series of GFUM station from 21 Nov 2004 to 21 May 2011. The actual data are in blue points. The red broken lines mark the onsets of the 01 Nov 2004 and 21 May 2011 eruptions. The horizontal black broken line is the zero-displacement reference. The shaded green area covers the time window of the inversion (see Step 1: MCMC of **Section 4.3.2**). The NS and EW components are corrected for tectonic trend whereas the vertical component (UD) is not corrected for GIA or seasonal effects.

the temporal evolution of the surface deformation. The estimated overpressures will later allow the probabilistic forecasting of the rupture of a magma chamber which may eventually lead to an eruption.

Basically, the model represents two magmatic reservoirs that are embedded in a homogenous elastic half-space and are connected by a hydraulic pipe. The magma is assumed incompressible. Reverso *et al.* [2014] illustrated that this model is consistent with the post-eruptive deformation patterns observed at Grímsvötn volcano at least for the last three eruptions. The overpressure evolutions are expressed as:

$$\frac{\Delta P_{s_{t_{i+1}}} - \Delta P_{s_{t_i}}}{t_{i+1} - t_i} = \frac{3\pi E {a_c}^4}{128(1-\nu^2)\mu H_c {a_s}^3}(((\rho_r - \rho_m) g H_c + (\Delta P_{d_{t_0}} - \Delta P_{s_{t_0}})) + \Delta P_{d_{t_i}} - \Delta P_{s_{t_i}}) \tag{4.1}$$

$$\frac{\Delta P_{d_{t_{i+1}}} - \Delta P_{d_{t_i}}}{t_{i+1} - t_i} = \frac{3E}{16(1-\nu^2){a_d}^3} Q_{in} - \frac{{a_s}^3}{{a_d}^3} \frac{\Delta P_{s_{t_{i+1}}} - \Delta P_{s_{t_i}}}{t_{i+1} - t_i} \tag{4.2}$$

and the corresponding analytical solutions to the differential equations are of the form:

$$\Delta P_{s_{t_i}} = A(1 - e^{-\frac{t_i}{\tau}}) + \frac{3E}{16(1-\nu^2)} \frac{Q_{in}}{({a_s}^3 + {a_d}^3)} t_i + \Delta P_{s_{t_0}} \tag{4.3}$$

$$\Delta P_{d_{t_i}} = A(1 - e^{-\frac{t_i}{\tau}}) + \frac{3E}{16(1-\nu^2)} \frac{Q_{in}}{({a_s}^3 + {a_d}^3)} t_i + \Delta P_{d_{t_0}} \tag{4.4}$$

with $A = \frac{{a_d}^3}{{a_s}^3 + {a_d}^3}[\Delta P_{d_{t_0}} - \Delta P_{s_{t_0}} + (\rho_r - \rho_m) g H_c - \frac{8 Q_{in} \mu H_c {a_s}^3}{\pi {a_c}^4 ({a_s}^3 + {a_d}^3)}]$. We assume that the shapes of the reservoirs are sills, the Young's modulus, $E = 25$ GPa, the depth and the radius of the shallow reservoir are $H_s = 1.7$ km and $a_s = 2.0$ km, respectively (Hreinsdóttir *et al.* [2014]).

4.3.2 Inversion and data assimilation

In simple terms, there can only be three up to four free parameters that can be inferred from the model given one GPS time series as it actually takes the form: $A(1-e^{Bx})+Cx+D$. However, in reality, we have at least six "uncertain" parameters (e.g. radius and depth of the deep reservoir, basal magma inflow rate, density difference between the magma and the surrounding medium, initial pressure values present in the system and the characteristic of the hydraulic connection) to estimate in order to properly fit with the data. The problem further complicates because only the NS and EW components of the time series can be useful for us. Given the said limitations, it is worth noting that it is not possible to find a single optimal set of values for the six uncertain parameters (i.e. no unique solution). Fortunately, our main goal is not to find the exact values of each uncertain parameter. Rather, we are mainly focused on tracking the evolution of the overpressures while consistently ensuring that the inferred values agree with the physics of the model and are well-fitted with the measured surface deformation data. In particular, we are interested in following the evolution of the shallow overpressure since this is the key parameter that would indicate if an eruption is about to happen.

In **Chapter 3**, we demonstrated through synthetic tests that the performance of inversion (i.e. MCMC) and data assimilation (i.e. EnKF) is relatively similar when estimating both the state variables (i.e. overpressures) and uncertain model parameters (i.e. radius of the deep reservoir, a_d, and a fix basal magma inflow, Q_{in}). The main advantage of MCMC is its faster convergence to the “truth” when compared to EnKF (**Figure 3.15**).

Recall that the overpressures are considered state variables in this work. State variables have direct link to the observations, hence model-predicted overpressures are corrected each time GPS data become available. Whereas, uncertain parameters are only updated by the covariance between them and the state variables. It follows that in a sequential data assimilation method such as the EnKF, performing state-parameter estimation can produce inconsistent results if the parameters being estimated are expected to remain constant in time. In sequential data assimilation, the model errors are only propagated forward in time. This is can be demonstrated when we take the values of non-evolving parameters at t_i, use them as inputs to the forward model at $t = 0$ and afterwards simulate the model up to t_i to obtain the overpressures. The resulting overpressures when compared to the EnKF-derived ones are not in agreement with each other. Another scenario to illustrate the inconsistency is when observations are not available anymore and the non-evolving uncertain model parameters have not converged yet to their true values as shown in **Figure B.1**. Indeed, EnKF could not properly estimate the overpressures since the model is propagated using incorrect values of non-evolving parameters. An approach to circumvent the issue is to “re-propagate” the dynamical model using the values of the uncertain model parameters at the analysis step (**Appendix B.1**). The results are obviously improved as shown in **Figure B.2**. However, this approach requires restarting the forward model which is computationally expensive particularly if the forward model is solved through a numerical method such as FEM. Obviously, in the framework of real-time forecasting, this is not an efficient approach especially when precursors start to indicate that an eruption might occur very soon. Zhan et Gregg [2017] performed intra-EnKF iterations but in practice, it is very difficult to infer the number of times the recursive EnKF algorithm should be implemented to ensure consistency and convergence of the state variables and uncertain model parameters to their true values. Furthermore, performing all these additional steps may lead to depreciating the strong capability of EnKF to track parameters that can vary in time.

Given the aforementioned arguments, the number of uncertain parameters that we need to infer and the spatially limited GPS data at Grímsvötn, we therefore propose a two-step strategy: 1) we first fix non-evolving uncertain parameters of the model through bayesian-based inversion and then 2) we estimate the shallow and deep overpressures as well as the parameter/s that may tend to vary in time. In our case, we consider all the aforementioned uncertain parameters as constant parameters except for the basal magma inflow, Q_{in}. The latter is known to fluctate in time (Parks *et al.* [2012], Poland *et al.* [2012], Menand *et al.* [2015]).

Step 1: MCMC. The MCMC approach is built using the PyMC2 python module. The classic linear inverse problem is of the form:

$$D = \mathcal{G}(m) + \epsilon \tag{4.5}$$

In our case, D is the radial component of the 2004-2011 inter-eruptive dataset (i.e. we used up to $d = 769$ for the inversion), $\mathcal{G}$ is the analytical solution (i.e. **equations (4.3)** and **(4.4)**), $m = [a_d, H_d, C, \Delta\rho, \Delta P_{d_{t_0}}, Q_{in}]$ is a vector of the uncertain model parameters that we intend to estimate, and $\epsilon = 0.03$ is the observation error (i.e. ϵ is slightly increased in order to compensate for other sources of error).

We scaled m and then we compute for the posterior distributions using the concept of Bayesian probability (i.e. **equation (2.13)**). In order to avoid “trade-offs” between the six uncertain parameters, we adopted the AM step method. The AM technique fits the parameters by block updating them using multivariate jump distribution. We choose a sampling size equal to 2.0×10^5 where we burned 50% of the samples and subsequently applied a thinning factor of 100 to guarantee convergence and absence of autocorrelation in our results. Once the posterior distributions are generated, we pick the set of best-fit parameters by calculating the misfit relative to the radial displacement data used during the inversion (i.e. data points within the dotted green box in **Figure 4.5**).

Step 2: EnKF. The step-by-step EnKF strategy is illustrated in **Figure C.2**. Basically, we adopted a similar approach implemented in section **3.3** except that we define the state vector, X, as:

$$X = \begin{bmatrix} \Delta P_s \\ \Delta P_d \\ Q_{in} \end{bmatrix} \tag{4.6}$$

The dynamical model can be propagated from t_i to t_{i+1} using the following (i.e. from **equations (4.1)** and **(4.2)**):

$$\begin{bmatrix} \Delta P_{s_{t_{i+1}}} \\ \Delta P_{d_{t_{i+1}}} \\ Q_{in_{t_{i+1}}} \end{bmatrix} = \begin{bmatrix} 1 - C_1\Delta t & C_1\Delta t & 0 \\ C_1C_2\Delta t & 1 - C_1C_2\Delta t & 0 \\ 0 & 0 & 1 \end{bmatrix} \begin{bmatrix} \Delta P_{s_{t_i}} \\ \Delta P_{d_{t_i}} \\ Q_{in_{t_i}} \end{bmatrix} + \begin{bmatrix} C_1A_1\Delta t \\ (A_2 - C_1C_2A_1)\Delta t \\ 0 \end{bmatrix} \tag{4.7}$$

where $C_1 = \frac{3\pi E {a_c}^4}{128(1-\nu^2)\mu H_c {a_s}^3}$, $A_1 = (\rho_r - \rho_m)gH_c + (\Delta P_{d_{t_0}} - \Delta P_{s_{t_0}})$, $A_2 = \frac{3EQ_{in}}{16(1-\nu^2){a_d}^3}$ and $C_2 = \frac{{a_s}^3}{{a_d}^3}$. It follows that the model operator, $\mathcal{M}$, is of the form:

$$\mathcal{M} = \begin{bmatrix} 1 - C_1\Delta t & C_1\Delta t & 0 \\ C_1C_2\Delta t & 1 - C_1C_2\Delta t & 0 \\ 0 & 0 & 1 \end{bmatrix} \tag{4.8}$$

The observation operator, $\mathcal{H}$, which links the state vector and the observations is expressed as:

$$\mathcal{H} = \begin{bmatrix} \Gamma D_s r & \Gamma D_d r & 0 \end{bmatrix} \tag{4.9}$$

since we are only using the radial component of the 2004-2011 dataset (i.e. u_R). The observation-state relationship is described as:

$$D_{t_i} = u_{R_{t_i}} = \begin{bmatrix} \Gamma D_s r & \Gamma D_d r & 0 \end{bmatrix} \begin{bmatrix} \Delta P_{s_{t_i}} \\ \Delta P_{d_{t_i}} \\ Q_{in_{t_i}} \end{bmatrix} + \epsilon_{t_i} \tag{4.10}$$

where $\Gamma = \frac{8(1-\nu^2)}{\pi E}$, $D_s = \frac{H_s^2 a_s^3}{R_s^5}$, $D_d = \frac{H_d^2 a_d{}^3}{R_d^5}$ and r is the distance of GFUM GPS station from the center of the volcanic system (e.g. 3.5 ± 0.2 km). We then use an observation covariance error, $R = \mathcal{E}(\epsilon\epsilon^T) = (0.015 \text{ m})^2$.

We assume that there is a GPS measurement available everyday (i.e. frequency of observation, $f_{obs} = 1$) and we fix the assimilation interval to $\Delta t = 1$ d. **Figure 4.5C** shows the truncated normal distribution of Q_{in} which is used as a prior information to perform EnKF. The mean value is the best-fit value of Q_{in} determined from step-1, the standard deviation is set to 0.003 km^3 yr^{-1} and the upper and lower boundaries are $a = 0$ and $b = 0.19$ km^3 yr^{-1}, respectively. The initial shallow overpressure value is 0 MPa supposing that the reservoir has fully depressurized after the previous eruption.

We scaled the state vector, X, before the analysis step and then we imposed a multiplicative inflation (i.e. $\rho_{infl} = 0.05$) whenever the standard deviation of Q_{in} at t_{i+1} falls below its initial standard deviation (i.e. 0.003 km^3 yr−1). The inflation is to prevent the ensemble from collapsing and also to help the filter track the value of the time-dependent parameter, Q_{in}.

4.3.3 Forecasting method

The magma chamber will rupture and initiate dyke propagation if the deviatoric component of the minimum compressive stress, $\Delta\sigma_3$, compensates the tensile strength of the surrounding rock, T_s (Pinel et Jaupart [2003]):

$$\Delta\sigma_3 = \sigma_3 - \frac{\sigma_1 + \sigma_2 + \sigma_3}{3} \geq -T_s \tag{4.11}$$

where $\sigma_1, \sigma_2, \sigma_3$ are the principal stresses. For a two-dimensional magmatic body in an infinite elastic medium, the tensile stress on the walls of the source is constant along the walls and is proportional to the overpressure such that: $\Delta\sigma_3 = -\frac{\Delta P_f}{k}$, where k is an amplification factor that depends on the geometry of the magmatic source and edifice of the volcano (e.g. $k = 2$ for a spherical source in an infinite elastic half-space with no edifice, Pinel *et al.* [2010]). The critical overpressure needed for the tensile failure is therefore given by:

$$\Delta P_f = kT_s \tag{4.12}$$

where $\Delta P_f = P_f - P_L$, with P_f as the critical failure pressure within the reservoir and P_L as the lithostatic pressure, $\rho_r g H_s$. Note that this criterion also corresponds to the case where fluids are present in the rock adjacent to the reservoir (i.e. Albino *et al.* [2018]).

The tensile strength of rocks can be measured *in situ* through uniaxial tests of natural samples, with values ranging from 8.6 ± 1.4 MPa for pristine basalts to 13.8 ± 2.1 MPa for granites (Touloukian [1989], Albino *et al.* [2018]). In Iceland for example, tensile strength values are between 1 and 10 MPa (Haimson et Rummel [1982]) with reported upper boundary estimates of 13.88 MPa and 22 MPa for a spherical and oblate-shaped magma chamber at Grímsvötn volcano (Albino *et al.* [2010]).

In this study, we will rather consider a probability distribution for the failure overpressure criterion in order to forecast the rupture of the shallow magma chamber at Grímsvötn. The distribution is Gaussian with the mean value centered at $\mu = \Delta P_f = 2T_s = 44$ MPa and the standard deviation fixed to $\sigma = 11$ MPa. We then introduce the so-called “eruption zones” based on the evolution of the shallow overpressure values, ΔP_s, at each time step:

1. No eruption zone, (i.e. $0 \leq \Delta P_s \leq \Delta P_f - 2\sigma$).
2. Sub-critical zone, (i.e. $\Delta P_f - 2\sigma < \Delta P_s \leq \Delta P_f - \sigma$).
3. Critical zone, (i.e. $\Delta P_f - \sigma < \Delta P_s \leq \Delta P_f$).
4. Super-critical zone, (i.e. $\Delta P_s > \Delta P_f$).

To compute for the probability of rupture, we first assign a failure overpressure at $t = 0$ for each of the ensemble member, e (i.e. $\Delta P_{f_{e,t_0}}$, with e = 1, ..., $N_n = 1000$ based on the strategy that we adopted in **Chapter 3**). Note that these values are drawn randomly from the Gaussian distribution described above for the failure criterion (see the histogram in **Figure 4.7D**). In simple terms, the failure overpressure value fixed for each ensemble member is their reference failure overpressure that remains constant for the entire assimilation time window (i.e. $t_K = 2371$ d for the 2004-2011 inter-eruptive dataset). The probability of rupture at each step is then calculated based on the percentage of ensemble members that exceeded their assigned failure overpressure value. For example, given 1000 model ensembles, 400 of them exceeded their overpressure criterion, therefore the probability of rupture is 0.25 .

4.4 Results

Inversion

The PDF and the best-fit values of the uncertain parameters after inverting the initial part of the radial displacement dataset are shown in **Figure 4.3**. We used the best-fit values of the non-evolving uncertain parameters and the re-defined Q_{in} distribution (i.e. truncated Gaussian) as inputs to the forward model to check how well they fit the data (**Figure 4.4**). Despite the non-uniqueness of the results, the data fits are good. In fact, even if we have only inverted the initial part of the dataset, the MCMC-derived values can fit well within the entire 2004-2011 dataset. In **Table 4.1**, we compared the best-fit values when we rather inverted the whole inter-eruptive dataset. We find that the two sets of uncertain parameters have small discrepancies and that both have remained consistent with the physics of the model and results of previous studies (e.g. Hreinsdóttir *et al.* [2014], Reverso *et al.* [2014], Haddadi *et al.* [2017]).

Data assimilation

Figure 4.5 illustrates the result of sequentially assimilating the radial displacement data via EnKF. Indeed, we are able to closely follow the evolution of the radial displacement, the time-varying uncertain parameter, Q_{in} and the overpressures (**Figure 4.6**). In **Appendix B.2** we show the robustness of our results by presenting common diagnostic tools in data assimilation. The distance between the radial displacement data and the model-predictions after (A) the forecast step (i.e. innovation) and (B) the analysis step (i.e. residual) are illustrated in **Figure B.3**. The norm of the cumulative mean innovation and residual as a function of time (**Figure B.3 C** and **D**) converges to zero, which is what should be expected as the number of forecast increases. EnKF equations assume that the observation error as well as the forecast and analysis errors are unbiased, hence the innovation and the residual must be close to zero (Bocher *et al.* [2018]). The evolution of the covariance error of the state variables are shown in **Figure B.4** after the forecast and analysis steps. Note that the correction is in the order of (0.001 MPa)^2 such that it appears almost overlapping in the figure. The spikes in the error covariances indicate large model errors due to the lack of radial displacement data to correct the model forecasts. Recall that if the dynamics is unstable and the interval without observation is sufficiently long, the model error will grow uncontrolled and only the re-introduction of data will reduce the model error. A closer look at the covariances after the forecast and analysis steps are provided in **Figure B.5**.

It is important to emphasize that even without performing EnKF, the result of inverting the initial part of the dataset and then "free-running" the dynamical model (i.e. green results in **Figure 4.6**) is already satisfying since the uncertain parameters are already well-constrained. The difference is evident only on the spread of the ensemble, which is wider for the free-run. However, in the case that the fluctuation in the magma inflow rate is more significant (i.e. $Q_{in} = 0$), the result given by the inversion will not be sufficient anymore. We will further discuss this in the subsequent chapter of this thesis.

Forecasting the rupture of a magma chamber

We plotted the shallow overpressure as a function of time on the eruption zones as shown in **Figure 4.7A**. Here, we noted that the mean overpressure that triggered the 2011 eruption is 38.09 MPa. This value lies at ~ 0.30 of the failure overpressure's CDF (**Figure 4.7B**). Indeed, before the eruption, all of the ensemble members are already in the critical state with a probability of rupture equal to $\sim 24\%$ (**Figure 4.7C** and **E**). However, since the probability of rupture can have a small dependence on the set of non-evolving uncertain parameters that we intially fixed (i.e. step-1) due to the limitation of finding a unique solution, we then assessed the difference when the whole 2004-2011 dataset is rather exploited to fix the non-evolving uncertain parameters. We find that the probability of rupture is only higher by one percent (**Figure B.7**). In this case, we conclude that an eruption is imminent if $25 \pm 1\%$ of the ensembles exceeded their corresponding failure overpressure values.

If we analyze the EnKF-derived shallow overpressures at each time step and afterwards propagate the model (i.e. green results in **Figure 4.7A**), then we can actually forecast

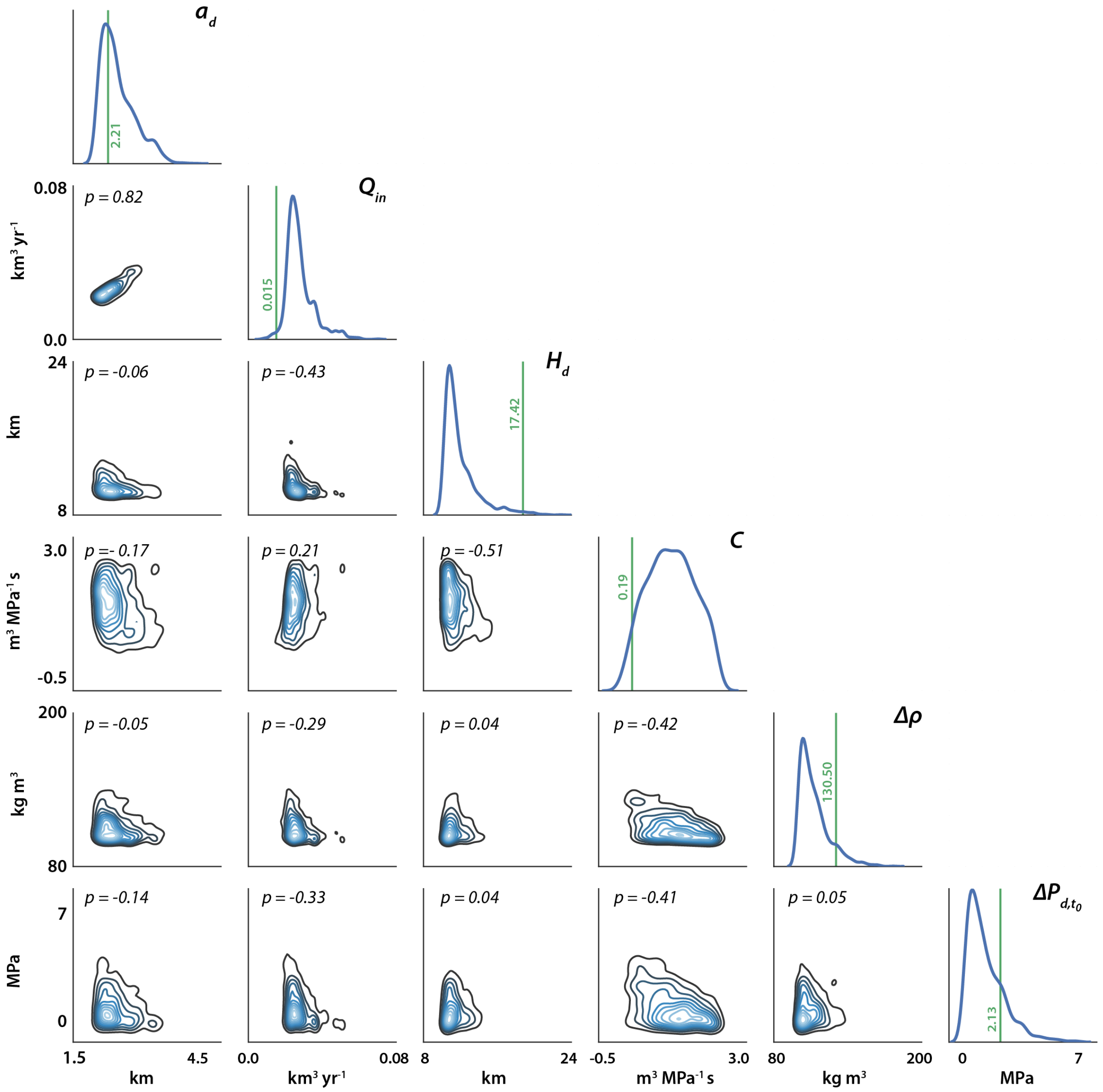

Figure 4.3: Posterior probability density functions (PDF) of the uncertain model parameters after performing MCMC inversion using only the initial part of the 2004-2011 inter-eruptive dataset. The marginal PDF for each uncertain parameter is shown in the diagonal histogram plots. The green vertical lines with numbers indicate the best-fit values of the parameters. The off-diagonal contour plots are the joint kernel-density estimate between pairs of parameters with their corresponding Pearson correlation coefficients. A p-value close to ±1 implies strong correlation between the parameters.

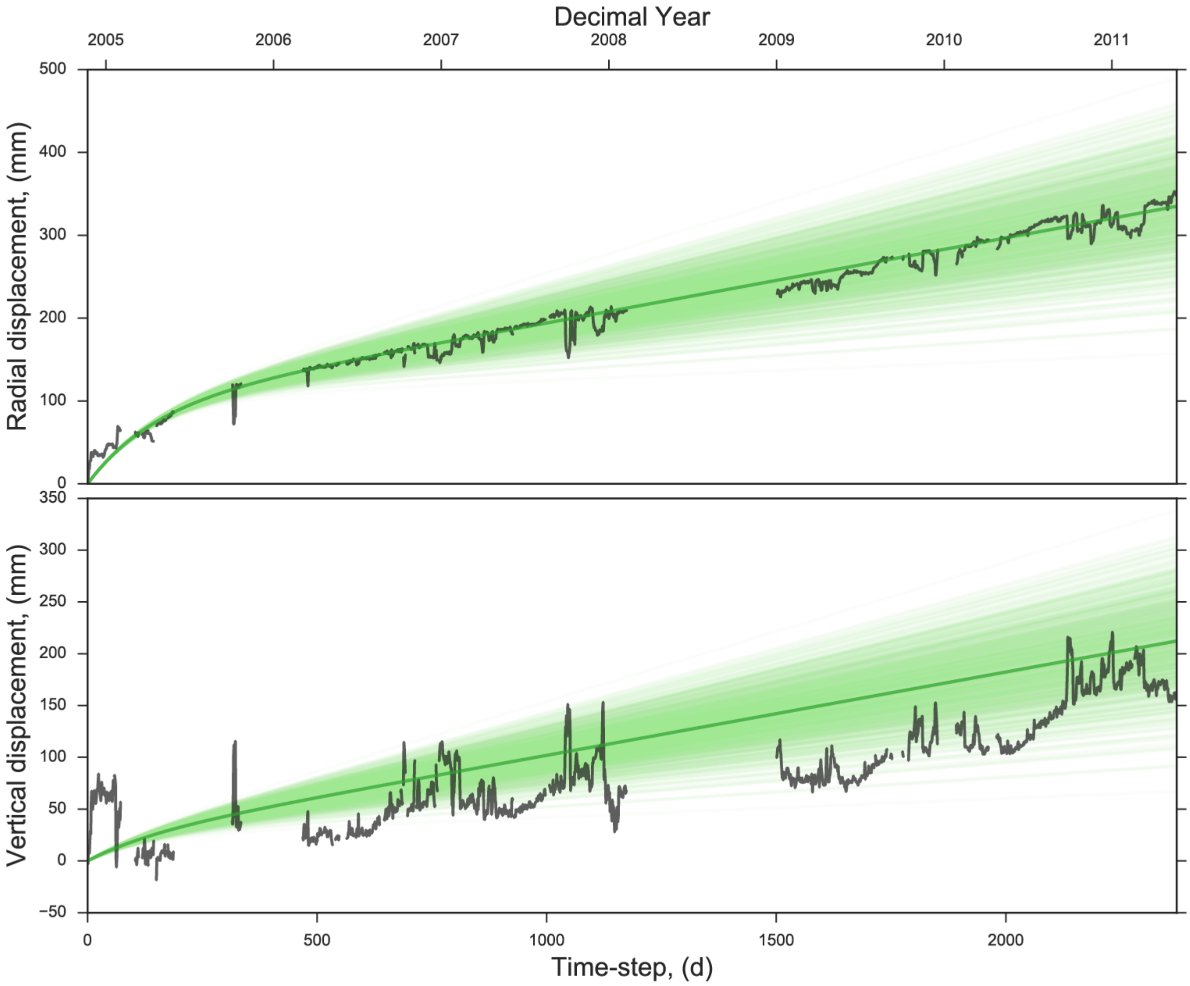

Figure 4.4: Data fit (green) for the radial and vertical displacement using the MCMC-derived best-fit values of the uncertain model parameters and re-defined Q_{in} distribution. The actual data are represented by black solid lines. Note that the vertical component is not corrected either for GIA or seasonal effects. The radial component is corrected for tectonic trend.

Table 4.1: Best-fit values of the uncertain model parameters obtained from the MCMC posterior distribution using a) only the inital part of the dataset (i.e. up to d=769) and b) the entire 2004-2011 inter-eruptive dataset. Except for Q_{in} (highlighted), all the other parameters are considered constant in time and are fixed to their values during data assimilation. Estimates from previous works are also presented.(Fixed parameters are: E=25 GPa, $\nu = 0.25$, $H_s = 1.7$ km, $a_s = 2$ km)

Parameters	Prior Condition	**Estimated Values**		
		Initial Part	Full Dataset	Prev. Studies
Geometry				
a_d (km), radius of the deep reservoir.	$\mathcal{N}(2.2, 2.52, [2.0, 6.0])$	2.21	2.11	< 10 Reverso *et al.* [2014]
H_d (km), depth of the deep reservoir.	*U(10, 40)*	17.42	19.74	10-35 Reverso *et al.* [2014]; 10-20 Haddadi *et al.* [2017]
Physics				
$\Delta\rho = \rho_r - \rho_m$ (kg m^{-3}), density contrast.	U(100, 300)	130.50	105.28	
C (m^3 MPa^{-1} s^{-1}), characteristic of the hydraulic connection, $C = \frac{a_c^4}{\mu H_c}$, where a_c is the radius of the conduit, μ is the viscosity and $H_c = H_d - H_s$ is the height of the hydraulic connection.	*U(0.01, 2.35)*	0.19	0.26	
Basal condition				
Q_{in} (km^3 yr^{-1}), deep magma inflow rate.	U(0.0, 0.19)	0.015	0.015	0.01-0.05 Reverso *et al.* [2014]
Initial condition				
$\Delta P_{d_{t_0}}$ (MPa), initial value of the overpressure in the deep reservoir.	U(0, 20)	2.13	2.55	

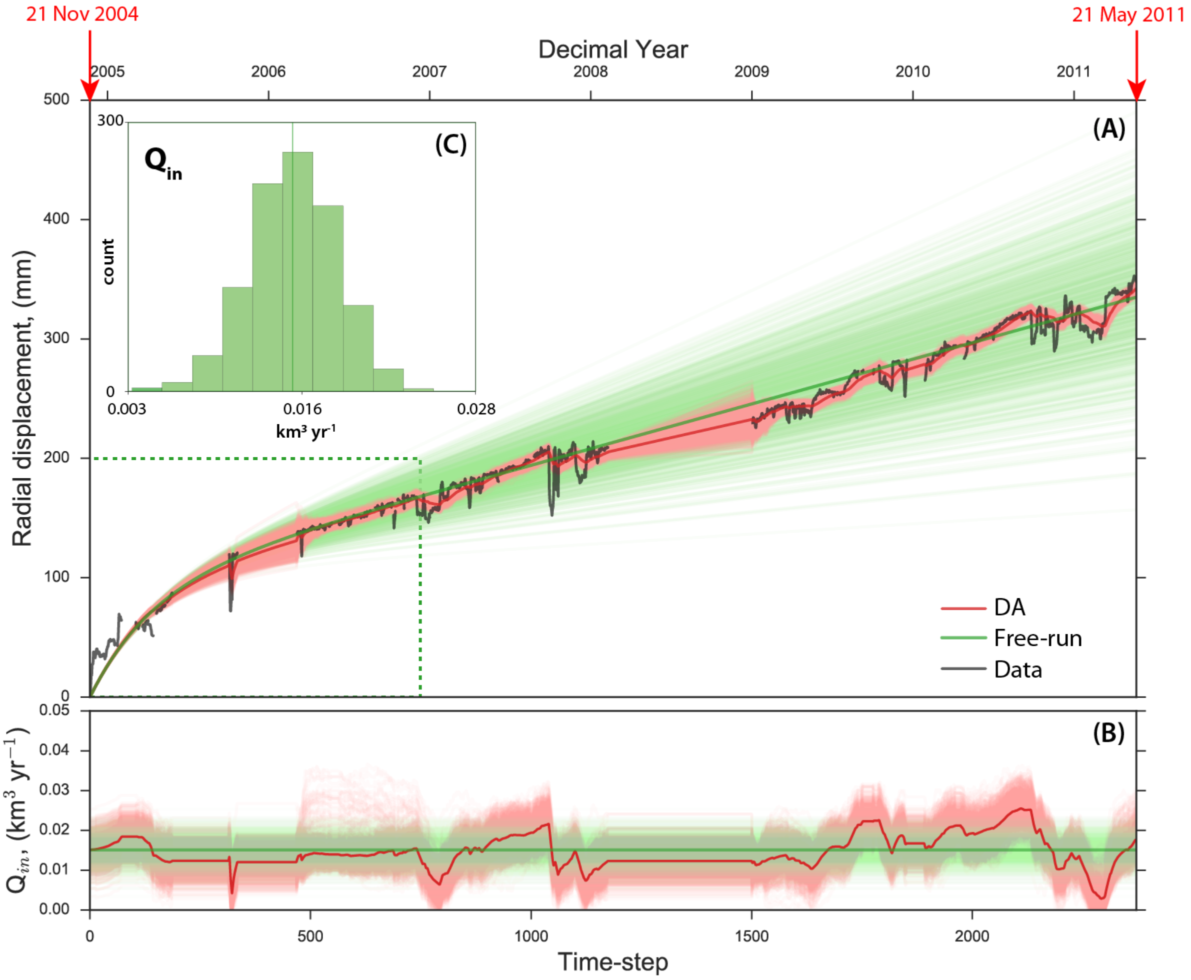

Figure 4.5: Data-fits and Q_{in} estimates. (A) The entire 2004-2011 inter-eruptive radial dataset used in this study (black) and the resulting data-fits by: 1) solely free-running the dynamical model (green) and 2) data assimilation via EnKF (red). The green dotted box covers the dataset used to estimate the non-evolving uncertain parameters (step 1). (B) Estimated value of the magma inflow rate, Q_{in}, as a function of time using: the free-run (green) and EnKF (red). (C) The distribution of Q_{in} used as a prior information for the free-run and the data assimilation.

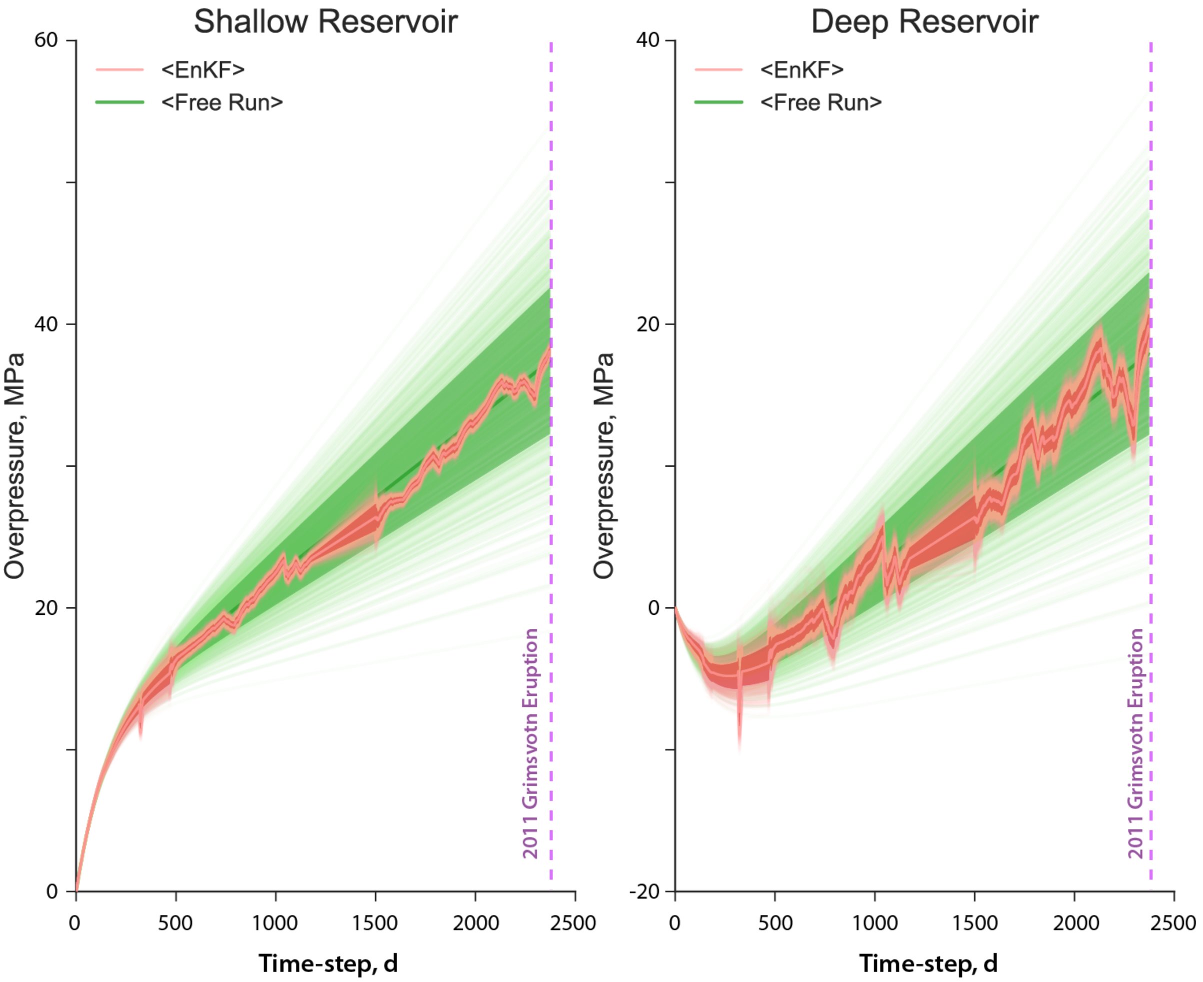

Figure 4.6: The shallow and deep overpressure values after performing EnKF (red). Note that the corresponding data fit is illustrated in **Figure 4.5**. The pink color represents each model ensemble members whereas the dark red shade is the standard deviation. It follows that the pink line within the dark red shade is the mean of the ensemble. For comparison, we also presented the result of “free-running” the dynamical model (green) using the prior distribution of Q_{in} and the MCMC-derived non-evolving uncertain parameters from **Figure 4.3**. Similarly, the light green colors are the ensemble members and the darker green shade is the standard deviation. The purple broken lines mark the 2011 eruption at Grímsvötn.

the timing of the eruption simply by finding the day where the probability equals 25 ± 1 % within the green line in **Figure 4.7C**. **Figure 4.8** illustrates the (A) forecast day of eruption and the (B) relative distance (in days) of this forecast-day to the assimilation time step. For example, if we evaluate the shallow overpressure at time step $t_i = 1700$d, the forecast day of eruption is $d = 2498^{2526}_{2485}$ (i.e. day at which 25 ± 1 % is located), which is 798^{826}_{785} days away from the assimilation time step. Clearly, at least ~ 2 weeks prior to the 2011 Grímsvötn eruption, we are able to forecast that this eruption is very soon to happen; with the last three days even indicating that we are at 'zero-distance' to eruption day. Note that the "no-data" values in **Figure 4.8A** and **B** mean that the predicted day and distance to eruption is outside our chosen time window (i.e. time window used for "free-running" the model is up to $d = 3337$). Moreover, the cumulative number of earthquakes (i.e. data from Got *et al.* [2017]) actually shows correlation with the 25 ± 1 % probability of rupture that we observed, at least for the 2004-2011 inter-eruptive deformation data at Grímsvötn (**Figure 4.8C**). Lengliné *et al.* [2008] have previously demonstrated through joint interpretation of deformation and seismic data that the exponential acceleration of seismicity before an eruption is linked to the accumulation of magma in a reservoir.

4.5 Further Discussions

4.5.1 Bayesian-based inversion vs. data assimilation

Instead of using EnKF and the differential equations (i.e. **equations (4.1)** and **(4.2)**) as a step-2 of our approach, we rather used MCMC and the analytical solutions to the diffrential equations (i.e. **equations (4.3)** and **(4.4)**) to determine the evolution of the overpressures and the bottom magma inflow rate as well as the fit with the radial displacement data. In **Figures 4.9** and **4.10**, we overlaid the results of MCMC on the EnKF-derived estimates, showing that, in general, they both fitted well with the radial displacement time series and that the estimated overpressures and magma inflow rate are almost similar. Although as time progresses, MCMC tends to give smoother results than EnKF (e.g. noisier Q_{in} estimates in **Figure 4.9B** for EnKF). This is expected, since in inversion we use all the data available from t_0 until the observation time, t_i, hence we somehow filter more the noise embedded within the data. The mean residual of MCMC and and EnKF are shown in **Figure B.6**.

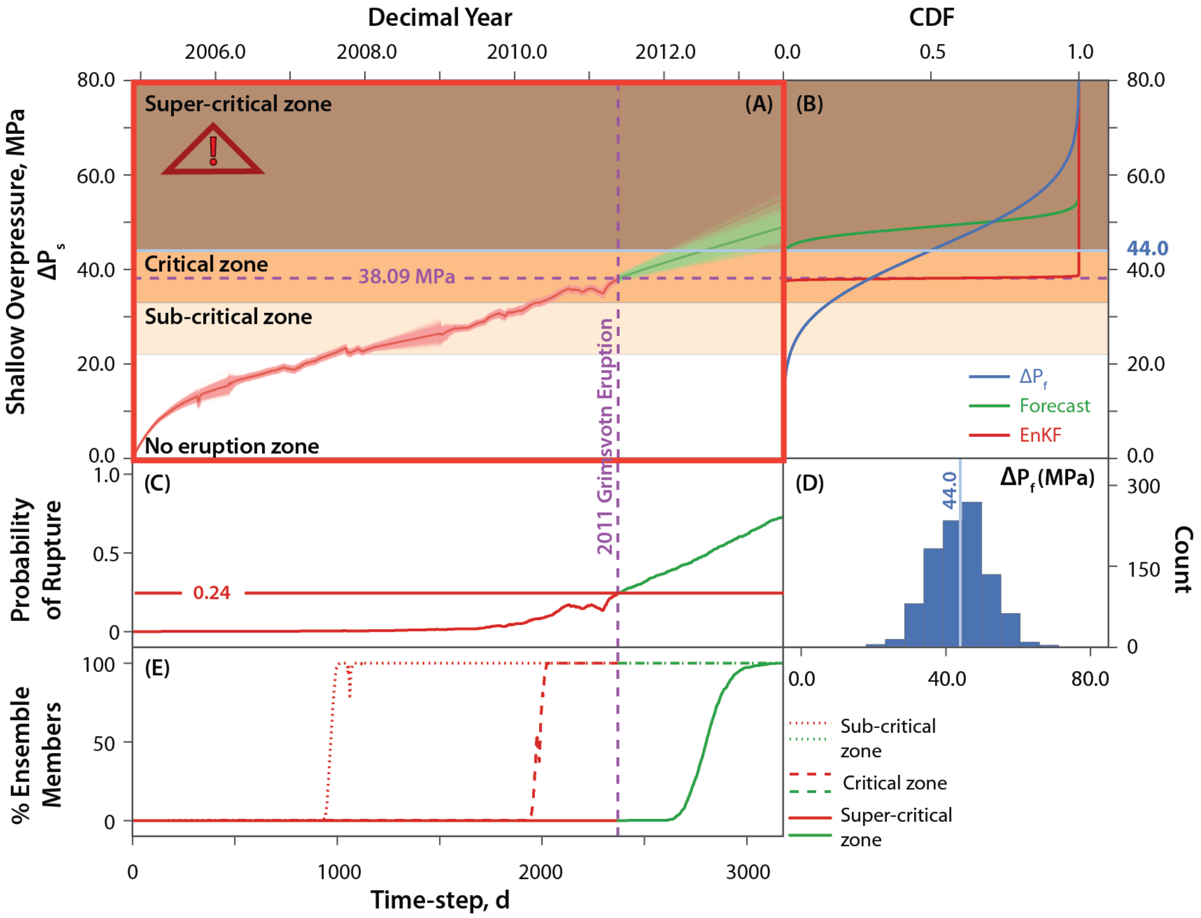

Figure 4.7: (A) The evolution of the EnKF-derived shallow overpressure—constrained by the initial part of the 2004-2011 radial displacement dataset (i.e. **Figure 4.6**)—embedded on the eruption zones. Note that we define the eruption zones based on the estimated rock tensile strength in Iceland which consequently provides the failure overpressure distribution (i.e. P_f) needed to trigger the rupture of a magma chamber (i.e. Albino *et al.* [2010]). (B) The cumulative distribution function (CDF) illustrating the failure overpressue (blue) as well as the overpressures at the end of the assimilation window (red) and at the end of free-run (green). Note that the latter is performed just after the assimilation to further predict the evolution of the overpressure. (C) The probability of rupture calculated from the N-ensemble of models that exceeded the failure overpressure described by the distribution in (D). (E) The percentage of ensemble members entering each eruption zones as a function of time.

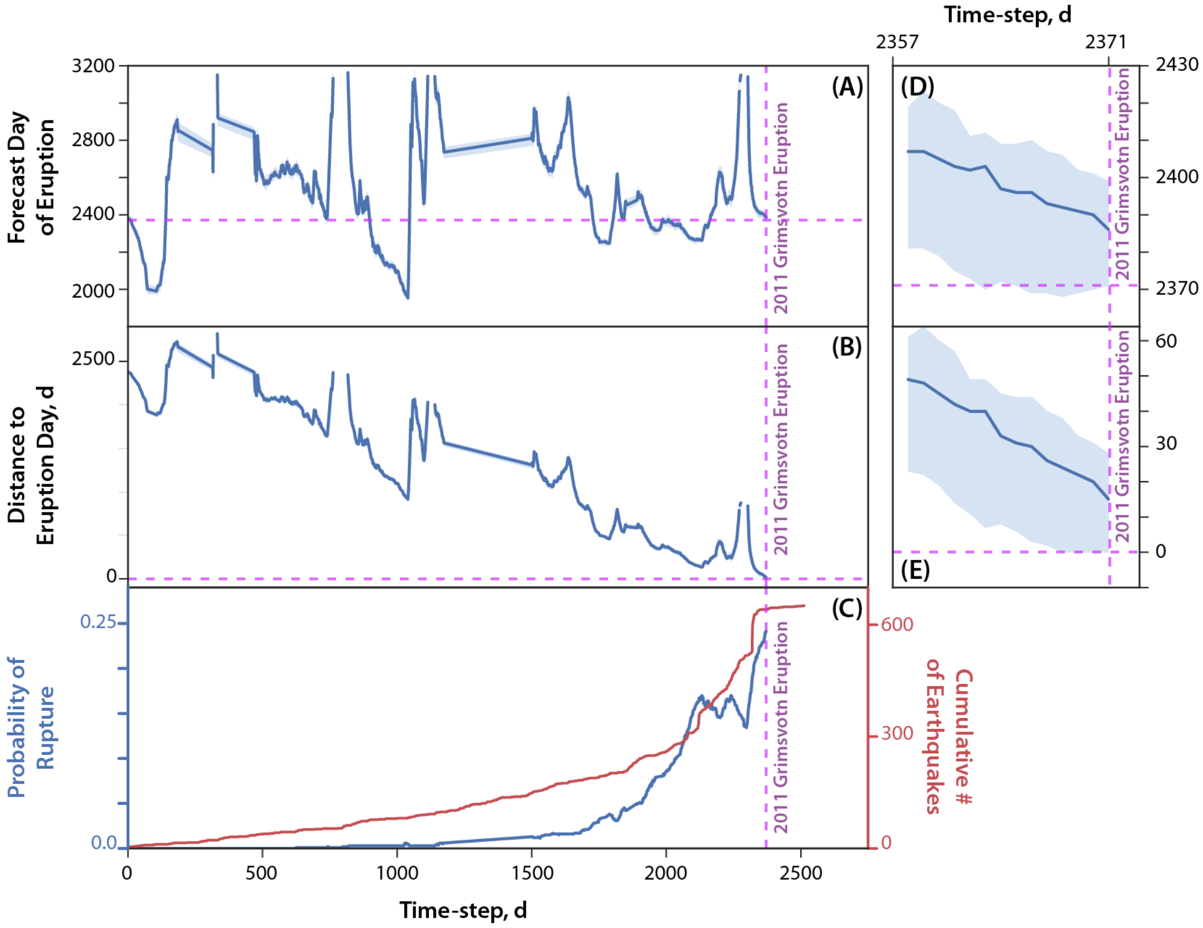

Figure 4.8: (A) Forecast day of eruption based on a “probability of rupture” criterion (i.e. 0.25 ± 0.01). The blue line is the forecast day based on the 25% probability whereas the light blue shade corresponds to the ±1%. (B) Number of days prior to eruption as a function of time calculated from **Figure 4.8A**. (C) The probability of rupture at the end of the assimilation window (blue) as shown in **Figure 4.7C** along with the cumulative number of earthquakes (red). Note that **Figure 4.8D** and **E** provide a closer look at the forecast roughly 14 days prior to the actual eruption.

It is worth emphasizing that the forecasting strategy that we propose here can also be applied when inversion, such as MCMC, is rather used to infer the shallow overpressure values. Basically, MCMC will still provide a probability of rupture at each step based on the number of model ensemble that exceeded the critical overpressure that we initially define. However, one notable feature of sequential data assimilation, in particular, EnKF, is that it takes into account model errors that can be related to time-dependent model parameter/s. In our case, if the fluctuation in Q_{in} is a “true” surge or decrease, meaning that the fluctuation is higher than the observed background noise (i.e. $>\sim$ 0.015 km^3 yr^{-1}), then EnKF can be more useful than the MCMC approach since in classic inversion setup, models are assumed “perfect”. We will further discuss and demonstrate this in the subsequent chapter. Furthermore, inversion techniques are computationally expensive as it uses all the available data to infer the uncertain model parameters which is indeed a limitation in real-time forecasting of magma-chamber rupture. Being able to determine the value of the shallow overpressure and update it at each time step until rupture is crucial, since this value will indicate if the pressure is sufficient to drive the magma up to the surface and cause an eruption.

4.5.2 Forecasting the magma-chamber rupture after 2011

We applied the same procedure discussed in **Section 4.3** to the radial dataset after the 2011 eruption at Grímsvötn. **Figure 4.11** shows that just before the 2014 rifting event, the shallow overpressure at Grímsvötn is already in a critical stage with probability of rupture equal to 18%. Given the trend prior to the rifting event, Grímsvötn could have erupted in year 2015 since this is where the 25 ± 1 % probability falls. However, the probability of rupture decreased after the rifting event until around early 2016, before accelerating once again as shown in **Figure 4.12**. Based on these findings, we can say that some transient event may have affected the behavior of Grímsvötn volcano by postponing its supposed eruption. Given the current dataset we have (i.e. up to 01 Sep 2016), we analyzed the value of the shallow overpressure and the probability of rupture after the 2014 rifting event (**Figure 4.12**). Results indicate that by 01 Sep 2016, the shallow overpressure is already at 39.11 MPa with probability of rupture equal to 28 %. However, it is difficult to say if the shallow magma chamber beneath Grímsvötn is truly in a critical point of tensile failure since the measured radial displacement at GFUM GPS station after the 2014 rifting event is not anymore related solely to volcanic deformation. After the rifting event, the displacement time series is already a mix of

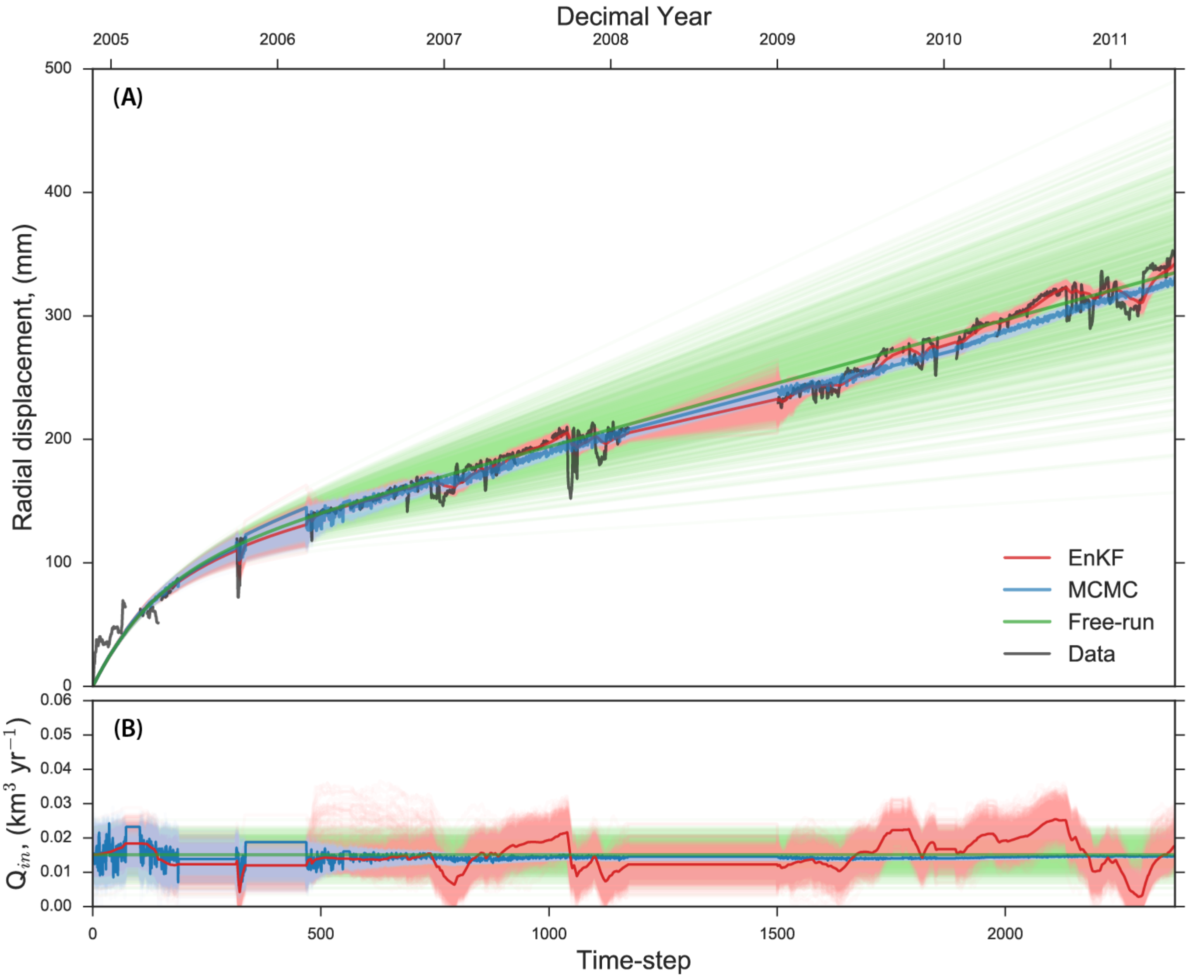

Figure 4.9: Data-fits and Q_{in} estimates of MCMC as compared to EnKF. (A) The entire 2004-2011 inter-eruptive radial dataset used in this study (black) and the resulting data-fits by: 1) solely free-running the dynamical model (green), 2) data assimilation via EnKF (red) and 3) Bayesian-based inversion through MCMC (blue). (B) Estimated value of the magma inflow rate, Q_{in}, as a function of time using: the free-run (green), EnKF (red) and MCMC (blue). Note that both in (A) and (B), the dark solid lines correspond to the mean of the free-run (green), EnKF (red) and MCMC (blue), whereas the lighter colors represent the model ensembles.

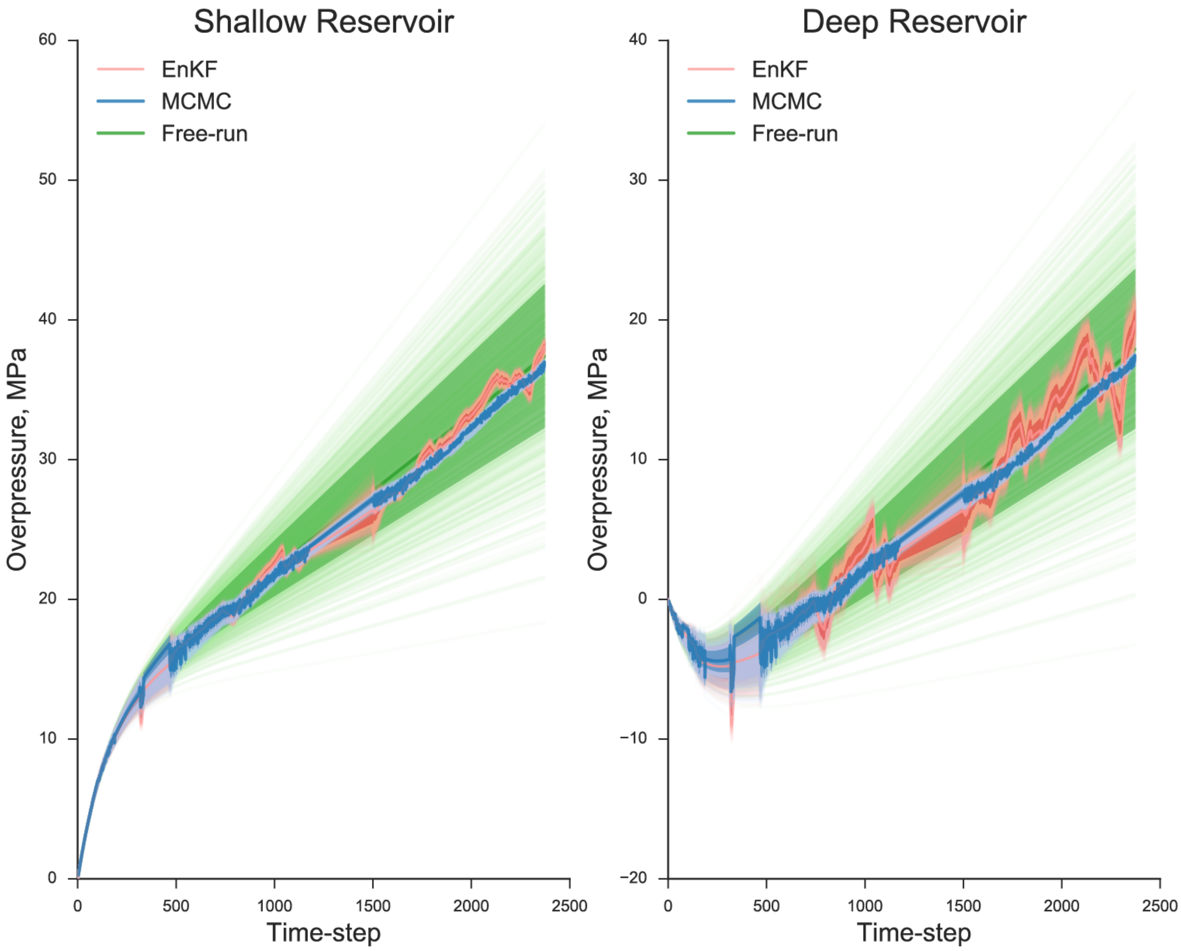

Figure 4.10: The MCMC-derived shallow and deep overpressure values (blue) as compared to EnKF-derived estimates (red). Note that the corresponding data fit is illustrated in **Figure 4.10**. Note that we also presented the result of "free-running" the dynamical model (green) using the prior distribution of Q_{in} (**Figure 4.5C**) and the MCMC-derived non-evolving uncertain parameters from **Figure 4.3**.

contributions related to the 2014 rifting event itself, the 6-month long eruption, the subsequent visco-elastic relaxation of the ground after the rifting, and of course, the activities beneath Grímsvötn's volcano.

4.5.3 Failure criterion

The failure overpressure criterion, ΔP_f, that we used to forecast if the magma chamber will reach tensile failure and initiate dyke propagation is highly dependent on the rock tensile strength, T_s. We emphasize that the mean value we used (e.g. $T_s = 22$ MPa) is in fact an upper bound of what is measured *in situ*. Although a key parameter, the estimate of the rock tensile strength is poorly constrained. Furthermore, the failure overpressure can vary depending on the geometry of the magmatic reservoir and local stress field that can actually change through time due to the effects of processes that include (but are not limited to): faulting, fracturing or presence of hydrothermal activity (Pinel *et al.* [2010], Albino *et al.* [2018]). It follows that the value of the failure overpressure has a large uncertainty and should be defined carefully per individual volcano. These arguments justify our use of a wide Gaussian distribution for the failure overpressure criterion at Grímsvötn in order to account for its large variability. However, we also stress the fact that further studies must be taken in order to constrain this failure overpressure criterion (e.g. revisit the failure overpressure values and conditions that triggered past eruptions).

4.6 Conclusions and Perspectives

In this work, we introduced a new approach to forecast the failure of a magma chamber in real-time by sequentially assimilating geodetic data and by defining a failure overpressure criterion in the form of a wide Gaussian distribution for Grímsvötn volcano. We tested our strategy by forecasting the 2011 Grímsvötn eruption using the 2004-2011 inter-eruptive dataset recorded at GFUM GPS station. Blake et Cortés [2018] explored the idea of producing forecasts of the type, "The probability that a deflation will start during the next N days is p". In our case, we give forecasts in the form of, "[Given that an eruption is imminent when the probability of rupture reaches p], an eruption might occur within the next N_{min}^{max} days". Indeed we obtained succesful results based on $p = 25 \pm 1\%$, with the last three days prior to the 2011 eruption even indicating [a minimum forecast of] "zero days to eruption". Note however, that the probability of rup-

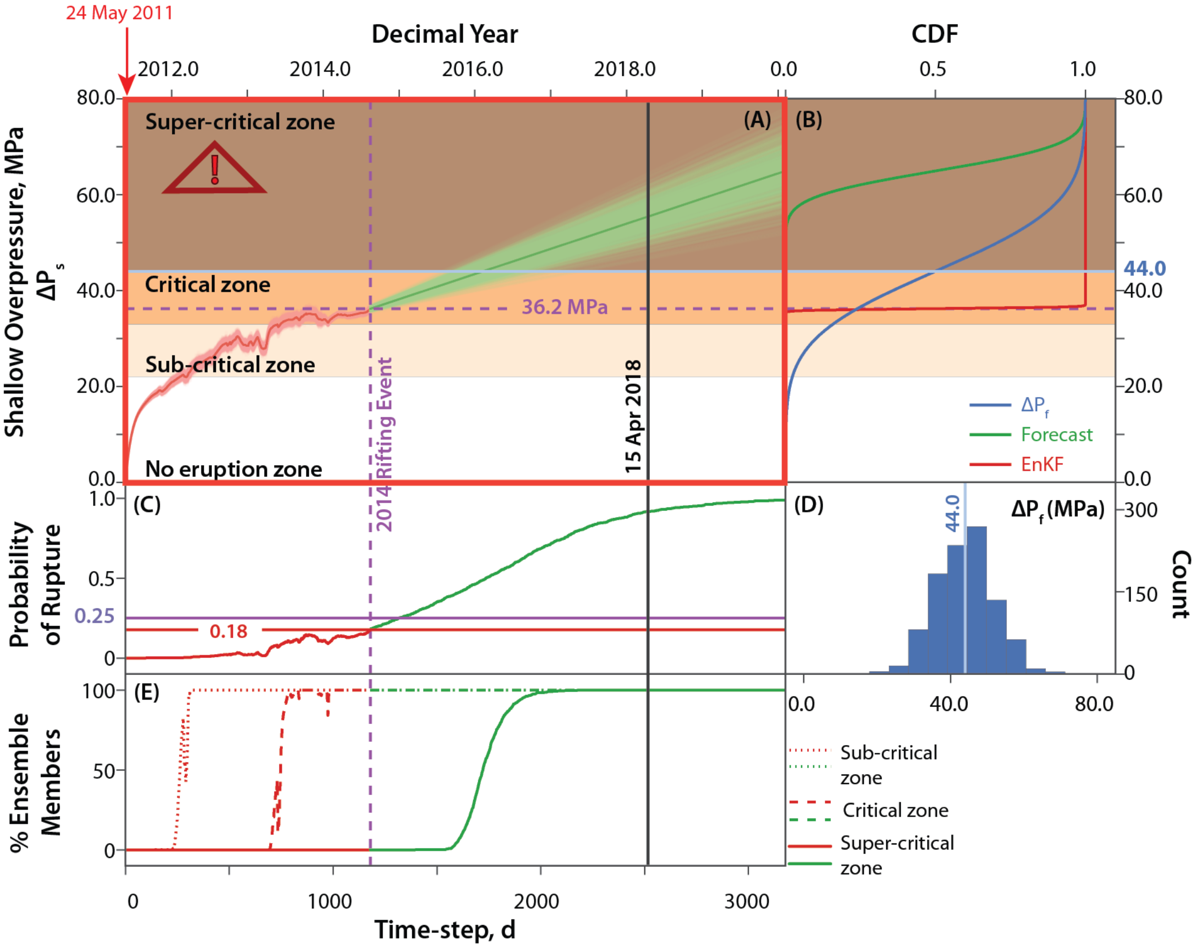

Figure 4.11: (A) The eruption zones with the evolution of the shallow overpressures **after the 2011 Grímsvötn eruption until the 2014 rifting event**. (B) The cumulative distribution function (CDF) illustrating the failure overpressue (blue) as well as the overpressures at the end of the assimilation window (red) and at the end of free-run (green). Note that the latter is performed just after the assimilation to further predict the evolution of the overpressure. (C) The probability of rupture calculated from the N-ensemble of models that exceeded the failure overpressure described by the distribution in (D). (E) The percentage of ensemble members entering each eruption zones as a function of time.

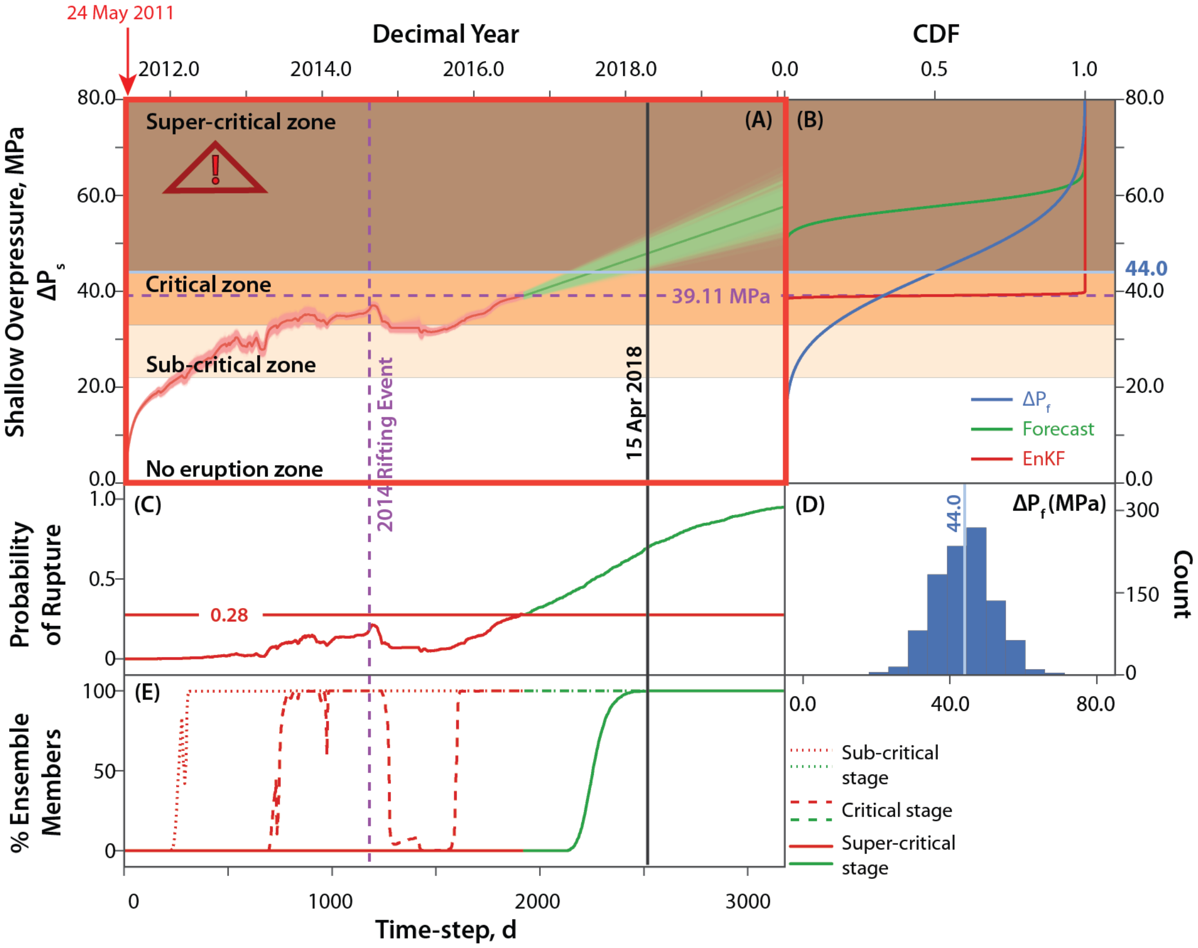

Figure 4.12: (A) The eruption zones with the evolution of the shallow overpressures **after the 2011 Grímsvötn eruption until 01 September 2016**. (B) The cumulative distribution function (CDF) illustrating the failure overpressue (blue) as well as the overpressures at the end of the assimilation window (red) and at the end of free-run (green). Note that the latter is performed just after the assimilation to further predict the evolution of the overpressure. (C) The probability of rupture calculated from the N-ensemble of models that exceeded the failure overpressure described by the distribution in (D). (E) The percentage of ensemble members entering each eruption zones as a function of time.

ture, p, may or may not be similar to other volcanoes and hence must be further validated.

We also tested our approach for the 2011 dataset until and after the 2014 rifting event. Our findings indicate that Grímsvötn could have erupted in 2015 but was postponed after the Bárdarbunga-Holuhraun event in 2014-2015, implying that there might be a transient event that occurred and affected Grímsvötn's volcanic system. In **Chapter 5**, we will present evidences of this transient event and discuss how nearby volcanoes possibly interact with each other.

The strategy that we propose is simple and can be used as a fast and first-order approximation to forecast the possible failure of a magma chamber. Indeed, it can be applied to other basaltic type of volcanoes that also exhibit inflation-deflation behavior. Although we only used deformation data alone for the real-time forecasting, we emphasize that integrating other datasets (e.g. seismic, gas emission data) are highly encouraged along with more realistic physics-based models to provide stronger and much deterministic results. However, when developing more sophisticated models, one must consider the computational cost since this is very crucial in real-time forecasting of volcanic unrest.

We believe that the approach developed in this study can open doors to a whole lot of new perspectives in eruption forecasting. In particular, we can now have real-time information about the evolution of the overpressures that can be used not only to evaluate the possible failure of a magma chamber but also as an initial input to dyke propagation models. Once evidences indicate that the magma chamber has ruptured, the overpressure becomes a key parameter to initialize dyke propagation models in order to assess whether or not the dyke will be able to reach the surface. If there is enough driving pressure, then the next step is to forecast the exact timing and location of the eruption.

Chapter 5

Deep connection between volcanic systems evidenced by sequential assimilation of geodetic data

Contents

This chapter was published as "Possible deep connection between volcanic systems evidenced by sequential assimilation of geodetic data", *Nature Scientific Reports* (2018) 8:11702, https://doi.org/10.1038/s41598-018-29811-x.

Abstract

The existence of possible deep connections between nearby volcanoes has so far only been formulated on the basis of correlation in their eruptive activities or geochemical arguments. The use of geodetic data to monitor the deep dynamics of magmatic systems and the possible interference between them has remained limited due to the lack of techniques to follow transient processes. Here, for the first time, we use sequential data assimilation technique (Ensemble Kalman Filter) on ground displacement data to evaluate a possible interplay between the activities of Grímsvötn and Bárdarbunga volcanoes in Iceland. Using a two-reservoir dynamical model for Grímsvötn plumbing system and assuming a fixed geometry and constant magma properties, we retrieve the temporal evolution of the basal magma inflow beneath Grímsvötn that drops up to 85% during the 10 months preceding the initiation of the Bárdarbunga rifting event. We interpret the loss of at least 0.016 km^3 in the magma supply of Grímsvötn as a consequence of magma accumulation beneath Bárdarbunga and subsequent feeding of the Holuhraun eruption 41 km away. We demonstrate that, in addition to its interest for predicting volcanic eruptions, sequential assimilation of geodetic data has a unique potential to give insights into volcanic system roots.

5.1 Introduction

The rate of magma supply to volcanic systems which fundamentally controls the eruptive activity is a determinant information mostly retrieved by geodesy and/or gas measurements. However, this key input remains difficult to constrain. One reason is that the ability of geodetic observations to detect or quantify magma accumulation decreases with the increasing depth of storage zones involved. Despite this flaw, geodesy sometimes in combination with gas measurements has been essential to estimate magma flux entering subsurface reservoirs, proving that this supply was most probably occurring by pulse or surge of magmas (Parks *et al.* [2012], Poland *et al.* [2012]). Indeed, this behavior is consistent with the observation that long-term pluton growth rates, inferred from isotopic studies, are much smaller than the minimum rates of magma supply required to ensure magma transfer through dykes (Menand *et al.* [2015]). Despite this known transient behavior in deep magma supply, classical methods used so far to invert geodetic data always consider steady-state systems with constant basal inflow (Anderson et Poland [2017]).

Another open question related to magmatic sources concerns their spatial extent at depth, whether or not a common deep source can be shared by different volcanic systems or can distinct magmatic sources be mechanically connected at depth. Geochemical arguments based on major element compositions or ratios as well as isotopic compositions are commonly used to discriminate samples from different volcanic systems and address the question of the lateral extension of volcanic roots (Weis *et al.* [2011], Hartley et Thordarson [2013]). More recently, thanks to the improvement of deformation data spatial coverage brought by satellite radar interferometry, geodesy has provided some significant insights into the lateral extent of magmatic domains (Biggs *et al.* [2016]). In particular, based on a statistical analysis, deformation occurring at more than 5 km away from the nearest active volcanic vent is common, suggesting that magmatic storage zones are not focused beneath volcanoes (Ebmeier *et al.* [2018]). Rifting areas where long dikes are emplaced, represent ideal context to track lateral connections between nearby volcanic systems.

Here, we propose a new methodology suitable to retrieve magma supply changes from temporal series of geodetic data even with limited amount of spatial information, allowing us to evidence a connection between two nearby volcanic systems in the Icelandic Eastern Volcanic Rift Zone. While several studies have used real geodetic data and applied variants of Kalman Filter as an optimization or statistical interpolation tool to solve problems in volcanology in the past (Fournier *et al.* [2009], Shirzaei et Walter [2010], Zhan et Gregg [2017]), this study is the first one to apply sequential data assimilation based on a dynamical model as proposed in **Chapter 3** using a real dataset recorded on a volcano.

5.2 Bárdarbunga and Grímsvötn volcanoes

Bárdarbunga and Grímsvötn are two subglacial basaltic volcanoes located ~ 27 km apart beneath the Vatnajökull ice cap (**Figure 5.1**). They are isotopically distinct systems (Sigmarsson *et al.* [2000]) and are both sitting at the center-top of the mantle plume in Iceland (Wolfe *et al.* [1997]). Grímsvötn volcano hosts a 10-12 km wide and 200-300 m deep caldera complex. Geodetic measurements from its last eruption reveal a 1.7 km-deep shallow magma chamber (Hreinsdóttir *et al.* [2014]). Although, a low seismic velocity anomaly at around 3-4 km depth has been previously observed and identified as a magma chamber along with a deeper dense body inferred from gravity

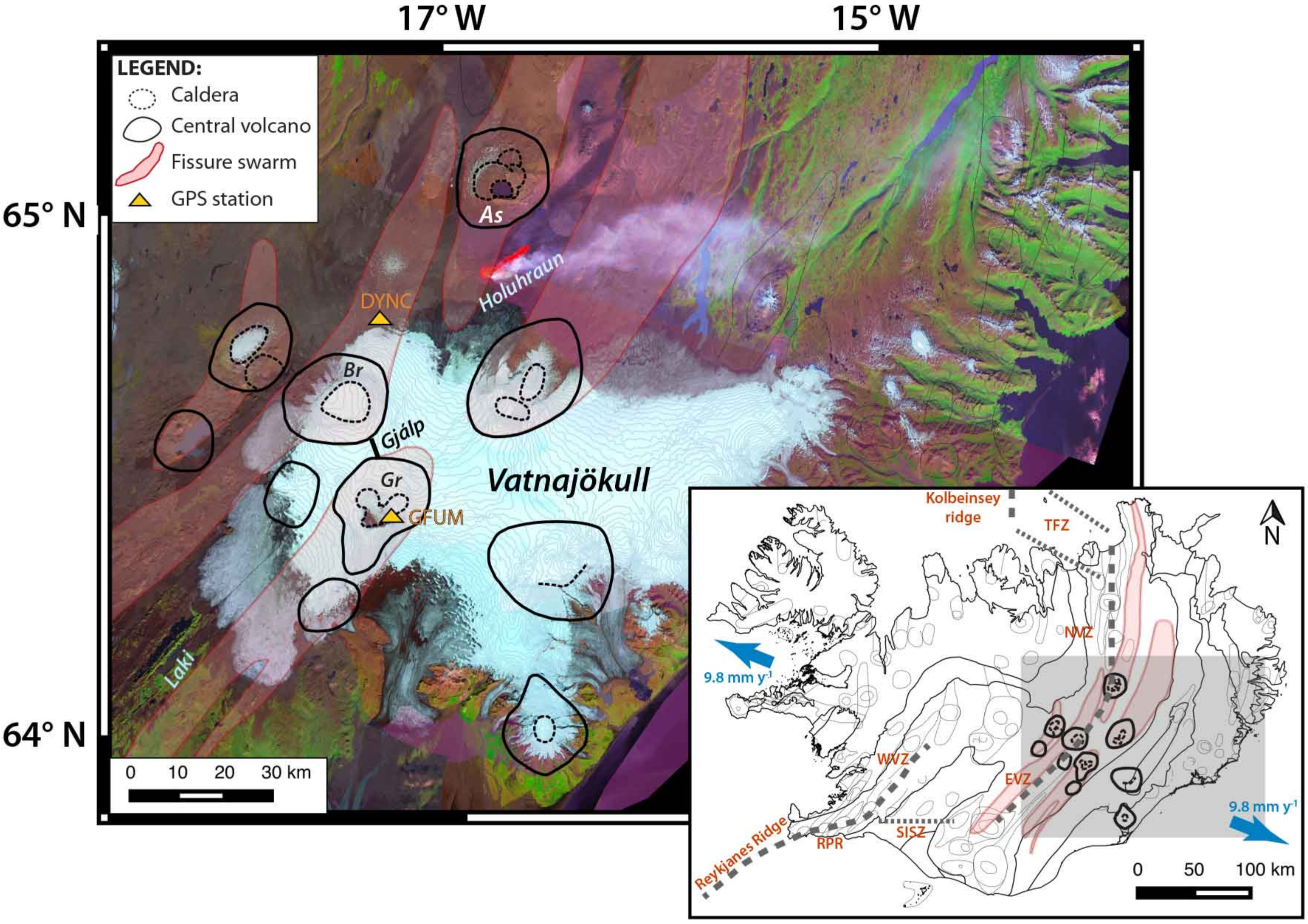

Figure 5.1: Landsat-8 image taken on 06 September 2014, showing the principal volcanoes and fissure swarms (e.g. Bárdarbunga (Br), Grímsvötn (Gr) and Askja(As)) near the Vatnajökull icecap. The image is based on the mosaicked data from the National Land Survey of Iceland (NASA Landsat Program [2014], Landmaelingar Islands [2015])). Fissure eruptions of Laki (1783-1784) and Gjálp (1996) as well as the on-going Holuhraun eruption when the image is captured are also presented. The locations of GFUM and DYNC GPS stations which are discussed in the main article are marked as yellow triangles. Inset: map of Iceland (modified after Reverso *et al.* [2014]) outlining its volcanic zones (e.g. West Volcanic Zone (WVZ), East Volcanic Zone (EVZ), North Volcanic Zone (NVZ)) and transform zones (e.g. South Iceland Seismic Zone (SISZ) and Tjornes Fracture Zone (TFZ)). The Reykjanes Ridge and Reykjanes Peninsula Rift (RPR), and the Kolbeinsey Ridge which mark the limits of the volcanic zone are illustrated for reference. The rate of the plate spreading is 9.8 mm yr^{-1} (DeMets *et al.* [2010], Reverso *et al.* [2014]). The shaded gray area is the region covered by the Landsat-8 image in the main figure.

measurements (Alfaro *et al.* [2007], Hreinsdóttir *et al.* [2014]). Grímsvötn is Iceland's most active volcano erupting once per decade. Its post-eruptive deformation patterns for the last three eruptions (i.e. 1998, 2004 and 2011) are very similar and suggest a plumbing system characterized by at least two connected magma reservoirs (Reverso *et al.* [2014]) beneath the volcano. In October 1996, a subglacial eruption termed as the Gjálp eruption (Gudmundsson *et al.* [1997]) occurred between Grímsvötn and Bárdarbunga volcanoes. However, contrasting geochemical and geophysical analyses result to unresolved debates on whether the eruption was fed by Bárdarbunga or Grímsvötn (Einarsson *et al.* [1997], Sigmarsson *et al.* [2000], Sturkell *et al.* [2006], Pagli *et al.* [2007]). Bárdarbunga volcano has an 11-by-18 km wide and 500-700 m deep elliptic caldera (Gudmundsson *et al.* [2016]) with an associated fissure swarm extending 115 km to the southwest and 55 km north-northeast (Sigmundsson *et al.* [2015], Gudmundsson *et al.* [2016]). Activities at Bárdarbunga consist in (i) subglacial or (ii) major effusive fissure eruptions for the last 2000 years (Sigmundsson *et al.* [2015]). In August 2014, an eruptive fissure called Holuhraun (**Figure 5.1**) has been reactivated between the Bárdarbunga and Askja volcanic systems (Sigmundsson *et al.* [2015]). The activity began with intense shallow seismicity that originated from Bárdarbunga and migrated toward Askja during the weeks that followed (Gudmundsson *et al.* [2016]). The magmatic dyke was fed by a reservoir located at $\sim$ 12 km depth beneath Bardarbunga caldera (Gudmundsson *et al.* [2016]). It propagated at a distance of $\sim$ 41 km before it breached the surface resulting to the Holuhraun fissure eruption. The effusive eruption lasted for 6 months and produced 1.5 ± 0.2 km^3 of lava, a volume similar to the erupted lava of the 1783-1784 Laki eruption (Gudmundsson *et al.* [2016]).

5.3 Related deformation before the 2014-2015 eruptive activity

Between October 2013 and August 2014, NS and EW surface displacement patterns observed at GFUM—the sole GPS station at Grímsvötn volcano located on Mount Grímsfjall (**Figure 5.1**)—shifted from a positive linear to a nearly-constant trend (i.e. gray area in **Figure 5.2**). Such change of slope has not been observed during the previous post-eruptive displacement time series (**Figure 5.3**). The GPS times series thus clearly shows a significant change in behavior compared to the regular trend continuously recorded over the last 10 years (i.e. 1.5 eruptive cycle) and this change does occur

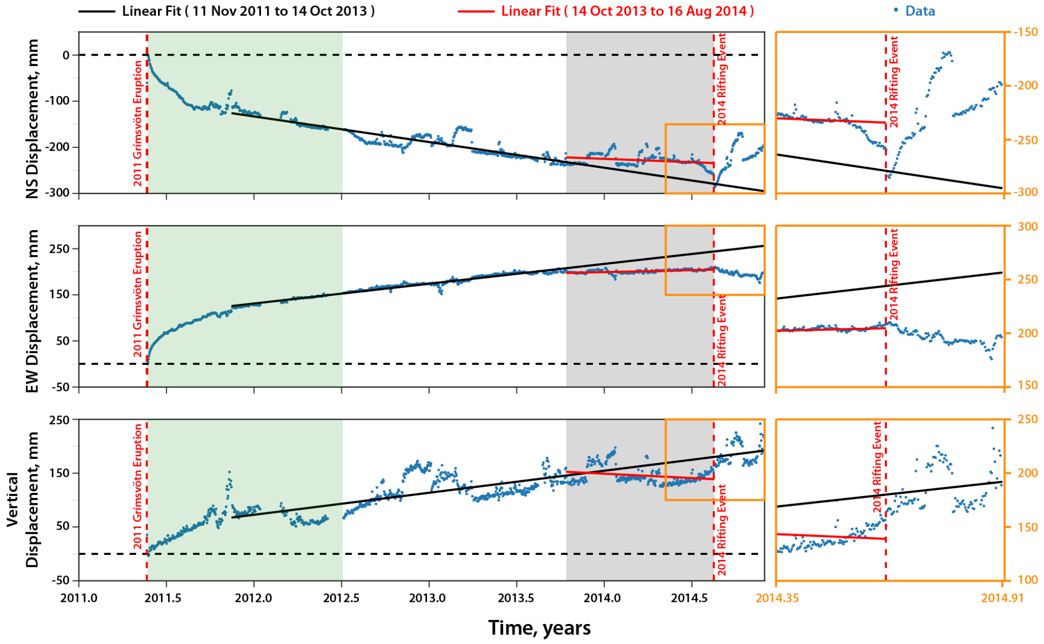

Figure 5.2: GPS time series of GFUM station from 22 May 2011 to 30 Nov 2014. The actual data are in blue points, the red solid line is the linear fit of the points within the shaded gray area (assumed shift from linear to constant trend), and the black solid line represents the linear fit prior to the shaded gray area. The latter was extended up to the end of the dataset to estimate the expected displacements after the assumed change of slope (14 October 2013). The red broken lines mark the onset of the May 2011 eruption and the August 2014 rifting event at Grímsvötn and Bárdarbunga, respectively. The horizontal black broken line is the zero-displacement reference. The shaded green area covers the dataset used during the inversion (step 1 of our approach). The insets (orange box) provide a closer look on the data points near the time of the rifting episode. Note that the vertical displacement is not corrected for GIA and seasonal effects. We applied a tectonic correction for the NS and EW components following the estimations of Reverso *et al.* [2014].

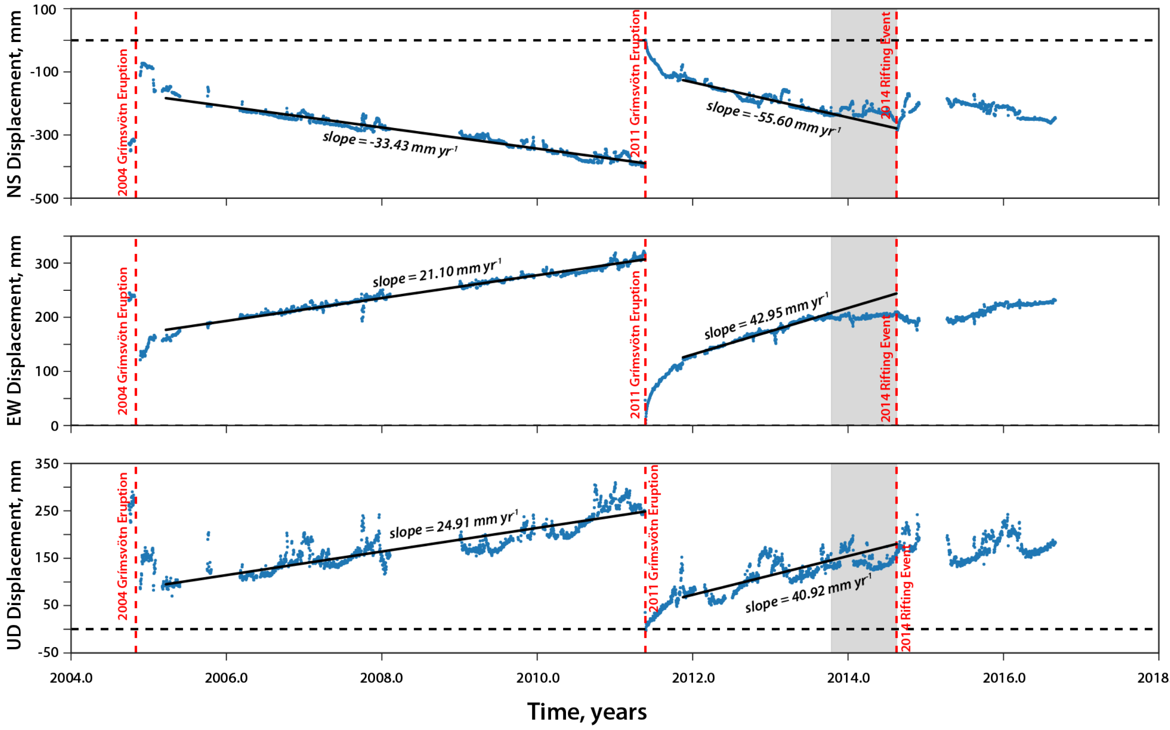

Figure 5.3: GPS time series measured at GFUM station from 30 Sep 2004 to 01 Sep 2016. The blue dots are the actual data. The red broken lines mark the 2004 and 2011 Grímsvötn eruptions as well as the 2014 major rifting event. The black solid lines are the linear fit to the linear part of each post-eruptive event. The black broken lines are shown as a reference for the zero-displacement value. The shaded gray area corresponds to the assumed shift from linear to constant trend around 10 months before the 2014 rifting event. Note that the vertical component of the time series is not corrected for either GIA or seasonal effects. The horizontal component is however, corrected for tectonic trend.

Table 5.1: Analyzed displacements at GFUM GPS station at the start of the rifting event (marked as the red broken line in **Figure 5.2**). Linear Fit corresponds to the expected displacement value (black solid line in **Figure 5.2**), and "Actual" means the actual displacement value.

	Linear Fit	**Actual**	**Actual - Linear Fit**
u_Y (mm)	-279.03	-259.48	19.55
u_X (mm)	243.99	208.83	-35.16
u_d (mm)	180.13	151.33	-28.80

$\sim$ 10 months before the 2014 major rifting event.

To quantify the displacement change, we apply a simple linear regression technique using only the linear part of the dataset prior to the assumed change in behavior (i.e. November 2011 to October 2013) and then we use the resulting slope to estimate the expected displacements at the time of the rifting (i.e. 4 UTC, 16 August 2014 is marked as the start of the major rifting event, Gudmundsson *et al.* [2016]). We obtained significant discrepancies of up to -39.31 mm and 44.88 mm for the EW and NS directions, respectively (see **Figure 5.2** and **Table 5.1**).

An inflating reservoir beneath Bárdarbunga could not explain such discrepancies as displacement contributions toward the south and the east directions are expected instead. To demonstrate this, we modeled the expected displacements at GFUM GPS station induced by an inflating source beneath Bárdarbunga using the results of previous studies (Auriac *et al.* [2014], Gudmundsson *et al.* [2016], Coppola *et al.* [2017]) as input parameters (**Table 5.2**) to a generalized point-pressure source equation:

$$\begin{bmatrix} u_Y \\ u_X \\ u_d \end{bmatrix} = \begin{bmatrix} \alpha\frac{(1-\nu)}{G}a^3\Delta P\left(\frac{Y}{R^3}\right) \\ \alpha\frac{(1-\nu)}{G}a^3\Delta P\left(\frac{X}{R^3}\right) \\ \alpha\frac{(1-\nu)}{G}a^3\Delta P\left(\frac{d}{R^3}\right) \end{bmatrix} \tag{5.1}$$

As expected, the modeled displacements could not fit the observed displacements at GFUM (**Table 5.2**). Moreover, we find no similar trend variation at neighboring GPS stations close to Bárdarbunga, in particular the DYNC station which is $\sim$ 22 km away from Bárdarbunga (**Table 5.3** and **Figure 5.4**). These arguments imply that the sudden change of behavior at GFUM, one year prior to the 2014-2015 Bárdarbunga-Holuhraun

Table 5.2: Description of the parameters and the values at GFUM and DYNC stations used to model the displacements induced by an inflating Bárdarbunga reservoir.

	Description	**GFUM**	**DYNC**	**Reference**
Y (m)	Distance between the GPS station and Bárdarbunga along NS	-26317.002	20164.004	
X (m)	Distance between the GPS station and Bárdarbunga along EW	7663.885	8727.437	
d (km)	Depth of the Bárdarbunga reservoir	11.0 to 16.0		Gudmundsson *et al.* [2016]
R (km)	Radial distance between Bárdarbunga's reservoir and the GPS station	29.54 to 31.74	24.57 to 27.18	
a (km)	Radius of the Bárdarbunga reservoir	3.0 to 4.0		Gudmundsson *et al.* [2016]
α	Shape of the reservoir: 1.0 for spherical source, $(4d^2)/(\pi R^2)$ for sill	0.18 to 0.32; 1.0	0.26 to 0.44; 1.0	Gudmundsson *et al.* [2016], Coppola *et al.* [2017]
ν	Poisson's ratio	0.25		Auriac *et al.* [2014]
$\Delta P/E$	Ratio of the overpressure over the Young's modulus	1.95×10^{-5} to 6.67×10^{-4}		Auriac *et al.* [2014], Coppola *et al.* [2017]
u_Y (mm)	Modeled displacement along NS direction	-65.85 to -0.18	0.34 to 80.34	
u_X (mm)	Modeled displacement along EW direction	0.05 to 19.18	0.15 to 34.77	
u_d (mm)	Modeled displacement along the vertical direction	0.07 to 40.04	0.19 to 63.75	

eruptive activity, is most likely not directly induced by Bárdarbunga's plumbing system.

Furthermore, the ratio between the vertical and radial displacements measured at Grímsvötn remains constant through time (see **Figure 5.5**) indicating that the location of the source inducing the surface displacement has not changed through time. Based on these observations, we conclude that the change of slope observed in the radial component should rather be explained by some transient processes affecting Grímsvötn's shallow reservoir—such as the variation of the deep magma supply rate feeding this reservoir.

5.4 Methods

5.4.1 Forward dynamical model

We utilize the two-magma reservoir model of Reverso *et al.* [2014] (**Figure C.1**) as the source of ground deformation at Grímsvötn volcano that is based on simple reservoir systems embedded in a homogeneous elastic crust and incompressible magma. Note that this model only represents the upper part of a multiple-reservoir system.

In this work, we slightly modified the original equations to account for initial overpressure values present in the system:

$$\frac{\Delta P_{s_{t_{i+1}}} - \Delta P_{s_{t_i}}}{t_{i+1} - t_i} = \frac{3\pi E {a_c}^4}{128(1-\nu^2)\mu H_c {a_s}^3}(((\rho_r - \rho_m) g H_c + (\Delta P_{d_{t_0}} - \Delta P_{s_{t_0}})) + \Delta P_{d_{t_i}} - \Delta P_{s_{t_i}}) \tag{5.2}$$

$$\frac{\Delta P_{d_{t_{i+1}}} - \Delta P_{d_{t_i}}}{t_{i+1} - t_i} = \frac{3E}{16(1-\nu^2){a_d}^3} Q_{in} - \frac{{a_s}^3}{{a_d}^3} \frac{\Delta P_{s_{t_{i+1}}} - \Delta P_{s_{t_i}}}{t_{i+1} - t_i} \tag{5.3}$$

Given a set of known and uncertain model parameters, the forward model computes the evolution of the overpressures in the shallow and deep reservoirs which are directly related to the deformation measured at the surface. We assume the following for the known parameters of our model: the shapes of the reservoirs are sills, the Young's modulus, $E = 25$ GPa, the depth and the radius of the shallow reservoir are $H_s = 1.7$ km and $a_s = 2.0$ km, respectively (Hreinsdóttir *et al.* [2014]). We expect that geometrical parameters as well as parameters related to magma properties remain unchanged in

Table 5.3: Analyzed displacements at DYNC GPS station at the start of the rifting event (marked as the red broken line in **Figure 5.4**). Linear Fit corresponds to the expected displacement value (black solid line in **Figure 5.4**), and "Actual" means the actual displacement value.

	Linear Fit	**Actual**	**Actual - Linear Fit**
u_Y (mm)	17.63	24.81	7.18
u_X (mm)	172.74	173.45	0.71
u_d (mm)	16.72	17.91	1.19

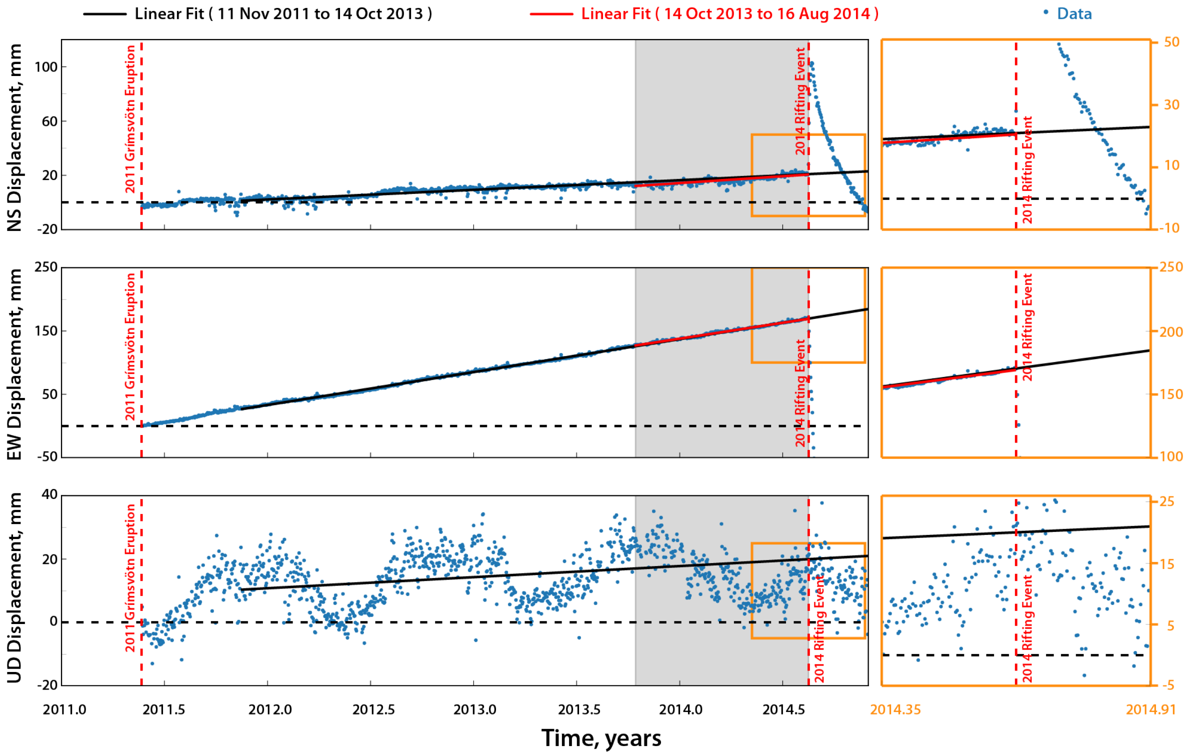

Figure 5.4: GPS time series measured at DYNC station from 22 May 2011 to 30 Nov 2014. The blue dots are the actual data, the red solid line is the linear fit of the points within the shaded gray area (i.e. area that corresponds to the assumed shift from linear to constant trend detected at GFUM station), and the black solid line represents the linear fit prior to the shaded gray area. The latter was extended up to the end of the dataset. The red broken lines mark the onset of the May 2011 eruption and the August 2014 rifting event at Grímsvötn and Bárdarbunga, respectively. The horizontal black broken line is the zero-displacement reference. The insets (orange box) provide a closer look on the data points near the time of the rifting episode.

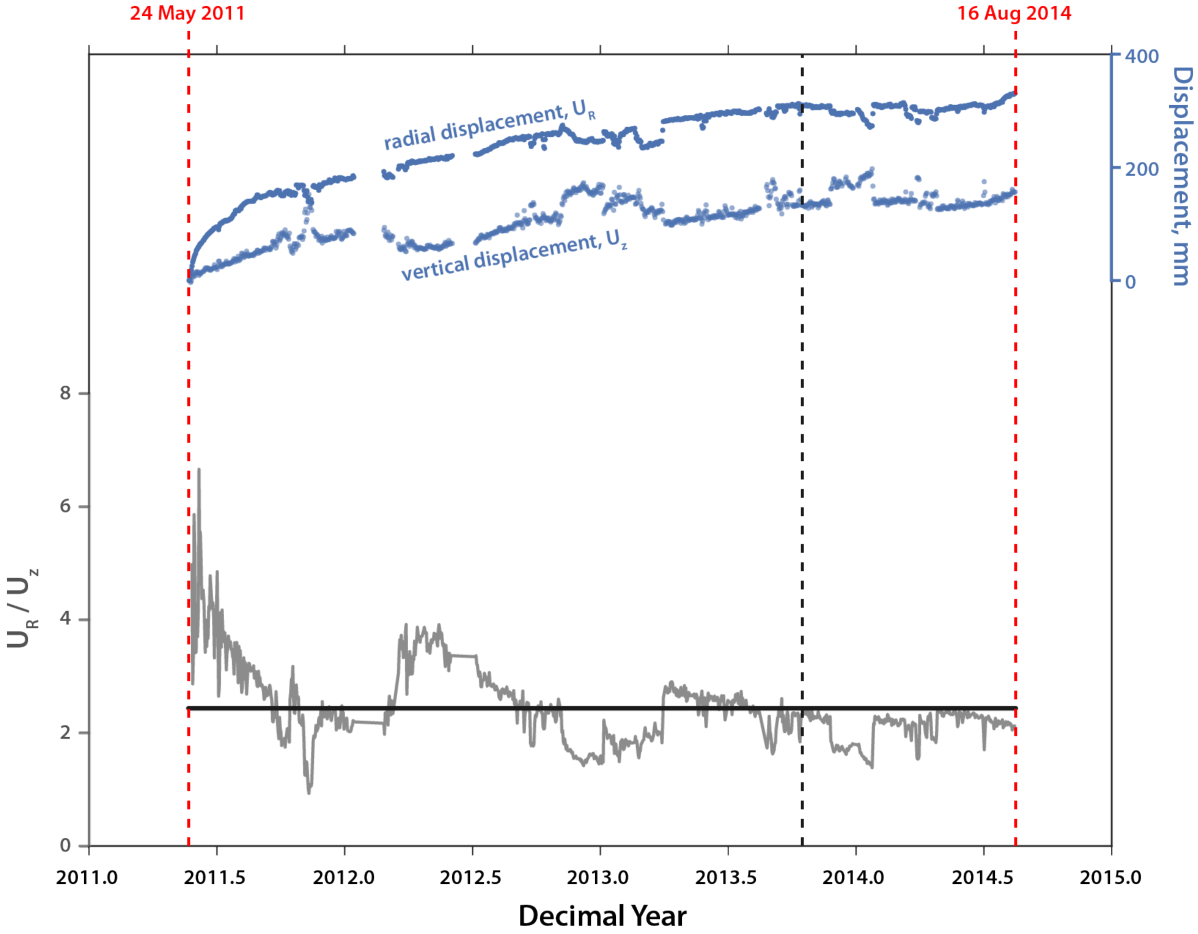

Figure 5.5: The ratio of the radial and vertical displacements (gray solid line) at GFUM GPS station from 24 May 2011 to 16 Aug 2014. The horizontal black line is the mean ratio (i.e. $U_R/U_z = 2.4$). The blue points are the actual radial and vertical displacements. Tectonic correction is applied on the radial component. The vertical component is neither corrected for GIA nor seasonal effects. The black broken line marks the assumed change of slope.

one eruption cycle hence, we assume that all the other uncertain model parameters are constant except for the basal magma inflow, Q_{in} (see **Table 5.4** for the description of the uncertain parameters and **Figure C.1** for the schematic diagram).

Note that any dynamical model can be used for data assimilation, however, the interpretation we made clearly depends on our model choice. We used the two-reservoir model because of its ability to well explain the temporal evolution of the displacement recorded at Grímsvötn (i.e. exponential followed by a linear trend) after each eruptive event. Other models considering only one reservoir fed by a deep and constant pressure source could potentially explain the same temporal evolution by introducing either a complexity in the encasing medium rheology (i.e. damage, viscoelastic behavior (Got *et al.* [2017], Segall [2016])) and/or in the magma properties (i.e. crystallisation, degassing, compressibility (Caricchi *et al.* [2014], Segall [2016])). However, there is a strong geochemical evidence for probably at least several deep reservoirs beneath the Grímsvötn system (Haddadi *et al.* [2017]). Besides, the deep magma supply rate is expected to fluctuate through time (Parks *et al.* [2012], Poland *et al.* [2012], Menand *et al.* [2015]). The facts that 1) such fluctuation is not observed during the previous eruptive cycle, 2) it seems to be transient and 3) it occurs simultaneously with a rifting event mobilizing a large volume of magma in a close volcanic system, are strong arguments in favor of the model preferred in this study. Having GPS data at a distance of 15 km from Grímsvötn could confirm this effect of the deep reservoir (see **Figure 5.6**).

5.4.2 Inversion and data assimilation

For the inversion and data assimilation, only the radial component of the 2011 post-eruptive dataset is exploited due to uncertain GIA contribution and low accuracy of the vertical component at GFUM station (Reverso *et al.* [2014]). We perform a synthetic test to first check that the evolution of Q_{in} can be tracked even with only the radial component of one GPS station. Basically, we adopted the setup discussed in **Chapter 3** in generating the synthetic observations, except that in this case, we only produce the radial component of a GPS time series measured at one station (i.e. at $r = 3.5$ km). The frequency of incoming GPS observation is daily. Also, while generating the synthetic observations, we assumed that after $t_{step} = 875$ d, the value of Q_{in} suddenly drops to zero such that the synthetic displacement becomes constant afterwards (i.e. “Truth” in **Figure 5.7**). We considered a white Gaussian observation error appropriate for the GFUM

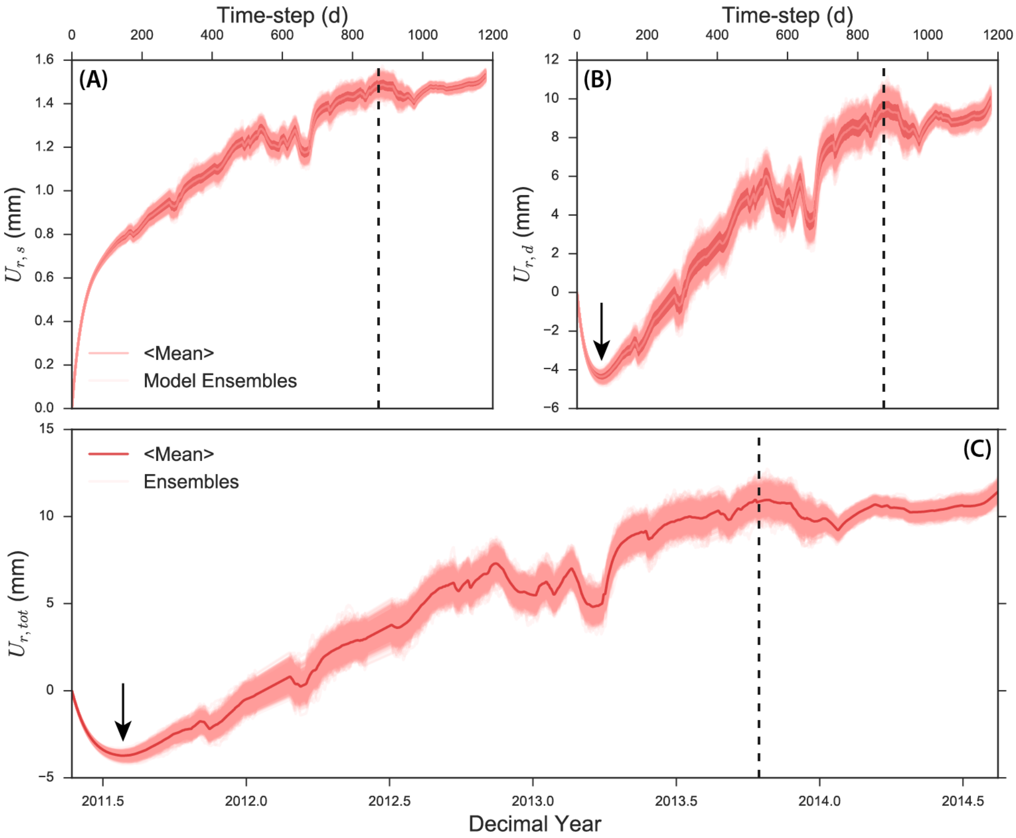

Figure 5.6: The expected radial displacement time series measured at a GPS station located 15 km away from Grímsvötn's volcanic center. (A) $U_{r,s}$ and (B) $U_{r,d}$ are the radial displacements contributed by the shallow and deep reservoirs, respectively. (C) $U_{r,tot}$ is the combined displacement of the two reservoirs (the data measured at the surface). The black arrow in **Figure 5.6C** points at the deflected part of the surface displacement curve. This is similarly observed in the radial displacement contribution of the deep reservoir (**Figure 5.6B**), implying that the measured radial displacement at 15km is mainly dominated by the deep reservoir. The black broken line marks the assumed change of slope prior to the start of the 2014 rifting event ($t_{step} = 875$ d).

dataset (i.e. $R = 0.015^2$ m). Afterwards, we performed state-parameter estimation following the strategy in **Chapter 3** with the state vector, X, expressed as:

$$X = \begin{bmatrix} \Delta P_s \\ \Delta P_d \\ Q_{in} \end{bmatrix} \tag{5.4}$$

Clearly, successful results are obtained provided that non-evolving uncertain model parameters are well-estimated and fixed prior to data assimilation (**Figure 5.7**). For the context of data assimilation experiments, we also presented the result of "Free-run".

Given the results of the synthetic case, we developed a two-step approach to follow the behaviour of Q_{in} in real time: (1) We apply a Bayesian-based inversion through the Markov Chain Monte Carlo (MCMC) algorithm to first constrain the non-evolving uncertain model parameters (e.g. $a_d, H_d, C, \Delta\rho, \Delta P_{d_{t_0}}$) and obtain a prior distribution for Q_{in} using only the initial part of the 2011 post-eruptive dataset. (2) Then we implement the Ensemble Kalman Filter (Evensen [2003]) as a data assimilation technique, following the strategy developed in **Chapter 3** using the entire 2011 post-eruptive radial data until before the rifting event.

Step 1: Bayesian-based inversion. We performed a Bayesian-based inversion using the Markov Chain Monte Carlo (MCMC) algorithm. In MCMC, uncertain model parameters independently drawn from given a priori distributions are constrained by accepting model predictions that better fit observations and by randomly accepting those that do not fit to avoid being trapped to a local minima (Segall [2013]). In particular, we built our approach using the PyMC2 python module. The classic linear inverse problem is described as:

$$D = \mathcal{G}(m) + \epsilon \tag{5.5}$$

where D is the vector of observation or data, $\mathcal{G}$ is the forward model, m is a vector of the uncertain model parameters and ϵ is the observation error. In our case, $m = [a_d, H_d, C, \Delta\rho, \Delta P_{d_{t_0}}, Q_{in}]$, D is the 2011 post-eruptive GPS dataset (we only use the radial displacement component up to $t_{step} = 409$ d) and $\mathcal{G}$ is the analytical solution (**Chapter 3**) to the forward model described in equations (5.2) and (5.3).

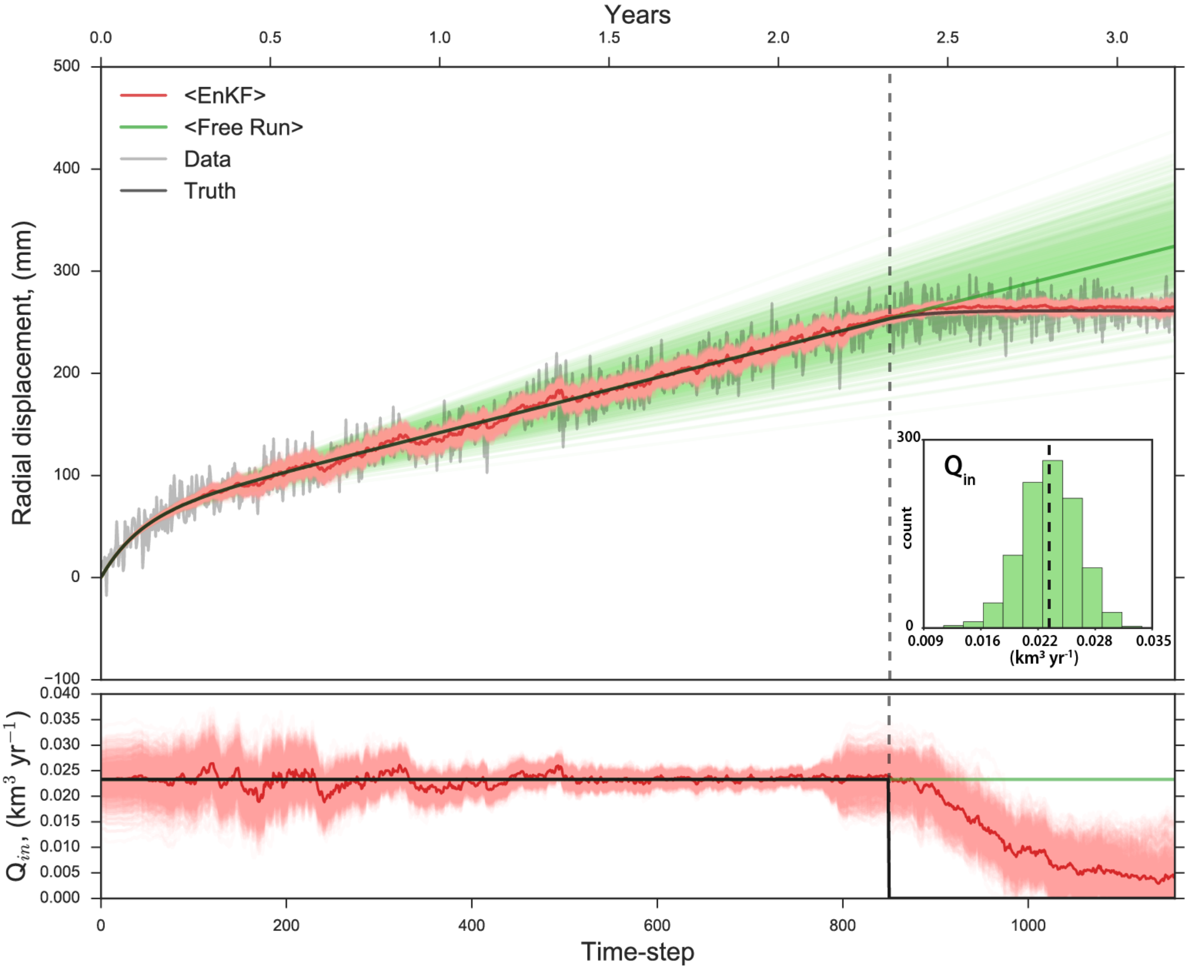

Figure 5.7: EnKF synthetic test to track sudden change in Q_{in} value. The true behavior of the system is the black solid line. The radial displacement data used for the EnKF is in gray. The result of free running the forward model is in green (the darker green is the mean and the lighter green lines are the ensemble members of the model state), whereas the EnKF result is in red (dark red is the mean value and the lighter red color are the ensemble members of the model state). The vertical black broken lines mark the change of slope (i.e. 875 d). Note that the prior distribution of Q_{in} used for the assimilation is also presented.

In the Bayesian framework, the posterior probability associated with m is sampled based on a likelihood function, $P(D|m)$, that calculates how well the data fits the model and a prior knowledge about the uncertain model parameters, $P(m)$:

$$P(m|D) \propto P(D|m)P(m) \tag{5.6}$$

Note that the errors in the resulting posterior distributions are only related to the observation error and uncertainties of the prior distribution of m. Any error related to how the model, $\mathcal{G}$, represents the reality is not taken into account. Such that in the case of a time-varying parameter, this approach is not the optimal strategy to use.

We first scale m and then we compute for the posterior distributions incorporating an Adaptive Metropolis (AM) step method. The latter is to avoid the problem of convergence due to possible “trade-offs” between the six uncertain model parameters. The AM method is a more intelligent way of fitting the parameters by block updating them using a multivariate jump distribution. We performed 2.0×10^5 individual samples with each calling the forward model $\mathcal{G}$. To make sure we converged to a good estimate and maintain no autocorrelation, half of the samples are burned and the remaining samples are thinned by a factor of 100 such that we end up by having 1000 samples. Because of the simplicity of the forward model, it only took around 30 minutes to simultaneously obtain the posterior distributions of the uncertain model parameters.

From the constructed posterior distribution, we pick the set of best-fit parameters by computing the misfit relative to the data points within the time frame we used during the inversion (dotted green box in **Figure 5.9**).

Step 2: Data assimilation. We closely followed the strategy developed in **Chapter 3** to assimilate geodetic data into a forward dynamical model. A step-by-step data assimilation strategy using EnKF is presented in **Figure C.2**. The assimilation is divided into two steps: 1) the forecast step and 2) the update step (or analysis). The forecast step is the part where an N-ensemble of models (i.e. $N = 1000$) are generated using the forward dynamical model given a previous or prior distribution of the state vector, X:

$$X^f_{t_{i+1}} = \mathcal{M} X^a_{t_i} + q_{t_i} \tag{5.7}$$

f and a: denote the forecast and analysis, respectively, $\mathcal{M}$: the model operator that relates the system from time t_i to t_{i+1} and q: the model error. **Equation 5.7** is fully expressed as:

$$\begin{bmatrix} \Delta P_{s_{t_{i+1}}} \\ \Delta P_{d_{t_{i+1}}} \\ Q_{in_{t_{i+1}}} \end{bmatrix} = \begin{bmatrix} 1 - C_1\Delta t & C_1\Delta t & 0 \\ C_1C_2\Delta t & 1 - C_1C_2\Delta t & 0 \\ 0 & 0 & 1 \end{bmatrix} \begin{bmatrix} \Delta P_{s_{t_i}} \\ \Delta P_{d_{t_i}} \\ Q_{in_{t_i}} \end{bmatrix} + \begin{bmatrix} C_1A_1\Delta t \\ (A_2 - C_1C_2A_1)\Delta t \\ 0 \end{bmatrix} \tag{5.8}$$

where $C_1 = \frac{3\pi E {a_c}^4}{128(1-\nu^2)\mu H_c {a_s}^3}$, $A_1 = (\rho_r - \rho_m)gH_c + (\Delta P_{d_{t_0}} - \Delta P_{s_{t_0}})$, $A_2 = \frac{3EQ_{in}}{16(1-\nu^2){a_d}^3}$ and $C_2 = \frac{{a_s}^3}{{a_d}^3}$. Note that the model operator has the form, $\mathcal{M} = \begin{bmatrix} 1 - C_1\Delta t & C_1\Delta t & 0 \\ C_1C_2\Delta t & 1 - C_1C_2\Delta t & 0 \\ 0 & 0 & 1 \end{bmatrix}$.

The assimilation interval is set to $\Delta t = 1$ day and we expect to have GPS data every day (i.e. frequency of observation, $f_{obs} = 1$). A Gaussian prior for the uncertain model parameter is required by EnKF to achieve an unbiased and optimal estimate. However, to ensure that the predicted value is within the correct physical boundaries, we redefine the distribution of Q_{in} (expressed in km^3 yr^{-1}) prior to the implementation of EnKF to a truncated Gaussian distribution with the mean centered on its best-fit value obtained from the inversion, the standard deviation is set to ~ 0.003 km^3 yr^{-1} and the upper and lower limits are fixed to $[a = 0, b = 0.19]$ (see **Figure 5.9C**).

In the context of data assimilation, ΔP_s and ΔP_d are called state variables because they are directly linked to the observations, while Q_{in} is termed as an uncertain model parameter and is only updated by the covariance between it and the state variables during the update step. We scaled the forecast state vector, X^f, (i.e. 10^7 and 10^{-1} for the overpressures and Q_{in}, respectively) and then we imposed an inflation factor, $\rho_{infl} = 0.05$ (i.e. $X^f = (1 + \rho_{infl})X^f$, see **Chapter 3**) if the standard deviation of Q_{in} at t_{i+1} falls below its standard deviation at t_0. The latter is to prevent the ensemble from collapsing to a single value and also to help the filter to track the value of the time-varying parameter, Q_{in}.

Once observation is available, X^f is updated by computing the Kalman Gain, K, (**equation 3.8**) and then applying the update equation,

$$X^a = X^f + K(D - \mathcal{H}X^f) \tag{5.9}$$

to obtain the vector of analysis, X^a. Note that the value of Q_{in} remains unchanged if there is no observation. Since we only use the radial component of the displacement time series, we define the observation operator, $\mathcal{H} = \begin{bmatrix} \Gamma D_s r & \Gamma D_d r & 0 \end{bmatrix}$, such that:

$$D_{t_i} = u_{R_{t_i}} = \begin{bmatrix} \Gamma D_s r & \Gamma D_d r & 0 \end{bmatrix} \begin{bmatrix} \Delta P_{s_{t_i}} \\ \Delta P_{d_{t_i}} \\ Q_{in_{t_i}} \end{bmatrix} + \epsilon_{t_i} \tag{5.10}$$

where $\Gamma = \frac{8(1-\nu^2)}{\pi E}$, $D_s = \frac{H_s^2 a_s^3}{R_s^5}$, $D_d = \frac{H_d^2 a_d{}^3}{R_d^5}$ and r is the distance of GFUM GPS station from the center of the volcanic system (e.g. 3.5 ± 0.2 km). Lastly, we use an observation error covariance, $R = \mathcal{E}(\epsilon\epsilon^T) = (0.015 \text{ m})^2$.

5.5 Results

The best-fit values of the uncertain model parameters after step 1 are summarized in **Table 5.4** and are also marked as green lines in **Figure 5.8**. Despite the non-uniqueness, these values are consistent with the data, physics of the model and results of previous studies (e.g. Hreinsdóttir *et al.* [2014], Reverso *et al.* [2014], Haddadi *et al.* [2017]).

If no observation is used to correct the dynamical model, the result is called the "Free-run" (**Figure 5.9**) where the model is only propagated forward in time. Obviously, if the model is almost a perfect representation of the observations wherein the model parameters are well-constrained and remain constant in time as in the case of the initial part of our dataset, we expect to have a good fit with the radial dataset. Note that although we only use radial displacement data within the dotted green box in **Figure 5.9** for the inversion, the inferred best-fit values of the uncertain model parameters are able to match the dataset for the radial component up to $t_{step} = 545$ d and appear to be consistent with the vertical component (**Figure 5.10**). It is unclear though if $t_{step} = 545$ d marks an episode of a true decrease in magma inflow rate or is just a part of some transient noise that affected the dataset. The latter case would require a lower value of Q_{in} at $t_{step} = 0$ to fit the time series up to our assumed change of slope using the forward model.

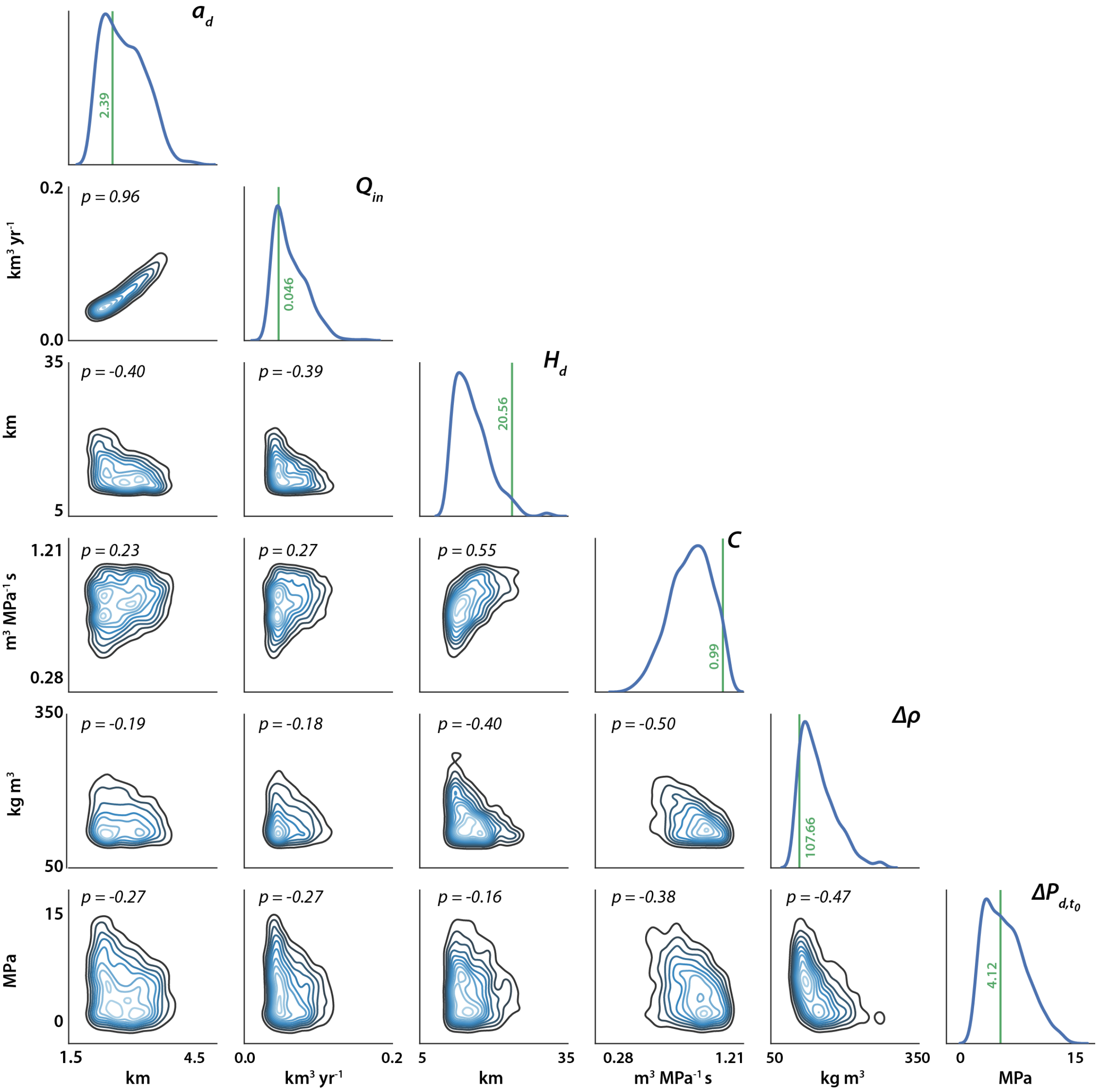

Figure 5.8: Posterior probability density functions (PDF) of the uncertain model parameters after MCMC inversion (step 1). The marginal PDF for each uncertain parameter is shown in the diagonal histogram plots. The green vertical lines with numbers indicate the best-fit values of the parameters. The off-diagonal contour plots are the joint kernel-density estimate between pairs of parameters with their corresponding Pearson correlation coefficients. A p-value close to ±1 implies strong correlation between the parameters.

Table 5.4: Best-fit values of the uncertain model parameters obtained from the MCMC posterior distribution (**Figure 5.8**). Except for Q_{in} (highlighted), all the other parameters are considered constant in time and are fixed to their values during data assimilation. Estimates from previous works are also presented.(Fixed parameters are: E=25 GPa, $\nu = 0.25$, $H_s = 1.7$ km, $a_s = 2$ km)

Parameters	Prior Condition	**Estimated Values**	
		This study	Prev. Studies
Geometry			
a_d (km), radius of the deep reservoir.	$\mathcal{N}(2.2, 2.52, [2.0, 6.0])$	2.39	< 10 Reverso *et al.* [2014]
H_d (km), depth of the deep reservoir.	*U(10, 40)*	20.56	10-35 Reverso *et al.* [2014]; 10-20 Haddadi *et al.* [2017]
Physics			
$\Delta\rho = \rho_r - \rho_m$ (kg m^{-3}), density contrast.	U(100, 300)	107.66	
C (m^3 MPa^{-1} s^{-1}), characteristic of the hydraulic connection, $C = \frac{a_c^4}{\mu H_c}$, where a_c is the radius of the conduit, μ is the viscosity and $H_c = H_d - H_s$ is the height of the hydraulic connection.	*U(0.01, 2.35)*	0.99	
Basal condition			
Q_{in} (km^3 yr^{-1}), deep magma inflow rate.	U(0.0, 0.19)	0.046	0.01-0.05 Reverso *et al.* [2014]
Initial condition			
$\Delta P_{d_{t_0}}$ (MPa), initial value of the overpressure in the deep reservoir.	U(0, 20)	4.12	

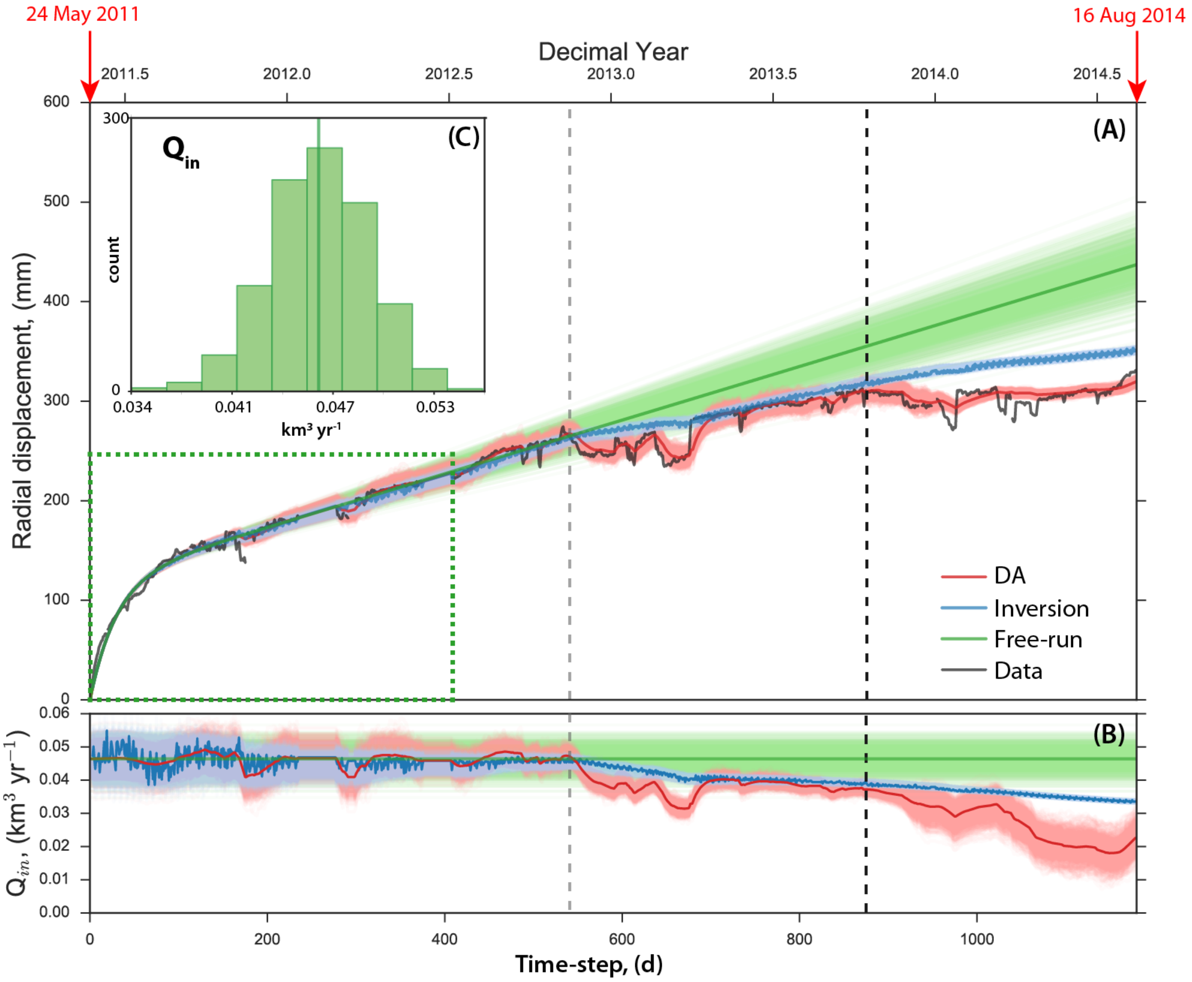

Figure 5.9: Data-fits and Q_{in} estimates. (A) The entire 2011 post-eruptive dataset used in this study (black) and the resulting data-fits by: 1) solely free-running the dynamical model (green), 2) performing MCMC based on a classical inversion approach/setup (blue), and 3) data assimilation via EnKF (red). The green dotted box covers the dataset used to estimate the non-evolving uncertain parameters (step 1). The robustness of each approach is depicted on how it fits the radial displacement dataset which clearly favors the EnKF method. (B) Estimated value of the magma inflow rate, Q_{in}, as a function of time using: the free-run (green), EnKF (red) and MCMC (blue). Note that the gray and black broken lines (**Figure 5.9A** and **5.9B**) correspond to the points where a decreasing trend in Q_{in}, tracked via EnKF, are observed. (C) The distribution of Q_{in} used as a prior information for the free-run, the data assimilation and the inversion.

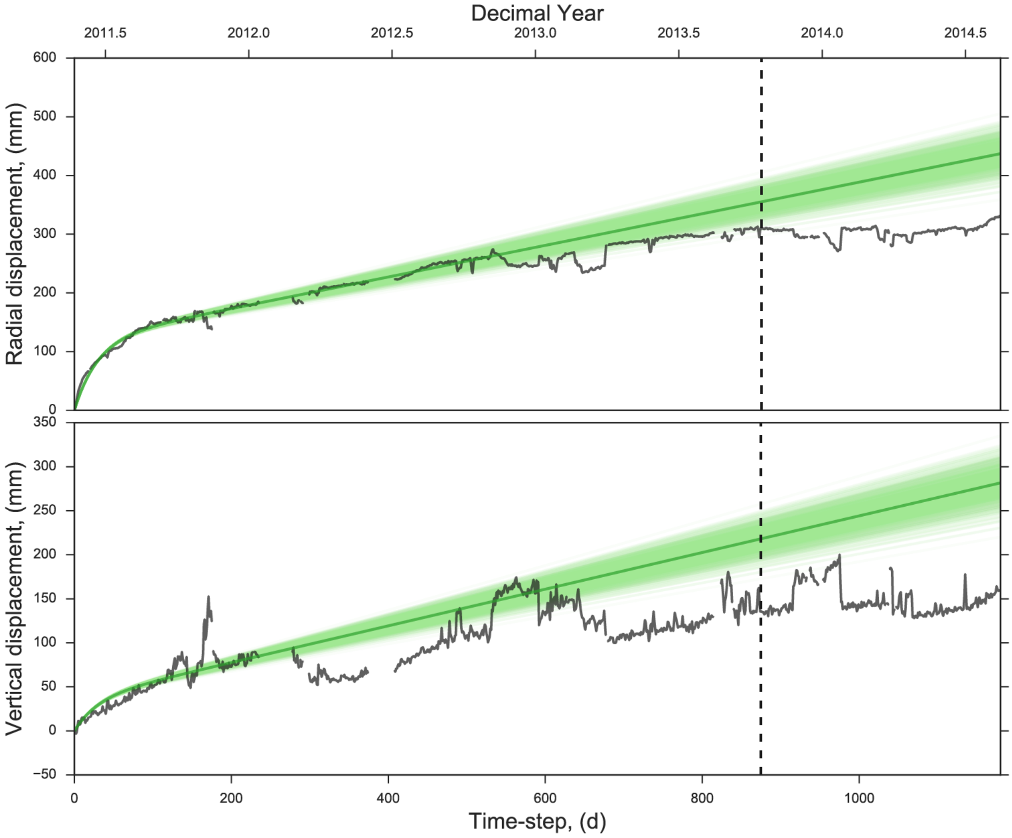

Figure 5.10: Data fit (green) using the MCMC-derived values of the uncertain model parameters as inputs to the forward model. The actual data are represented by gray solid lines. Note that the vertical component is not corrected either for GIA or seasonal effects. The black broken line marks the assumed change of slope preceding the start of the 2014 rifting event ($t_{step} = 875$ d).

The assimilation of radial displacement using the strategy that we have developed not only results to a robust fit to the entire dataset but also enables us to follow closely the decreasing trend of Q_{in} (**Figure 5.9**). We obtain a minimum rate of 0.007 km^3 yr^{-1} from the ensemble of Q_{in} estimates which corresponds to a drop of 0.039 km^3 yr^{-1} (85% decrease) relative to its prior value.

Bayesian-based inversion vs. data assimilation

Another interesting result is that if we follow the similar approach to track Q_{in} by first fixing non-evolving uncertain parameters, but use an inversion approach (i.e. MCMC) as a second step instead of data assimilation, we find that MCMC was able to slightly detect the change in Q_{in} but the resulting fit with the data is not satisfying (**Figure 5.9**). The main difference comes from the fact that with MCMC, we invert at each given time step all the observations that are previously acquired considering an effective constant value of Q_{in} over the whole period (i.e. integral analytic formula). Whereas with the assimilation strategy, we apply the differential equation between each time step such considering an evolving magma supply rate, Q_{in}.

In classic inversion setup, the model used to interpret the data is assumed “perfect”. In that case, the source of error is often only attributed to the data, whether due to perturbation in acquisition, instrument noise, data pre-processing or sum of these errors. However, in reality, models are embedded with noise and are oversimplified representations of the complex system that we observe. In **Chapter 3**, we illustrated through synthetic case that if the dynamical model used well-explains the observed data time series and that there is no transient change in the uncertain model parameters (i.e. they are constant through time), both data assimilation through EnKF and inversion via MCMC can track the state variables (i.e. overpressures within the reservoirs) and also estimate the true values of the uncertain model parameters (i.e. basal magma inflow rate and radius of the deep reservoir).

However, if the uncertain model parameter varies through time, such as the case of Q_{in} in this study, EnKF is then most useful. In EnKF, the model error covariance, $P = \overline{(X - \overline{X})(X - \overline{X})^T}$, computed from a large number of perturbations of uncertain model parameters (Q_{in} for example) is an approximation of the real model error. In practice, we use a large ensemble of models to represent the model error. Furthermore, by using a multiplicative inflation (**Chapter 2**) which is a tuning step in data assimilation, underestimated model errors related to external process in EnKF and/or unaccounted source of model error are compensated.

The influence of the set of uncertain model parameters as prior input to EnKF

Note that the set of best-fit values summarized in **Table 5.4** and illustrated in **Figure 5.8** is only one of the many solutions that could satisfy the observed displacement we used for the inversion. The non-uniqueness of the solution is a consequence of the poor spatial resolution of the dataset since we only have one GPS station at Grímsvötn with six uncertain model parameters to infer. However, our main goal is not to find a unique solution to our inverse problem rather to obtain values that are consistent with the data, physics of the model and results of previous studies (e.g. Hreinsdóttir *et al.* [2014], Reverso *et al.* [2014], Haddadi *et al.* [2017]) such that we can fix the non-evolving ones and follow the variation of Q_{in}.

To ensure that the decrease in Q_{in} is a true episode after our assumed change of slope and is not influenced by the set of values that we fixed, we run two independent cases of data assimilation. We perform similar inversion procedure described in the **section 5.4** (i.e. bayesian-based inversion) to obtain the two other set of priors that we tested. In the first case, we obtain a set of values for the six uncertain model parameters using the 2004 post-eruptive radial dataset. In the second case, we assume that a_d, H_d and $\Delta\rho$ are constant from one eruption to another so we adopted their values from case 1 and then recalculated Q_{in}, C and $\Delta P_{d,t_0}$ using only the initial part of the 2011 radial displacement time series. **Figure 5.11** clearly shows that regardless of the set of prior values used as inputs to the EnKF scheme, a sudden drop in the magma inflow rate is evident after the observed change of slope, $\sim$ 10 months before the rifting event.

5.6 Implications of the change in magma supply rate at Grímsvötn

The estimated decrease of the magma supply rate measured at Grímsvötn corresponds to a mimimum deficit of 0.016 km^3 of magma for the Grímsvötn plumbing system when

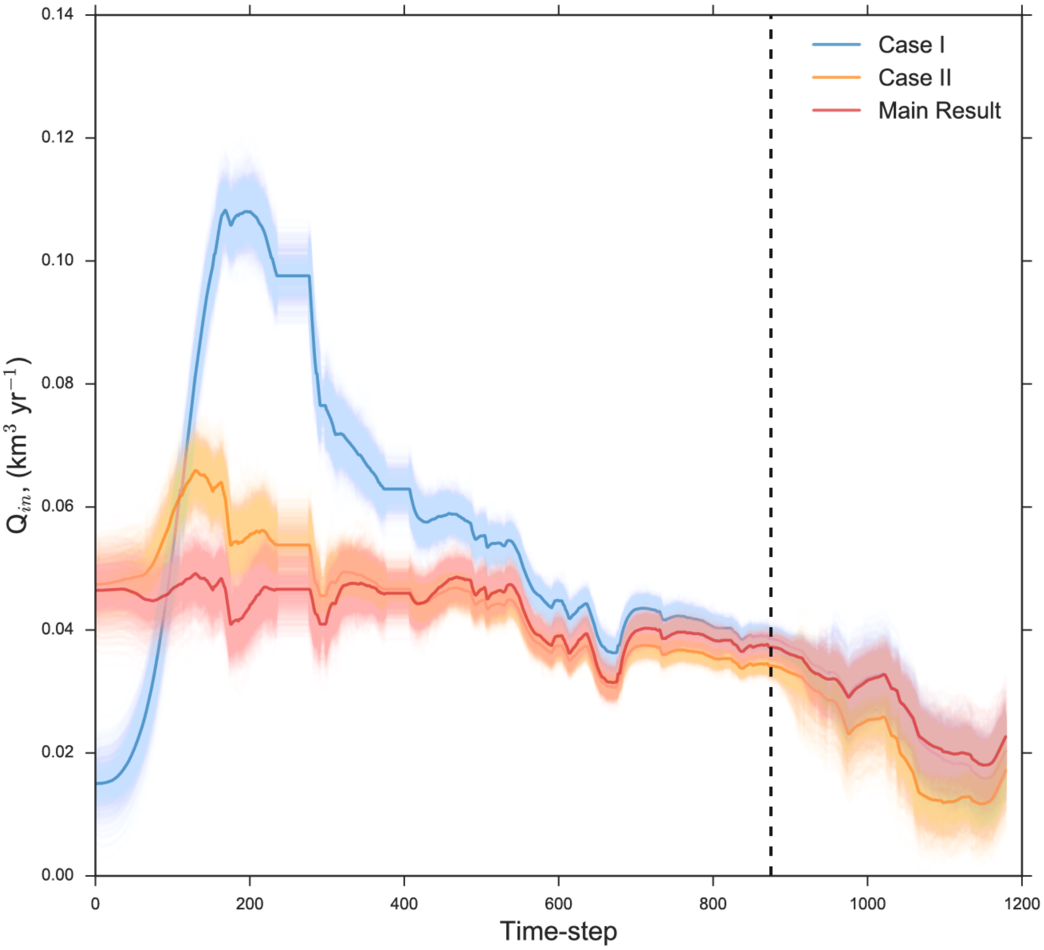

Figure 5.11: Testing different sets of uncertain model parameters as prior inputs to EnKF to track the evolution of Q_{in}. Case I: The values of the 6 uncertain parameters are derived using the entire 2004 post-eruptive radial dataset. Case II: Values of a_d, H_d and $\Delta\rho$ from Case I are adopted, whereas the remaining 3 uncertain parameters are determined by inverting the initial part of the 2011 post-eruptive radial dataset. Case III (Main result discussed in the paper): The 6 uncertain model parameters are estimated using the initial part of the 2011 post-eruptive radial dataset. The black broken line marks the assumed change of slope before the start of the 2014 rifting event ($t_{step} = 875$ d).

during the same period, magma accumulation is expected at Bárdarbunga (Gudmundsson *et al.* [2016]). A similar anti-correlated behavior has previously been observed between Kilauea and Mauna Loa based on their eruptive activities, however characterized by isotopically different magmas (Gonnermann *et al.* [2012]). It was then interpreted as due to stress transfer over the 35 km distance separating the two systems through pore-pressure variations in a thin asthenospheric melt accumulation layer. Connections between volcanic systems have also been evidenced by geodetic observations previously but only for systems spaced less than 10 km apart (Biggs *et al.* [2016]). Mechanisms invoked to explain nearby volcanic systems interactions include stress changes, lateral hydraulic connections and a common asthenospheric magma supply as for the Hawaiian case. In the Grímsvötn-Bárdarbunga case, we can exclude the stress change effect due to the large distance separating the two systems (Biggs *et al.* [2016]). Two possible scenarios caused the decrease in magma supply to Grímsvötn between October 2013 and August 2014 **(Figure 5.12)**: 1) the magma that feeds Grímsvötn's mid-crustal reservoir at $\sim$ 20 km depth was transported toward Bárdarbunga's volcanic system through an existing deep fracture, and 2) there was a drop in the relative pressure difference between Grímsvötn's mid-crustal reservoir and a much deeper reservoir shared by Bárdarbunga and Grímsvötn at more than 20 km depth.

For the first case, we estimate a minimum of 0.016 km^3 of magma that flowed toward Bárdarbunga's magmatic system assuming that the magma is an incompressible fluid. Although this is only $\sim 4-20\%$ of the estimated 2014 dyke intrusion (Sigmundsson *et al.* [2015], Gudmundsson *et al.* [2016]), the volume of transported magma could be enough to trigger a magmatic reservoir rupture beneath Bárdarbunga and initiate magma propagation from the storage zone. It is possible, provided that this storage zone was already in a pressurized stage before this additional magma inflow. Note that the true volume may be largely underestimated due to magma compressibility (Poland *et al.* [2012], Rivalta et Segall [2008]) and also due to the lack of spatial information having only one GPS point that we can exploit at Grímsvötn. Our synthetic case shows the ability of sequential assimilation to detect the sudden change in Q_{in} however, the convergence to the true value may require some time (**Figure 5.7**). An argument against this scenario is that no increase of deep seismicity was recorded during the 10 months preceding the rifting event. Deep seismicity rather indicates a continuous vertical rise of magma 12 km to the south-east of Bárdarbunga caldera (Hudson *et al.* [2017]).

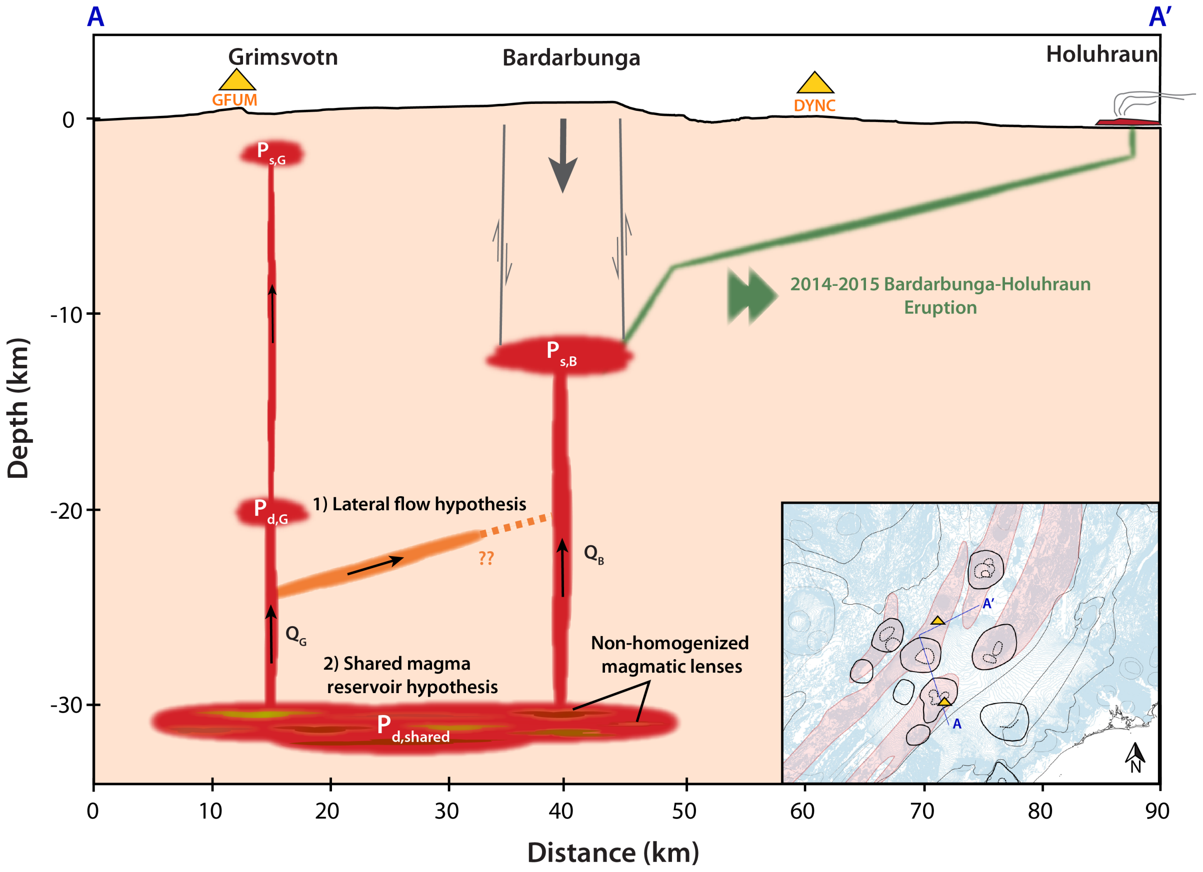

Figure 5.12: Proposed schematic cross-section beneath Grímsvötn and Bárdarbunga illustrating the two possible deep mechanism connecting the two volcanic systems: 1) lateral flow hypothesis and 2) magma reservoir hypothesis. GFUM and DYNC GPS stations are represented as yellow triangles. The link between Bárdarbunga and Holuhraun during the 2014-2015 eruption (green sketch) is shown after Gudmundsson *et al.* [2016]; however it does not follow the cross-section path in the inset figure.

For case 2, assuming that the ascent of magma from a deep source to an upper magma chamber (**Figure 5.12**) follows a Poiseuille flow (Pinel et Jaupart [2003]), a drop in the pressure between the common reservoir of Grímsvötn and Bárdarbunga ($P_{d,shared}$) and the mid-crustal reservoir of Grímsvötn ($P_{d,G}$) will decrease the magma inflow rate toward the latter (Q_G). The sudden pressure drop is due to the withdrawal of a large amount of magma in the shared reservoir ($P_{d,shared}$) that may have been caused by the activation or reactivation of a connection between Bárdarbunga ($P_{s,B}$) and the shared ($P_{d,shared}$) reservoirs. Bjarnason [2008] estimated the mantle-crust boundary in Iceland to be at $\sim$ 30 km depth. This mantle-crust boundary is a suitable place for the accumulation of melt which can be the source of magma for both Grímsvötn (Haddadi *et al.* [2017]) and Bárdarbunga's magmatic systems (Hartley *et al.* [2018]). As Grímsvötn and Bardabunga basalts have distinct isotopic signatures, the term of "shared reservoir" has to be considered as a magmatic domain sharing a mechanical connection, by pore pressure for instance, and containing different and non-homogenized magma lenses.

We provide evidences of magma inflow beneath Bárdarbunga starting at least 10 months before the dyke rifting initiation. We consequently argue that a strong interplay between the surge in magma supply on a pressurized source and the rifting episode favored the rupture of Bárdarbunga's magma chamber, rather than the reduction of the minimum principal compressive stress linked to rifting alone as proposed by Coppola *et al.* [2017]. Bárdarbunga's location, being on top of Iceland's mantle plume and in a rift zone, makes it a suitable place for the interplay. Subsequently, the withdrawal of magma and the gradual collapse of the caldera are both responsible to sustain the eruption for up to $\sim$ 6 months(Gudmundsson *et al.* [2016]).

5.7 Lessons learned

Although geodetic observations have greatly improved over the last decades, our ability to infer the characteristics of the deep systems underlying volcanoes remains a great challenge up to now. On one hand, we do not have a direct observation of the plumbing system beneath volcanoes such that we only infer their characteristics based on ground surface measurements, thus only an oversimplified representation of their complex nature is possible. On the other hand, model-data fusion techniques applied to inverse problems in volcanology have remained under the assumption of a "perfect" model therefore largely ignoring errors related to the representation of the dynamics of the real system. In the case of estimating a parameter that varies through time, this results to an incorrect knowledge about the parameter's true behavior as we have shown previously when classical static inversion was used to track the time-varying Q_{in}.

The advantage of using sequential data assimilation over a classic bayesian-based inversion method to follow the evolution of the deep magma supply rate is clear and represents a first successful application of EnKF in volcanology. Our framework is simple, but it help us better understand subsurface processes occurring between magmatic reservoirs (e.g. Grímsvötn and Bárdarbunga). We thus demonstrate that in addition to the interest of predicting volcanic eruptions (Bato *et al.* [2017]), sequential assimilation of geodetic data based on a dynamical model has a real and unique potential to give insights into the deep plumbing system of volcanoes and evolution of bottom conditions though time.

The sudden decrease of magma supply to Grímsvötn between 2013 and 2014 was a transient phenomenon caused by the accumulation of magma beneath Bárdarbunga's reservoir. The absence of such similar event based on previous post-eruptive displacement patterns at Grímsvötn suggests that the observed shift is an unusual event. After the 2014 rifting episode, radial displacement pattern at GFUM GPS station began increasing again, following a positive linear trend (**Figure 5.3**). However, it is difficult to analyze the displacements after August 2014 due to the mix contributions of viscoelastic relaxation caused by the rifting, the migration of the dyke and volcanic deformation related to Grímsvötn's activity alone. We suggest a strong interplay between surge in magma supply at Bárdarbunga and the rifting episode that triggered the 2014-2015 eruptive activity which was subsequently followed by gradual caldera collapse resulting to a $\sim$ 6-month long eruption. This transient reduction of magma supply rate at Grímsvötn could postpone the next eruption, increasing the duration of the inter-eruptive period (see **Chapter 4**).

Acknowledgements

This study was supported by CNES through the TOSCA project AssimSAR. We thank Freysteinn Sigmundsson for his valuable comments on this work.

Author contributions

All the authors contributed to the conceptualization and design of the study. MB and VP wrote the manuscript with assistance from the others. MB performed the data assimilation, inversion and detailed analyses in collaboration with VP and YY. VP and JV contributed to the analyses and volcanological point-of-view. YY helped in the implementation of data assimilation. FJ processed the GPS data.

Additional Information

The authors declare that they have no competing interests.

Chapter 6

General conclusions and future directions

6.1 Summary and contributions

"What [else] can data assimilation bring new to the volcano community?"

—this is the big question that I posed at the introductory part of this thesis. As the manuscript comes to an end, let me summarize the contributions of this thesis:

In **Chapter 3**, I presented two synthetic cases where I successfully demonstrated the potential of EnKF to follow the behavior of the A) state variables alone (i.e. state estimation) and simultaneously estimate both B) the state variables and uncertain model parameters (i.e. state-parameter estimation). Strategies in order to appropriately assimilate GNSS and InSAR data are also discussed. Indeed, there is no surprise that GNSS data have good temporal resolution whereas InSAR data have good spatial resolution and assimilating them jointly yields optimal results in terms of both determining the true values of the state variables and uncertain parameters of our model. Furthermore, bayesian-based inversion such as MCMC when compared to EnKF showed similar robust performance. Although, MCMC was able to converge faster than EnKF when estimating uncertain model parameters that are assumed constant in time. One significant advantage of EnKF over MCMC [at this point], is that EnKF only uses incoming data which is less expensive in terms of computational cost than MCMC.

In **Chapter 4**, I demonstrated the application of sequentially assimilating GNSS data recorded at Grímsvötn volcano in Iceland via EnKF in order to forecast the failure of a magma chamber that will initiate dyke propagation which may eventually lead to an eruption. The strategy implemented in this chapter is slightly modified in order to adapt to our main problem—there is only one GNSS station at Grímsvötn, however we have six uncertain parameters to constrain; five of which are considered non-evolving parameters. Basically, we jointly used MCMC and EnKF such that we can estimate only the overpressures and the basal magma inflow rate, Q_{in}, since the latter is considered as a parameter that may or may not vary in time. The approach is tested for the 2004-2011 inter-eruptive dataset, aiming to provide real-time forecast up to the 2011 Grímsvötn euption. The concept of "eruption zones" was introduced in this chapter as well as the probability of the magma chamber to rupture at each time step, estimated as the percentage of model ensembles that exceeded their failure overpressure values initially assigned following a Gaussian distribution. It is important to note that bayesian-based inversion, MCMC can provide the same results as that of EnKF (i.e. in terms of estimating the overpressures and Q_{in}) confirming the findings based on synthetic test in **Chapter 3**. However, I would like to reiterate that in terms of real-time forecasting, EnKF may be more advantageous in terms of computational cost. In this chapter, forecasts are provided in the form of "[Given that an eruption is imminent when the probability of rupture reaches p], an eruption might occur within the next N_{min}^{max} days". Succesful results based on $p = 25 \pm 1\%$ are obtained with the last three days prior to the 2011 eruption even indicating [a minimum forecast of] "zero days to eruption". When the strategy is further extended using the 2011 post-eruptive dataset, findings show that just before the 2014 rifting event, Grímsvötn's shallow magma chamber was already at the critical stage of rupturing and could have erupted in 2015. However, no eruption has occurred up to now which suggests that a transient event may have happened and postponed Grímsvötn's supposed eruption. This hypothesis is further confirmed in the subsequent chapter. Furthermore, one of the important contributions of this work is that, for the first time, information about the evolution of the [shallow] overpressure is achievable in real-time which can be used not only to evaluate the possible failure of a magma chamber but also as an initial input to dyke propagation models to assess whether or not the migrating magma would end up as an intrusion or rather, an eruption.

In **Chapter 5**, I went beyond volcanic eruption forecasting and showcased the capability of EnKF to track parameter/s that can suddenly fluctuate in time—in this case, the basal magma inflow rate. This is difficult to follow with MCMC in a classic inversion framework, hence, EnKF has a significant advantage over MCMC not only in terms of computational cost but also in terms of tracking sudden change in the behavior of an uncertain model parameter. In a volcanological point-of-view, this is more than detecting transient events. We are able to estimate that the basal magma inflow beneath Grímsvötn dropped up to 85% during the 10 months preceding the initiation of the Bárdarbunga rifting event. We provided evidences and arguments that can support our claim. The loss of at least 0.016 km^3 in the magma supply of Grímsvötn is interpreted as a consequence of magma accumulation beneath Bárdarbunga and subsequent feeding of the Holuhraun eruption 41 km away. This transient event might have postponed Grímsvötn's supposed eruption in 2015 as inferred in **Chapter 4**.

6.2 Future directions

Despite the important advancements in our understanding of volcanoes, there are many more processes occurring beneath the Earth that are yet to be unraveled. In fact, at the moment, I think that there are a lot more things about volcanic processes that we don't know rather than we know. Volcanoes are indeed complex systems, and slight changes in system properties could actually result to sudden failure, hence, some systems may be inherently unpredictable (Sparks *et al.* [2012]).

Thanks to data assimilation, its remarkable potentials (e.g. follow transient processes) can open a whole new lot of perspectives in addressing current challenges in volcanology. Although, I believe that three years of a PhD is not enough to cover all the capabilities of data assimilation, particularly, EnKF. Below, I outline some suggestions for the future directions of this work.

6.2.1 Data assimilation

The EnKF approach that has been proposed here is based on the stochastic EnKF (e.g. Burgers *et al.* [1998], Evensen [2003]), wherein I randomly perturb the observations prior to the analysis step in order to avoid an underestimation of the analysis error covariance, however it may induce additional source of sampling errors (Whitaker et Hamill [2002], Kalnay [2010]). A much deterministic EnKF approach that produces analysis mean and covariance which can satisfy the Kalman Filter equations is the family of ensemble square root filters which has not been explored in this thesis and should be considered in future works.

Also a much accurate procedure in implementing the inflation (i.e. tuning step in ensemble filters to avoid filter divergence) can be implemented in the future by using an adaptive inflation algorithm (e.g. hierarchical Bayesian approach, Anderson [2007]). In this inflation approach, observations are used to adjust the ensemble filter estimate of the state in order to determine the appropriate values of covariance inflation rather than empirically adjusting the inflation factor through additive or multiplicative inflation.

6.2.2 Dynamical Model

The model that I explored in this thesis is based solely on Reverso *et al.* [2014]'s two-chamber model. Indeed, in **Chapter 5**, I have mentioned that although EnKF can account for model errors that can be related to the misrepresentation of the true state of the system, there are also other models that can explain the same temporal evolution of the dataset. However, we have definitely strong arguments that support the model that we used (e.g. 1) the fluctuation of Q_{in} has not been observed during the previous eruptive cycle, 2) it seems to be transient and 3) occurs simultaneously with a rifting event mobilizing a large volume of magma in a close volcanic system). Some of the other models consider only one reservoir fed by a deep and constant pressure source with additional complexity in the encasing medium rheology (i.e. damage, viscoelastic behavior (Got *et al.* [2017], Segall [2016])) and/or in the magma properties (i.e. crystallisation, degassing, compressibility (Caricchi *et al.* [2014], Segall [2016])). At the moment, there is no way to distinguish which is the "true" model that represents the volcanic system but additonal observations such as gravity data might be useful to discriminate between the presence of a deeper pressure source (i.e. deep reservoir) and the effects of the crustal and magmatic rheological properties. It will therefore be interesting to test other models in order to compare the results to what we have so far explained in this work.

Furthermore, the genericness of the two-magma chamber model should be tested to other basaltic volcanoes having either one or multiple reservoir systems. The two-magma chamber model should be able to distinguish between the two latter cases. Having one reservoir means that the basal magma inflow rate is almost zero and that the radius of the deep reservoir is infinitely large. For multiple reservoirs, Reverso *et al.* [2014]'s model can only represent the upper part of the system. Moreover, I agree that the two-magma chamber model involves several assumptions that simplify the problem and there is indeed a need to develop physics-based models that could be more realistic in nature and can incorporate diverse observations (e.g. Anderson et Segall [2011], Anderson et Segall [2013], Wong *et al.* [2017]).

Also, beyond understanding the properties of deep magmatic reservoirs and the emplacement of magma at shallow depths, we have yet to explore data assimilation to other volcanic processes such as dyke propagation models which is much important in eruption forecasting since dyke propagation models are used to predict the exact timing and location of an impending eruption (Pinel *et al.* [2017]).

6.2.3 Other datasets

It has long been recognized the need to use various datasets and combine them with realistic physics-based dynamical models (Sparks [2003], Segall [2013]) to give us more constraints. One notable feature of data assimilation is that any data can be used, provided that there is a link between the data and the dynamical model which is basically described by the operator $\mathcal{H}$. In data-driven machine learning such as neural network, predictions can be made through a "black box" which can definitely approximate a certain function describing a system but won't necessarily provide any insights on what is happening within it.

In this thesis, I have only explored deformation datasets. In particular, for the real-case applications, I have only used GNSS data. When exploiting InSAR data, there are a lot more things to be tested such as the way we have to define the observation covariance error (i.e. which may have spatio-temporally correlated noise embedded within the signal), as well as, the subsampling of InSAR data prior to assimilation. Furthermore, there is also a "quality check" that needs to be considered as we cannot use all the observations available at each time step as input to the data assimilation algorithm especially if the signal-to-noise ratio is very low. All these have yet to be explored through synthetic tests and real-case dataset.

Fifteen years ago, Sparks [2003] has already discussed about data assimilation methods and bayesian updates as tools that would improve our forecasting models. He further mentioned, as I quote,

"What is likely to happen in the next decades is the development of ensemble models, which make volcanic forecasts that take account of both uncertainties and nonlinear dynamics."

It is astonishing how this "prediction" slowly unfolds.

All in all, there is indeed much more work to be done! But the future is getting more exciting for all of us working in the field of eruption forecasting and as I always say, I could not wait for the day that we can deliver eruption warnings the same way meteorologists are capable in providing weather reports nowadays.

Bibliography

Albino, F., Amelung, F. et Gregg, P. (2018). The role of pore fluid pressure on the failure of magma reservoirs: Insights from Indonesian and Aleutian arc volcanoes. *Journal of Geophysical Research: Solid Earth*, 123(2):1328–1349.

Albino, F., Pinel, V. et Sigmundsson, F. (2010). Influence of surface load variations on eruption likelihood: Application to two Icelandic subglacial volcanoes, Grímsvötn and Katla. *Geophysical Journal International*, 181(3):1510–1524.

Alfaro, R., Brandsdóttir, B., Rowlands, D. P., White, R. S. et Gudmundsson, M. T. (2007). Structure of the Grímsvötn central volcano under the Vatnajökull icecap, Iceland. *Geophysical Journal International*, 168(2):863–876.

Allard, P., Carbonnelle, J., Metrich, N., Loyer, H. et Zettwoog, P. (1994). Sulphur output and magma degassing budget of Stromboli volcano. *Nature*, 368(6469): 326.

Amoruso, A. et Crescentini, L. (2009). Shape and volume change of pressurized ellipsoidal cavities from deformation and seismic data. *Journal of Geophysical Research: Solid Earth*, 114(B2).

Anderson, J. L. (2007). An adaptive covariance inflation error correction algorithm for ensemble filters. *Tellus A*, 59(2):210–224.

Anderson, K. et Segall, P. (2011). Physics-based models of ground deformation and extrusion rate at effusively erupting volcanoes. *Journal of Geophysical Research: Solid Earth*, 116(B7).

Anderson, K. et Segall, P. (2013). Bayesian inversion of data from effusive volcanic eruptions using physics-based models: Application to Mount St. Helens 2004–2008. *Journal of Geophysical Research: Solid Earth*, 118(5):2017–2037.

Anderson, K. R. et Poland, M. P. (2017). Abundant carbon in the mantle beneath Hawaii. *Nature Geoscience*, 10(9):704.

Aoki, Y., Segall, P., Kato, T., Cervelli, P. et Shimada, S. (1999). Imaging magma transport during the 1997 seismic swarm off the Izu Peninsula, Japan. *Science*, 286(5441):927–930.

Aspinall, W. P. et Woo, G. (2014). Santorini unrest 2011-2012: An immediate bayesian belief network analysis of eruption scenario probabilities for urgent decision support under uncertainty. *Journal of Applied Volcanology*, 3(1):12.

Auriac, a., Sigmundsson, F., Hooper, a., Spaans, K. H., Björnsson, H., Pálsson, F., Pinel, V. et Feigl, K. L. (2014). InSAR observations and models of crustal deformation due to a glacial surge in Iceland. *Geophys. J. Int.*, 198:1329–1341.

Bagnardi, M. et Amelung, F. (2012). Space-geodetic evidence for multiple magma reservoirs and subvolcanic lateral intrusions at Fernandina Volcano, Galápagos Islands. *Journal of Geophysical Research: Solid Earth*, 117(B10).

Barbu, A., Calvet, J.-C., Mahfouf, J.-F., Albergel, C. et Lafont, S. (2011). Assimilation of Soil Wetness Index and Leaf Area Index into the ISBA-A-gs land surface model: grassland case study. *Biogeosciences*, 8(7):1971–1986.

Barth, A., Yan, Y., Alvera-Azcárate, A. et Beckers, J.-M. (2016). Local ensemble assimilation scheme with global constraints and conservation. *Ocean Dynamics*, 66(12): 1651–1664.

Bartlow, N. M., Wallace, L. M., Beavan, R. J., Bannister, S. et Segall, P. (2014). Time-dependent modeling of slow slip events and associated seismicity and tremor at the Hikurangi subduction zone, New Zealand. *Journal of Geophysical Research: Solid Earth*, 119(1):734–753.

Bato, M., Froger, J., Harris, A. et Villeneuve, N. (2016). Monitoring an effusive eruption at Piton de la Fournaise using radar and thermal infrared remote sensing data: insights into the October 2010 eruption and its lava flows. *Geological Society, London, Special Publications*, 426(1):533–552.

Bato, M. G., Pinel, V. et Yan, Y. (2017). Assimilation of deformation data for eruption forecasting: Potentiality assessment based on synthetic cases. *Frontiers in Earth Science*, 5:48.

Bekaert, D., Segall, P., Wright, T. et Hooper, A. (2016). A Network Inversion Filter combining GNSS and InSAR for tectonic slip modeling. *Journal of Geophysical Research: Solid Earth.*

Berardino, P., Fornaro, G., Lanari, R. et Sansosti, E. (2002). A new algorithm for surface deformation monitoring based on small baseline differential SAR interferograms. *IEEE Transactions on Geoscience and Remote Sensing*, 40(11):2375–2383.

Biggs, J., Ebmeier, S., Aspinall, W., Lu, Z., Pritchard, M., Sparks, R. et Mather, T. (2014). Global link between deformation and volcanic eruption quantified by satellite imagery. *Nature communications*, 5:3471.

Biggs, J., Robertson, E. et Cashman, K. (2016). The lateral extent of volcanic interactions during unrest and eruption. *Nature Geoscience*, 9(4):308–311.

Bjarnason, I. T. (2008). An Iceland hotspot saga. *Jökull*, 58:3–16.

Björnsson, H. et Einarsson, P. (1990). Volcanoes beneath Vatnajökull, Iceland: Evidence from radio echo-sounding, earthquakes and jökulhlaups. *Jökull*, 40:147–168.

Blake, S. et Cortés, J. A. (2018). Forecasting deflation, intrusion and eruption at inflating volcanoes. *Earth and Planetary Science Letters*, 481:246–254.

Bocher, M., Fournier, A. et Coltice, N. (2018). Ensemble Kalman filter for the reconstruction of the Earth's mantle circulation. *Nonlinear Processes in Geophysics*, 25(1):99.

Bocquet, M. (2017). Introduction to the principles and methods of data assimilation in the geosciences.

Boué, A. (2015). *Data mining and volcanic eruption forcasting.* Thèse de doctorat, Grenoble Alpes.

Boué, A., Lesage, P., Cortés, G., Valette, B. et Reyes-Dávila, G. (2015). Real-time eruption forecasting using the material failure forecast method with a bayesian approach. *Journal of Geophysical Research: Solid Earth*, 120(4):2143–2161.

Brankart, J.-M., Ubelmann, C., Testut, C.-E., Cosme, E., Brasseur, P. et Verron, J. (2009). Efficient parameterization of the observation error covariance matrix for square root or ensemble kalman filters: application to ocean altimetry. *Monthly Weather Review*, 137(6):1908–1927.

Briole, P., Massonnet, D. et Delacourt, C. (1997). Post-eruptive deformation associated with the 1986-87 and 1989 lava flows of Etna detected by radar interferometry. *Geophysical Research Letters*, 24(1):37–40.

Burgers, G., Jan van Leeuwen, P. et Evensen, G. (1998). Analysis scheme in the ensemble Kalman filter. *Monthly weather review*, 126(6):1719–1724.

Cannavò, F., Camacho, A. G., González, P. J., Mattia, M., Puglisi, G. et Fernández, J. (2015). Real time tracking of magmatic intrusions by means of ground deformation modeling during volcanic crises. *Scientific reports*, 5:10970.

Caricchi, L., Biggs, J., Annen, C. et Ebmeier, S. (2014). The influence of cooling, crystallisation and re-melting on the interpretation of geodetic signals in volcanic systems. *Earth and Planetary Science Letters*, 388:166–174.

Carn, S., Clarisse, L. et Prata, A. (2016). Multi-decadal satellite measurements of global volcanic degassing. *Journal of Volcanology and Geothermal Research*, 311:99–134.

Carrier, A., Got, J.-l., Peltier, A., Ferrazzini, V., Staudacher, T., Kowalski, P. et Boissier, P. (2014). Journal of Geophysical Research : Solid Earth A damage model for volcanic edifices : Implications for edifice strength , magma pressure , and eruptive processes Special Section :. *J. Geophys. Res. Solid Earth*, pages 1–17.

Caya, A., Sun, J. et Snyder, C. (2005). A comparison between the 4DVAR and the ensemble Kalman filter techniques for radar data assimilation. *Monthly Weather Review*, 133(11):3081–3094.

Cayol, V. et Cornet, F. (1997). 3D mixed boundary elements for elastostatic deformation field analysis. *International journal of rock mechanics and mining sciences*, 34(2):275–287.

Chadwick, W. W., Jónsson, S., Geist, D. J., Poland, M., Johnson, D. J., Batt, S., Harpp, K. S. et Ruiz, A. (2011). The May 2005 eruption of Fernandina volcano, Galápagos: The first circumferential dike intrusion observed by GPS and InSAR. *Bulletin of volcanology*, 73(6):679–697.

Chen, Y., Oliver, D. S. *et al.* (2010). Ensemble-based closed-loop optimization applied to Brugge field. *SPE Reservoir Evaluation & Engineering*, 13(01):56–71.

Chen, Y., Remy, D., Froger, J.-L., Peltier, A., Villeneuve, N., Darrozes, J., Perfettini, H. et Bonvalot, S. (2017). Long-term ground displacement observations using InSAR and GNSS at Piton de la Fournaise volcano between 2009 and 2014. *Remote Sensing of Environment*, 194:230–247.

Clarke, D., Brenguier, F., Froger, J.-L., Shapiro, N., Peltier, A. et Staudacher, T. (2013). Timing of a large volcanic flank movement at Piton de la Fournaise Volcano using noise-based seismic monitoring and ground deformation measurements. *Geophysical Journal International*, 195(2):1132–1140.

Coppola, D., Ripepe, M., Laiolo, M. et Cigolini, C. (2017). Modelling satellite-derived magma discharge to explain caldera collapse. *Geology*, 45(6):523–526.

Cosme, E. (2017). Data assimilation based on estimation theory: Some fundamentals.

Daag, A. S., Tubianosa, B. S., Newhall, C., Tungol, N., Javier, D., Dolan, M., Delos Reyes, P., Arboleda, R., Martinez, M. et Regalado, T. (1996). Monitoring sulfur dioxide emission at mount pinatubo. *Fire and Mud: eruptions and lahars of Mount Pinatubo, Philippines*, pages 409–414.

Dach, R., Lutz, S., Walser, P. et Fridez, P. (2015). Bernese GNSS software version 5.2.

De Natale, G., Petrazzuoli, S. M. et Pingue, F. (1997). The effect of collapse structures on ground deformations in calderas. *Geophysical Research Letters*, 24(13): 1555–1558.

Delaney, P. et McTigue, D. (1994). Volume of magma accumulation or withdrawal estimated from surface uplift or subsidence, with application to the 1960 collapse of Kilauea Volcano. *Bulletin of Volcanology*, 56(6-7):417–424.

DeMets, C., Gordon, R. G. et Argus, D. F. (2010). Geologically current plate motions. *Geophysical Journal International*, 181(1):1–80.

Doin, M.-P., Guillaso, S., Jolivet, R., Lasserre, C., Lodge, F., Ducret, G. et Grandin, R. (2011). Presentation of the small baseline NSBAS processing chain on a case example: the Etna deformation monitoring from 2003 to 2010 using Envisat data. *In Proceedings of the Fringe Symposium*, pages 3434–3437. ES.

Dvorak, J. J. et Dzurisin, D. (1993). Variations in magma supply rate at Kilauea Volcano, Hawaii. *Journal of Geophysical Research: Solid Earth*, 98(B12):22255–22268.

Dzurisin, D. (2003). A comprehensive approach to monitoring volcano deformation as a window on the eruption cycle. *Reviews of Geophysics*, 41(1).

Ebmeier, S. K., Andrews, B. J., Araya, M. C., Arnold, D. W. D., Biggs, J., Cooper, C., Cottrell, E., Furtney, M., Hickey, J., Jay, J., Lloyd, R., Parker, A. L., Pritchard, M. E., Robertson, E., Venzke, E. et Williamson, J. L. (2018). Synthesis of global satellite observations of magmatic and volcanic deformation: Implications for volcano monitoring and the lateral extent of magmatic domains. *Journal of Applied Volcanology.*

Einarsson, P., Brandsdóttir, B., Gudmundsson, M. T., Björnsson, H., Grínvold, K. et Sigmundsson, F. (1997). Center of the Iceland hotspot experiences volcanic unrest. *Eos, Transactions American Geophysical Union*, 78(35):369–375.

Elsworth, D., Mattioli, G., Taron, J., Voight, B. et Herd, R. (2008). Implications of magma transfer between multiple reservoirs on eruption cycling. *Science*, 322(5899): 246–248.

Endo, E. T., Murray, T. L. et Power, J. A. (1996). A comparison of preeruption real-time seismic amplitude measurements for eruptions at Mount St. Helens, Redoubt Volcano, Mount Spurr, and Mount Pinatubo. *Fire and Mud*, pages 233–247.

Evensen, G. (1994). Sequential data assimilation with a nonlinear quasi-geostrophic model using monte carlo methods to forecast error statistics. *Journal of Geophysical Research: Oceans*, 99(C5):10143–10162.

Evensen, G. (2003). The Ensemble Kalman Filter: Theoretical formulation and practical implementation. *Ocean Dyn.*, 53(4):343–367.

Evensen, G. (2004). Sampling strategies and square root analysis schemes for the EnKF. *Ocean dynamics*, 54(6):539–560.

Evensen, G. (2009). *Data assimilation: the ensemble Kalman filter.* Springer Science & Business Media.

Ferretti, A., Fumagalli, A., Novali, F., Prati, C., Rocca, F. et Rucci, A. (2011). A new algorithm for processing interferometric data-stacks: SqueeSAR. *IEEE Transactions on Geoscience and Remote Sensing*, 49(9):3460–3470.

Fletcher, S. J. (2017). *Data Assimilation for the Geosciences: From Theory to Application.* Elsevier.

FORNARO, G., VERDE, S., REALE, D. et PAUCIULLO, A. (2015). CAESAR: An approach based on covariance matrix decomposition to improve multibaseline–multitemporal interferometric SAR processing. *IEEE Transactions on Geoscience and Remote Sensing*, 53(4):2050–2065.

FOURNIER, A., EYMIN, C. et ALBOUSSIERE, T. (2007). A case for variational geomagnetic data assimilation: Insights from a one-dimensional, nonlinear, and sparsely observed MHD system. *arXiv preprint arXiv:0705.1777*.

FOURNIER, A., HULOT, G., JAULT, D., KUANG, W., TANGBORN, A., GILLET, N., CANET, E., AUBERT, J. et LHUILLIER, F. (2010). An introduction to data assimilation and predictability in geomagnetism. *Space science reviews*, 155(1-4):247–291.

FOURNIER, T., FREYMUELLER, J. et CERVELLI, P. (2009). Tracking magma volume recovery at Okmok volcano using GPS and an unscented Kalman filter. *Journal of Geophysical Research: Solid Earth*, 114(B2).

FREYMUELLER, J. T., MURRAY, J. B., RYMER, H. et LOCKE, C. A. (2015). Ground deformation, gravity, and magnetics. *In The Encyclopedia of Volcanoes (Second Edition)*, pages 1101–1123. Elsevier.

FROGER, J.-L., FUKUSHIMA, Y., BRIOLE, P., STAUDACHER, T., SOURIOT, T. et VILLENEUVE, N. (2004). The deformation field of the August 2003 eruption at Piton de la Fournaise, Reunion Island, mapped by ASAR interferometry. *Geophysical research letters*, 31(14).

GEIR, N., JOHNSEN, L. M., AANONSEN, S. I., VEFRING, E. H. *et al.* (2003). Reservoir monitoring and continuous model updating using ensemble Kalman filter. *In SPE Annual Technical Conference and Exhibition*. Society of Petroleum Engineers.

GEIRSSON, H., LAFEMINA, P., ARNADOTTIR, T., STURKELL, E., SIGMUNDSSON, F., TRAVIS, M., SCHMIDT, P., LUND, B., HREINSDOTTIR, S. et BENNETT, R. (2012). Volcano deformation at active plate boundaries: Deep magma accumulation at Hekla volcano and plate boundary deformation in south Iceland. *Journal of Geophysical Research: Solid Earth*, 117(B11).

GILLET, N., BARROIS, O. et FINLAY, C. C. (2015). Stochastic forecasting of the geomagnetic field from the COV-OBS. x1 geomagnetic field model, and candidate models for IGRF-12. *Earth, Planets and Space*, 67(1):71.

Gonnermann, H. M., Foster, J. H., Poland, M., Wolfe, C. J., Brooks, B. A. et Miklius, A. (2012). Coupling at Mauna Loa and Kilauea by stress transfer in an asthenospheric melt layer. *Nature Geoscience*, 5(11):826–829.

Got, J.-L., Carrier, A., Marsan, D., Jouanne, F., Vogfjörd, K. et Villemin, T. (2017). An Analysis of the non-linear magma-edifice coupling at Grimsvötn volcano (Iceland). *Journal of Geophysical Research: Solid Earth.*

Grandin, R., Socquet, A., Jacques, E., Mazzoni, N., de Chabalier, J.-B. et King, G. (2010). Sequence of rifting in afar, manda-hararo rift, ethiopia, 2005–2009: Time-space evolution and interactions between dikes from interferometric synthetic aperture radar and static stress change modeling. *Journal of Geophysical Research: Solid Earth*, 115(B10).

Gregg, P. M. et Pettijohn, J. C. (2016). A multi-data stream assimilation framework for the assessment of volcanic unrest. *Journal of Volcanology and Geothermal Research*, 309:63–77.

Gresse, M., Vandemeulebrouck, J., Byrdina, S., Chiodini, G., Revil, A., Johnson, T. C., Ricci, T., Vilardo, G., Mangiacapra, A., Lebourg, T. *et al.* (2017). Three-Dimensional Electrical Resistivity Tomography of the Solfatara Crater (Italy): Implication for the Multiphase Flow Structure of the Shallow Hydrothermal System. *Journal of Geophysical Research: Solid Earth*, 122(11):8749–8768.

Grewal, M. S. et Andrews, A. P. (2008). Practical considerations. *Kalman Filtering, Third Edition, Third Edition*, pages 355–426.

Gu, Y., Oliver, D. S. *et al.* (2005). History matching of the PUNQ-S3 reservoir model using the ensemble Kalman filter. *SPE journal*, 10(02):217–224.

Gudmundsson, M. T., Jónsdóttir, K., Hooper, A., Holohan, E. P., Halldórsson, S. A., Ófeigsson, B. G., Cesca, S., Vogfjörd, K. S., Sigmundsson, F., Högnadóttir, T. *et al.* (2016). Gradual caldera collapse at Bárdarbunga volcano, Iceland, regulated by lateral magma outflow. *Science*, 353(6296).

Gudmundsson, M. T., Sigmundsson, F. et Björnsson, H. (1997). Ice–volcano interaction of the 1996 Gjálp subglacial eruption, Vatnajökull, Iceland. *Nature*, 389(6654):954–957.

Guldstrand, F., Galland, O., Hallot, E. et Burchardt, S. (2018). Experimental constraints on forecasting the location of volcanic eruptions from pre-eruptive surface deformation. *Frontiers in Earth Science*, 6:7.

Haddadi, B., Sigmarsson, O. et Larsen, G. (2017). Magma storage beneath Grímsvötn volcano, Iceland, constrained by clinopyroxene-melt thermobarometry and volatiles in melt inclusions and groundmass glass. *Journal of Geophysical Research: Solid Earth*.

Haimson, B. C. et Rummel, F. (1982). Hydrofracturing stress measurements in the Iceland research drilling project drill hole at Reydarfjordur, Iceland. *Journal of Geophysical Research: Solid Earth*, 87(B8):6631–6649.

Hamill, T. M., Whitaker, J. S. et Snyder, C. (2001). Distance-dependent filtering of background error covariance estimates in an ensemble Kalman filter. *Monthly Weather Review*, 129(11):2776–2790.

Hanssen, R. F. (2001). *Radar interferometry: data interpretation and error analysis*, volume 2. Springer Science & Business Media.

Harris, A. J., Dehn, J. et Calvari, S. (2007). Lava effusion rate definition and measurement: a review. *Bulletin of Volcanology*, 70(1):1.

Harris, A. J. et Stevenson, D. S. (1997). Magma budgets and steady-state activity of Vulcano and Stromboli. *Geophysical Research Letters*, 24(9):1043–1046.

Hartley, M. E., Bali, E., Maclennan, J., Neave, D. A. et Halldórsson, S. A. (2018). Melt inclusion constraints on petrogenesis of the 2014-2015 Holuhraun eruption, Iceland. *Contributions to Mineralogy and Petrology*, 173(2):10.

Hartley, M. E. et Thordarson, T. (2013). The 1874-1876 volcano-tectonic episode at Askja, North Iceland: Lateral flow revisited. *Geochemistry, Geophysics, Geosystems*, 14(7):2286–2309.

Hautmann, S., Witham, F., Christopher, T., Cole, P., Linde, A. T., Sacks, I. S. et Sparks, R. S. J. (2014). Strain field analysis on Montserrat (WI) as tool for assessing permeable flow paths in the magmatic system of Soufrière Hills Volcano. *Geochemistry, Geophysics, Geosystems*, 15(3):676–690.

Hincks, T. K., Komorowski, J.-C., Sparks, S. R. et Aspinall, W. P. (2014). Retrospective analysis of uncertain eruption precursors at La Soufrière volcano, Guadeloupe, 1975-77: volcanic hazard assessment using a Bayesian Belief Network approach. *Journal of Applied Volcanology*, 3(1):3.

Hooper, A., Bekaert, D., Spaans, K. et Arikan, M. (2012). Recent advances in SAR interferometry time series analysis for measuring crustal deformation. *Tectonophysics*, 514:1–13.

Hooper, A., Zebker, H., Segall, P. et Kampes, B. (2004). A new method for measuring deformation on volcanoes and other natural terrains using InSAR persistent scatterers. *Geophysical research letters*, 31(23).

Houtekamer, P. L. et Mitchell, H. L. (2001). A sequential ensemble Kalman Fillter for atmospheric data assimilation. *Monthly Weather Review*, 129(1):123–137.

Houtekamer, P. L. et Mitchell, H. L. (2005). Ensemble kalman filtering. *Quarterly Journal of the Royal Meteorological Society*, 131(613):3269–3289.

Hreinsdóttir, S., Sigmundsson, F., Roberts, M. J., Björnsson, H., Grapenthin, R., Arason, P., Árnadóttir, T., Hólmjárn, J., Geirsson, H., Bennett, R. A. *et al.* (2014). Volcanic plume height correlated with magma-pressure change at Grimsvotn Volcano, Iceland. *Nature geoscience*, 7(3):214–218.

Hudson, T. S., White, R. S., Greenfield, T., Ágústsdóttir, T., Brisbourne, A. et Green, R. G. (2017). Deep crustal melt plumbing of Bardarbunga volcano, Iceland. 44:8,785–8,794.

Hunt, B. R. (2005). An efficient implementation of the local ensemble Kalman filter. *Available from bhunt@ipst. umd. edu.*

Jarlan, L. et Boulet, G. (2014). Data assimilation for the monitoring of continental surfaces. *Remote Sensing Imagery*, pages 283–319.

Johnson, D. J., Sigmundsson, F. et Delaney, P. T. (2000). Comment on "Volume of magma accumulation or withdrawal estimated from surface uplift or subsidence, with application to the 1960 collapse of Kīlauea volcano" by PT Delaney and DF McTigue. *Bulletin of Volcanology*, 61(7):491–493.

Julier, S. J. et Uhlmann, J. K. (1997). A new extension of the kalman filter to nonlinear systems. *In Int. symp. aerospace/defense sensing, simul. and controls*, volume 3, pages 182–193. Orlando, FL.

JULIER, S. J. et UHLMANN, J. K. (2004). Unscented filtering and nonlinear estimation. *Proceedings of the IEEE*, 92(3):401–422.

KALMAN, R. E. (1960). A new approach to linear filtering and prediction problems. *Journal of basic Engineering*, 82(1):35–45.

KALNAY, E. (2010). Ensemble Kalman Filter: Current Status and Potential. *In* LAHOZ, W., KHATTATOV, B. et MENARD, R., éditeurs : *Data Assimilation: Making Sense Of Observations*. Berlin: Springer.

KARLSTROM, L., DUFEK, J. et MANGA, M. (2009). Organization of volcanic plumbing through magmatic lensing by magma chambers and volcanic loads. *Journal of Geophysical Research: Solid Earth*, 114(B10).

KILBURN, C. R., DE NATALE, G. et CARLINO, S. (2017). Progressive approach to eruption at Campi Flegrei caldera in southern Italy. *Nature communications*, 8:15312.

KUANG, W., WEI, Z., HOLME, R. et TANGBORN, A. (2010). Prediction of geomagnetic field with data assimilation: a candidate secular variation model for IGRF-11. *Earth, planets and space*, 62(10):775–785.

LAHOZ, W., KHATTATOV, B. et MENARD, R. (2010). *Data assimilation: making sense of observations*. Springer Science & Business Media.

LANDMAELINGAR ISLANDS (1995). Landsat mynd í náttúrulegum litum (B,G,R) 30m greinihæfni.

LANDMAELINGAR ISLANDS (2015). Landsat-8 mosaic af Íslandi 2014.

LARSEN, G., GUDMUNDSSON, M. et BJORNSSON, H. (1998). Eight centuries of periodic volcanism at the center of the Iceland hotspot revealed by glacier tephrostratigraphy. *Geology*, 26(10):943–946.

LE DIMET, F.-X. et TALAGRAND, O. (1986). Variational algorithms for analysis and assimilation of meteorological observations: theoretical aspects. *Tellus A: Dynamic Meteorology and Oceanography*, 38(2):97–110.

LENGLINÉ, O., MARSAN, D., GOT, J. L., THE, V., FERRAZZINI, V. et OKUBO, P. G. (2008). Seismicity and deformation induced by magma accumulation at three basaltic volcanoes. *J. Geophys. Res. Solid Earth*, 113:1–12.

Lesparre, N., Gibert, D., Marteau, J., Komorowski, J.-C., Nicollin, F. et Coutant, O. (2012). Density muon radiography of La Soufriere of Guadeloupe volcano: comparison with geological, electrical resistivity and gravity data. *Geophysical Journal International*, 190(2):1008–1019.

Lisowski, M. (2007). Analytical volcano deformation source models. *In Volcano Deformation*, pages 279–304. Springer.

Lorenc, A. (2003). Relative merits of 4d-var and ensemble kalman filter. Rapport technique, NWP Internal Report.

Lorentzen, R. J., Fjelde, K. K., Frøyen, J., Lage, A. C., Nævdal, G., Vefring, E. H. *et al.* (2001). Underbalanced and low-head drilling operations: Real time interpretation of measured data and operational support. *In SPE Annual Technical Conference and Exhibition*. Society of Petroleum Engineers.

Lu, Z. et Dzurisin, D. (2014). Role of ground surface deformation in volcano monitoring. *In InSAR Imaging of Aleutian Volcanoes*, pages 71–85. Springer.

Lu, Z., Masterlark, T., Dzurisin, D., Rykhus, R. et Wicks, C. (2003). Magma supply dynamics at Westdahl volcano, Alaska, modeled from satellite radar interferometry. *Journal of Geophysical Research: Solid Earth*, 108(B7).

Lu, Z., Wicks, C., Dzurisin, D., Thatcher, W., Freymueller, J. T., McNutt, S. R. et Mann, D. (2000). Aseismic inflation of Westdahl volcano, Alaska, revealed by satellite radar interferometry. *Geophysical Research Letters*, 27(11):1567–1570.

Marzocchi, W., Sandri, L. et Selva, J. (2008). BET_EF: a probabilistic tool for long-and short-term eruption forecasting. *Bulletin of Volcanology*, 70(5):623–632.

Massonnet, D. et Feigl, K. L. (1998). Radar interferometry and its application to changes in the Earth's surface. *Reviews of geophysics*, 36(4):441–500.

Mastin, L. G., Roeloffs, E., Beeler, N. M. et Quick, J. E. (2008). Constraints on the size, overpressure, and volatile content of the Mount St. Helens magma system from geodetic and dome-growth measurements during the 2004–2006+ eruption. *US Geol. Surv. Prof. Pap*, 1750:461–488.

McGuire, J. J. et Segall, P. (2003). Imaging of aseismic fault slip transients recorded by dense geodetic networks. *Geophysical Journal International*, 155(3):778–788.

McNutt, S. R., Rymer, H. et Stix, J. (2000). Synthesis of volcano monitoring.

McTigue, D. (1987). Elastic stress and deformation near a finite spherical magma body: resolution of the point source paradox. *Journal of Geophysical Research: Solid Earth*, 92(B12):12931–12940.

Melnik, O. et Sparks, R. (1999). Nonlinear dynamics of lava dome extrusion. *Nature*, 402(6757):37.

Melnik, O. et Sparks, R. (2002). Dynamics of magma ascent and lava extrusion at Soufriere Hills Volcano, Montserrat. *Geological Society, London, Memoirs*, 21(1):153–171.

Menand, T., Annen, C. et de Saint Blanquat, M. (2015). Rates of magma transfer in the crust: Insights into magma reservoir recharge and pluton growth. *Geology*, 43(3):199–202.

Miyoshi, T. (2005). *Ensemble Kalman filter experiments with a primitive-equation global model.* Thèse de doctorat.

Mogi, K. (1958). Relations between the eruptions of various volcanoes and the deformations of the ground surfaces around them. *Bulletin of the Earthquake Research Institute University of Tokyo*, 36:99–134.

NASA Landsat Program (2014). Landsat-8 scene LC82170152014249LGN01, L1G, USGS, Sioux Falls, 09/06/2014.

Neri, A., Aspinall, W. P., Cioni, R., Bertagnini, A., Baxter, P. J., Zuccaro, G., Andronico, D., Barsotti, S., Cole, P. D., Ongaro, T. E. *et al.* (2008). Developing an event tree for probabilistic hazard and risk assessment at Vesuvius. *Journal of volcanology and geothermal research*, 178(3):397–415.

Newhall, C. (2000). Volcano warnings. *Encyclopedia of volcanoes*, pages 1–185.

Newhall, C. (2007). Volcanology 101 for seismologists.

Newhall, C. et Hoblitt, R. (2002). Constructing event trees for volcanic crises. *Bulletin of Volcanology*, 64(1):3–20.

Nooner, S. L. et Chadwick, W. W. (2009). Volcanic inflation measured in the caldera of Axial Seamount: Implications for magma supply and future eruptions. *Geochemistry, Geophysics, Geosystems*, 10(2).

Nooner, S. L. et Chadwick, W. W. (2016). Inflation-predictable behavior and co-eruption deformation at Axial Seamount. *Science*, 354(6318):1399–1403.

Ostini, L., Dach, R., Meindl, M., Schaer, S. et Hugentobler, U. (2008). Fodits: A new tool of the BERNESE GPS software. *In Proceedings of EUREF 2008 Symposium, edited by Torres, JA, and H. Hornik, Brussels, Belgium.*

Pagli, C., Sigmundsson, F., Pedersen, R., Einarsson, P., Árnadóttir, T. et Feigl, K. L. (2007). Crustal deformation associated with the 1996 Gjálp subglacial eruption, Iceland: InSAR studies in affected areas adjacent to the Vatnajökull ice cap. *Earth and Planetary Science Letters*, 259(1):24–33.

Pallister, J. et McNutt, S. R. (2015). Synthesis of volcano monitoring. *In The Encyclopedia of Volcanoes (Second Edition)*, pages 1151–1171. Elsevier.

Parks, M. M., Biggs, J., England, P., Mather, T. A., Nomikou, P., Palamartchouk, K., Papanikolaou, X., Paradissis, D., Parsons, B., Pyle, D. M. *et al.* (2012). Evolution of Santorini Volcano dominated by episodic and rapid fluxes of melt from depth. *Nature Geoscience*, 5(10):749–754.

Peltier, A., Beauducel, F., Villeneuve, N., Ferrazzini, V., Di Muro, A., Aiuppa, A., Derrien, A., Jourde, K. et Taisne, B. (2016). Deep fluid transfer evidenced by surface deformation during the 2014–2015 unrest at Piton de la Fournaise volcano. *Journal of Volcanology and Geothermal Research*, 321:140–148.

Perissin, D. et Ferretti, A. (2007). Urban-target recognition by means of repeated spaceborne sar images. *IEEE Transactions on Geoscience and Remote Sensing*, 45(12):4043–4058.

PHIVOLCS (2018). Mayon volcano bulletin, 12 January 2018 8:00 A.M.

Pinel, V. (2015). Personal communications.

Pinel, V., Carrara, A., Maccaferri, F., Rivalta, E. et Corbi, F. (2017). A two-step model for dynamical dike propagation in two dimensions: Application to the July 2001 Etna eruption. *Journal of Geophysical Research: Solid Earth*, 122(2):1107–1125.

Pinel, V. et Jaupart, C. (2003). Magma chamber behavior beneath a volcanic edifice. *Journal of Geophysical Research: Solid Earth*, 108(B2).

Pinel, V., Jaupart, C. et Albino, F. (2010). On the relationship between cycles of eruptive activity and growth of a volcanic edifice. *Journal of Volcanology and Geothermal Research*, 194(4):150–164.

Pinel, V., Poland, M. P. et Hooper, A. (2014). Volcanology: Lessons learned from synthetic aperture radar imagery. *Journal of Volcanology and Geothermal Research*, 289:81–113.

Poland, M. P., Miklius, A., Sutton, A. J. et Thornber, C. R. (2012). A mantle-driven surge in magma suply to Kilauea Volcano during 2003-2007. 5:295–300.

Reichle, R. H., Koster, R. D., Liu, P., Mahanama, S. P., Njoku, E. G. et Owe, M. (2007). Comparison and assimilation of global soil moisture retrievals from the Advanced Microwave Scanning Radiometer for the Earth Observing System (AMSR-E) and the Scanning Multichannel Microwave Radiometer (SMMR). *Journal of Geophysical Research: Atmospheres*, 112(D9).

Reverso, T., Vandemeulebrouck, J., Jouanne, F., Pinel, V., Villemin, T., Sturkell, E. et Bascou, P. (2014). A two-magma chamber model as a source of deformation at Grímsvötn Volcano, Iceland. *J. Geophys. Res. Solid Earth*, 119:4666–4683.

Rivalta, E. et Segall, P. (2008). Magma compressibility and the missing source for some dike intrusions. *Geophysical Research Letters*, 35(4).

Rivalta, E., Taisne, B., Bunger, A. et Katz, R. (2015). A review of mechanical models of dike propagation: Schools of thought, results and future directions. *Tectonophysics*, 638:1–42.

Roult, G., Peltier, A., Taisne, B., Staudacher, T., Ferrazzini, V., Di Muro, A. *et al.* (2012). A new comprehensive classification of the Piton de la Fournaise activity spanning the 1985–2010 period. Search and analysis of short-term precursors from a broad-band seismological station. *Journal of Volcanology and Geothermal Research*, 241:78–104.

Ruggiero, G. A., Cosme, E., Brankart, J.-M., Le Sommer, J. et Ubelmann, C. (2016). An Efficient Way to Account for Observation Error Correlations in the Assimilation of Data from the Future SWOT High-Resolution Altimeter Mission. *Journal of Atmospheric and Oceanic Technology*, 33(12):2755–2768.

SAMIEI-ESFAHANY, S. et HANSSEN, R. F. (2013). New algorithm for InSAR stack phase triangulation using integer least squares estimation. *In Geoscience and Remote Sensing Symposium (IGARSS), 2013 IEEE International*, pages 884–887. IEEE.

SANCHEZ, S. (2016). *Assimilation of geomagnetic data into dynamo models: An archeomagnetic study.* Thèse de doctorat, IPGP, Université Sorbonne Paris Cité.

SEGALL, P. (2013). Volcano deformation and eruption forecasting. *Geological Society, London, Special Publications*, 380(1):85–106.

SEGALL, P. (2016). Repressurization following eruption from a magma chamber with a viscoelastic aureole. *Journal of Geophysical Research: Solid Earth.*

SEGALL, P. et MATTHEWS, M. (1997). Time dependent inversion of geodetic data. *Journal of Geophysical Research:*, 102:22–391.

SHIRZAEI, M. et WALTER, T. (2010). Time-dependent volcano source monitoring using interferometric synthetic aperture radar time series: A combined genetic algorithm and Kalman filter approach. *Journal of Geophysical Research: Solid Earth*, 115(B10).

SIGMARSSON, O., KARLSSON, H. et LARSEN, G. (2000). The 1996 and 1998 subglacial eruptions beneath the Vatnajökull ice sheet in Iceland: contrasting geochemical and geophysical inferences on magma migration. *Bulletin of Volcanology*, 61(7):468–476.

SIGMUNDSSON, F. (2006). *Iceland geodynamics: crustal deformation and divergent plate tectonics.* Springer Science & Business Media.

SIGMUNDSSON, F., HOOPER, A., HREINSDÓTTIR, S., VOGFJÖRD, K. S., ÓFEIGSSON, B. G., HEIMISSON, E. R., DUMONT, S., PARKS, M., SPAANS, K., GUDMUNDSSON, G. B. *et al.* (2015). Segmented lateral dyke growth in a rifting event at Bardarbunga volcanic system, Iceland. *Nature*, 517(7533):191–195.

SIMONS, M., FIALKO, Y. et RIVERA, L. (2002). Coseismic deformation from the 1999 Mw 7.1 Hector Mine, California, earthquake as inferred from InSAR and GPS observations. *Bulletin of the Seismological Society of America*, 92(4):1390–1402.

SPAANS, K., HREINSDÓTTIR, S., HOOPER, A. et ÓFEIGSSON, B. G. (2015). Crustal movements due to iceland's shrinking ice caps mimic magma inflow signal at katla volcano. *Scientific reports*, 5:10285.

Sparks, R. (2003). Forecasting volcanic eruptions. *Earth and Planetary Science Letters*, 210(1):1–15.

Sparks, R., Biggs, J. et Neuberg, J. (2012). Monitoring volcanoes. *Science*, 335(6074): 1310–1311.

Stix, J. et Gaonach, H. (2000). Gas, plume and thermal monitoring. *Encyclopedia of Volcanoes*, pages 1141–1165.

Sturkell, E., Einarsson, P., Sigmundsson, F., Geirsson, H., Olafsson, H., Pedersen, R., de Zeeuw-van Dalfsen, E., Linde, A. T., Sacks, S. I. et Stefánsson, R. (2006). Volcano geodesy and magma dynamics in Iceland. *Journal of Volcanology and Geothermal Research*, 150(1):14–34.

Sudhaus, H. et Sigurjón, J. (2009). Improved source modelling through combined use of InSAR and GPS under consideration of correlated data errors: application to the June 2000 Kleifarvatn earthquake, Iceland. *Geophysical Journal International*, 176(2):389–404.

Sutton, A. J., McGee, K. A., Casadevall, T. J. et Stokes, B. (1992). 18. fundamental volcanic-gas-study techniques: An integrated approach to monitoring. *Monitoring Volcanoes: Techniques and Strategies Used by the Staff of the Cascades Volcano Observatory, 1980-90*, (1966):181.

Swanson, D., Casadevall, T., Dzurisin, D., Malone, S., Newhall, C. et Weaver, C. (1983). Predicting eruptions at Mount St. Helens, June 1980 through December 1982. *Science*, 221(4618):1369–1376.

Talagrand, O. (1997). Assimilation of observations, an introduction. *Journal of the Meteorological Society of Japan. Ser. II*, 75(1B):191–209.

Talagrand, O. (2010). Data assimilation. *In* Lahoz, W., Khattatov, B. et Menard, R., éditeurs : *Data Assimilation: Making Sense Of Observations*. Berlin: Springer.

Talagrand, O. et Courtier, P. (1987). Variational assimilation of meteorological observations with the adjoint vorticity equation. i: Theory. *Quarterly Journal of the Royal Meteorological Society*, 113(478):1311–1328.

Tárraga, M., Carniel, R., Ortiz, R. et García, A. (2008). The failure forecast method: Review and application for the real-time detection of precursory patterns at reawakening volcanoes. *Developments in Volcanology*, 10:447–469.

TOULOUKIAN, Y. S. (1989). Physical properties of rocks and minerals. *CINDAS Data Series on Materials Properties*, (2):63–76.

TRIDON, M., CAYOL, V., FROGER, J.-L., AUGIER, A. et BACHÈLERY, P. (2016). Inversion of coeval shear and normal stress of Piton de la Fournaise flank displacement. *Journal of Geophysical Research: Solid Earth*, 121(11):7846–7866.

VADON, H. et SIGMUNDSSON, F. (1997). Crustal deformation from 1992 to 1995 at the Mid-Atlantic Ridge, southwest Iceland, mapped by satellite radar interferometry. *Science*, 275(5297):194–197.

VOGFJÖRD, K., JAKOBSDÓTTIR, S., GUDMUNDSSON, G., ROBERTS, M., ÁGÚSTSSON, K., ARASON, T., GEIRSSON, H., KARLSDÓTTIR, S., HJALTADÓTTIR, S., ÓLAFSDÓTTIR, U. *et al.* (2005). Forecasting and monitoring a subglacial eruption in Iceland. *Eos, Transactions American Geophysical Union*, 86(26):245–248.

VOIGHT, B. (1981). Time scale for the first moments of the May 18 eruption. *US Geol. Surv. Prof. Pap*, 1250:69–86.

VOIGHT, B. (1988). A method for prediction of volcanic eruptions. *Nature*, 332(6160):125.

VOIGHT, B., HOBLITT, R., CLARKE, A., LOCKHART, A., MILLER, A., LYNCH, L. et MCMAHON, J. (1998). Remarkable cyclic ground deformation monitored in real-time on Montserrat, and its use in eruption forecasting. *Geophysical Research Letters*, 25(18):3405–3408.

WAN, E. A. et VAN DER MERWE, R. (2000). The unscented kalman filter for nonlinear estimation. *In Adaptive Systems for Signal Processing, Communications, and Control Symposium 2000. AS-SPCC. The IEEE 2000*, pages 153–158. IEEE.

WEIS, D., GARCIA, M. O., RHODES, J. M., JELLINEK, M. et SCOATES, J. S. (2011). Role of the deep mantle in generating the compositional asymmetry of the Hawaiian mantle plume. *Nature Geoscience*, 4:831 EP –.

WHITAKER, J. S. et HAMILL, T. M. (2002). Ensemble data assimilation without perturbed observations. *Monthly Weather Review*, 130(7):1913–1924.

WOLFE, C. J., BJARNASON, I. T., VANDECAR, J. C. et SOLOMON, S. C. (1997). Seismic structure of the Iceland mantle plume. *Nature*, 385(6613):245.

Wong, Y.-Q., Segall, P., Bradley, A. et Anderson, K. (2017). Constraining the Magmatic System at Mount St. Helens (2004–2008) Using Bayesian Inversion With Physics-Based Models Including Gas Escape and Crystallization. *Journal of Geophysical Research: Solid Earth*, 122(10):7789–7812.

Wright, R., Flynn, L., Garbeil, H., Harris, A. et Pilger, E. (2002). Automated volcanic eruption detection using MODIS. *Remote sensing of environment*, 82(1):135–155.

Wright, R., Flynn, L. P., Garbeil, H., Harris, A. J. et Pilger, E. (2004). MODVOLC: near-real-time thermal monitoring of global volcanism. *Journal of Volcanology and Geothermal Research*, 135(1-2):29–49.

Wübbena, G. (1985). Software developments for geodetic positioning with gps using ti-4100 code and carrier measurements. *In Proceedings of the first international symposium on precise positioning with the global positioning system*, volume 19.

Yan, Y. (2011). *Fusion de mesures de déplacement issues d'imagerie SAR: Application aux modélisations séismo-volcaniques*. Thèse de doctorat, Université de Grenoble.

Yan, Y., Barth, A. et Beckers, J.-M. (2014). Comparison of different assimilation schemes in a sequential Kalman filter assimilation system. *Ocean Modelling*, 73:123–137.

Yan, Y., Barth, A., Beckers, J.-M., Candille, G., Brankart, J.-M. et Brasseur, P. (2015). Ensemble assimilation of argo temperature profile, sea surface temperature, and altimetric satellite data into an eddy permitting primitive equation model of the north atlantic ocean. *Journal of Geophysical Research: Oceans*, 120(7):5134–5157.

Yang, X.-M., Davis, P. M. et Dieterich, J. H. (1988). Deformation from inflation of a dipping finite prolate spheroid in an elastic half-space as a model for volcanic stressing. *Journal of Geophysical Research: Solid Earth*, 93(B5):4249–4257.

Zhan, Y. et Gregg, P. M. (2017). Data assimilation strategies for volcano geodesy. *Journal of Volcanology and Geothermal Research*, 344:13–25.

Zhan, Y., Gregg, P. M., Chaussard, E. et Aoki, Y. (2017). Sequential Assimilation of Volcanic Monitoring Data to Quantify Eruption Potential: Application to Kerinci Volcano, Sumatra.

Zoccarato, C., Baù, D., Ferronato, M., Gambolati, G., Alzraiee, A. et Teatini, P. (2016). Data assimilation of surface displacements to improve geomechanical parameters of gas storage reservoirs. *Journal of Geophysical Research: Solid Earth*.

Appendix A

Supplementary material: Chapter 3

A.1 The overpressures as state variables

The state vector, X, can be expressed as:

$$X = \begin{bmatrix} \Delta P_s \\ \Delta P_d \end{bmatrix} \tag{A.1}$$

where ΔP_s is the overpressure in the shallow reservoir and ΔP_d is the overpressure in the deep reservoir.

From equations (3.1) and (3.2), if we let, $C_1 = \frac{G{a_c}^4}{8\mu\gamma_s H_c {a_s}^3}$, $A_1 = (\rho_r - \rho_m)gH_c$, $A_2 = \frac{GQ_{in}}{\gamma_d \pi {a_d}^3}$ and $C_2 = \frac{\gamma_s {a_s}^3}{\gamma_d {a_d}^3}$, then we can write the dynamical model as:

$$\begin{bmatrix} \Delta P_{s_{t_{i+1}}} \\ \Delta P_{d_{t_{i+1}}} \end{bmatrix} = \begin{bmatrix} 1 - C_1\Delta t & C_1\Delta t \\ C_1C_2\Delta t & 1 - C_1C_2\Delta t \end{bmatrix} \begin{bmatrix} \Delta P_{s_{t_i}} \\ \Delta P_{d_{t_i}} \end{bmatrix} + \begin{bmatrix} C_1A_1\Delta t \\ (A_2 - C_1C_2A_1)\Delta t \end{bmatrix} \tag{A.2}$$

where the model operator, $\mathcal{M} = \begin{bmatrix} 1 - C_1\Delta t & C_1\Delta t \\ C_1C_2\Delta t & 1 - C_1C_2\Delta t \end{bmatrix}$.

The relationships of the surface displacements and the overpressures are described by equations (3.3) and 3.4, if we let $\Gamma = \frac{1-\nu}{G}$, $D_s = \alpha_s \frac{a_s^3}{R_s^3}$ and $D_d = \alpha_d \frac{{a_d}^3}{R_d^3}$, then we can rewrite them into a matrix of the form:

$$\begin{bmatrix} u_{R_{t_i}} \\ u_{z_{t_i}} \end{bmatrix} = \begin{bmatrix} \Gamma D_s r & \Gamma D_d r \\ \Gamma D_s H_s & \Gamma D_d H_d \end{bmatrix} \begin{bmatrix} \Delta P_{s_{t_i}} \\ \Delta P_{d_{t_i}} \end{bmatrix} \tag{A.3}$$

where the observation vector, $D = \begin{bmatrix} u_{R_{t_i}} \\ u_{z_{t_i}} \end{bmatrix}$ and the observation operator, $\mathcal{H} = \begin{bmatrix} \Gamma D_s r & \Gamma D_d r \\ \Gamma D_s H_s & \Gamma D_d H_d \end{bmatrix}$. Note that r are the GNSS locations of the observations (i.e. distance at the surface to the center of the volcanic system) and, H_s and H_d are the depths of the shallow and deep reservoirs, respectively (see Figure 3.1). The observation error covariance, $R = \begin{bmatrix} \sigma^2_{u_R} & 0 \\ 0 & \sigma^2_{u_z} \end{bmatrix}$, in which σ_{u_R} and σ_{u_z} are the typical GNSS instrument error values equal to 1 mm and 10 mm, respectively.

A.2 The overpressures and the uncertain parameters in the state vector

Let the state vector be expressed as:

$$X = \begin{bmatrix} \Delta P_s \\ \Delta P_d \\ a_d \\ Q_{in} \end{bmatrix} \tag{A.4}$$

where ΔP_s is the overpressure in the shallow reservoir, ΔP_d is the overpressure in the deep reservoir, a_d is the radius of the deep reservoir and Q_{in} is the basal magma inflow rate. We rewrite the dynamical model into matrix form, i.e.,

$$\begin{bmatrix} \Delta P_{s_{t_{i+1}}} \\ \Delta P_{d_{t_{i+1}}} \\ a_{d_{t_{i+1}}} \\ Q_{in_{t_{i+1}}} \end{bmatrix} = \begin{bmatrix} 1 - C_1 \Delta t & C_1 \Delta t & 0 & 0 \\ C_1 C_2 \Delta t & 1 - C_1 C_2 \Delta t & 0 & 0 \\ 0 & 0 & 1 & 0 \\ 0 & 0 & 0 & 1 \end{bmatrix} \begin{bmatrix} \Delta P_{s_{t_i}} \\ \Delta P_{d_{t_i}} \\ a_{d_{t_i}} \\ Q_{in_{t_i}} \end{bmatrix} + \begin{bmatrix} C_1 A_1 \Delta t \\ (A_2 - C_1 C_2 A_1) \Delta t \\ 0 \\ 0 \end{bmatrix} \tag{A.5}$$

such that the model operator is now $\mathcal{M} = \begin{bmatrix} 1-C_1\Delta t & C_1\Delta t & 0 & 0 \\ C_1C_2\Delta t & 1-C_1C_2\Delta t & 0 & 0 \\ 0 & 0 & 1 & 0 \\ 0 & 0 & 0 & 1 \end{bmatrix}$.

On the other hand, D and R will stay the same but the observation operator needs to be modified in order to be consistent with the equations. Hence, it should take the form, $\mathcal{H} = \begin{bmatrix} \Gamma D_s r & \Gamma D_d r & 0 & 0 \\ \Gamma D_s H_s & \Gamma D_d H_d & 0 & 0 \end{bmatrix}$.

Note however, that a_d is included within the observation operator, $\mathcal{H}$ which can add complexity to the assimilation process since a_d is treated as an uncertain model parameter. In simple terms, there is an additional source of error which comes from the observation operator that links the observations and the state vector. To incorporate this error in the assimilation process, we calculate for $\mathcal{H}$ at each time-step, t_{i+1}, and for each ensemble, n, by sampling from the distribution of a_d from the previous analysis step such that:

$$D_{t_{i+1}} = \mathcal{H}_{t_{i+1},n}[X^f_{t_{i+1},n}] \tag{A.6}$$

A.3 Deriving the $\mathcal{H}$ matrix for $u_{los,insar}$

Since we intend to perform state-parameter estimation, the state vector, X, can be expressed as:

$$X = \begin{bmatrix} \Delta P_s \\ \Delta P_d \\ a_d \\ Q_{in} \end{bmatrix} \tag{A.7}$$

where ΔP_s is the overpressure in the shallow reservoir and ΔP_d is the overpressure in the deep reservoir.

The displacement in the line-of-sight (LOS) is given by the following relationship

(Hanssen [2001]):

$$u_{los,insar} = \begin{bmatrix} sin\theta sin\phi & -sin\theta cos\phi & cos\theta \end{bmatrix} \begin{bmatrix} u_N \\ u_E \\ u_z \end{bmatrix} \tag{A.8}$$

where θ is the angle of incidence and ϕ is the track heading angle of the satellite.

Let $\Gamma = \frac{1-\nu}{G}$, $D_s = \alpha_s \frac{a_s^3}{R_s^3}$ and $D_d = \alpha_d \frac{{a_d}^3}{R_d^3}$. The surface displacements produced by a pressure point source embedded in an elastic medium (Lisowski [2007]) are given by:

$$\begin{bmatrix} u_N \\ u_E \\ u_z \end{bmatrix} = \begin{bmatrix} \Gamma D_s y & \Gamma D_d y & 0 & 0 \\ \Gamma D_s x & \Gamma D_d x & 0 & 0 \\ \Gamma D_s H_s & \Gamma D_d H_d & 0 & 0 \end{bmatrix} \begin{bmatrix} \Delta P_s \\ \Delta P_d \\ a_d \\ Q_{in} \end{bmatrix} \tag{A.9}$$

Let $U_1 = sin\theta sin\phi$, $U_2 = sin\theta cos\phi$ and $U_3 = cos\theta$. Using equations (A.8) and (A.9), we can derive the LOS displacement,

$$\begin{aligned} u_{los,insar} &= \begin{bmatrix} U_1 & -U_2 & U_3 \end{bmatrix} \begin{bmatrix} \Gamma D_s y & \Gamma D_d y & 0 & 0 \\ \Gamma D_s x & \Gamma D_d x & 0 & 0 \\ \Gamma D_s H_s & \Gamma D_d H_d & 0 & 0 \end{bmatrix} \begin{bmatrix} \Delta P_s \\ \Delta P_d \\ a_d \\ Q_{in} \end{bmatrix} \\ &= \begin{bmatrix} U_1 \Gamma D_s y - U_2 \Gamma D_s x + U_3 \Gamma D_s H_s & U_1 \Gamma D_d y - U_2 \Gamma D_d x + U_3 \Gamma D_d H_d & 0 & 0 \end{bmatrix} \begin{bmatrix} \Delta P_s \\ \Delta P_d \\ a_d \\ Q_{in} \end{bmatrix} \end{aligned} \tag{A.10}$$

Note that x and y are the map coordinates of the observations (i.e. GNSS locations) and, H_s and H_d are the depths of the shallow and deep reservoirs, respectively.

For the joint assimilation of GNSS and InSAR-los displacement, we can simply express the relationship between the state vector and the observation vector as:

$$\begin{bmatrix} u_{R,gnss} \\ u_{z,gnss} \\ u_{los,insar} \end{bmatrix} = \begin{bmatrix} \Gamma D_s r & \Gamma D_d r & 0 & 0 \\ \Gamma D_s H_s & \Gamma D_d H_d & 0 & 0 \\ U_1 \Gamma D_s y - U_2 \Gamma D_s x + U_3 \Gamma D_s H_s & U_1 \Gamma D_d y - U_2 \Gamma D_d x + U_3 \Gamma D_d H_d & 0 & 0 \end{bmatrix} \begin{bmatrix} \Delta P_s \\ \Delta P_d \\ a_d \\ Q_{in} \end{bmatrix} \tag{A.11}$$

where the observation operator, $\mathcal{H}$ is:

$$\mathcal{H} = \begin{bmatrix} \Gamma D_s r & \Gamma D_d r & 0 & 0 \\ \Gamma D_s H_s & \Gamma D_d H_d & 0 & 0 \\ U_1 \Gamma D_s y - U_2 \Gamma D_s x + U_3 \Gamma D_s H_s & U_1 \Gamma D_d y - U_2 \Gamma D_d x + U_3 \Gamma D_d H_d & 0 & 0 \end{bmatrix}$$

A.4 Joint Assimilation of GNSS and InSAR-in-LOS

The setup is somehow similar to the case where we jointly assimilated GNSS and InSAR radial and vertical displacements, except that in this case we only have InSAR in one direction—in the line-of-sight view. The InSAR-LOS displacement is an 11 x 11 grid, uniformly spaced every 1 km between -5 km to 5 km in x and y-axes that provides a total of 121 data points. The incidence angle (e.g. 33.44° for ascending and 37.53° for the descening pass) and the azimuth angle (e.g. $-12.27°$ for ascending and $-167.53°$ for the descending pass) that we defined to generate the synthetic LOS data are consistent with current satellite systems (i.e. in this case, the angles are similar to TerraSAR-X). We consider an observation error equal to 10 mm, similar to the observation error along the vertical component of GNSS since LOS data are more sensitive to the vertical direction. Figure A.1 shows an example of a synthetic InSAR-LOS displacement in (a) ascending and (b) descending orbital pass. GNSS observations are assimilated every 2 days, whereas the InSAR-LOS data are assimilated only every 12 days. Unlike in the previous joint-assimilation approach where we used a biased prior distribution for the uncertain parameters, here, the assimilation can only be successful if we use a prior distribution that is unbiased (i.e. uncertain parameters are well-constrained; similar to Figure 3C of the main manuscript) or a gaussian distribution that at least contains the true value of the uncertain parameters (i.e. Figure 15C of the article). Since there is no significant difference when ascending data is assimilated, here we only present the EnKF-predicted overpressures and uncertain parameters using descending InSAR data (Figure A.2), given that the a priori information about the uncertain parameters are similar to that of in Figure 15B. Results show that the true behavior of the overpressures can be well-recovered as well as the true values of the uncertain parameters.

Supplementary Figures

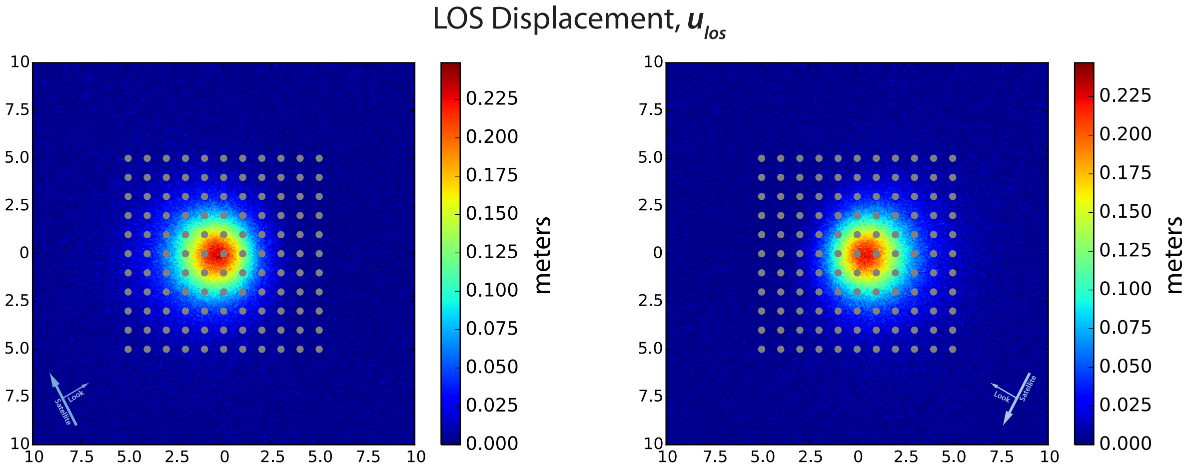

Figure A.1: An example of the InSAR displacement field at $t = 10$ in (a) ascending and (b) descending LOS view. The observation error is 10 mm. Note that the gray dots are the locations of the 121 observations used in the assimilation. The x and y-axes are in kilometers.

A) Estimated Overpressures

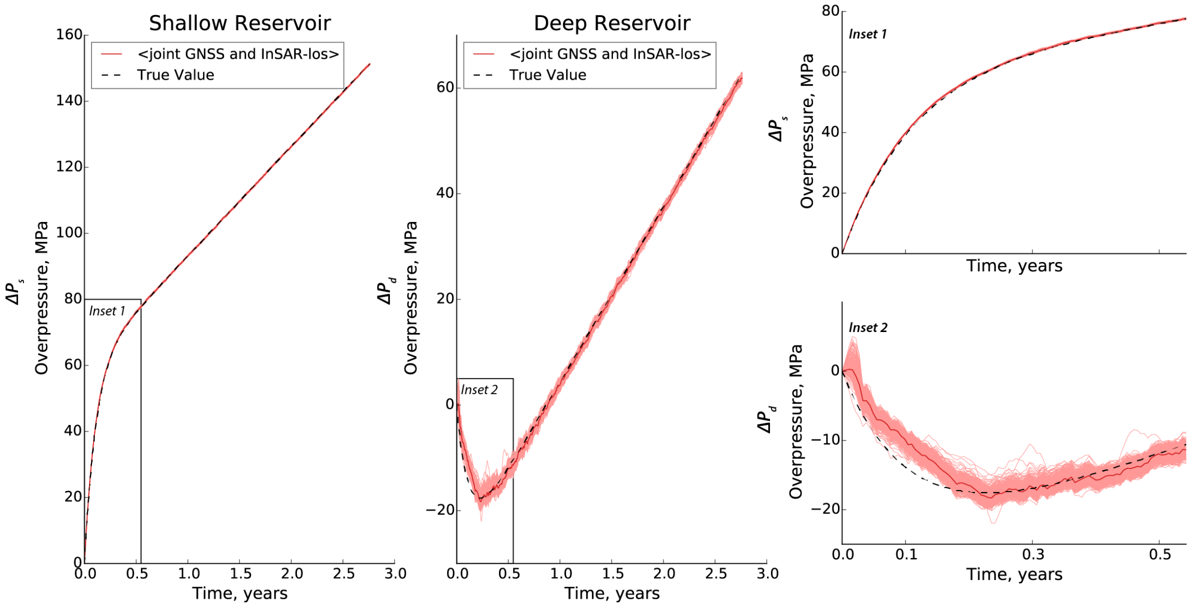

B) Estimated Uncertain Parameters

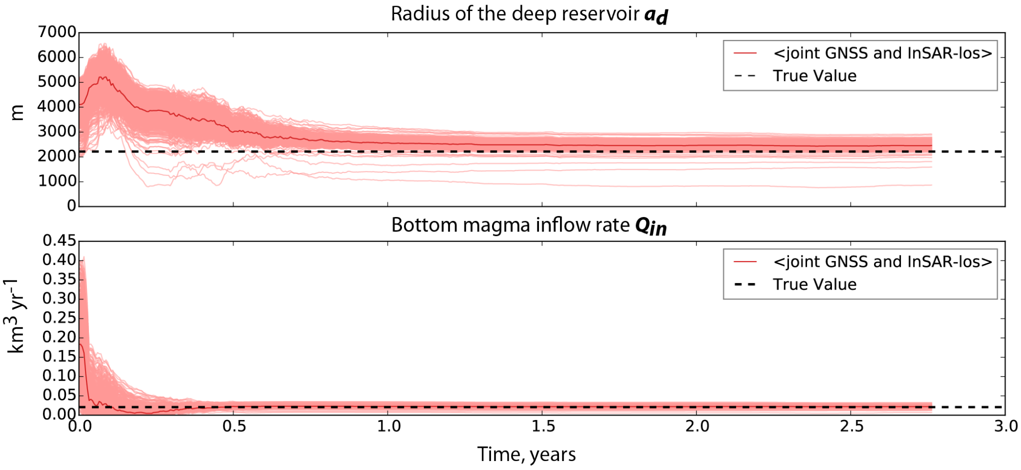

Figure A.2: The EnKF-estimated (A) overpressures and (B) uncertain model parameters after performing state-parameter estimation using jointly GNSS and descending InSAR data. Note that we used prior distribution for the uncertain parameters that are similar to Figure 15C. The red solid lines are the mean of the ensemble whereas the pink lines represent each of the ensemble members.

Appendix B

Supplementary material: Chapter 4

B.1 Assimilating limited amount of data with gaps

Recall that in **section 3.4**, we are able to estimate the overpressures but not the uncertain model parameters given a GNSS-like dataset with 10 data points (i.e. 5 radial and 5 vertical components) every assimilation time step. Here, we adopt a similar setup, except that in this case we introduce gaps in the data (i.e. gray areas in **Figures B.1** and **B.2**). Results show that if the gap in the data is relatively short, there is almost no effect in the estimations. However, significant results can be obtained once data is not available for a long period of time or if we try to forecast the behavior of the system in a relatively large time window (**Figure B.1**). Obviously, the inability of the filter to resolve the true behavior of the overpressures is due to the wrong estimations of the non-evolving uncertain parameters. One way to reconcile this is to "re-propagate" the dynamical model using the values of the uncertain model parameters at the analysis step. Basically, after each assimilation step, t_{i+1}: 1) we will take the values of the uncertain parameters (i.e. a_d and Q_{in}), 2) re-run the forward model from t_0 up to t_{i+1} using the values of the uncertain parameters and then 3) take the values of the state variables (i.e. overpressures) at t_{i+1}. **Figure B.2** illustrates the result of re-running the forward model after the analysis step. However, there is a caveat in doing this additional step—the uncertain parameters are assumed constant in time. When the uncertain parameters tend to vary in time, performing this additional step may force the parameter to behave "constant", hence it may depreciate the capability of EnKF to track parameters that can vary in time.

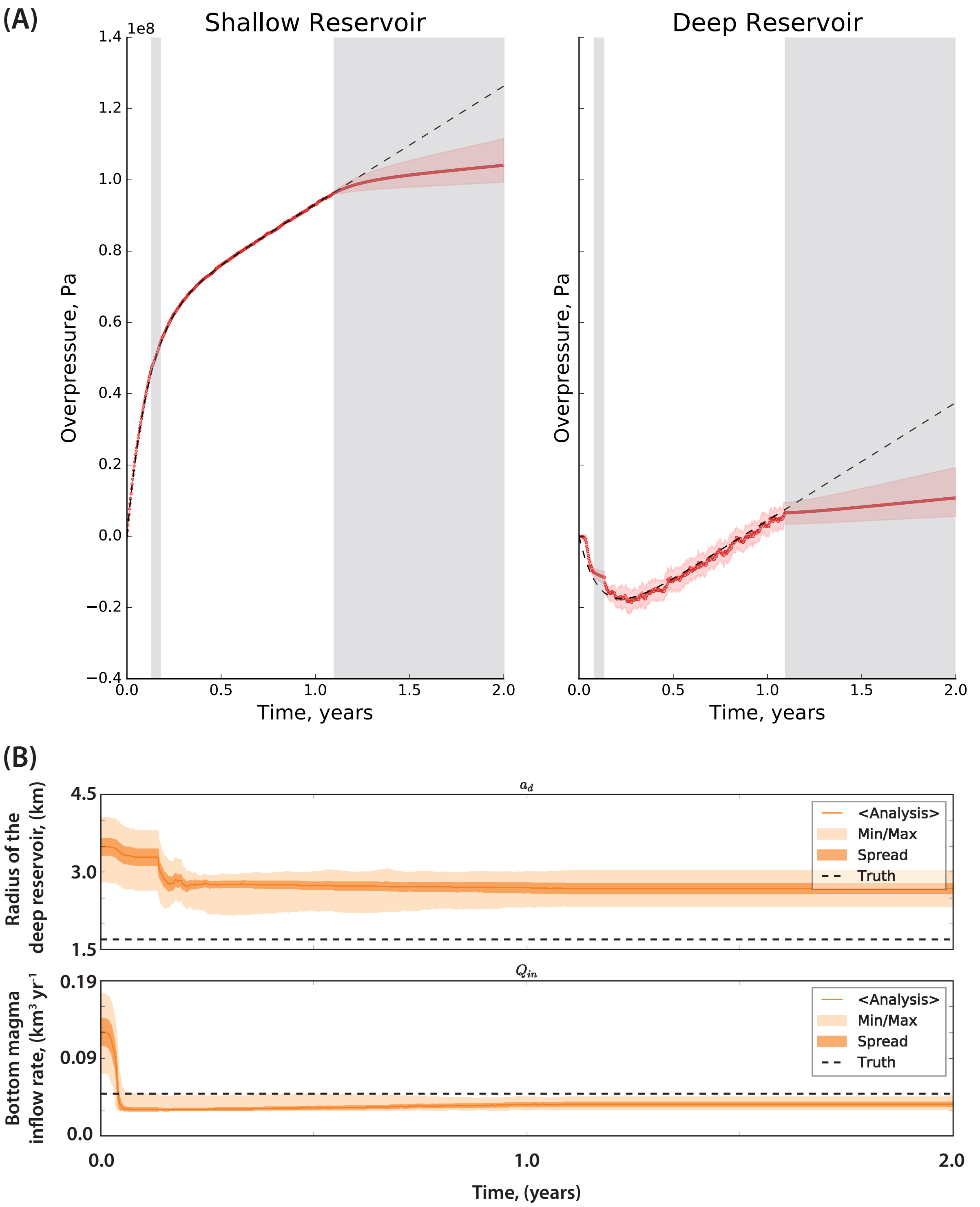

Figure B.1: The resulting (A) overpressures and (B) uncertain model parameters after assimilating data with gaps. The gray area in (A) emphasizes the time where gaps in the data are introduced. The black broken lines represent the ground truth.

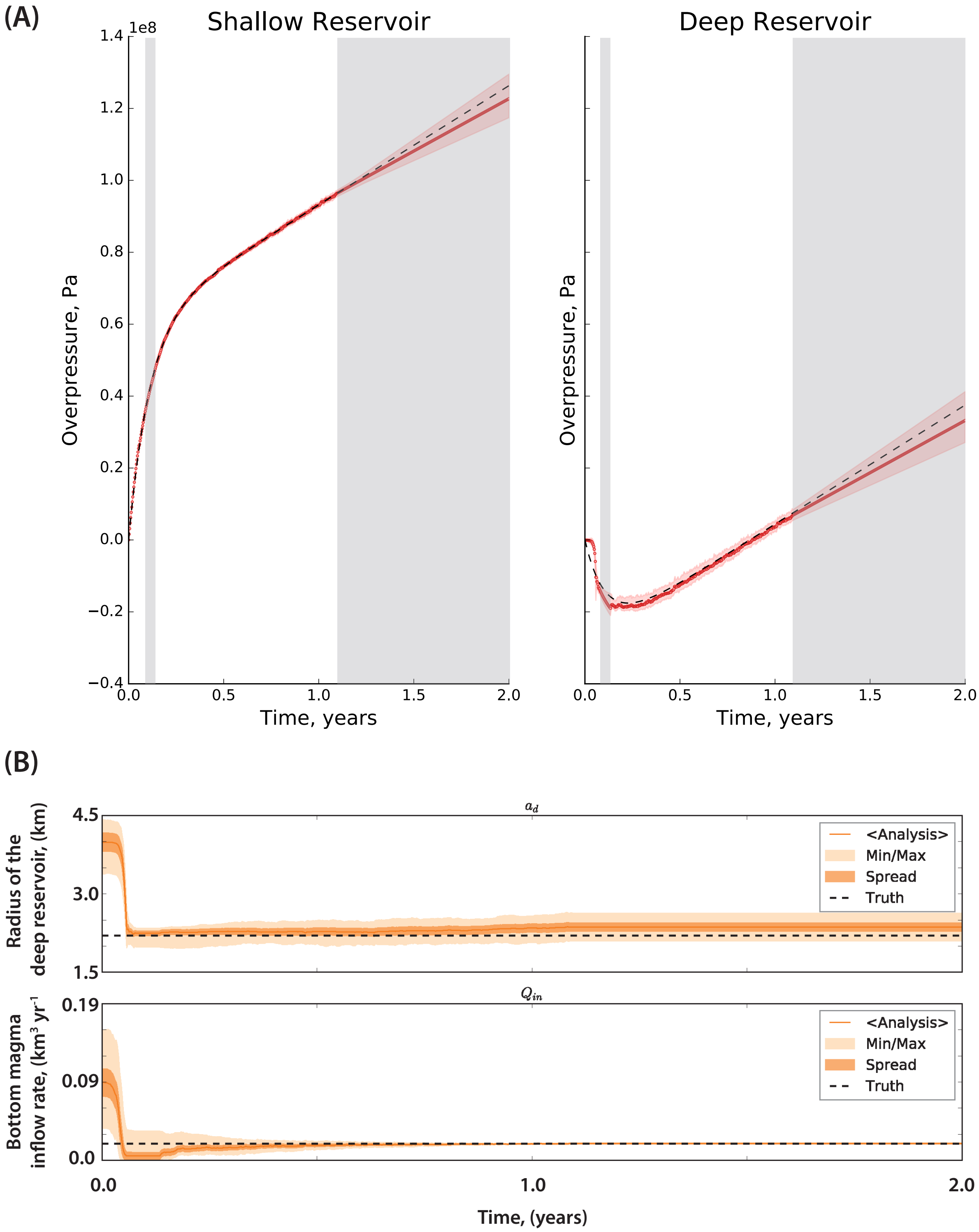

Figure B.2: The resulting (A) overpressures and (B) uncertain model parameters after assimilating data with gaps and subsequently "re-running" the forward model using the estimated values of the uncertain parameters at the analysis step (see **Appendix B.1** for details). The gray area in (A) emphasizes the time where gaps in the data are introduced. The black broken lines represent the ground truth.

B.2 Diagnostic tools

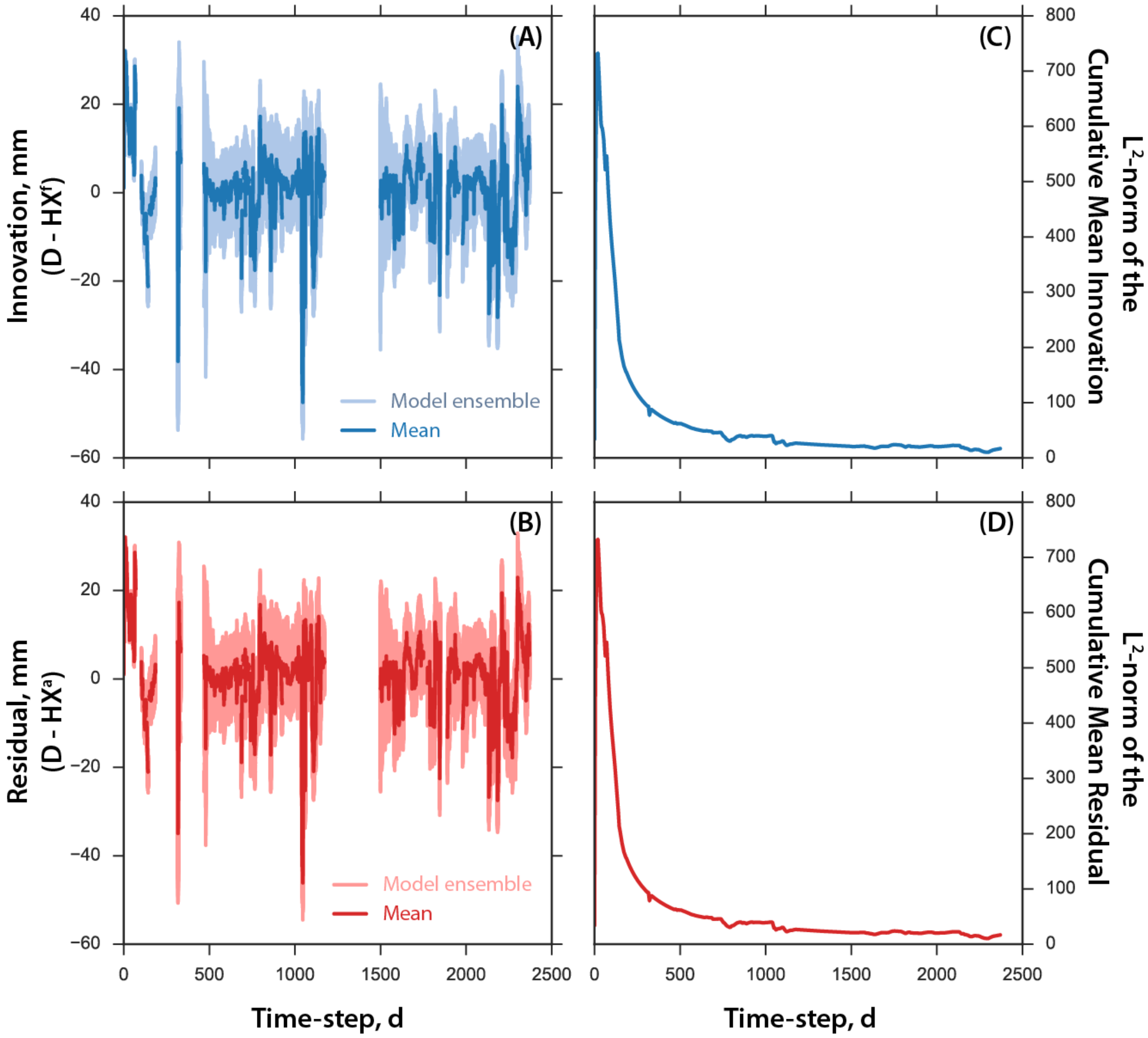

Figure B.3: The (A) innovation and (B) residual vectors as well as the L^2-norms of the (C) cumulative mean innovation and (D) cumulative mean residual.

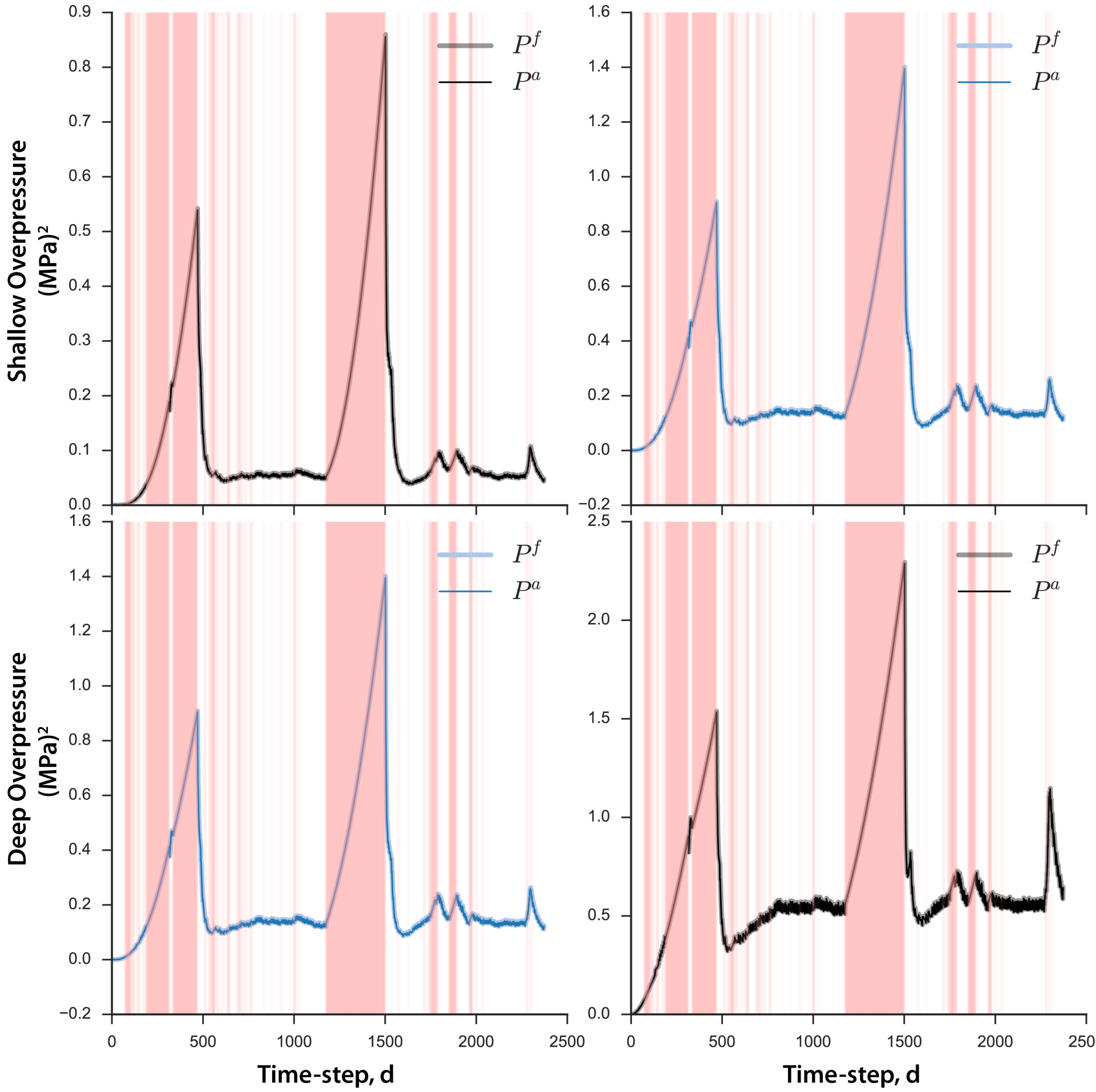

Figure B.4: The evolution of the error covariance of the state variables (ΔP_s and ΔP_d) before (i.e. forecast error covariance, P^f) and after (i.e. analysis error covariance, P^a) the correction given by the observations. The correction is in the order of $(0.001MPa)^2$ such that it appears almost overlapping in this figure. The pink lines correspond to the absence of data to assimilate. In **Figure B.5** we provide a closer look to the covariances during the last few days prior to the 2011 eruption. Note that the square root of the diagonal is simply the standard deviation of the overpressures.

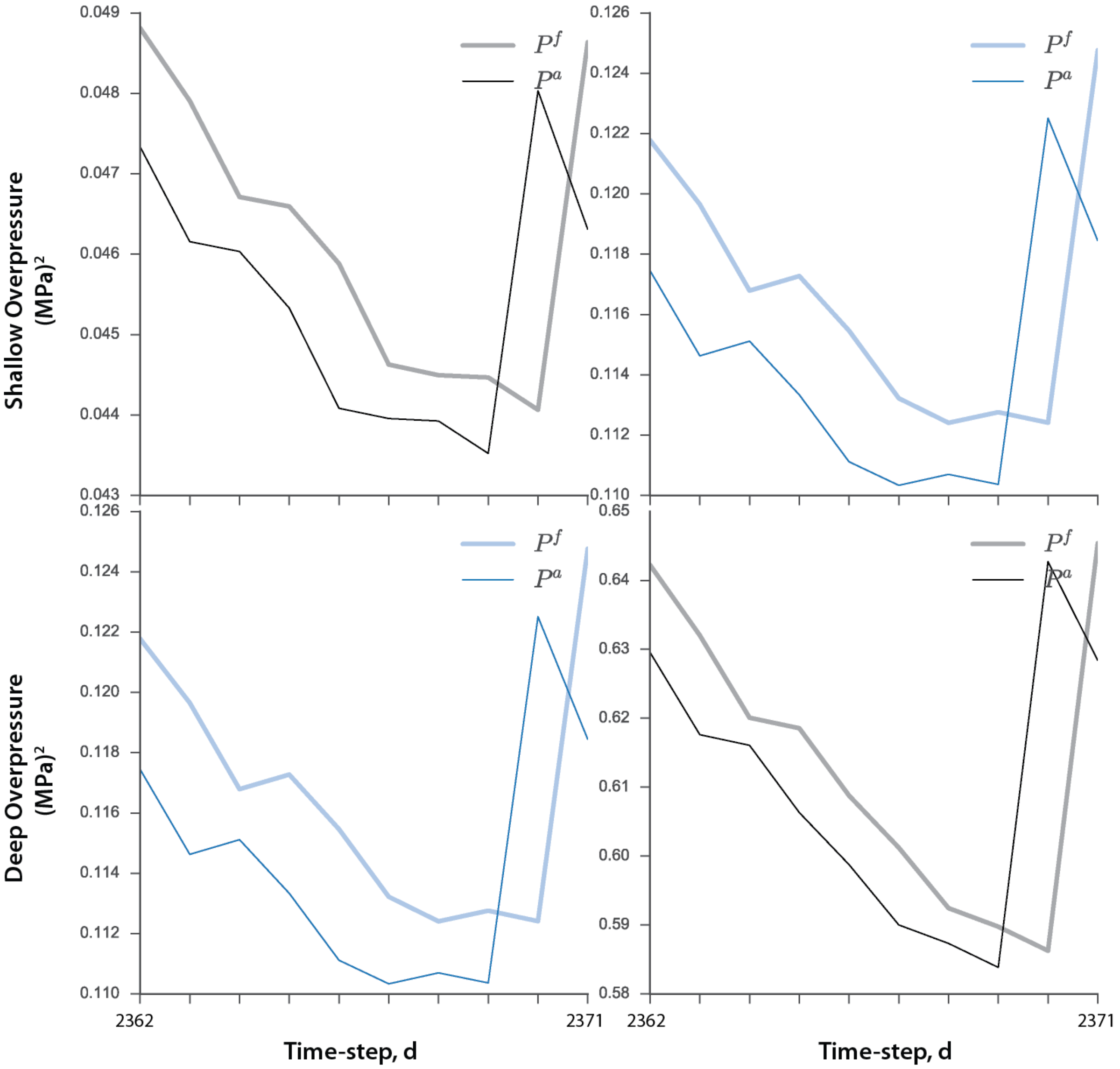

Figure B.5: A closer look on the evolution of the covariance of the state variables (ΔP_s and ΔP_d) before (i.e. forecast covariance, P^f) and after (i.e. analysis covariance, P^a) the correction given by the observations, 10 days to eruption. The square root of the diagonal is simply the standard deviation of the overpressures.

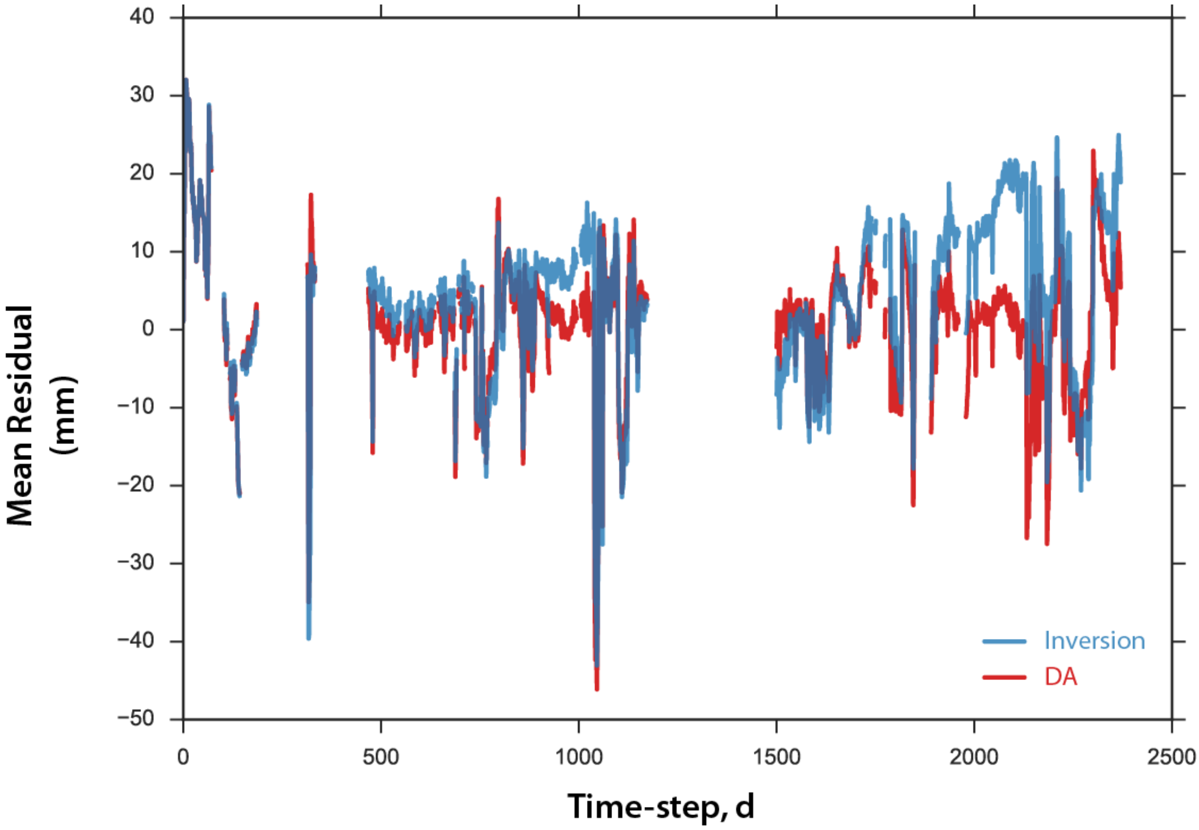

Figure B.6: Mean residual of Bayesian-based inversion (MCMC) and data assimilation (EnKF). The average residual over time is ~ 0.71 mm and ~ 4.10 mm for EnKF and MCMC, respectively.

B.3 Using the entire 2004-2011 inter-eruptive dataset

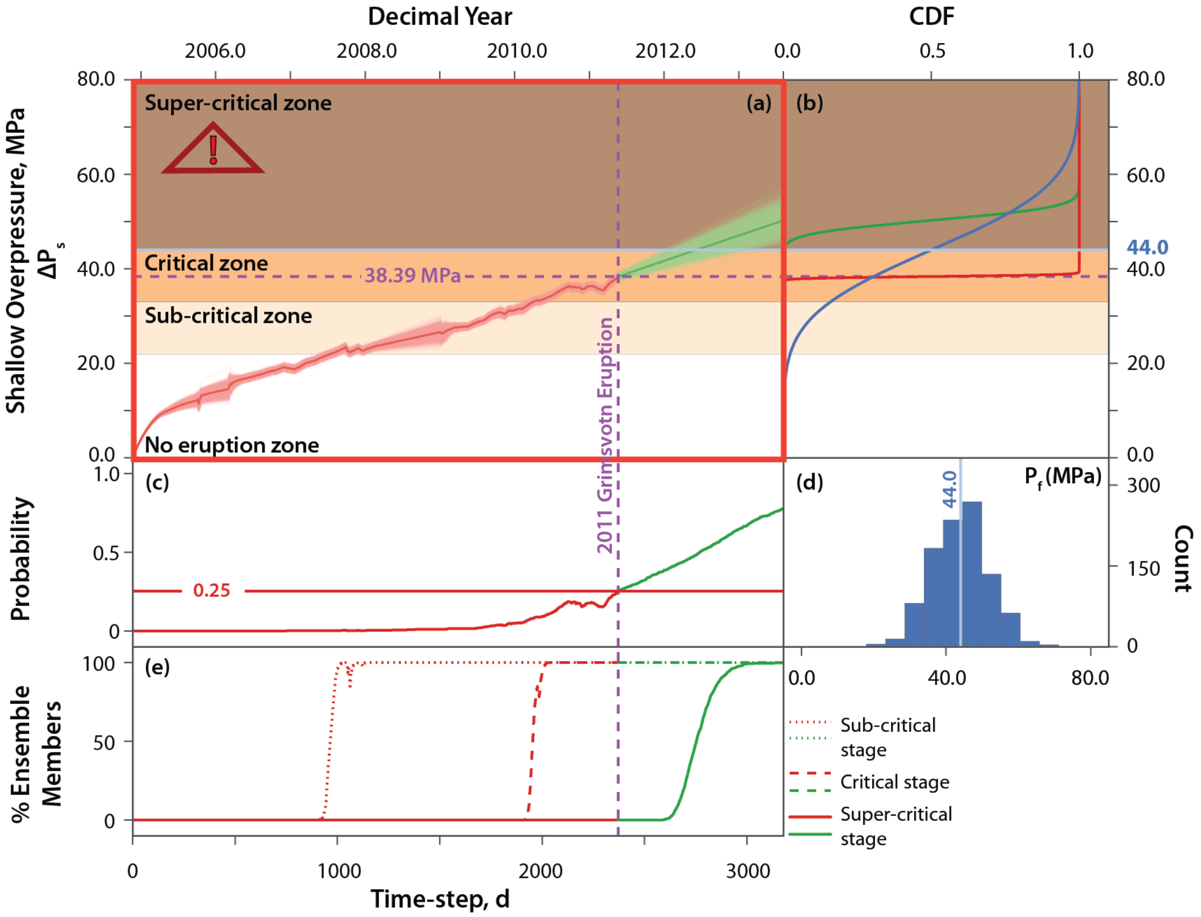

Figure B.7: (A) The evolution of the EnKF-derived shallow overpressure embedded on the eruption zones—based on using the entire 2004-2011 radial displacement dataset for the step-1 of our approach as described in **section 4.3.2**. Note that we define the eruption zones according to the estimated rock tensile strength in Iceland which consequently provides the failure overpressure value (i.e. P_f) needed to trigger the rupture of a magma chamber (i.e. Albino *et al.* [2010]). (B) The cumulative distribution function (CDF) illustrating the failure overpressue (blue) as well as the overpressures at the end of the assimilation window (red) and at the end of free-run (green). Note that the latter is performed just after the assimilation to further predict the evolution of the overpressure. (C) The probability of eruption calculated from the N-ensemble of models that exceeded the failure overpressure described by the distribution in (D). (E) The percentage of ensemble members entering each eruption zones as a function of time.

Appendix C

Supplementary material: Chapter 4 and 5

C.1 GPS data and pre-processing

GPS data are analyzed using the Bernese 5.2 software, with absolute antenna phase center offset models, together with precise orbits, earth rotation parameters, ocean tidal loading and atmospheric tidal loading estimates. Velocities and time series were estimated in the ITRF2014 reference frame (Dach *et al.* [2015]) with discontinuities associated with this reference frame and expressed in terms of the plate boundary reference frame (Reverso *et al.* [2014]). We followed the resolution strategy with (1) an initial ionosphere-free analysis with calculation of the residuals; (2) a residual analysis; (3) code-based wide-lane ambiguity resolution for all baselines (Wübbena [1985]), using differential code bias (DCB) files when available and calculation of the ionosphere-free solution with the introduction of resolved Melbourne-Wübbena linear combination ambiguities; (4) phase-based wide-lane (L5) ambiguity resolution for baselines < 200 km and computation of the ionosphere-free solution with the introduction of resolved ambiguities; (5) resolution of the previously unresolved ambiguities for baselines < 2000 km using the quasi ionosphere-free strategy of resolution; (6) direct L1/L2 ambiguity resolution for baselines < 20 km with the introduction of an ionosphere model; (7) calculation of the normal equations; (8) a compatibility test between the daily free solution and ITRF2014 solution, selection of compatible ITRF2014 stations and (9) transformation of the daily normal equation in the ITRF2014 reference frame with a six-parameter Helmert solution (three translation parameters and three rotation parameters) using the ITRF2014 selected stations (BARH, BOGO, EPRT, ESCU, HERT, HLFX, KARL, KHAR, NEWL, REDU, RIGA, SASS, SCH2, SHE2, SKE0, STAS, THU2, THU3, TRDS, VARS, VOL0). During these steps, site-specific troposphere parameters are estimated every two hours. Normal equations are analyzed together to determine accurate velocities in the ITRF2014 reference frame with the introduction of ITRF2014 coordinates and velocities. For time series of stations supposed to be linear (not GFUM), outliers and new discontinuities were detected using the "Find Outliers and Discontinuities in Time Series" tool in the Bernese 5.2 software that reduces, step-by-step, the discrepancy between the functional model and the time series due to statistical adjustment (Ostini *et al.* [2008]), taking annual and seasonal fluctuations into account. As the Bernese 5.2 software underestimates the daily errors given that systematic errors or mismodeled parameters are not included in the formal error (Dach *et al.* [2015]), we rescaled the formal errors by multiplying them by a factor of 10 to obtain a more realistic estimated error.

Note that the tectonic trend at GFUM GPS station is removed with slopes of -2.7 mm yr^{-1} and 7.5 mm yr^{-1} for the NS and EW components, respectively (Reverso *et al.* [2014]).

C.2 Model and DA strategy applied to Grímsvötn

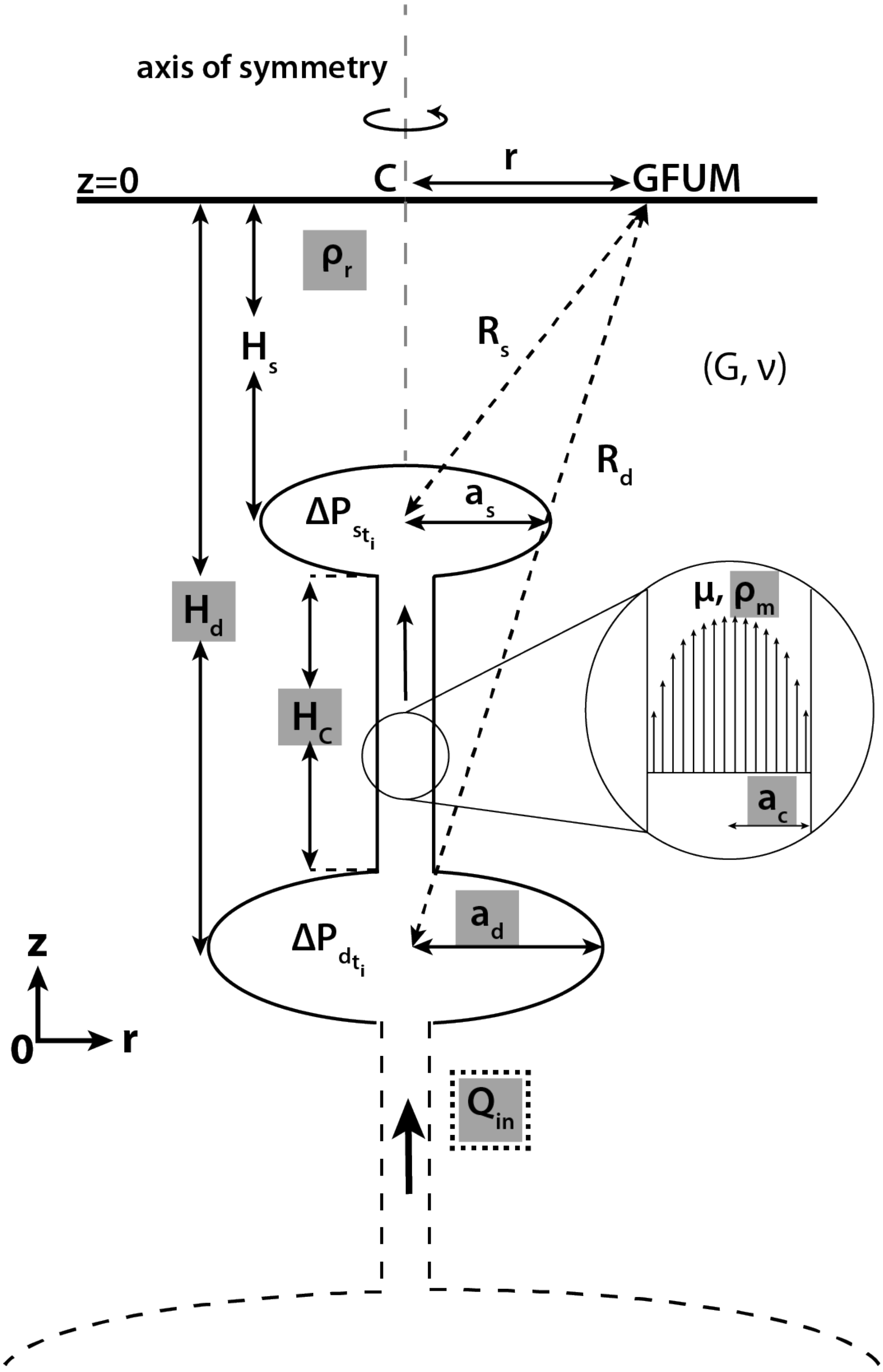

Figure C.1: Schematic sketch of the two-chamber model, modified after Reverso *et al.* [2014] and Bato *et al.* [2017]. The uncertain model parameters in this study are highlighted in gray. Except for the bottom magma inflow rate, Q_{in}, which is bounded by a dotted box, the rest are considered as non-evolving uncertain parameters. The GFUM GPS station, with a distance r from the center of the volcanic system C, records the displacement induced by the two reservoirs. $R_s = \sqrt{r^2 + {H_s}^2}$ and $R_d = \sqrt{r^2 + {H_d}^2}$ are the distances of the shallow and deep reservoirs from GFUM station, respectively.

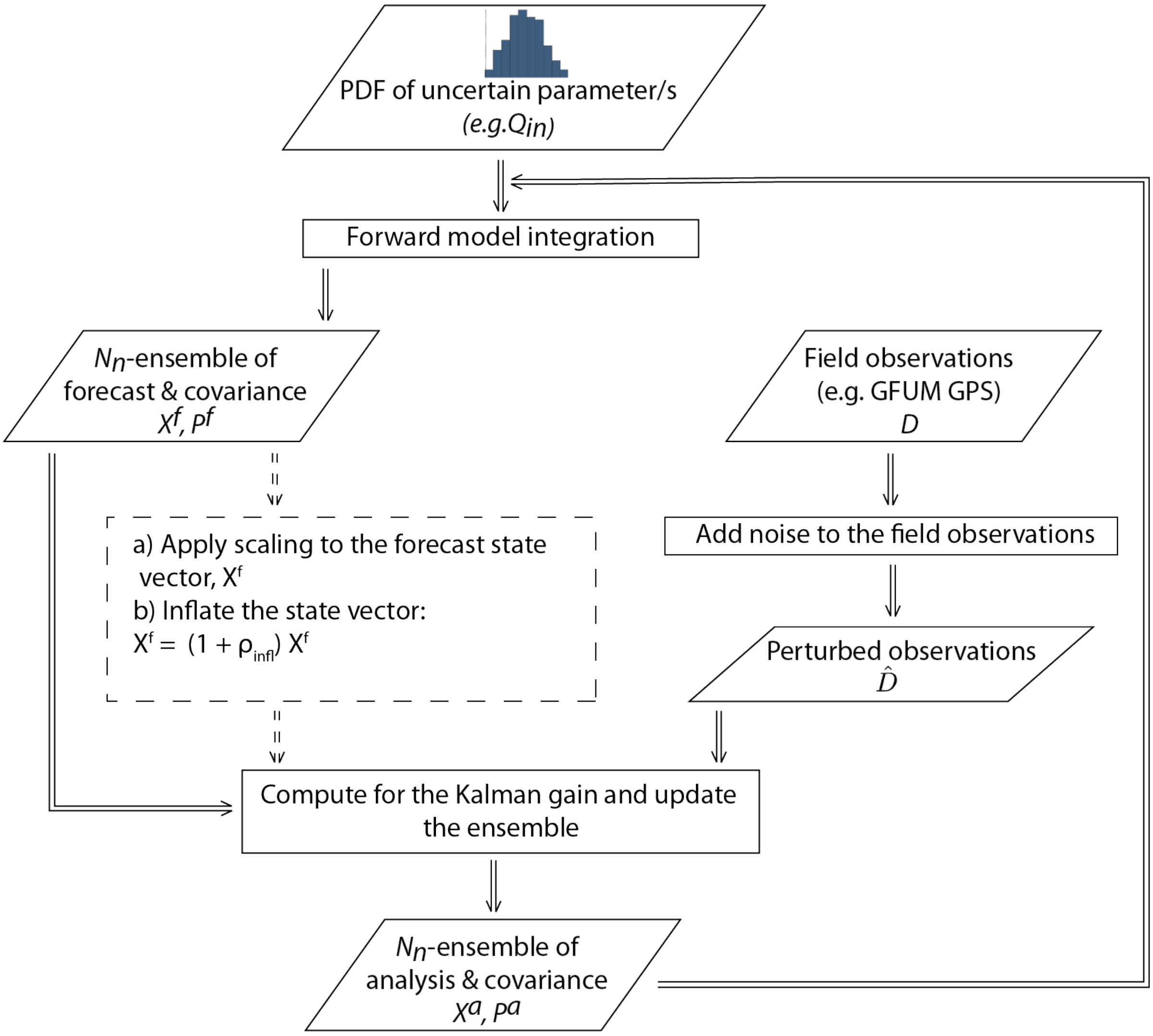

Figure C.2: The step-by-step EnKF strategy implemented in this study, modified from **Chapter 3**. The broken border and lines imply that the step is a tuning step for the assimilation.